UNIVERSITÀ DEGLI STUDI DELL'AQUILA

DIPARTIMENTO DI Ingegneria Industriale e dell'Informazione e di Economia

Dottorato di Ricerca in INGEGNERIA INDUSTRIALE, DELL'INFORMAZIONE E DI ECONOMIA
Curriculum INGEGNERIA MECCANICA E GESTIONALE
XXXVII ciclo

Titolo della tesi

Wire-arc additive manufacturing: Process optimization, advancements, in-process data monitoring, and material characterization.

SSD: IIND-04/A – TECNOLOGIE E SISTEMI DI LAVORAZIONE

Dottorando
Ing. Phanidra Babu Yanala

Coordinatore del corso	Tutor
Prof.ssa Katia Gallucci	Prof. Alfonso Paoletti
	Co-Tutor
	Prof. Francesco Lambiase

A.A. 2023/2024

Abstract

This thesis explores the optimization and characterization of Wire Arc Additive Manufacturing (WAAM) for low-carbon steel, aiming to enhance deposition quality, geometrical precision, and material properties. Preliminary experiments established a processing window by analyzing the influence of key process parameters power, travel speed, wire feed speed, and stand-off distance on bead geometry and material properties. Advanced methodologies, such as force air cooling, in-process data monitoring and microstructural analysis, were utilized to evaluate the thermal and mechanical behavior of WAAM-fabricated components. The research revealed that bead geometry is significantly influenced by travel speed and wire feed rate, while the impact of stand-off distance was minimal within the tested range. Multi-layer stacking highlighted the role of thermal cycling in inducing anisotropic material properties. Thermal analysis showed that the first layer endured thermal cycles exceeding 500°C even after the deposition of 10 layers. In-process data monitoring demonstrated that current fluctuations are more sensitive indicators of deposition conditions compared to voltage. Furthermore, the power flow was highest during the initial layers and stabilized as deposition progressed. A linear increase in resistance with thicker substrates and cumulative average power drop of less than 9% were observed. Geometrical challenges, such as overhanging angles and layer height reduction, were thoroughly investigated, identifying the limitations of unsupported deposition and emphasizing the necessity for real-time process adjustments. Defects, including porosity, spatter, oxidation layers, and microcracks, were analyzed, with a focus on the influence of melt-pool dynamics and thermal gradients. Material properties exhibited variation along the deposition height, with grain size decreasing from the bottom to the top of the structure. Faster travel speeds resulted in finer grains and higher microhardness due to accelerated cooling rates. The implementation of advanced techniques, such as forced air cooling between layers, demonstrated improvements in microhardness and overall mechanical properties. The integration of pre-processing strategies, such as G-code modification, proved effective in enabling the in-house fabrication of WAAM components. These findings underscore the importance of process optimization and defect mitigation strategies to advance WAAM as a reliable and efficient manufacturing technology for industrial applications.

Acknowledgment

Words can't express my gratitude towards my Professors, Alfonso Paoletti and Francesco Lambiase, for their expertise, invaluable patience and input I have received during this thesis, have been instrumental in shaping this thesis. My sincere gratitude to Prof. Antoniomaria Di Ilio for the intensive support at the beginning of the thesis.

Additionally, this endeavor would not have been possible without the support of the National Operational program (PON) on Research and Innovations, for funding my research. My extended appreciation goes to the faculty and staff of the Department of Engineering Industrial and Information and Economics (DIIIE) and university of L'Aquila (UNIVAQ) for providing the support and facilities.

And I would like to thank my family and friends, especially my parents, brother, sister and brother-in-law, for their unconditional love and support during this research.

Last, but not least, I am eternally grateful to the city of L'Aquila for becoming my second home.

Table of Contents

Table of Figures

Table of Tables

Chapter 1 – Introduction to AM

Additive manufacturing (AM), also known as rapid prototyping, Solid free-form manufacturing, Direct digital manufacturing directly uses a 3D model to fabricate three-dimensional parts by joining material, layer upon layer. In contrast to the conventional manufacturing process, AM does not need specific equipment like mold, or tools during manufacturing, for this reason, it is also known as direct manufacturing. The general steps involved in the AM process are the following:

1. Part design
2. part conversion
3. Part preparation
4. Part manufacturing
5. Post-processing

A 3D model will be created using standard 3D modeling software, which will later be converted to standard triangle language (STL) or other standard formats. The converted file will be loaded into the slicing/preprocessing software and operations like part orientation, support generation, manufacturing parameters, etc., will be performed. This preprocessing file contains all the information required by the 3D printing machine, such as tool path, material feed rate, deposition speed, etc., depending on which AM technology will be used to fabricate that part. The manufacturing phase involves loading the prepared file onto an additive manufacturing machine and parts will be fabricated layer by layer. Finally, the fabricated part will be dismounted from the machine, and post-processing operations like support removal, and machining will be performed.

Since the early development of AM processes such as stereolithography (SLA) and Fused Deposition Modeling (FDM) which were adopted to produce plastic prototypes, new technologies based on the same principle "build a 3D object layer-by-layer" have been developed. This has led to a new branch in the manufacturing outlook which has been standardized through the ISO/ASTM 52900:2021 standard. (revised from ASTM52900:2015). According to the ISO/ASTM standard, AM technologies are divided into 7 categories [1], namely Binder jetting (BJT), Direct energy deposition (DED), Material extrusion (MEX), Material jetting (MJT), Powder bed fusion (PBF), Sheet lamination (SHL), VAT photopolymerization (VPP).

Each AM process employs a unique approach to build a part layer by layer until the final structure is achieved. For instance, one method involves using a nozzle to melt and deposit material, creating a part directly from feedstock such as filament or wire [2]. Another technique melts powdered material (often metal) laid on a bed, using a high-energy source such as a laser or electron beam to fuse the particles together layer by layer [3]. Yet another method uses a polymer to bind powder layers, forming a green part that is later placed in a furnace. During the sintering process, the polymer binder melts away, and the powder particles fuse, resulting in the final part [4]. Each of these methods offers unique advantages and is suited to specific applications, and the intricacies of these processes are detailed in the following sections. The time required to additively manufacture a part varies significantly, depending on the chosen AM process and the size and complexity of the part. For smaller, less intricate components, the process may take only a few hours. However, for larger and more complex structures, especially those requiring intricate details or multiple material changes, the production time can extend to several days. This variability highlights the importance of process selection and optimization to meet specific manufacturing needs while ensuring efficiency and quality.

1.1 AM from rapid prototyping to new industrial revolution

Since its initial role as a tool for rapid prototyping, additive manufacturing (AM) has undergone remarkable advancements, transforming into a versatile technology capable of producing high-quality, production-ready parts. This evolution has been driven by continuous improvements in processes, materials, and associated technologies, enabling AM to expand its scope across diverse industries. From the aerospace and automotive sectors to healthcare and beyond, the adoption of AM is now largely attributed to these transformative advancements. Modern AM processes now accommodate a wide range of structural materials with enhanced mechanical and chemical properties, including plastics (thermoplastics and thermosetting polymers), composites, metals, and ceramics. These material advancements are critical for meeting the stringent requirements of industries like aerospace, automotive, and healthcare, where materials must demonstrate exceptional durability, strength, and precision. The demand for faster production is ever-increasing in today's fast-paced industrial landscape. Developments in print speed technologies, such as binder jetting and multi-laser scanning in powder bed fusion (PBF), have significantly reduced production time, making AM a viable alternative to traditional manufacturing techniques. These innovations not only boost scalability for large-scale production but also enhance the overall efficiency of manufacturing operations. AM has traditionally faced challenges related to surface quality, particularly the staircase effect, a byproduct of its layer-by-layer approach. However, significant enhancements in print resolution have improved the precision and quality of AM parts. This progress has enabled the creation of intricate designs with highly detailed features, which are critical in applications such as medical implants and microchip manufacturing. A defining innovation in AM is the advent of multi-material printing, which allows the integration of diverse material properties within a single build. This capability addresses challenges that are difficult to tackle with traditional processes. For instance, manufacturers can now produce multi-functional components, combining rigidity in some regions with flexibility in other regions, thereby broadening the functionality and versatility of AM-produced parts. Concerns about reliability and quality assurance have often slowed AM adoption in industrial manufacturing. The integration of automation and AI technologies into AM workflows has mitigated these concerns. By enabling real-time quality monitoring, optimized print paths, and predictive analytics for material properties, these advancements have reinforced confidence in the consistency and reliability of AM processes. One of the most compelling advantages of AM lies in its sustainability. Unlike traditional subtractive manufacturing, which generates significant waste by removing material, AM deposits material only where it is needed. This not only minimizes waste but also maximizes material utilization, reducing both cost and environmental impact.

These advantages have propelled AM into diverse sectors, including aerospace and defense, automotive, biomedical, and construction, where the ability to optimize material use is crucial. For example, aerospace and defense industries benefit from AM's ability to produce lightweight yet robust components while significantly reducing material waste. Moreover, AM's capability for on-demand production eliminates the need for large inventories, reducing storage costs and enabling manufacturers to respond swiftly to market demand. This lean manufacturing approach not only enhances resource efficiency but also minimizes risks of overproduction and associated losses. A wide variety of AM processes are available to produce metallic parts, including powder bed fusion, sheet lamination, binder jetting, direct energy deposition, and material extrusion. Indirect additive manufacturing methods, where metal parts are created using plastic models, also offer flexible solutions for specific applications. Comparisons between these processes continue to be a focus of research and industrial application, highlighting the strengths and limitations of each. Future advancements in AM are expected to further elevate its capabilities. Research into recyclable materials, intelligent systems, advanced simulation software, and high-speed hybrid manufacturing technologies is anticipated to enhance the competitiveness, efficiency, and sustainability of AM in industrial applications. These developments promise to strengthen AM's role as a cornerstone technology in modern manufacturing, enabling industries to achieve new heights of innovation and adaptability.

1.2 Metal AM Processes

This section explores the primary technologies within the metal additive manufacturing (AM), focusing on powder bed fusion (PBF), direct energy deposition (DED), composite extrusion modeling (CEM), and friction stir additive manufacturing (FSAM). Each of these technologies plays a pivotal role in advancing the capabilities of metal AM, catering to diverse industrial requirements through their unique methodologies and applications.

1.2.1 Direct energy deposition

Direct energy deposition of the AM process involves an energy source (laser/electron beam/electric arc), feedstock, torch head, shielding gas, carrying gas (if the feedstock is a powder), as schematized in Figure 1.

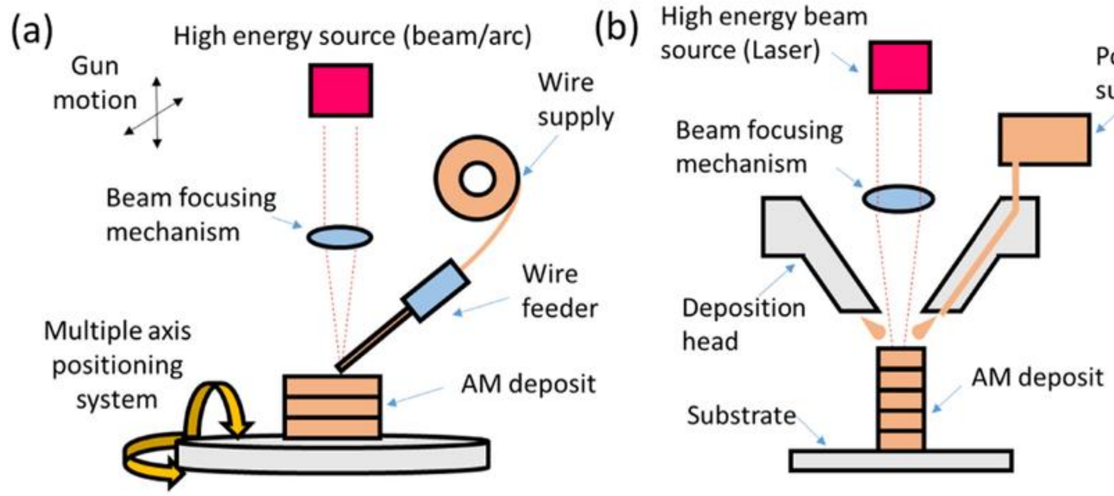

Figure 1. Schematic of DED method (a) Wire-feed DED, (b) Powder-feed DED [5]

During the process, the heat source melts the substrate, and the feed material will be deposited, by creating a bond between substrate and deposited layer. The DED process takes place in an open space and can be easily performed through a robotized motion system. A shielding gas is used to protect the melt-pool from atmospheric contaminants (e.g. Oxygen, nitrogen, moisture) [6], stabilizing the melt-pool, and ensuring the consistent material deposition. Typically, these shielding gases are pure Orgon or mix of Orgon. The DED system, origins from the cladding process which is used to repair or provide a functionalized (e.g. corrosion resistance, hardness) external layer of material to a substrate. In DED processes, the material is provided in the form of powder or wire. Limitations and drawbacks of DED process including:

- Use of expensive heat sources: DED processes often require high-power lasers or electron beams as heat sources, which can be costly to acquire and maintain. The need for these expensive heat sources adds to the overall equipment investment required for DED technology.
- Lower precision: Compared to some other additive manufacturing techniques, DED may exhibit lower precision in terms of dimensional accuracy and surface finish. This limitation can impact the suitability of DED for applications requiring tight tolerances or fine feature resolution.
- Higher distortion: DED processes typically involve localized heating and rapid cooling of deposited material, leading to higher levels of distortion compared to processes with heated chambers. The absence of a heated chamber in DED systems can exacerbate distortion issues, particularly for large or complex parts.
- Lower surface regularity: DED-produced parts may exhibit lower surface regularity or roughness due to factors such as material deposition patterns and rapid solidification. Achieving smooth and uniform surface finishes with DED may require additional post-processing steps, such as machining or polishing.
- Adoption of powders: DED processes rely on the use of metal powders as feedstock materials. The adoption of powders introduces challenges related to powder handling, storage, and quality control. Ensuring a consistent supply of high-quality powders that meet the specifications of DED systems can be a logistical and cost-related challenge.

When the feedstock material is in the form of wire, alternative heating sources are often adopted. Wire Arc Additive Manufacturing (WAAM) represents a valid alternative when wire feedstock material is adopted. This enables significant advantages over powder DED processes, including lower equipment and feedstock cost, no issues concerning powder handling and maintenance, and higher deposition rates. lower feedstock cost as well as lower investment cost and higher productivity. In addition, no beam reflections of X-Ray production are produced. Indeed, despite its advantages, WAAM processes also present certain drawbacks:

- Lower precision compared to Directed Energy Deposition (DED): WAAM typically offers lower precision in terms of dimensional accuracy and surface finish when compared to DED processes. This limitation may impact the suitability of WAAM for applications requiring fine feature resolution or tight tolerances.

- High distortion due to absence of heated chambers: Similar to DED, WAAM processes can experience significant distortion during fabrication, particularly for large or complex parts. The absence of a heated chamber in WAAM systems contributes to this issue by allowing rapid cooling of deposited material, leading to residual stresses and distortion.
- Even lower surface regularity: WAAM-produced parts may exhibit even lower surface regularity or roughness compared to DED processes. Factors such as material deposition patterns and arc stability issues can contribute to variations in surface finish, necessitating additional post-processing steps to achieve desired surface quality.
- Arc stability issues: WAAM processes rely on electric arcs to melt and deposit metal wire, and maintaining stable arc conditions is critical for consistent deposition. However, arc stability issues, such as arc wandering or flickering, can occur during WAAM fabrication, leading to variations in deposition quality and potentially affecting part integrity. Addressing these arc stability issues is essential for improving process reliability and product quality in WAAM.
- Limited resolution and feature size: WAAM processes generally offer lower resolution and feature size capabilities compared to DED techniques. The larger diameter wire used in WAAM deposition can limit the achievable level of detail and intricacy in fabricated parts, making it less suitable for applications requiring fine geometrical features or intricate designs.
- Increased material waste: WAAM processes may generate more material waste compared to DED methods, particularly during startup, shutdown, and transition between build layers. The nature of wire feedstock in WAAM can lead to inefficiencies in material usage, resulting in higher material costs and environmental impact.
- Limited surface quality and post-processing requirements: Parts produced using WAAM often require more extensive post-processing to achieve the desired surface finish and dimensional accuracy compared to DED processes. The inherent roughness and irregularities in WAAM-deposited surfaces may necessitate additional machining, grinding, or surface finishing operations, adding to the overall manufacturing time and cost.
- Greater susceptibility to porosity and inclusions: WAAM processes may exhibit increased susceptibility to defects such as porosity and inclusions compared to DED techniques. The interaction between the welding arc and wire feedstock can introduce gas entrapment and non-metallic inclusions in the deposited material, potentially compromising part quality and mechanical properties.

1.2.2 Powder bed fusion

Powder bed fusion (PBF) processes (typically, selective laser sintering, selective laser melting, electron beam melting) involve an energy source (Laser/electron beam), that sinters or melts metal particles inside a vacuum chamber. PBF requires different equipment including a vacuum chamber, heating chamber (to reduce thermal distortions within the chamber), powder metal particles, powder roller, as schematized in Figure 2.

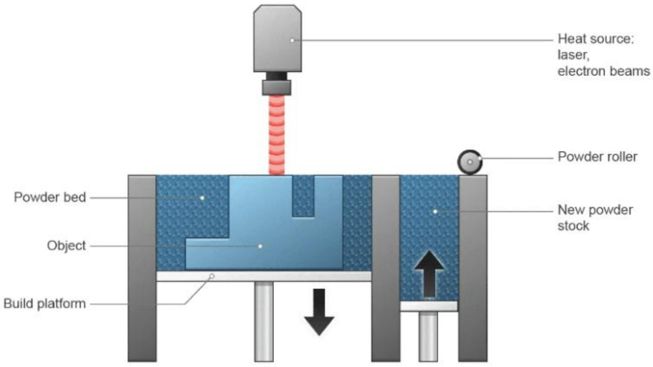

Figure 2. Schematic of powder bed fusion process

PBF is typically performed using two chambers: the build chamber where the metal powder is scanned by the heating source to produce the 3D part and the alimentation chamber which holds fresh powder which will be supplied at each layer through the rollerblade. The process can be subdivided into three steps: 1) build platform motion: the platform moves downwards by the height of layer, 2) powder supplying: the powder coming from the powder stock chamber is spread over the build chamber through a powder roller and 3) scanning the layer by laser or electron beam. This process continues until the job is completed. Therefore, the building process is affected by downtime owing to the powder spreading over the build chamber. This particularly reduces the productivity of the process since the leveling should be performed with relatively slow roller blade speeds. Indeed, a good and homogeneous filling of the build chamber with a uniform layer of fine powder is mandatory for the quality of the 3D print. This requires relatively slow powder roller motion. In addition, powder bed fusion processes are affected by the following limitations/drawbacks:

- Adoption of powders: Powder bed fusion processes require the adoption of specific powders with suitable characteristics, including particle size distribution, flowability, and chemical composition. Obtaining and maintaining a consistent supply of high-quality powders can be challenging and expensive.
- Build chamber leveling: Ensuring proper leveling of the build chamber is crucial for achieving uniform layer deposition and accurate part dimensions. However, maintaining precise chamber leveling throughout the printing process can be difficult, leading to potential geometric inaccuracies in printed parts.
- Adoption of high energy sources: Powder bed fusion processes typically utilizes high-energy sources such as lasers (200-1000 W) or electron beams (up to 10 kW) to selectively melt and fuse powder particles. The adoption of these high-energy sources introduces challenges related to equipment complexity, power management, and safety protocols.
- Reflectivity (laser source): Laser-based powder bed fusion processes are susceptible to issues related to laser beam reflectivity from metallic surfaces, which can cause undesired heating and melting of adjacent regions. Managing laser reflectivity requires careful control of laser parameters and material properties to minimize defects in printed parts.
- Electrical conductivity (electron beam melting): Electron beam melting (EBM) processes rely on the electrical conductivity of metallic powders to generate and control electron beams. However,

variations in powder conductivity can affect beam penetration and energy deposition, leading to inconsistencies in part quality and mechanical properties.

- Vacuum chamber: Electron beam melting processes typically require a vacuum chamber to maintain the necessary conditions for electron beam generation and control. Operating and maintaining a vacuum chamber adds complexity and cost to the manufacturing process.
- Heated chamber: To prevent premature cooling and thermal stresses in printed parts, powder bed fusion processes often utilize heated build chambers. However, maintaining precise chamber temperatures across large build volumes can be challenging, particularly for materials with high thermal conductivity or low melting points.
- X-ray protection (electron beam melting): Electron beam melting processes emit high-energy X-rays during electron beam interactions with the build material. Implementing adequate X-ray protection measures, such as shielding and safety protocols, is essential to ensure operator safety and regulatory compliance.
- High cost of equipment and powders: Powder bed fusion processes require specialized equipment and high-quality powders, which can be costly to acquire and maintain. The initial investment in equipment, as well as ongoing expenses related to powder procurement and equipment maintenance, contribute to the overall cost of implementing powder bed fusion technology.

1.2.3 Composite extrusion modeling

Composite Extrusion Modelling (CEM) involves metal powder filled thermoplastic composite wires. The amount of powder is typically higher than 95% in weight. The process is performed using a relatively cheap material extrusion machine that produces the “green part”. Thus, the 3D printed part is subjected to a debinding process (typically through a thermal and/or chemical process). This enables to produce the brown part. Then, a sintering phase is performed to achieve a high strength metal part [4], as schematized in Figure 3. The great advantage of Composite Extrusion Modeling relies in the possibility to use relatively low-cost equipment (FDM). However, the process is affected by the following limitations and drawbacks:

- Material Limitations: a reduced number of filaments and metals are available.
- Structural Integrity: Achieving consistent and reliable structural integrity in metal parts produced through CEM can be challenging, particularly in complex geometries or high-stress applications.
- Surface Finish: CEM may struggle to achieve high-quality surface finishes on metal parts, which can be crucial for certain applications or industries.
- Dimensional Accuracy: Maintaining precise dimensional accuracy can be difficult with CEM, leading to potential issues with part fit, assembly, and overall performance.
- Process Complexity: CEM processes may involve complex setups and parameter optimization, which can increase production time and costs.
- Post-Processing Requirements: Metal parts produced via CEM often require extensive post-processing steps, such as machining or surface treatments, to meet desired specifications.

- Cost Considerations: CEM for metal part production may involve significant equipment and material costs, making it less economically viable for certain applications compared to other manufacturing methods.
- Relatively low dimensions of the part (own to distortions occurring during debinding and sintering)
- Overall process complexity: The process requires three different steps (printing, debinding and sintering), as schematized in Figure 3**Error! Reference source not found.** In addition, inhomogeneous shrinkage occurring during debinding and sintering, and part distortion must be carefully accounted for correcting the component geometry previous of proceeding with 3D printing.

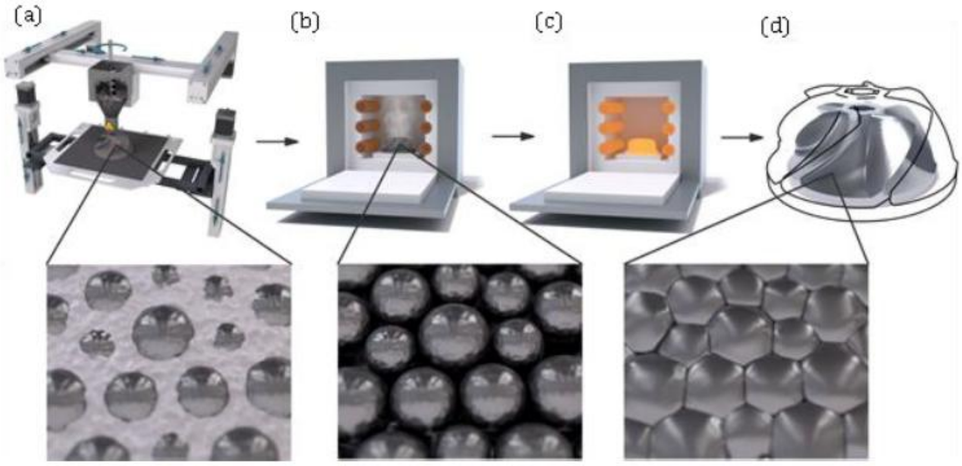

Figure 3. schematic of composite extrusion modeling process, a). 3D printing of green part, b) Debinding of green part in debinding furnace, c). Sintering of the resulting brown part in high temperature furnace, d). Final metal part. [4]

1.2.4 Friction stir AM

Similarly to friction stir welding, friction stir Additive Manufacturing involves the adoption of a consumable rod that is turned and pushed towards the substrate to deposit the material under a semisolid state, As reported in Figure 4. This involves several advantages over the DED processes since lower temperature and energy consumption, higher pressure and stirring effect which all promote the achievement of high strength components with fine microstructure and reduced porosity or gaseous inclusions.

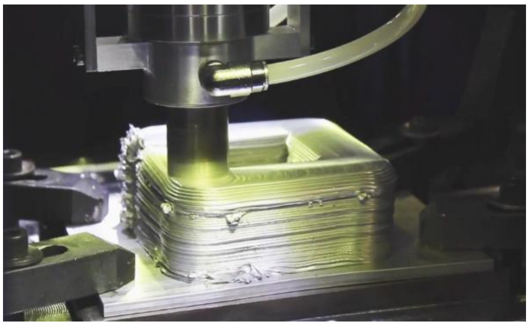

Figure 4. Friction stir AM

However, FSAM is also affected by the following drawbacks:

- Limited Build Speed: FSAM processes can be relatively slow compared to some traditional additive manufacturing techniques. This can be a limitation when rapid production is a key requirement.
- Equipment Complexity: The equipment required for FSAM can be complex and expensive. This may pose challenges for widespread adoption, particularly for smaller manufacturers.
- Surface Finish: Achieving a smooth surface finish can be challenging with FSAM. Post-processing steps may be required to achieve the desired surface quality, adding time and cost to the manufacturing process.
- Limited to Certain Geometries: FSAM may face challenges in producing complex geometries, and it may be more suitable for parts with simpler shapes.
- Material Restrictions: While FSAM can be applied to a variety of materials, there may still be limitations in terms of the types of alloys and composites that can be effectively processed using this technique.

1.3 Limits of metal AM processes compared to WAAM

A comprehensive comparison of WAAM with other additive manufacturing (AM) and traditional manufacturing techniques should address various aspects, such as complexity, part dimensions, production volume, dimensional accuracy, mechanical properties, and cost efficiency [7], [8]. Compared to other AM processes, DED processes like WAAM excel in producing large-scale components, with build sizes reaching cubic meters. This scalability is primarily constrained only by the CNC or robotic system reach [9]. In contrast, PBF techniques face significant limitations due to their reliance on enclosed build chambers and beam manipulation systems, such as galvanometers for laser sources. For instance, most selective laser melting machines are limited to parts no larger than 150 x 150 x 150 mm^3, with machines capable of building beyond 600 x 600 x 600 mm^3 being exceedingly rare [3], [10]. Similarly, CEM processes are not direct competitors to WAAM for large-scale objects, as their part size is limited by system constraints.

- Part Complexity: WAAM offers greater design freedom through its layer-by-layer deposition approach. It enables the creation of intricate geometries, including internal features and lightweight structures, that are often challenging or impossible to achieve with casting techniques.
- Speed and Efficiency: WAAM provides faster production for large components by eliminating the need for tooling or other intermediate steps involved in casting, significantly reducing lead times and enhancing production efficiency [11].
- Material Properties: While casting processes have long-established methods to achieve desirable mechanical properties through alloying and post-treatment, WAAM offers competitive material properties with further optimization. It produces denser components compared to PBF, which often suffers from porosity due to the melting of thin powder layers [12].

- Cost: WAAM can reduce costs by minimizing tooling requirements and material waste while shortening production cycles. However, initial investments in WAAM equipment and process optimization can be higher than casting or other traditional manufacturing methods [8, 11].
- Repairability: A unique advantage of WAAM is its ability to deposit material directly onto existing components, enabling cost-effective repairs. This capability is particularly valuable for industries like aerospace and heavy machinery, where repairing worn-out parts can save significant time and resources [13-15].
- Material Efficiency: AM processes generally have higher material efficiency compared to traditional manufacturing due to their ability to deposit material only where needed. WAAM, although requiring additional machining for dimensional accuracy, involves less material removal than metal casting. The machining allowance in casting is often higher to accommodate mold extraction requirements, leading to more significant material waste [16].
- Environmental Impact: Handling and preparation of powder for PBF involve complex and costly processes, often associated with health risks. WAAM, by relying on wire feedstock, eliminates these challenges and is considered less harmful to the environment compared to traditional manufacturing, which has high material waste and CO_2 emissions [12], [16], [17].

Sword et al. [16] compared WAAM to forging for titanium components, finding WAAM generates 2.3 times less material waste and produces 50% fewer CO_2 emissions during production. Specific energy consumption for WAAM was reported at 574.9 MJ/kg, significantly lower than 958 MJ/kg for forging. Similarly, Dias et al. [13] conducted a cost analysis, estimating 34% lower production costs when traditional manufacturing was replaced with WAAM.

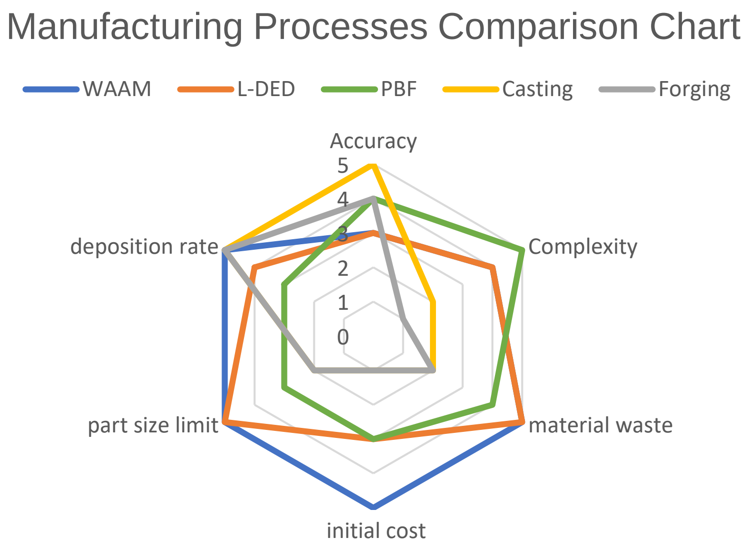

Figure 5. Metal manufacturing processes comparison

Based on the advantages and disadvantages of WAAM compared to other manufacturing processes, a case study was conducted to analyze various metal manufacturing techniques. The findings, summarized in Figure 5, offer insights into the performance of these processes across multiple aspects. WAAM and L-DED stand out for their material efficiency and ability to produce large parts, both of which surpass traditional manufacturing methods and other AM processes. In terms of deposition rate and initial equipment cost, WAAM offers a distinct advantage even over L-DED. This is due to WAAM's relatively straightforward equipment setup, primarily involving a MIG welding machine with wire feedstock, whereas L-DED typically involves more complex systems such as laser-based energy sources and powder delivery mechanisms, which contribute to higher initial investment costs.

On the other hand, the PBF process operates in a closed environment within a powder bed. This setup, combined with the laser’s ability to scan with extremely fine diameters, grants PBF a unique capability to produce highly detailed, intricate features with excellent dimensional accuracy. This makes PBF particularly suitable for applications where small and complex geometries are required, such as in medical implants or lightweight aerospace components. However, these advantages are offset by limitations such as higher material costs (due to the preparation of atomized powders) and the inability to scale effectively for larger parts, where WAAM excels. This comparative analysis underscores the complementary nature of these manufacturing processes. While WAAM leads in scalability, deposition rate, and cost-efficiency, PBF retains its niche in producing intricate, high-precision parts. Such evaluations allow industries to choose the most suitable technique based on application requirements, balancing factors like part size, complexity, material properties, and cost.

Chapter 2- Introduction to WAAM

The first patent for Wire Arc Additive Manufacturing (WAAM) was filed in 1925, initially described as a method for producing decorative objects [18] [19]. From this modest origin, WAAM has undergone an extraordinary evolution, transforming into a technology capable of producing industrial-scale components. This chapter is dedicated to providing a comprehensive exploration of WAAM, covering its classification, the various metal transfer modes involved, and the critical process parameters that define its operation. Additionally, the chapter delves into the materials commonly used in WAAM, their properties, and the challenges they present, including defects such as porosity, spatter, and thermal cracks. Finally, the chapter highlights the diverse applications of WAAM, showcasing its versatility across industries ranging from aerospace and automotive to marine and construction, emphasizing its role as a transformative technology in additive manufacturing.

2.1 WAAM classification

Wire arc additive manufacturing (WAAM) is rooted in welding processes such as GMAW, GTAW, PAW, as schematized in Figure 6. And the schematic of each process is reported in Figure 7.

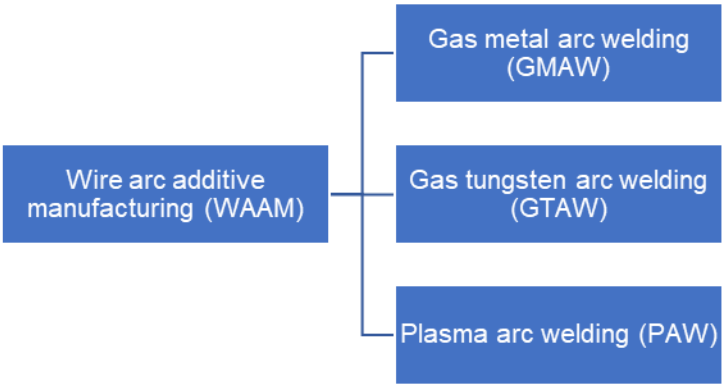

Figure 6. Classification of WAAM processes

In GMAW, a consumable wire of the proper material is used as an electrode. Thus, an electric arc is produced between the consumable electrode and the substrate material to melt the wire over the substrate or previously deposited layers. To protect the melting pool from the gases of the atmosphere, (typically hydrogen, oxygen, and nitrogen) a shielding gas provided by the torch head is adopted. The shielding gas is also useful to rapidly cooldown the melt pool leading to finer metallographic structures and protects from atmospheric contaminations. Depending on the gases adopted and their participation in the exothermic reactions, GMAW is typically divided into Metal Inert Gas (MIG) and Metal Active Gas (MAG). In PAW and GTAW, the electric arc is generated between a non-consumable tungsten electrode and substrate. A filler wire is fed to the arc zone, then it melts and is transferred to the substrate. The main difference between GTAW and PAW is represented by the torch and more specifically on the position of the electrode within the torch. PAW uses a retracted electrode as compared to GTAW. PAW uses two different gases; one is plasma gas, and another one is shielding gas. When the plasma gas passes through the arc zone of the torch it gets ionized. This plasma jet is transferred to the substrate through a small orifice. The filler wire turns into a molten form due to the higher heat from the plasma jet. In addition, typical shielding gases (argon, helium, CO2 …. etc.) are used as shielding gases to protect the deposited material from atmospheric contamination.

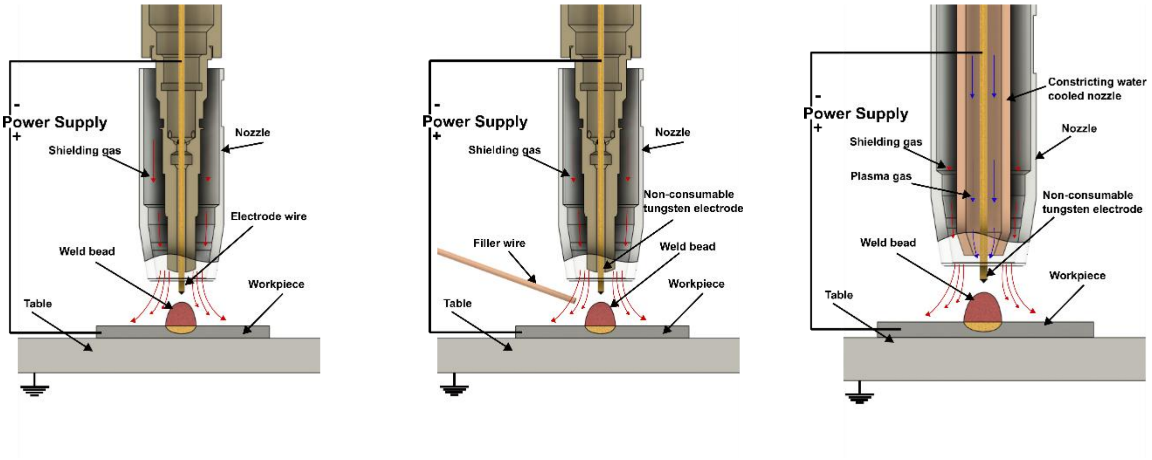

Figure 7. Schematic of different WAAM arc processes (a). MIG, (b). TIG, & (c). PAW

A brief comparison among the main WAAM sources is summarized in Table 1.

Table 1. Comparison among main WAAM sources

Characteristics	GMAW	GTAW	PAW
Quality	Provides good quality depositions suitable for most applications, but may have higher levels of spatter compared to GTAW and PAW	Offers high-quality depositions with excellent control over the deposition process, resulting in precise and clean depositions with minimal spatter	Delivers high-quality depositions with deep penetration and minimal distortion, making it suitable for depositions thin materials and complex geometries
Precision	Offers moderate precision and is suitable for a wide range of applications	Provides excellent precision and control, making it ideal for deposition of thin materials and intricate designs	Offers high precision and control, allowing for precise deposition even in challenging conditions
Arc Stability	Generally stable arc with minimal arc wander, suitable for deposition in various positions	Extremely stable arc with precise control on heat input, resulting in consistent deposition quality	Highly stable arc with good control on heat input, making it suitable for deposition thin materials and critical applications
Process	Semi-automatic or automatic process suitable for high-volume production and general fabrication	Commonly preferred for precision deposition of exotic materials, thin sections, and critical components	Suitable for high-quality depositions of thin materials, dissimilar metals, and complex geometries
Cost	Generally, the most cost-effective option due to lower equipment and consumable costs.	Tends to be more expensive due to higher equipment costs and slower deposition speeds	Typically, more expensive than GMAW and GTAW due to the complex equipment required and higher operating costs

According to the previous summary, while GMAW is cost-effective and versatile, GTAW and PAW offer superior quality, precision, and arc stability, making them ideal for applications that require high-quality depositions and precise control over the deposition process. However, they come at a higher cost and may require more specialized equipment and control.

In arc based WAAM processes, GMAW is the most used technology. Because of its high material deposition (Figure 8), can be used to fabricate medium to large-size components, is compatible with different materials, and is affordable. In both GTAW and PAW, the filler wire is fed separately. This non-coaxial wire feeding causes a difference in the process when the welding direction changes, making the arc length highly variable. However, in GMAW-based WAAM electric current acts directly on the feedstock wire, this causes arc instability and produces more weld smoke and spatters. GMAW has four metal transfer modes, which are globular, short-circuiting, spray, and pulsed spray.

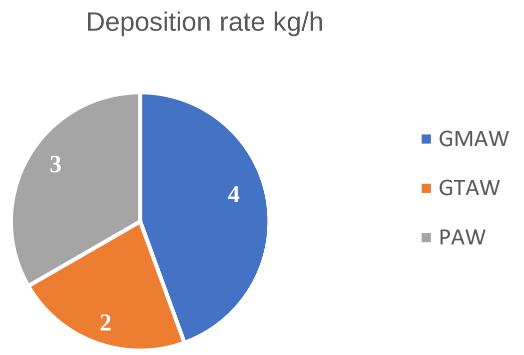

Figure 8. Material deposition rate of different WAAM processes

2.2 Metal transfer modes

Metal transfer modes, Globular, Spray, Short-circuiting, and Pulsed are only available in GMAW. These transfer modes significantly impact the productivity and quality of the deposited material. Depending on the selection of the process parameters like power source, current, voltage, shielding gas, electrode properties, and distance to work, different material transfer modes can be achieved. A concise comparison of the main characteristics of each metal transfer mode, including the conditions under which they occur, their characteristics, and typical applications is reported in Table 2.

Table 2 WAAM metal transfer modes

Transfer Mode	**Conditions**	**Characteristics**	**Applications**
Globular Transfer	Low welding current,	Large droplets detach and fall onto weld pool	Larger diameter electrodes, higher current settings
	electrode far from workpiece	Irregular beads, higher spatter levels	Not suitable for thin materials, precision welding
Spray Transfer	High welding current,	Fine spray of droplets across the arc	Stable arc, smooth, uniform beads, minimal spatter
	electrode close to workpiece	Ideal for thicker materials, high welding speeds	

Transfer Mode	Conditions	Characteristics	Applications
Short-Circuiting Transfer	Low welding current,	Brief contact with workpiece causes short circuit	Controlled droplets, rapid succession
	electrode briefly touches weld pool	Suitable for thin materials, positional welding	Low heat input, minimal spatter
Pulsed Transfer	Variable welding current,	Combines aspects of short-circuiting and spray modes	Greater control over, heat input and penetration
	controlled droplet transfer	Minimizes spatter and distortion, precise profiles	Thin materials, dissimilar metals, precise welding

Even though certain modes might be slower than others, every mode has a significance in a particular welding process. Figure 9 summarizes the percentage use of different metal transfer modes in WAAM.

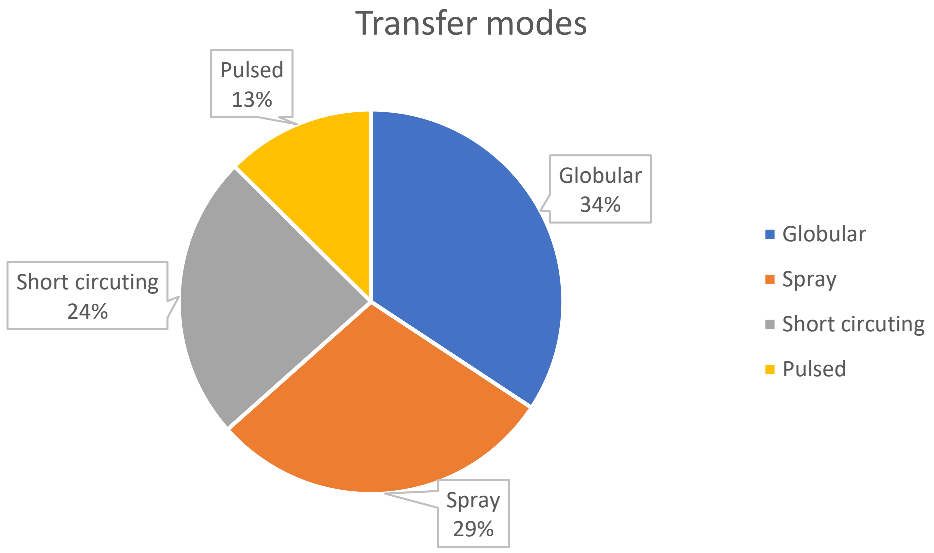

Figure 9. Percentage use of different WAAM transfer modes.

2.3 Process parameters

2.3.1 Current & Voltage

Welding current influences the melting rate of the electrode and, consequently, the rate of electrode deposition. It also regulates fusion depth (dilution) [20]. Both an increase in the current and voltage lead to an increase in the heat input (P*). As P* increases, the deposited bead width and fusion depth can increase, while the bead height typically decreases [citation]. Indeed, an increase in the current leads to higher energy provided per unit time; this increases the wetting angle leading to larger and shorter deposited beads. In addition, this also influences the dilution, since higher energy is transferred to the substrate allowing deeper material penetration.

When the current increases, bead roughness can decrease. The wetting angle and material deposition rate can also increase with the increase of P*. A two-stage investigation was carried out using Al0.1CoCrFeNi material and GTAW equipment by Ahsan et al. [21]. In the first stage single layer beads were deposited by varying the process parameters Current, Travel speed, and wire feed speed. Results showed that the energy density was identified as the primary factor governing the bead continuity, and an energy density higher than 80 J/ mm^3 (for MATERIAL= Al0.1CoCrFeNi) was required to achieve a uniform bead. In the second stage, multi-layered thin walls were deposited using high and low heat input. High heat input results in faster build speed, improved material efficiency (useable area) [ref: section machining, fig 39], and surface quality. Nevertheless, an excessively high heat input results in a low-profile, broad bead that will require the deposition of additional layers to attain a particular height. Barath Kumar et al. [22] built a Hastelloy C-276 thick wall using GTAW with pulsed and continuous current. Both pulsed and continuous current processes showed equiaxed grain, but Pulsed current allowed, controlled heat input and faster cooling, which promoted finer grain size (189 μm), enhanced hardness, and improved tensile strength compared to continuous current. The electrical potential difference between the tip of the electrode and the surface of the molten deposited pool is referred to as welding arc voltage [20]. It has an impact on the shape of the fusion zone, the melting rate of reinforcement electrodes, and so on.

$$Q = (\eta * V * I)/T_s \qquad \text{eq. 2}$$

Q is the Heat input, is the process efficiency (80%, ref), T_S is the travel speed of the torch, where V and I are the voltage and current, respectively.

2.3.2 Travel speed

Travel speed (Ts) is the relative speed of the torch to the component; thus, the travel speed is the reciprocal of the interaction time. Consequently, the adoption of high travel speed (which implies short interaction time) reduces the amount of heat per unit length [23]. According to Dinovitzer et al. [24], travel speed mainly affects dilution and wetting angle. Under high travel speed, the deposited bead becomes thinner; in addition, it also leads to increased height by weight ratio for the deposited bead as discussed in [24], [25], [26]. However, extremely high travel speed may result to insufficient heat supplied which may lead to irregular beads, low dilution, a smaller wetting angle. On the contrary, lower travel speed may come with overheating, extremely large beads, higher dilution rate (even perforation of the substrate, and higher wetting angle. Appropriate selection of the travel speed level is necessary to achieve regular beads. Adebayo et al. [11] investigated the travel speed effect on the humping phenomenon and travel speed on the bead geometry using ER 70S-6 material with CMT-WAAM. The results indicated that higher travel speed promoted pronounced humping defect due to the backflow of molten metal in the deposited pool. Therefore, limiting the travel speed could avoid the humping defect. Tawfik et al. [27] also showed that the increased travel speed improved the part quality. Zhou et al. [28] and Tawfik et al. [27], investigated the travel speed effect on microstructure and mechanical properties. Increased travel speed resulted in a smaller grain size, improved hardness, and tensile strength due to a faster cooling rate [29]. Rosli et al. [23] investigated the travel speed effect on the bead geometry, by depositing ER70S-6 filler wire on a mild steel plate using GMAW. Irregular bead geometry was noticed at a higher travel speed as depicted in Figure 10.

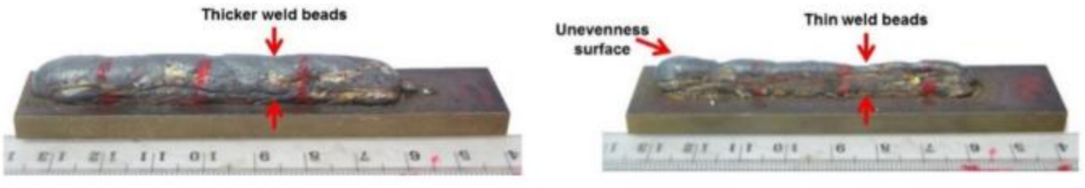

(a) (b)

Figure 10. Travel speed effect on WAAM bead geometry, (a) Travel speed 4 mm/s, (b) Travel speed 8 mm/s [23].

2.3.3 Wire feed rate

The wire feed rate/speed (WFS) influences the amount of material supplied. Thus, for a given torch speed, higher wire feed rates result in a higher amount of material per unit length. However, to achieve proper melting of the wire and adequate substrate preheating, the increase in the wire feed rate should be supported by higher voltages, as reported in eq.2.

If sufficient power is provided, higher wire feed rate can lead to larger cross section of the deposited bead. In addition, fixed power supplied and the torch speed, the adoption of higher wire feed rate also increases the height by weight ration of the deposited bead as reported in [26]. Indeed, under these conditions, lower power per unit volume of wire material is supplied leading to lower temperatures and consequently narrower deposited beads. Dinovitzer et al. [24] studied the different process parameter's effects on the bead geometry. The results showed that the WFS has a linear effect on the bead height. WFS/TS is one of the main parameters in the WAAM process to regulate the heat input. Yildiz et al. [30], investigated the influence of WFS/TS on bead dimensions, and mechanical properties. The WFS/TS ratio represented the most significant process parameter for controlling heat input. The results indicated that the WFS/TS ratio correlates linearly with characteristic bead dimensions (as said by Dinovitzer et al. [24]) and mechanical properties. Rosli et al. [23] found that the higher WFS increased the unevenness, height, and width of the deposit. This led to more material deposited per unit time, but this made the process unstable.

A summary table concerning the main process parameters to geometry of the deposited bead is summarized in Table 3.

Table 3. process parameters effect on WAAM deposition.

	Height	Width	Wetting angle	Dilution	Surface waviness	Layer-to-layer bonding	Melt-pool shape
Current	[21, 31-35]	[32, 33] [21, 34]	[21, 36]	[37]	[15, 21, 38]	[15, 34]	[34, 39]
Voltage	[32, 34, 40]	[32, 34, 40]	[36]	[37]	[15]	[15, 34]	[20, 34]
Travel speed	[21, 32, 37, 41] [35, 40]	[32, 35, 37] [21, 40, 42]	[21, 36, 41, 43]	[35, 37, 42]	[15, 35]	[15]	[31, 42]

Wire feed speed	[21, 35, 40, 41]	[21, 35, 40]	[21, 41, 43]	[35]	[35]		[43]
Stand-off distance							[31]
Shielding gas	[44]	[44]	[44]		[44, 45]		[45]
Scan strategy					[15, 46]		[47]
Dwell time	[36, 39, 48, 49]	[36, 39, 48-50]	[36, 39, 48, 49]	[36, 48]	[39, 49]	[36, 48]	[36, 39, 48, 49]
Base plate temperature	[42, 51]	[42, 51]		[42, 51]			[42, 51]
Torch tilting	[41, 52]	[52]	[41, 52]	[41, 52]	[52]	[52]	[52]
Part orientation	[53]	[53]				[54]	[54]

2.3.4 Stand-off distance

The stand of distance (SOD) is the distance between the weld torch tip (nozzle) to the workpiece. Figure 11, illustrates a schematic of SOD and CTWD. Electrode stick-out is the distance between the weld torch tip to the wire tip. Welding/deposition voltage also depends on the Distance between the electrode tip and the workpiece [55]. Ahsan et al. [21] demonstrated that whereas bead height increased in the beginning and subsequently dropped to a minimum at high WFS, bead width reduces as WFS increases. The results also indicated that the SOD plays a crucial role in arc stability. Increased SOD resulted in unstable arc, which leads to defects like porosity, lack of fusion, and irregular bead geometry [56]. Higher SODs also lead to lower heat input (since lowering of welding voltage), which further determines the microstructure and mechanical properties of the built part [56].

Henckell et al. [57] investigated the effect of heat input on geometrical features and metallurgical properties. They found that increasing CTWD by 10mm led to 10% reduction in energy input and by statistically adjusting the CTWD (increasing), the WAAM process can reduce the welding current by 40%. As the CTWD increases bead height increases and width decreases. They investigated the CTWD range 12-28-44mm by keeping the other process parameters constant, Figure 12. A total of 70 layers with a length of 160mm and interlayer temperature were kept at 100°C. The wall that was built using CTWD of 44mm showed an increase in height and surface roughness.

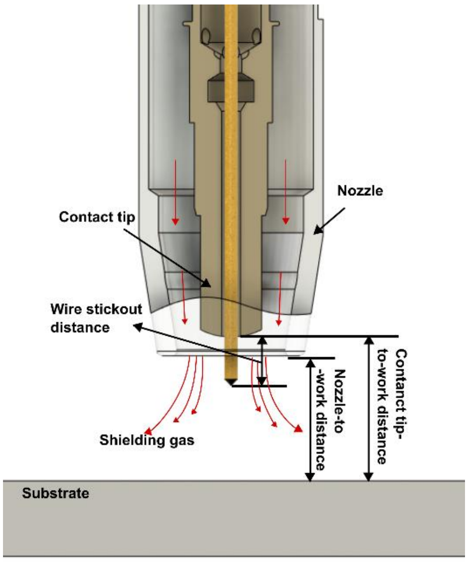

Figure 11. Schematic representation of CTWD and nozzle to work distance

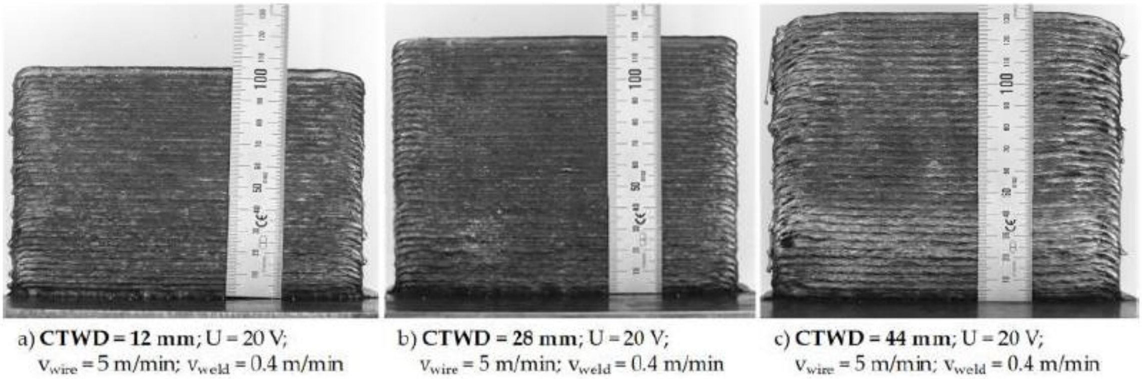

Figure 12. CTWD effect on WAAM deposited walls with 70 layers, (a) CTWD 12 mm, (b) CTWD 28 mm, (c) CTWD 44 mm [57].

2.3.5 Shielding gas

The main purpose of shielding gas is to protect the melt pool from being exposed to atmospheric gases (like hydrogen, nitrogen, oxygen… etc.) and prevent the degradation of deposited bead quality. The melt pool interaction with these atmospheric gases can cause oxidation formation on top of the weld bead when it gets solidified and the entrapment of atmospheric gas inside the melt pool causes a higher chance of porosity presence. The flow rate of shielding gas is also an important parameter because it affects the cooling rate of deposition. A higher flow rate leads to a faster cooling rate (by convection) and consequently it influences the microstructure of the deposited bead.

The shielding gas can be inert or active gases [58]. The inert gases prevent the negative impacts caused by the oxygen on the weld pool. However, a small quantity of oxygen is present in the active shielding gases itself, which serves as an oxygenating additive while melting [59], [45]. Oxygen facilitates the fluid transfer of material to the deposited region and stabilizes the arc. The various gas proportions can be adjusted to meet the needs of the material to be deposited. Like spattering, burn-in …etc are the negative effects. Figure 13, summarizes the types of shielding gases adopted in different works. Hauser et al. [60] investigation showed that the increased shielding gas (99.995% purity) flow rate caused the higher porosity. Since the higher gas flow rate allowed the melt pool to force convection, by not letting the gas inclusions escape from the melt pool. [45, 58, 59]

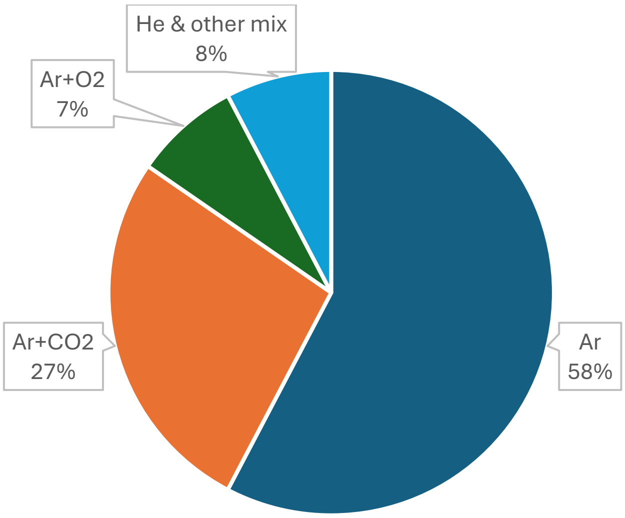

Figure 13. Percentage use of different shielding gas types. 1

2.3.6 Scan strategy

Scan strategy plays a crucial role in WAAM-built parts since it influences the temperature and material cooling. Thus the scan strategy directly influences the residual stresses, microstructural and mechanical properties as well as porosity, lack of fusion, deposited bead uniformity, temperature history, etc. [61]. Compared to other AM technologies, the WAAM scan strategy should be different. WAAM scan path should be planned in a continuous manner because defects at the starting and end point of deposition are extremely pronounced. In addition, before going under steady state deposition conditions, a certain length is required [62]. This indicates that the selection of the appropriate scan strategy is crucial to improve efficiency and part quality. According to Liu et al. [62] WAAM path planning can be classified into linear path, contour path, and combined linear and contour path Figure 14.

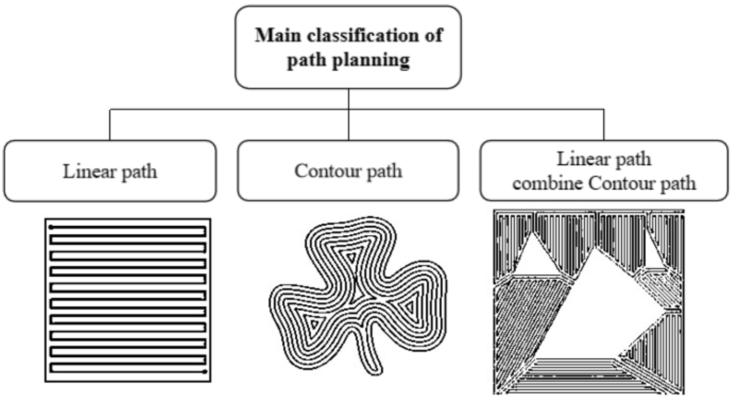

Figure 14. Main classification of tool path planning [62].

The linear path scanning strategy is the simplest. The scanning head moves in a straight path and this strategy can result in accurate, efficient, and time-saving solution when the component is a very simple structure like rectangular-shaped objects without any other features inside the object. The filling can be raster or zig-zag scanning. However, this strategy leads to high thermal gradients and higher temperatures since the depositions are performed close to the just deposited ones. Thus, this strategy can easily lead to some defects including residual stress, distortion, grains growth.

The contour path scanning strategy is easy to implement for complex parts, but it is complicated, time consuming, and insufficient to fill the centers of the contour. This strategy provides lower thermal orientation with consequently lower thermal distortions.

The "linear path combine contour path strategy" is the combination of both linear and contour paths. Here, the planning area will be divided into sections or island depending on the features of the part. Each section can be filled with different path planning depending on which strategy results in the better output.

WAAM components are prone to have higher surface waviness compared to the other metal AM technologies since of its higher material deposition [49] and full melting of such higher amount of material. Similarly to all the other AM processes, when the part walls are inclined, the part may suffer the stair-case effect Figure 15. However, in WAAM, as thicker layers are typically deposited, the stepwise defect is more pronounced. Thus, surface finishing operations (typically machining) are often mandatory to meet the tolerance limits.

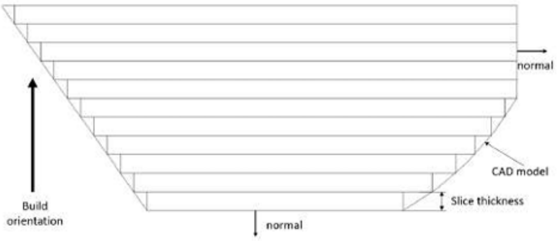

Figure 15. Schematic representation of stair-case effect

Chen et al. [63] investigated the scan strategy effect on the residual stresses using the SLM process with steel powder (24CrNiMo). They adopted six different scanning strategies including linear scanning 45°, 67°, 90°

rotation, island scanning, and strip rotation scanning. The results showed that the strip rotation promoted a uniform stress distribution while line scanning promoted higher peak stress. Line scanning with a rotation of 45° showed uniform stress distribution. Ma et al. [64] work showed that the WAAM-CMT technology and transverse arc oscillation promote equiaxed grain formation. The grain size decreases, and the microstructure exhibits good isotropy and low base texture strength. Top zone specimens showed higher material properties with UTS, YS, and El values.

2.3.7 Dwell time

Dwell time and inter-layer temperature are mutually dependent. After the completion of a layer, the welding torch rests idle before starts depositing the next layer, this idle time is called Dwell time. After the dwell time, the measured temperature (at the start position) is called inter-layer temperature. The WAAM build part goes through different thermal cycles during the process [65]. Fixed substrate dimensions and geometry of the component, higher temperature will result when shorter dwell time is adopted. Higher temperatures make the melt pool unstable, which results in an irregular bead shape. Proper cooling, which strongly depends on the adoption of proper power, governs microstructural growth and material properties. However, higher dwell time leads to longer production time and lower productivity. Xiong et al. [49] studied the inter-layer temperature effect on the wall quality using GMAW with h08Mn2Si feed wire on the Q235 B substrate. Walls were built with dimensions of 250 mm in length, 75 mm in width, and 10 mm in height with different inter-layer dwell times Figure 16. The results showed that longer dwell time led to lower temperature which led to great improvements of surface quality. However, production time is an important factor when it comes to manufacturing. Thien et al. [36] investigated the influence of dwell time on the part quality and production time. Thien experimental studies showed that the wall width increased by 3-4 mm with zero dwell time; on the contrary, when the dwell time was set to 60 sec, the wall geometry was closer to the target values, which in turn increased the production time. Therefore, this study used an alternating dwell time that varies between 0 to 60, which did not compromise the quality of the deposited wall or the production time.

C.R.Cunningham et al. [66], proved that the stainless steel material properties can be influenced by the interpass layer temperature. Small interlayer temperature and low heat input (Q) samples resulted in equiaxed grain growth and lower melt pool temperature due to higher thermal gradient. Longer interlayer temperature and high heat input (Q) samples experienced strong grain growth due to higher prolonged time at high temoperatures. C.R.Cunningham et al. also concluded that the higher interlayer temperatures could reduce the residual stress.

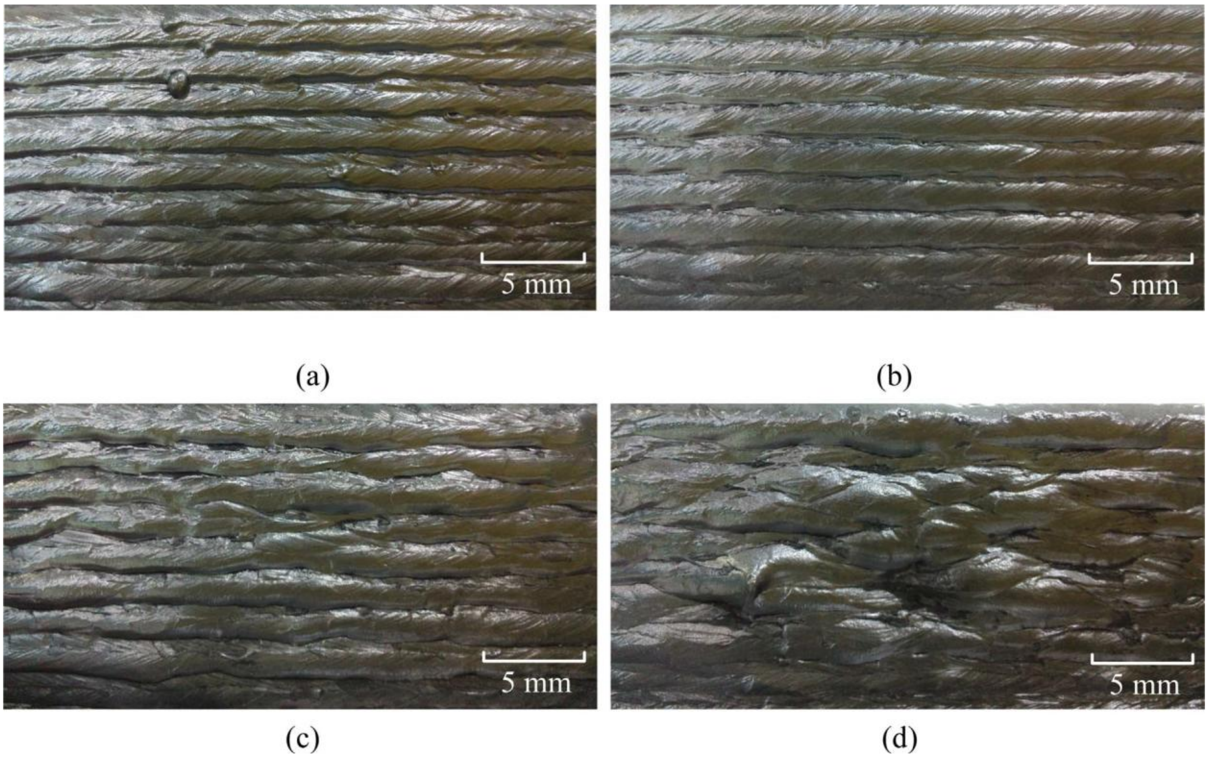

Figure 16. Inter-layer temperature effect on WAAM deposited wall geometry, using the WFS = 3.73 m/min & Ts = 0.3 m/min. a). 20°C, b). 120°C, c). 300°C, d). 450°C [49].

2.3.8 Substrate temperature

Substrate pre-heating represents a solution to reduce the residual stresses [67]. The temperature difference between the substrate and deposited layers is very high; this causes steep temperature gradients which may lead to part distortions, high residual stress and even cracks developments. Majumder et al. [51] and Gudur et al. [42] investigated the effect of a substrate at room temperature, pre-heating, and cooling conditions on the bead geometry of Inconel 625 on EN 8 steel. Pre-heating conditions increased the bead width, penetration depth, while reduced track height. The adoption of cooling substrate conditions led to decreased width, depth, and increased height were observed.

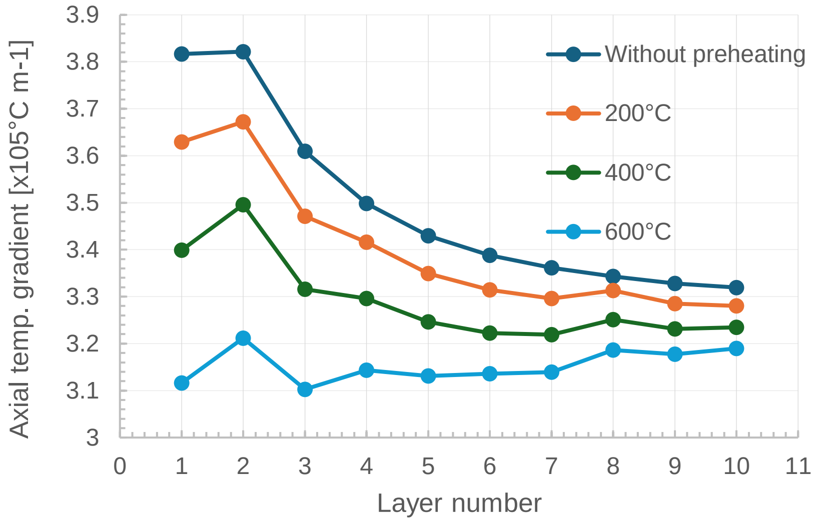

Figure 17. Substrate pre-heating temperature effect on temperature gradient [65].

Xiong et al. [65] investigated the thermal history of a circular ten-layer single pass part by creating a 3D transient heat transfer model in GMAW. Figure 17 depicts the maximum axial temperature gradient in the molten pool at the midpoint of each layer at varying substrate preheating temperatures. As the number of layers increased, the axial temperature gradient became flatter. As the preheating temperature increased, the axial temperature gradient decreased. Further, results showed that the substrate preheating smoothens the thermal cycle of the first layer; however, lower temperature homogeneity was achieved when the preheating temperature reached 600°C. The cooling rate of the melt-pool decreased as the preheating temperature increased. Chen et al. [63] also confirmed the results reported in Xiong et al. [65] work that the residual stresses gradually decreased as the substrate preheating temperature increased.

2.3.9 Torch angle

The multi-directional deposition process in GMAW-based WAAM is more challenging to control due to the influence of gravitational force. Yuan et al. [68] identified two major issues which demands multi-directional deposition. Indeed, molten metal droplet should transfer to a particular position and the weld bead profile formation due to the melt-pool. Baffa et al. [41] studied the effect of torch inclination on repair layer deposition. The tilt between the welding torch and substrate promoted stability, which permits parallel bead overlap without voids. The authors concluded that torch inclination doesn't have a significant effect on dilution. During WAAM, the torch tilt angle is kept perpendicular to the built direction, to avoid the influence of gravitational force and this can change the deposition geometry [68]. Yuan et al. [68] investigated the torch tilting angle effect on the weld beads using CMT-GMAW. The authors experimented different torch angles (45°, 60°, 75°, & 90°) and concluded that the smaller the torch angle (45°) provided the less sag and better bead geometry.

2.3.10 Part orientation

Similarly to many AM processes with localized material deposition, in WAAM, part orientation must be carefully considered to satisfy geometrical characteristics and promote mechanical properties [69, 70]. This phenomenon arises from the intricate interplay among process parameters, residual stresses, microstructural characteristics, and material properties inherent to both as-fabricated and post-fabrication treated components manufactured via WAAM. The variation in these aspects is notably influenced by the orientation of the fabricated part [52].

Alomari et al. [53] developed an algorithm to minimize WAAM-specific manufacturing defects by determining the optimal print orientation. The algorithm prioritizes fewer uninterrupted surfaces and selects the optimal orientation with the maximal initial layer.

Numerical simulations show that build orientation strongly affects the shape and rigidity of ideal designs [71, 72]

2.4 Materials

Several structural materials including aluminum, titanium, and steel alloys have been involved in WAAM. Even though studies concerning these alloys represent almost 75% of the literature other alloys have been also investigated including: nickel-based superalloys, magnesium, copper, refractory alloys etc. In this section, the main materials used in WAAM, their properties and key aspects are reported. Saleh et al. [18] summarized the most used material in WAAM for the period of 2010 to 2022, Figure 18a. Figure 18b visualizes the updated version from 2010 to 2024.

It can be observed that, still the main alloy types like steel, Aluminum, and Titanium represent more than 70% of the WAAM used materials. Comparatively copper and steel alloys use increased around 5%, titanium and aluminum alloys use decreased 7% and 2% respectively. This is mainly due to the cost effect of titanium and processing defects in aluminum.

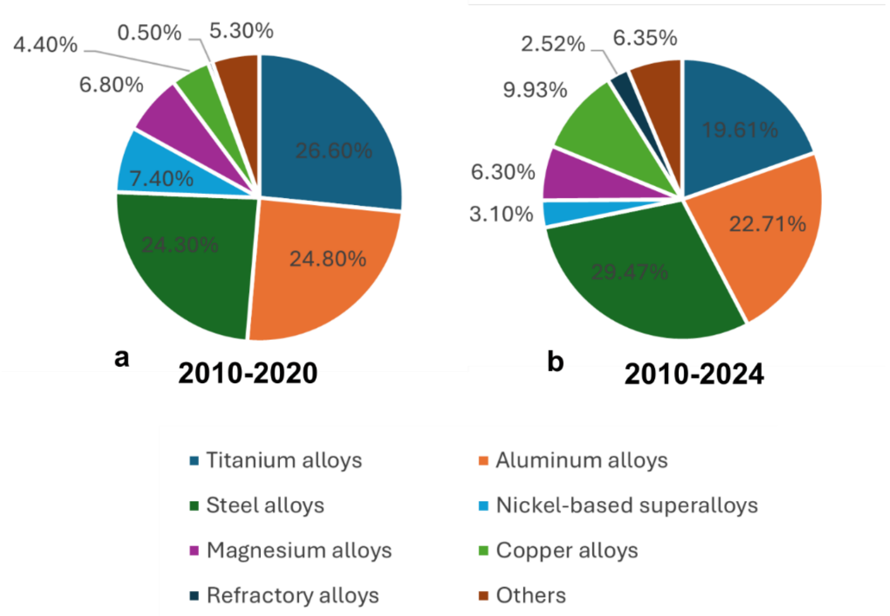

Figure 18. WAAM most used material

2.4.1 Titanium alloys

Titanium alloys exhibit exceptional strength and durability, retaining these properties even at high temperatures. They are lightweight, possess excellent corrosion resistance, and are extensively utilized across various industrial sectors [73] [s6]. Standard processing techniques for titanium alloys include molding, casting, and forging. However, aerospace-grade titanium alloys present challenges due to their low thermal conductivity and high viscosity, necessitating robust tools and expensive equipment. Additionally, their high strength leads to increased machining costs due to significant tool wear. Lin et al. [74] said that, in aerospace and defense applications, where components typically have high buy-to-fly ratios, conventional machining is inefficient and costly due to material waste. Conversely, WAAM offers a cost-effective and efficient alternative for titanium alloy processing [75], [76].

Wang et al. [54] investigated the microstructural evolution and mechanical properties of Ti-6Al-4V components fabricated via WAAM. They identified a fine α+β Widmanstätten microstructure in the top section of the wall and coarser α colonies within the bands. The WAAM samples exhibited anisotropic behavior, with horizontal yield strength (870 MPa) being approximately 10% higher than vertical yield strength (800 MPa). These values were slightly lower than those of forged samples, which averaged 930 MPa in yield strength. Nevertheless, WAAM samples demonstrated superior fatigue life compared to forged samples, although some failed prematurely due to gas porosity from wire contamination, indicating a need for process stabilization. Palacios et al. [77] examined the mechanical and electrochemical properties of pure titanium produced using WAAM, employing X-ray diffraction and optical microscopy. The resulting single-phase α-Ti structure was free from visible deposition tracks and interfaces, with titanium oxide traces and homogeneous nucleation at low solidification rates leading to coarse grains. The samples displayed enhanced corrosion resistance. Artaza et al. [78] conducted a microstructural analysis of Ti6Al4V produced by WAAM, revealing a dual-phase α+β configuration with a prior-β structure. Bright α needles and a dark β matrix were observed, with the matrix being vanadium-rich and the needles aluminum-rich. The needle size was smaller at the bottom due to higher heat transfer during the process.

2.4.2 Aluminum alloys

Aluminum alloys exhibit prominent properties, including ductility, a high strength-to-weight ratio, excellent thermal conductivity, ease of manufacture and machining, and high chemical resistance to corrosive environments. Recently, WAAM has been effectively applied to the fabrication of aluminum alloys. Due to its low production costs, WAAM's economic value is primarily justified for producing large, complex structures with high buy-to-fly ratios and intricate geometries [79]. Common challenges in aluminum manufacturing using WAAM include porosity, cracks, an unstable melt pool, and suboptimal mechanical properties [80].

Vimal et al. [81] discussed these issues extensively. A summary of the problems associated with WAAM components made from aluminum alloys is presented in Table 4. Wu et al. [82] identified characteristic defects specific to particular materials (Figure 20). Many of these defects can be mitigated by optimizing process parameters [52], [83]. The high difficulty of welding aluminum components using arc welding processes contributes to these defects, suggesting that friction stir additive manufacturing for aluminum may be a promising alternative in the near future [52].

Nagasai et al. [84] investigated the properties of Al-Mg alloys produced using GMAW. Scanning Electron Microscopy (SEM) and Energy Dispersive Spectroscopy (EDS) analyses revealed that the microstructure of the Al-Mg alloy comprises α-Al as the primary phase and β-(Al3Mg2) as the secondary phase, with β-(Al3Mg2) being the main segregated phase. An increase in deposition height led to a decrease in the segregated β-(Al3Mg2) phases, resulting in anisotropic material properties.

Porosity is a significant issue in WAAM components made from aluminum alloys, affecting both density and mechanical properties [85]. Two primary causes of porosity have been identified: process-induced porosity, resulting from the entrapment of shielding gas, and wire-induced porosity, caused by voids within the feed wire and contaminants (such as grease, moisture, and hydrocarbons) on the wire surface [86], [87] [s28]. Hauser et al. [60] investigated the reduction of porosity in aluminum WAAM by monitoring the process and the flow of shielding gas. The CMT-P mode resulted in higher porosity compared to the standard CMT mode, Figure 19. Additionally, a higher shielding gas flow rate increased porosity by promoting faster cooling, which trapped gas within the deposited bead. However, higher shielding gas flow rates also produced smoother surfaces [52, 60, 79, 80, 82-87].

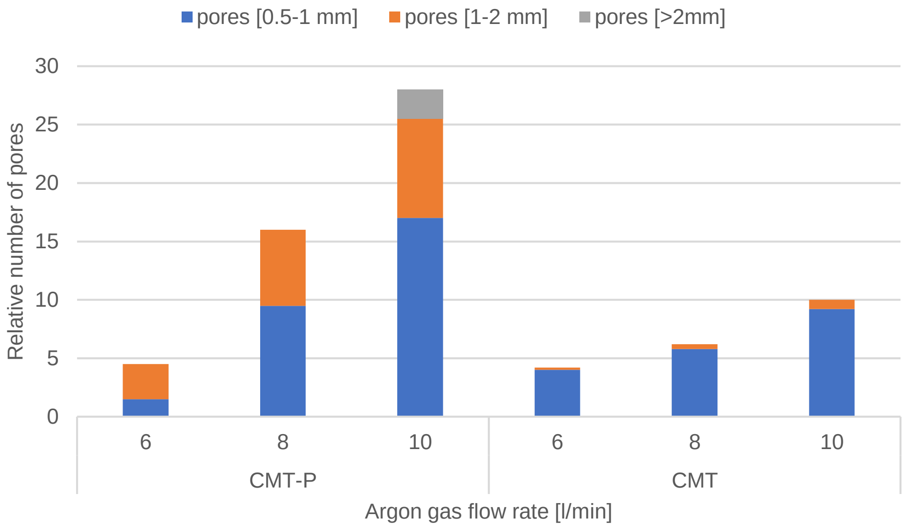

Figure 19. Shielding gas flow rate effect on aluminum alloy porosity. [60]

Table 4. Problems associated with the WAAM produced aluminum samples. [81]

	Cause	Ref
Porosity	Inappropriate hydrogen and faster cooling rate	[88]
Tensile residual stress	Without an external force	[89]
Cracks	Rs > UTs	[90], [91]

Deformation	Ys < Rs < UTs	[90], [91]
Delamination	Improper re-melting of previous layer	[82]
Turbulence	Occurs in 6xxx & 7xxx series.	[82]

2.4.3 Steel alloys

Steel alloys are widely utilized due to their superior mechanical properties, excellent corrosion resistance, and cost-effectiveness, making them suitable for various applications [14]. WAAM has been employed with numerous steel alloys, including 316L and 17-4 PH stainless steels, ER70, ER80, ER90, ER120, and Maraging grades 250 and 350 [92]. Niu et al. [93] compared 304 stainless steel produced by WAAM and L-DED. In MIG-WAAM samples, secondary dendrites were rarely observed due to their proximity to the molten pool. Lathy and skeletal ferrite zones were identified in the MIG-WAAM samples. The microstructure of L-DED samples comprised secondary dendrites with a well-developed, slender columnar crystal morphology, and skeletal ferrite was present. During the cooling process, thin ferrite articles fully dissolved into austenite, while thick dendrites did not dissolve completely, resulting in skeletal ferrite in the final microstructure. Al-Nabulsi et al. [94] investigated the mechanical properties of union K40 steel produced via WAAM. X-ray computed tomography (XCT) analysis revealed that the interfacial region of the sample had lower density compared to the bulk steel, with a porosity volume fraction of 0.2%. The mechanical properties of union K40 steel were compared to EN 8 carbon medium steel, demonstrating that WAAM steel meets the Eurocode 3 structural steel grade requirements for building structures.

High-carbon steel presents significant challenges in WAAM due to its elevated carbon content, which complicates microstructural control and necessitates stringent preheating and post-processing procedures. These conditions elevate the risks of cracking, residual stresses, and heterogeneity in the microstructure, thereby increasing production costs. Ensuring the quality of WAAM-fabricated components demands meticulous control of process parameters, alongside rigorous preheating and post-processing measures [18], [92].

2.4.4 Other materials

Nickel-based superalloys are favored materials in additive manufacturing due to their advantageous combination of high strength and cost-effectiveness in fabrication. These alloys find extensive applications across aerospace, aeronautical, petrochemical, chemical, and marine industries [82], owing to their ability to maintain mechanical integrity under elevated temperatures and varying loading conditions.

Xu et al. [95] conducted an investigation into Inconel 625 fabricated via PAW, employing both continuous and interpass cooling strategies between layers. Their findings demonstrated a beneficial impact of prolonged interpass cooling, particularly enhancing mechanical properties. Additionally, the researchers applied post-heat treatment to both sets of samples, resulting in improved material characteristics. Samples subjected to interpass cooling and post-heat treatment exhibited elevated tensile strength (851 MPa) and yield strength (535 MPa). Conversely, samples deposited continuously without post-heat treatment displayed larger dendritic arm spacing and interconnected laves particles, contributing to inferior tensile properties. In contrast, specimens with interpass cooling but without post-heat treatment exhibited reduced dendritic arm spacing and discrete laves particles, thereby mitigating adverse effects. Furthermore, Kumar et al. [96] investigated the microstructural and mechanical attributes of Nickel-based superalloy C-276, crucial for nuclear, oil, and gas industries. Their study revealed varied grain morphologies: equiaxed at the surface, cellular in the middle, and columnar at the base. SEM analysis indicated variations in Ni content and increased presence of Mo and W elements in interdendritic regions. In a separate study, Islam et al. [55] explored the mechanical and microstructural characteristics of a refractory alloy (Titanium-Zirconium-molybdenum) using GTAW. Their analysis identified defects such as porosity and cracks in the samples, accompanied by the presence of columnar grains under all conditions. The brittle fracture behavior observed during tensile testing was attributed to these porosities.

WAAM shows promising applications across various diverse material applications including titanium, aluminum, steel, and many others. Its capability to manufacture intricate geometry and customize material properties makes it a valuable method for industries seeking high-performance components.

In conclusion, while WAAM offers significant advantages in producing large, complex metal components, several material-related challenges persist. Issues such as residual stresses, porosity, cracks, and anisotropic mechanical properties can compromise the integrity and performance of the final product. Additionally, the large thermal gradients inherent in the process can lead to grain growth and uneven microstructures, affecting material strength and fatigue resistance. Addressing these challenges through process optimization and post-processing techniques is crucial for realizing the full potential of WAAM in industrial applications. Bintao Wu et al. [82] summarized these occurrence of material based defects in WAAM process, as shown in Figure 20. The article mentions that issues such as oxidation in titanium alloys, porosity in aluminum alloys, poor surface roughness in steel, and significant deformation and cracking in bimetal components are commonly observed.

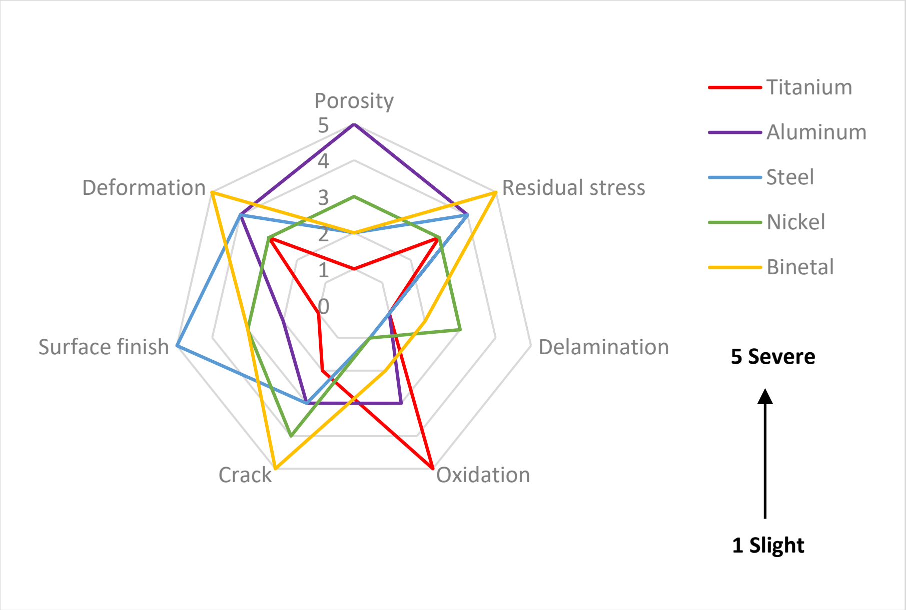

Figure 20. Radar diagram of problems associated with WAAM materials. [82]

2.5 Defects

Most of the defects are related to the process parameters and these defects can be mitigated and even avoided by the adoption of optimal process parameters (Briefly discussed in the section). Optimal process parameters also depend on the type of material (especially the melting point, heat capacitance, thermal conductivity), type of machine and experimental conditions. Besides the process parameters, there are some other factors that could cause these defects. The main causes and possible solutions are summarized in the Table 5.

Table 5. WAAM defects Summarization.

Defect	Causes	Remedies	Ref
Distortion	• Higher temperatures	• Lower heat input	[97], [88], [63], [98], [39], [99], [21], [21, 34, 88, 97]
Porosity	• Faster cooling rate • Entrapment of atmospheric gas	• Reduce the use of aluminum alloys • Applying vibrations to the substrate • Post heat treatment	[60], [88], [100], [101], [102], [99], [21], [21, 34, 60, 88]
Cracks	• High thermal stresses • Faster solidification rate	• Low heat input • Controlling the cooling rate • Post heat treatment	[101], [88], [102], [99], [21], [21, 34, 88, 101]
Undercut	• Unstable arc • Insufficient heat input	• Optimal heat input	Nguyen, 2013 #235}, [99], [21], [21, 34]
Burn through	• Higher heat input	• Optimal heat input	Nguyen, 2013 #235}, [99], [21], [21, 34]
Humping	• Improper WFS/TS • Molten metal backward flow	• Proper WFS/TS • Increase the part size • Apply suitable magnetic flux fields	[53], [103], [104], [105], [99], [21, 53] , [34]
Spatter	• Poor quality of wire • Improper section of nozzle • Improper selection of shielding gas flow	• Proper section of material • Proper section of nozzle • Proper section of shielding gas	[106], [99], [21], [21, 34]
Surface waviness	• Higher material deposition rate • Lower dwell time	• Optimal dwell time • Optimal WFS/TS	[107],, [99], [21], [21, 34, 107]

2.5.1 Distortions and residual stresses

During WAAM process, the workpiece undergoes multiple thermal cycles due to the layer-by-layer deposition process [39]. Localized heating induces uneven expansion and contraction, resulting in heterogeneous thermal cycles and the formation of residual stresses. These thermal dynamics contribute significantly to part distortion, as depicted in Figure 21, and can potentially lead to fracturing. The severe plastic deformation inherent in WAAM introduces considerable residual stresses, adversely affecting dimensional accuracy during subsequent machining operations.

Addressing these challenges, heat treatment emerges as a viable strategy, offering potential relief from residual stresses and enhancement of mechanical properties [97]. Research across various AM methods reveals that substrate preheating, power reduction, increased scanning speed, and thinner substrates can mitigate residual stresses [98]. For instance, Wandtke et al. [108] demonstrated that heat input significantly influences residual stresses, with higher heat inputs resulting in increased residual stress levels. The study further indicated that part size affects the sidewall residual stress distribution, highlighting the importance of considering both local and global restraint during design and manufacturing. Furthermore, Chen et al. [63] also explored the effects of scanning strategies, preheating temperatures, and heat treatment on residual stresses in SLM of high-strength steels. Their findings indicated that employing a preheating temperature of 100 °C reduced residual stresses by 37.5% compared to room temperature forming (800 MPa), with further reductions to 62.5% at 200 °C preheating.

Figure 21. Distortion in WAAM produced parts [99].

2.5.2 Porosity

The formation of porosities is a critical issue during the material deposition process in WAAM. This problem is particularly prevalent in the production of materials with low melting temperatures, such as aluminum alloys and magnesium alloys [60]. These materials, unlike steel alloys, exhibit low melting points and high thermal conductivity, leading to higher solidification rates that hinder the escape of gases trapped within the melt pool. Sources of porosity include moisture and oil content on the substrate surface, as well as gases from the shielding gas and atmosphere trapped during the melting process.

Cong et al. [100] investigated the impact of different arc modes—Conventional CMT, CMT-pulsed, CMT-advanced, and CMT-pulse advanced—on the porosity of Al-6.3%Cu alloy. Their findings indicated that Conventional CMT is unsuitable for additive manufacturing of these materials due to gas pores, whereas CMT-PADV significantly reduced porosities [101].

Post-processing techniques, such as hot isostatic pressing (HIP), have been shown to reduce porosity volume by up to 95% compared to as-built parts [102]. Additionally, Gu et al. [102] study examined the effects of inter-layer rolling and heat treatment on the porosity of aluminum alloys (see Figure 22). Various inter-layer rolling processes were found to decrease the number of pores, while subsequent heat treatment further eliminated pores larger than 5 μm.

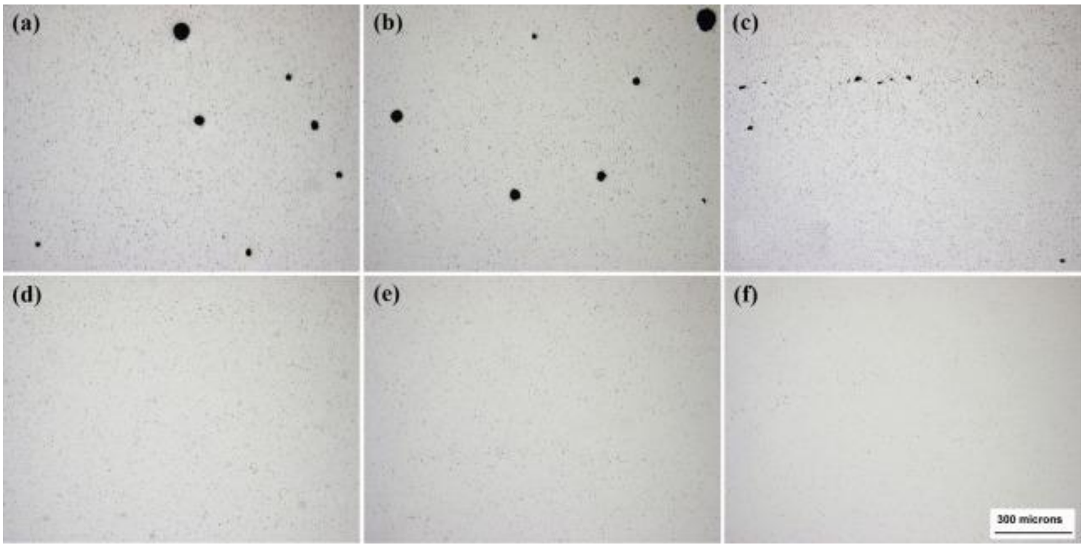

Figure 22. Optical microscopic analysis on WAAM produced aluminum alloy porosity, a). as deposited without rolling and heat treatment, b). Post-deposition heat treatment, (c-e). 15kN, 30kN, 45kN inter-pass rolled, f). 45kN inter-pass rolled and post heat treated [104].

2.5.3 Cracks

Cracks in the WAAM process arise from various causes, including thermally induced stress, porosity, wire surface irregularities, inappropriate process parameters, and unsuitable post-processing techniques. Schematic of crack propagation in weld pool and localized stain is reported in Figure 23. These factors can collectively contribute to crack formation, compromising structural integrity, fatigue life cycle, and overall safety [99]. Optimizing process parameters and adopting specific deposition strategies can mitigate crack development. Albannai et al. [109] introduced a novel welding method, tandem side-by-side GTAW, applied to AA2024 to address centerline solidification cracking. Their findings highlighted significant differences compared to the straight welding approach; the tandem weld pool motion resulted in a 60% reduction in crack length, while the weaving weld pool motion decreased the overall crack length by 50%. This innovative method offers a promising solution for reducing and preventing crack development in WAAM.

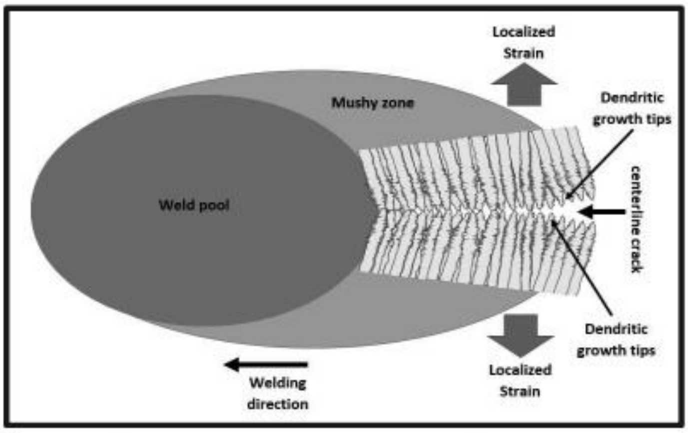

Fig. 2 *Schematic of a weld pool and localized strain on the trailing edge in the mushy zone*

Figure 23. crack defect [109].

2.5.4 Undercut and burn through

When the electric arc is unstable, an undercutting defect, characterized by an unfilled groove adjacent to the weld bead, may develop (Figure 24a). An unstable arc can result in insufficient heat transfer to the electrode, causing this undesirable groove formation [99].

Burn-through is another defect that occurs when the wire electrode penetrates through the bottom of the substrate, creating a hole in the weld bead (Figure 24b). This defect is commonly linked to excessive heat input, which can result from low travel speed or high current, causing the electrode to melt too quickly and increasing the risk of burn-through [105]. Both undercutting and burn-through significantly compromise part quality, highlighting the necessity for effective mitigation strategies and the implementation of optimized process parameters.

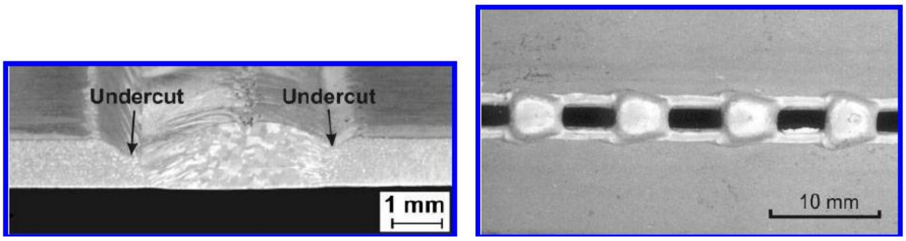

Figure 24. undercut and burn through defects [105].

2.5.5 Humping

The humping defect is characterized by uneven bead deposition [53], resulting from the backward momentum of fluid metal, as depicted in Figure 25. This phenomenon is influenced by various factors, including inappropriate process parameters, wire feed issues, and poor scan strategy [103]. The WFS/TS ratio and arc current significantly affect humping, playing a critical role in the material deposition rate [104], [110]. The development of humping impacts part characteristics, leading to irregular shapes, uneven surfaces, reduced accuracy, and material waste. Jafari et al. [104] identified that humping is likely to occur under process conditions that produce a weld pool with a width-to-length ratio below 0.1. They also provided a summary of possible causes and solutions for humping, as reported in Table 6. Nguyen et al. [105] examined factors such as fluid flow, high velocity, arc pressure, metallostatic pressure, capillary forces, and lateral instability of a cylindrical or curved wall jet, all of which contribute to the humping phenomenon, highlighting the complexity of its underlying mechanisms.

Table 6. Humping- effect of important factor on the bead geometry [104].

Process and material [Ref]	Control factors	Discussion/suppression mechanism
GMAW Mild steel [111]	Magnetic field, current, TS	A good weld bead can be obtained without the humping with suitable magnetic flux density; however, the introduction of the magnetic field causes increases in spatter. The minimum excitation current required to suppress humping bead increased by increasing the TS and correlations were established between them.
GMAW Mild steel [112]	Magnetic field	Used an external magnetic field to produce an extra electromagnetic force in front of the welding pond to reduce the momentum of the molten backward flow, improving bead quality considerably and an enhancement of critical TS.
GTAW SS 304 [113]	Magnetic field	The upward electromagnetic force was used to lift the molten metal, and it was shown that the shape of the bead was significantly improved.
GTAW SS 304 [114]	Magnetic field	Used cusp-type magnetic to change the cross-section of the arc plasma from a circular to an elliptical shape, therefore decreasing the occurrence tendency of humping bead and a good bead appearance.
GMAW ER 70S-6 [115]	Laser power	Hybrid heat source improved fluid flow and heat transfer in the molten pool, reducing the momentum of the backward molten metal flow and suppressing the humping bead, however, in addition to adding cost to equipment, hybrid heat source would make equipment more complex.
GMAW ER 70S-6, SS 304 [116], [117], [118]	WFS, current	The fluid flow and heat transfer within the welding pool can be improved by Tandem, decreasing the momentum of the backward molten metal flow and suppressing the humping. However, two modules contribute to the investment in equipment and complicate the operation of equipment.
GTAW ER 70S-6 [119]	Shielding gas	The addition of helium can increase the heat transfer into the work-piece to increase the welding speed without the humping.

GMAW ER70S-6 [120], [121], [122]	Magnetic field, current, TS	The magnetic field had significant effects on the flow dynamics of the weld, arc column, and the metal transfer, and the optimized excitation currents were determined. Combining a suitable electromagnetic field and the backward inclined welding torch can result in the successful welding bead with neither humping nor spatter.
GMAW ER480S-6 [123]	TS, power	The humping was enlarged and formed with the strong backward fluid flow of molten metal, which was mainly induced by the arc plasma force and droplet impact force.
GMAW ER70S-6 [124]	Current, TS	Two factors were determined to drive bumping: the effective momentum of backward fluid flow and the capillary instability of the fluid channel.
GMAW ER70S-6 [125]	TS, power	They suggested the formation of a thin liquid channel and rapid solidification of the melt associated with the humping phenomenon.
CMT ER70S-6 [110]	WFS, TS, welding position	Humping can be avoided through planning an elaborate robot trajectory (vertical-down path is the most recommended direction). They found that it is necessary to use the TS with the most restricted condition (vertical-up) to guarantee a humping free deposition.

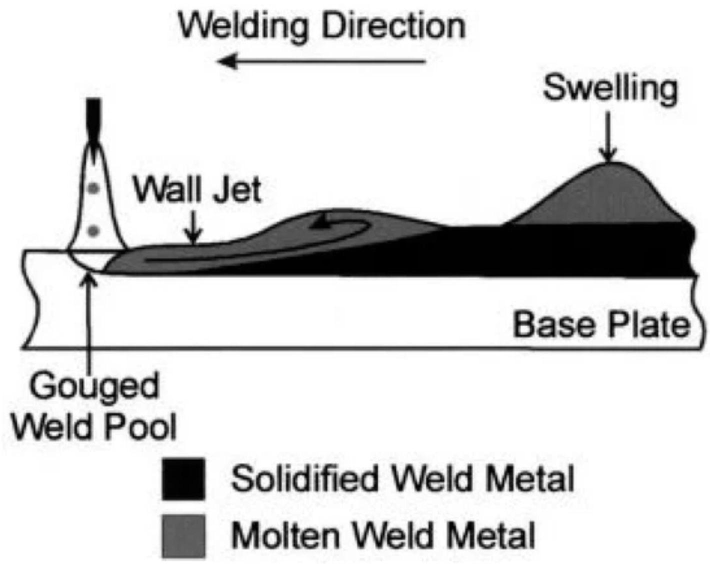

Figure 25. Humping defect [104].

2.5.6 Spatter

Spatter formation involves the generation of small droplets expelled from the torch during the deposition process, as illustrated in Figure 26. This phenomenon is commonly attributed to poor quality feed wire and suboptimal process parameters, such as current, welding speed, CTWD, and shielding gas composition [106]. The presence of spatter can significantly degrade part quality, impacting surface finish, durability, and functionality. Although post-processing operations like machining can remove spatter droplets, their initial formation may compromise the overall integrity of the part. Ji et al. [106] identified heat input, layer thickness, scan strategy, and wire curvature as critical factors influencing macro defects, including spatter, in gas tungsten arc welding (GTAW) with TC4 titanium alloy. Their findings indicated that optimizing process parameters can prevent spatter and other micro defects. Additionally, Serrati et al. [99] suggested applying hydrophobic chemicals to the workpiece surface to prevent spatter adhesion, offering a potential mitigation strategy for spatter in WAAM.

Figure 26. spatters defect [106].

2.5.7 Surface waviness

Surface waviness is a common defect in various AM processes due to their layer-by-layer construction. This defect is particularly pronounced in wire arc additive manufacturing (WAAM) because of its higher material deposition rates. The prominence of surface waviness often necessitates additional finishing processes. Shamir et al. [107] emphasized that mid-span waviness significantly affects the mechanical properties of WAAM components. To achieve optimal part quality and performance, precise control of surface waviness is essential. This can be achieved through process optimization and post-processing techniques such as machining and polishing. Addressing surface waviness is crucial to ensure the functionality and integrity of WAAM-produced parts.

2.6 Applications

2.6.1 Aerospace & Defense

WAAM is emerging as a transformative technology in metal manufacturing, particularly in aerospace and defense applications [76], [76]. Its capability to produce large-scale components offers unparalleled advantages, including cost-efficiency, on-site manufacturing, streamlined repair and maintenance processes, significant time savings, enhanced material efficiency, and increased flexibility in supply chain operations. WAAM is also pivotal for prototyping and testing, reducing reliance on foreign supply chains [126], [127]. Market trends emphasize WAAM's relevance, with the Global Aerospace Additive Manufacturing Market projected to grow to approximately $1.9 billion by 2026 [128], [128]. The aerospace sector's drive for material optimization and lightweighting aligns seamlessly with WAAM's strengths. Given the high costs and strict requirements for aerospace-grade materials, WAAM supports efforts to minimize carbon footprints, enhance fuel efficiency, and maximize payload capacities. However, to meet the aerospace industry's stringent safety, reliability, and sustainability standards, WAAM-produced components must demonstrate robust mechanical properties and defect-free manufacturing. WAAM has already shown proficiency in processing critical aerospace materials like aluminum and titanium alloys [129],[76, 126, 128-130].

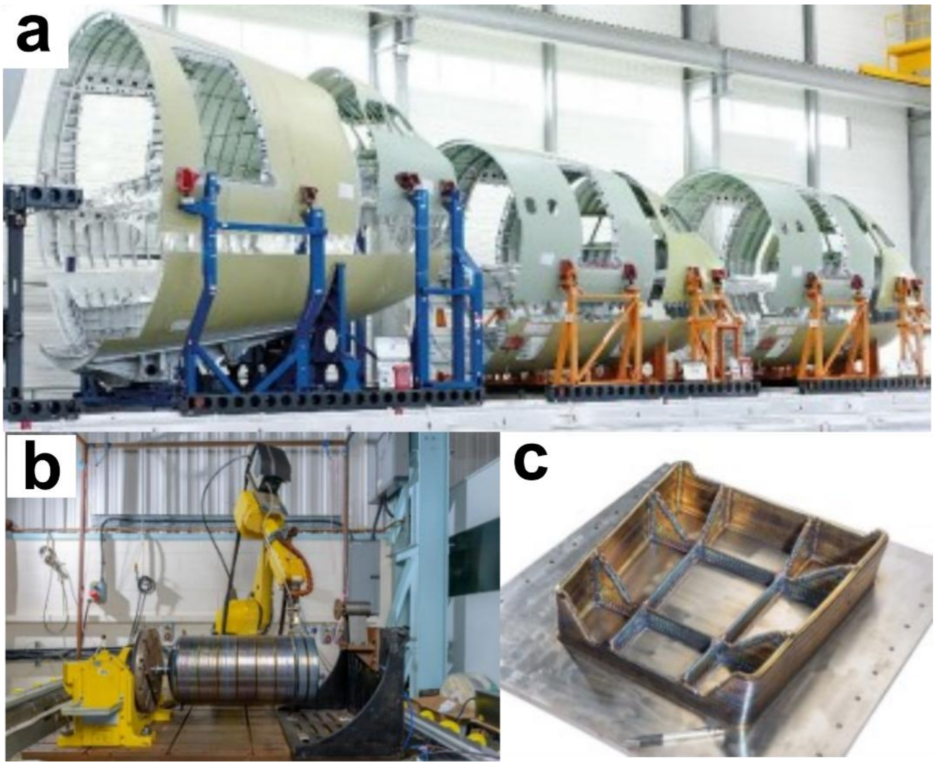

Figure 27. WAAM aerospace applications, a). plane fuselage [131], b). Titanium pressure vessel [132], c). landing gear [Plasma Transferred arc]

Collaborative efforts are pushing the boundaries of WAAM applications. For instance, Thales Alenia Space, WAAM3D, Cranfield University, and Glenalmond Technologies collaborated to develop a full-scale titanium pressure vessel for space exploration, Figure 27b. This project highlighted WAAM's ability to drastically improve lead times, material utilization, and cost-effectiveness, despite leaving room for further optimization [132], [132]. Similarly, Constellium partnered with STELIA Aerospace and CT INGENIERIE on the FAST project, integrating additive manufacturing with topological optimization to revolutionize large-scale aircraft structure production [131], in Figure 27a. This collaboration showcases how WAAM facilitates the fabrication of previously unattainable complex shapes, promoting the broader adoption of AM technologies. WAAM's integration into aerospace extends to propulsion systems. Rolls-Royce has validated the use of 100% Sustainable Aviation Fuel (SAF) in its civil aero engines, demonstrating that WAAM does not compromise engine performance. Additionally, the company is exploring titanium applications in fan blades and fan cases to achieve weight reductions in engine components, further underscoring WAAM's potential to improve component performance and efficiency [129], [129]. Despite these promising developments, challenges persist that limit WAAM's widespread adoption in aerospace manufacturing. These include the complexity of optimizing process parameters, material selection, defect mitigation, and ensuring consistent part quality. The selection of suitable materials impacts both deposition behavior and microstructural evolution, ultimately influencing the mechanical properties of WAAM components [133],[75]. Looking ahead, WAAM is poised to become an indispensable tool in aerospace design and manufacturing. Continuous advancements and innovations are expected to overcome current challenges, solidifying WAAM's role as a pivotal technology in addressing the aerospace industry's evolving demands [133].

2.6.2 Automotive & civil transport

Since the 1980s, additive manufacturing (AM) has been an integral part of the automotive industry, with WAAM emerging as a transformative alternative to traditional subtractive manufacturing due to its cost-effectiveness, high deposition rates, and ability to create large-scale components [92]. Since 1989, General Motors has strategically embraced AM, leveraging both metal and polymer-based AM machines to achieve critical manufacturing goals, including weight reduction, improved ergonomics, cost efficiency, and productivity enhancements [134], [134]. This integration highlights the automotive sector's ongoing pursuit of innovative manufacturing techniques to remain competitive and sustainable.

WAAM's potential to revolutionize automotive manufacturing is evident in projects such as PIX [8], which utilized WAAM to develop lightweight and manufacturable chassis structures for sustainable autonomous mobility, in Figure 28b. The project explored generative design structures using advanced tools like Autodesk Generative Design and PTC Frustum. However, recognizing the limitations of these tools for WAAM-specific applications, PIX developed a proprietary generative design algorithm inspired by slime mold organisms. This innovative algorithm optimized material pathways by discarding inefficient paths, focusing on minimizing mass while maximizing structural strength and functionality. Another remarkable application of WAAM in the automotive sector was demonstrated by Josten et al. [135], who employed WAAM to fabricate a gusset plate for zinc-coated automobile body parts, in Figure 28a. Utilizing a short arc welding process with controlled heat input, the project explored various weld grid configurations, such as orthogonal and diagonal patterns to enhance the rigidity of flat car body sheets. The gusset plate, composed of strategically applied weld deposits, reinforced angular sections, significantly increasing the flexural stiffness of the overall structure. This achievement underscores WAAM's ability to produce structurally optimized components that enhance mechanical performance. MX3D [136], [136], in collaboration with students from Delft University of Technology in the Netherlands, further showcased the potential of WAAM in civil transport by designing and fabricating the Arc Bicycle, a lightweight stainless steel bicycle produced entirely using WAAM, in Figure 28c. The project, completed in just three months, marked a significant milestone as the first fully metal bicycle crafted through WAAM. This achievement demonstrates WAAM's feasibility for producing functional and innovative designs within stringent timelines.

The application of WAAM in the automotive and civil transport sectors demonstrates its significant potential for enhancing innovation, efficiency, and sustainability. These projects highlight WAAM's ability to produce lightweight, structurally optimized components, improve material properties, and enable novel design solutions. With its promise of cost-effective and sustainable manufacturing processes, WAAM is poised to play a pivotal role in shaping the future of automotive production. As industries continue to innovate, WAAM's adaptability and efficiency ensure its growing relevance in addressing the challenges of modern manufacturing.

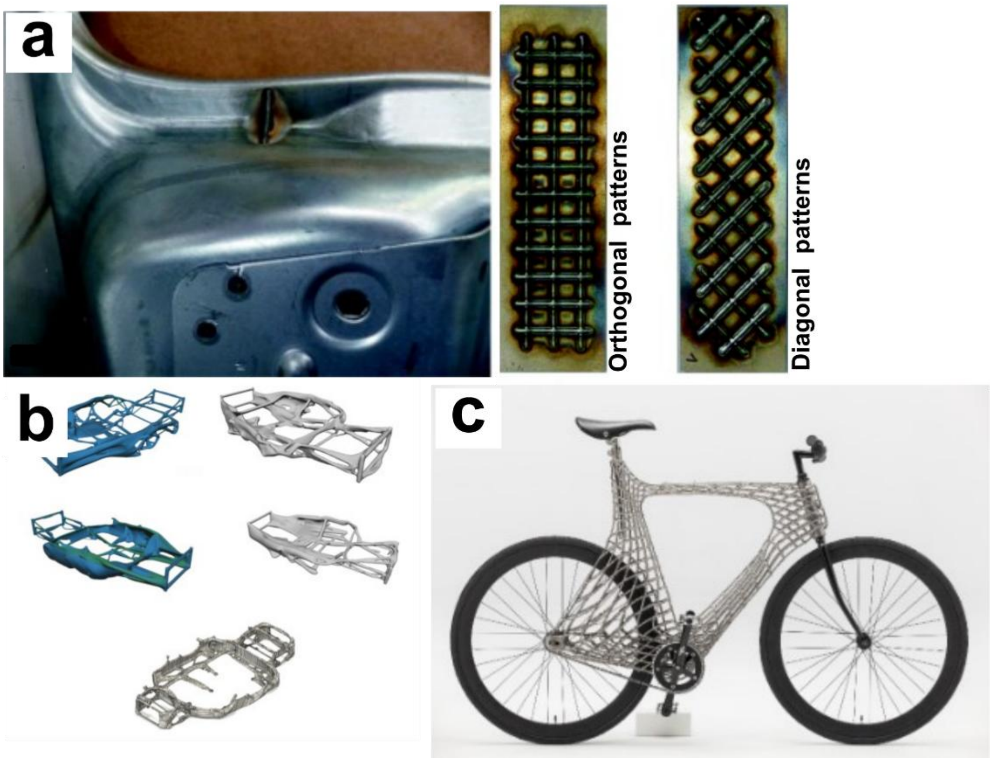

Figure 28. WAAM automobile applications, a). gusset plate on car body & Diagonal and orthogonal grid on a plane plate [135], b). Car body [8], c). Bicycle [136].

2.6.3 Marine

Within the marine industry, significant advancements have been achieved in exploring innovative manufacturing methodologies as alternatives to conventional techniques. Over the past decade, WAAM has emerged as a transformative technology capable of addressing the sector's challenges, including the production of large-scale components on-site. This capability significantly reduces supply chain complexities, enabling greater operational efficiency and offering the added advantage of customizing material properties for specific applications.

Ya et al. [137] investigated WAAM's potential in fabricating marine propellers with a diameter of 1000 mm from tip to tip, in Figure 29a. The findings underscored the value of WAAM in industrial applications, especially in reducing lead times. Traditional propeller manufacturing requires approximately 30 days, whereas WAAM eliminates several time-intensive steps such as molding, casting, and transportation. The incorporation of winglets in these propellers further enhanced efficiency by 1-4%, an improvement that is challenging and costly to achieve through conventional manufacturing techniques. A pioneering project by the USACE Detroit District demonstrated WAAM's utility in addressing infrastructure needs. This effort involved producing the largest U.S. civil works component created using 3D printing, a 12-foot-long metal part for the

Poe Lock's ship arrestor system at the Soo Locks facility [138], in Figure 29c. The component was fabricated in just 12 weeks, a stark contrast to the 18 months typically required using traditional methods. Developed in collaboration with the U.S. Army Engineer Research and Development Center and Lincoln Electric, the part played a critical role in the lock's winter maintenance cycle. This project highlights WAAM's ability to reduce lead times and operational downtime while maintaining the functionality of critical infrastructure such as the Poe Lock, vital for domestic iron ore transit. Another compelling application of WAAM involved manufacturing a large marine propeller weighing approximately 180 kg from bronze alloys. This case study demonstrated both the technological strengths and limitations of WAAM [139], [139]. Additionally, the Joint Laboratory for Marine Technology, established between Naval Group and Centrale Nantes, successfully utilized WAAM to fabricate a spare propeller blade for the French navy minesweeper “Andromède” [140], in Figure 29b. This application exemplifies WAAM's capacity to produce replacement parts efficiently, ensuring operational readiness and reducing dependency on extended supply chains.

Collectively, these examples showcase WAAM's transformative potential in the maritime sector. Its advantages include cost-effectiveness, high deposition rates, and the ability to produce complex and substantial metal components. As a viable alternative to traditional casting methods, WAAM not only streamlines production processes but also enhances sustainability by minimizing material waste. These attributes solidify WAAM's role as a pivotal technology in advancing marine manufacturing capabilities.

Figure 29. WAAM marine applications, a). marine propeller[137], b). spare part propeller blade [140], c). Poe Lock's ship arrestor system [138].

2.6.4 Construction

The construction industry is undergoing a transformative phase with the integration of WAAM. This technology offers unparalleled advantages in terms of design flexibility, customization, and operational efficiency, allowing for the creation of large-scale structural components and unique architectural features. WAAM's capability for layer-by-layer fabrication facilitates complex geometries and reduces material wastage, contributing to enhanced environmental sustainability. In disaster-prone regions, WAAM has demonstrated its potential by providing rapid solutions for constructing temporary shelters and emergency housing [141], [141].

One of the most iconic demonstrations of WAAM's capabilities is the MX3D bridge in Amsterdam [9], [9], in Figure 30a. Spanning 12.5 meters and weighing approximately 4500 kilograms, this stainless-steel structure was fabricated over six months using WAAM technology. Initiated in 2017, the bridge was a collaborative effort involving multiple partners and showcased WAAM's technological sophistication. It features sensors developed by Autodesk, enabling real-time structural health monitoring. Initially installed for a two-year permit period, the bridge was relocated in 2023 to its new site [142], [142]. This project illustrates WAAM's capacity to produce large, intricately designed components that balance functionality and aesthetic appeal.

Another noteworthy application is the fabrication of a structural steel connector weighing nearly 40 kilograms [143], [143], in Figure 30b. This component was designed to automate and optimize the production of complex connections essential for large-scale construction projects, addressing challenges like labor shortages [24], [225]. Additionally, WAAM's potential was highlighted through the 3D printing of a 2.5-meter low-alloyed carbon steel truss for the INTEGRADDE consortium [144], [144], in Figure 30c. This collaborative project, involving institutions such as Imperial College London and the University of Sheffield, achieved a structure with twice the structural efficiency of traditional designs.

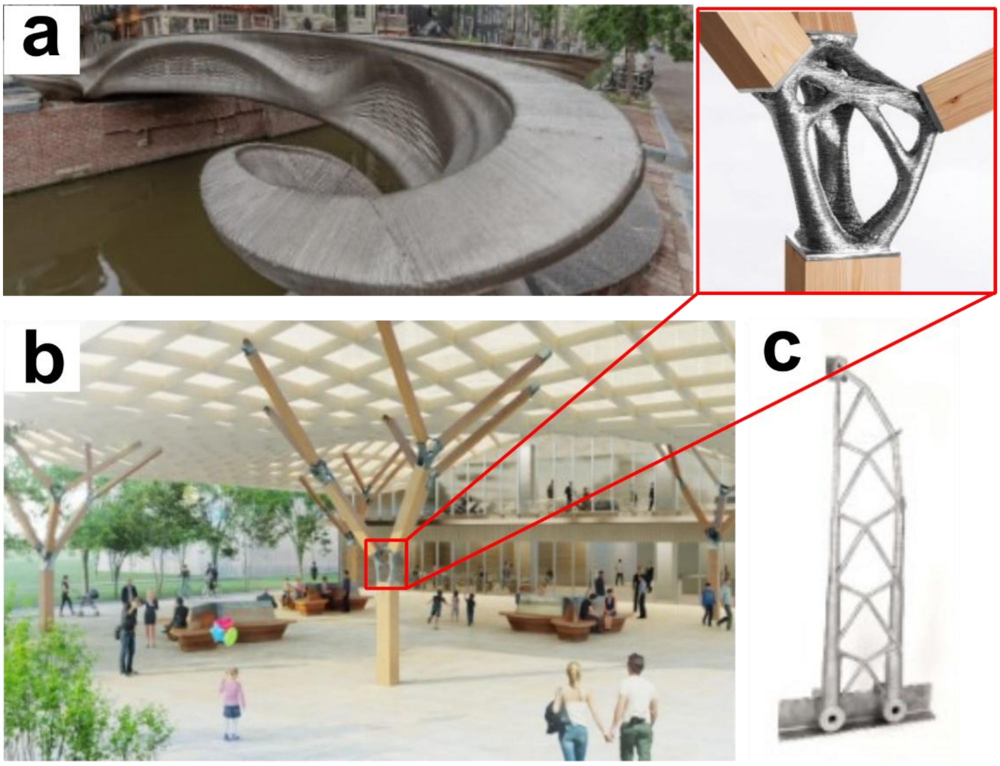

Figure 30. WAAM construction applications, a). Amsterdam bridge [9], b). structural steel connector [143], c). Truss [144].

2.6.5 Energy

WAAM technology presents transformative benefits for the energy sector, offering solutions for manufacturing large, intricate, and high-performance components, aligning with industrial needs for efficiency and sustainability. One standout accomplishment in this domain is the collaboration between Andritz Savonlinna and the Finnish Additive Manufacturing Ecosystem (FAME) [145], [145]. This partnership produced Finland's largest metal 3D-printed component, a 300 kg pressure vessel with a diameter of 900 mm and a height of 1600 mm, designed to operate at pressures of up to 10 bars, with significant safety margins, in Figure 31b. Initial predictions estimated failure at 90 bars, but in destructive testing, the vessel exceeded expectations, withstanding an impressive 111 bars. This demonstrates WAAM's potential for producing components with exceptional mechanical integrity. Another noteworthy application of WAAM in the energy sector comes from WAAM3D, based in Milton Keynes, which partnered with the Aircraft Research Association Ltd (ARA) [131], [131]. This collaboration successfully fabricated an aluminum wind tunnel nose cone, in Figure 31a. The nose cone was integrated into a wind tunnel model and underwent rigorous testing in 2022. By leveraging WAAM technology, the project achieved a 74% reduction in both lead time and material usage, highlighting the process's advantages in optimizing production efficiency and cost-effectiveness. The ongoing collaboration aims to broaden WAAM's applications to other components and investigate its suitability for diverse alloys, further extending its utility in advanced manufacturing. A further example of WAAM's success in the energy sector is its application in producing a 350 kg CuAl8Ni2 impeller for ENGIE's gas-fired power plant cooling system in Belgium [146], [146]. Manufactured by MX3D in Frankfurt, Germany, this impeller measured 1 meter in diameter and 53 cm in height, in Figure 31c. Utilizing a robotic WAAM process, the component was printed in just nine days with an average deposition rate of 3.2 kg per hour. In stark contrast, traditional casting methods would require six to eight months for a similar component. This remarkable improvement underscores WAAM's capacity to drastically accelerate production timelines while maintaining or even exceeding the quality of conventional manufacturing processes.

The success of these projects highlights WAAM's potential to address critical challenges in the energy sector by enabling rapid, cost-effective, and material-efficient production of essential components. This positions WAAM as a valuable and forward-thinking solution for advancing the capabilities and sustainability of energy infrastructure.

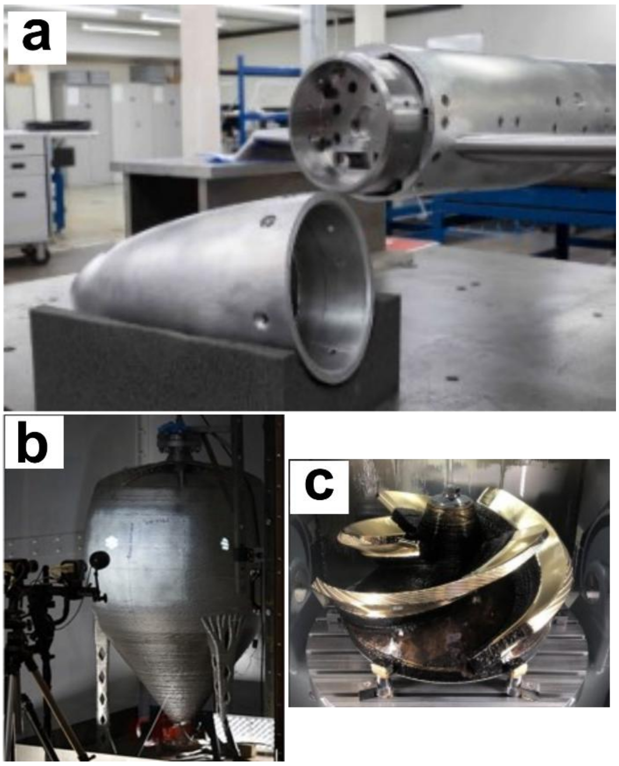

Figure 31. WAAM energy sector applications, a). Aluminum wind tunnel nose cone [131], b). pressure vessel [145], c). impeller [146].

Chapter 3 – WAAM current state of art

This section of the thesis delves into the significant advancements achieved in the WAAM process over recent years, with a specific focus on the improvements in WAAM part material properties. This section aims to provide a detailed examination of the technological progress in WAAM, covering innovations in process optimization, material science, and their combined impact on the performance and reliability of WAAM-fabricated parts.

3.1 Advancements in WAAM

3.1.1 Process parameters optimization

The selection and optimization of process parameters are crucial for enhancing product quality in WAAM. However, selecting these parameters involves balancing various requirements and machine limitations. The critical process parameters in WAAM include current, voltage, travel speed, wire feed speed, stand-off distance, shielding gas flow rate, and interlayer dwell time. These parameters also depend on the wire material, substrate dimensions and thickness, and component size. Optimizing process parameters for a single bead is essential before depositing multi-layer objects to ensure process efficiency. however, this is only a starting point as different deposition conditions develop as the process proceeds during subsequent layers. Ahsan et al. [21] developed a design of experiments for a single bead, analyzing welding current, travel speed, and wire feed speed. Using analysis of variance (ANOVA), they optimized the process parameters to achieve the minimum required energy density for uniform and continuous beads.

Vora et al. [40] also utilized the ANOVA method to optimize WAAM process parameters for low alloy steel using the GMAW process. Travel speed, wire feed speed, and voltage were the input parameters, while bead height and width were the output parameters. Similarly, Han et al. [31] optimized parameters such as current, voltage, travel speed, and Contact Tip-to-work distance (CTWD) and applied these optimal parameters to manufacture a curved propeller-shaped blade. The optimization of parameters not only enhances the material quality but also improves production time. Thien et al. [36] investigated the effects of CTWD and dwell time on bead geometry to minimize production time. They found that increasing dwell time correlated with longer production times. Samples produced with zero dwell time exhibited more surface irregularities and less height compared to those with a 60s dwell time, necessitating more machining time. Additionally, they demonstrated that a higher CTWD could reduce the shielding effect on geometry, leading to significant build failures in samples with elevated CTWD.

Some of the other studies on process parameter optimization are reported in *Table 7.*

Table 7 Some papers on the importance of process parameters optimization (need to report it in the text)

Ref	Studied process parameters	Discussion & Suggestions
Le et al. [37]	Current, Voltage, travel speed	The input process parameters were optimized based on output parameters such as bead height, width, penetration,

		and dilution using ANOVA, with further optimization identified through grey-relation analysis (GRA) and techniques for order-preferences by similarity-to-ideal solution (TOPSIS) methods.
Ayed et al. [43]	Travel speed, Wire feed speed	P.P.'s effect on the microstructural evaluation and material properties was studied.
Ji et al. [106]	Heat input (Current, Voltage, Travel speed), layer thickness, tool path, wire curvature	macro defects like spatter and collapse of bead were noticed and this was caused due to inappropriate selection of process parameters.
Dinovitzer et al. [24]	Current, Travel speed, Wire feed speed, shielding gas flow rate	Optimization techniques like Taguchi and ANOVA analysis were used to find the process parameters effect on the geometry and microstructural properties of SS304 WAAM.
Gopal et al. [20]	Current, Voltage, Travel speed	Depth of penetration increased linearly with the decrease in travel speed and depth of penetration decreased after optimal value of travel speed.
Chernovol et al. [147]	Heat input (Current, Voltage, Travel speed)	Effect of HI on the microstructural and mechanical properties of mild steel were explored. Increased HI, might degrade the material properties.
Liberini et al. [148]	Current, Voltage, Travel speed, Wire feed speed	Optimized the P.P's based on the microstructural and mechanical properties of final samples.
Nguyen et al. [15]	Current, Voltage, Travel speed	Optimized the P.P's based on the microstructural and mechanical properties of final samples.
Novelino et al. [149]	Current, Voltage, Travel speed, Wire feed speed	Studied the correlation between input P.P's and geometry of deposited walls.
Rosli et al. [23]	Travel speed, Wire feed speed	Optimized the P.P's based the Geometry and defects in multi-layered deposition.
Thien et al. [36]	Power (Current, Voltage), CTWD, Dwell time	Optimized the P.P's based on the geometry and production time.
Trad et al. [56]	Travel speed, wire feed speed, Shielding gas flow rate	Optimized the P.P's based on the beads geometry.
Xiong et al. [49]	Travel speed, wire feed speed, Interlayer temperature	Optimized the P.P's based the multi-layer single wall lateral surface roughness.

3.1.2 Inline process improvements

3.1.2.1 Friction stirring

The friction stir improvement process is a mechanical technique used in the context of WAAM to enhance the quality of deposited beads. In this method, a friction stir spindle apparatus is integrated with the WAAM system. The spindle moves synchronously with the torch head, maintaining a fixed distance from it, Figure 32. By rotating at a specified speed over the deposited beads, the spindle flattens the bead for subsequent deposition. Concurrently, this process mitigates residual stresses and refines the grain structure. He et al. [150] demonstrated that the friction stir process significantly reduced porosity, disrupted the Si-rich eutectic phase, and refined the microstructure of aluminum alloy. Samples treated with friction stir showed a 108% increase in elongation and a 28% improvement in fatigue life. Similarly, Liu et al. [151] investigated the impact of the friction stir process on microstructure and mechanical properties. Their study reported a notable decrease in both the diameter and frequency of porosity, along with a reduction in grain size. The friction stir process was found to enhance mechanical properties, including yield strength, tensile strength, and elongation. This process can be used during, or after the deposition, as a post-processing operation.
Some more studies that explored this friction stir process are reported in *Table 8*.

Table 8 Friction stir process effect on WAAM produce samples material properties.

Ref	Effect
Qie et al. [152]	Fine equiaxed grains Improved tensile properties Isotropic properties
Yuan et al. [153]	Improved microhardness Improved tensile strength Improved elongational properties
Zhang et al. [154]	As a post-processing operation Reduced porosity Fine equiaxed grains Improved tensile and elongation properties Reduced microhardness

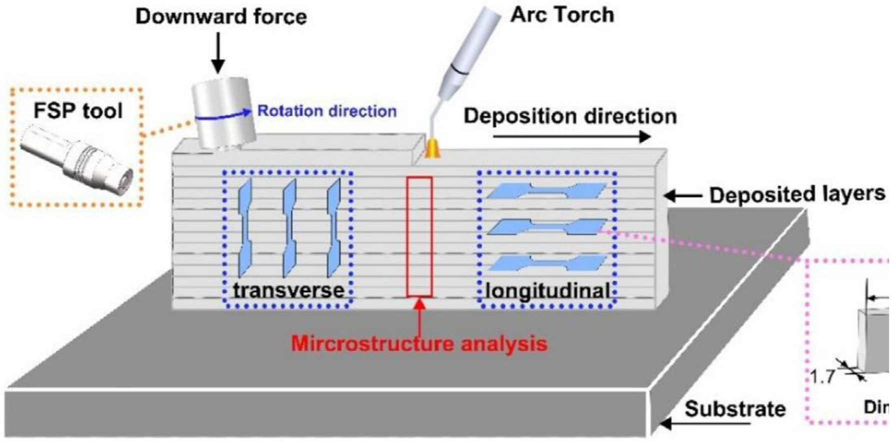

Figure 32. Schematic of Friction stir process in WAAM.

3.1.2.2 Rolling

Inter-pass rolling employs a circular roll over the deposited bead to achieve homogeneity in the bead structure, as illustrated in Figure 33. This process not only promotes bead homogeneity, but also refines the microstructure, reduces residual stresses, and eliminates porosity. However, inter-pass rolling necessitates more complex equipment and is limited to simple geometries due to the geometric constraints of the roller [82]. Fu et al. [155] demonstrated that micro-rolling can mitigate anisotropy and enhance the mechanical properties of bainitic steel. Their study outcomes demonstrated more uniform deformation, a flat surface, and a more equiaxed grain structure. The specimens exhibited improved impact toughness, elongation, and ductile fracture surfaces. Colegrove et al. [156] investigated various rolling conditions, including rollers with and without slots and varying loads. Components processed with rolling exhibited two distinct regions: one with refined grains beneath the fusion zone and another with non-refined grains. The findings indicated that in the construction of straight walls, rolling significantly reduced distortions and residual stress. Additionally, slotted rolling decreased lateral distortion, increased deposition efficiency, and minimized the need for further machining.

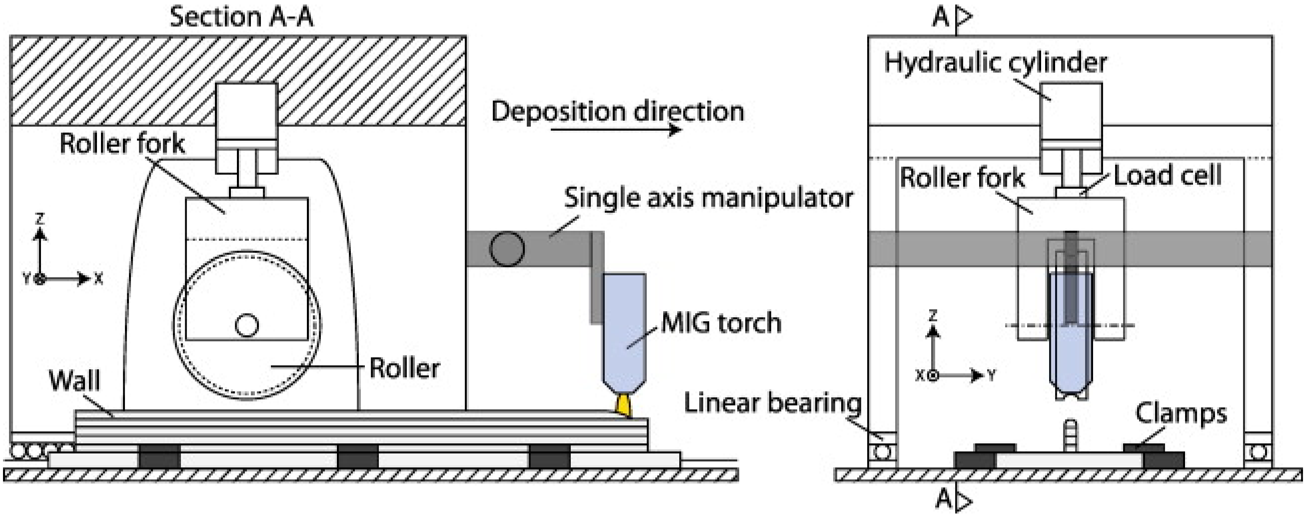

Figure 33. Schematic of rolling process in WAAM [156]

3.1.2.3 Hammer peening

Hammering in WAAM is similar to the forging process, where heated material undergoes controlled impacts to achieve a desired shape. In WAAM, hammering is specifically utilized to flatten the deposited surface, influencing material properties with reduced force and scale.

According to Zhou et al. [157] extended hammering time reduced the porosity, enhanced the recrystallization, and improved the mechanical properties. Additionally, Niu et al. [158] demonstrated that hammering mitigated molten material flow, reducing the need for machining processes, decreasing porosity, and improving both grain size and overall mechanical properties. Honnige et al. [159] applied machine hammer peening to WAAM-produced Ti-6Al-4V, resulting in grain reorientation and refinement. The maximum refined grain depth reached nearly 2 mm. Their findings also indicated that interpass peening produced larger grain sizes compared to interpass rolling, due to shallower indentation and reduced plastic strain. Xiong et al. [160] examined the effect of different hammering temperatures on the microstructural and mechanical properties of repaired hydraulic turbine blades. Their results revealed that hammering mitigated molten pool flow during deposition by providing a flat surface, thereby increasing the yield strength of the deposited layers through improved grain size.

3.1.2.4 Interpass cooling

Interpass cooling employs pressurized air between successive layers to cool the deposited layer and reduce the temperature gradient, as illustrated in Figure 34. Kozamernik et al. [161] utilized high-pressure air for cooling the deposited layers, using the same deposition head as a nozzle for the cooling air. The deposition head traversed the scan path twice: once for material deposition and subsequently for the application of cooling air. Comparative analysis between samples with and without interpass cooling revealed that interpass cooling improved dimensional accuracy and resulted in a 30% increase in productivity without compromising the part quality. Wu et al. [162] on the other hand, CO2-forced interpass cooling was applied immediately after each deposition with a separate nozzle. The study demonstrated that interpass cooling significantly influenced bead geometry and enhanced both hardness and strength.

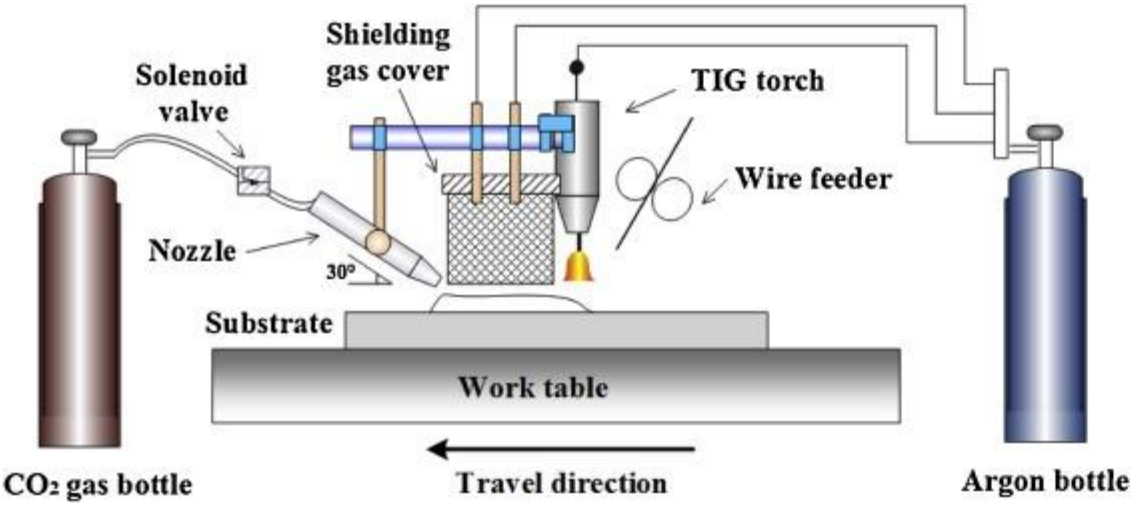

Figure 34. Schematic of interpass cooling process in WAAM [162]

3.1.2.5 Ultrasonic vibrations & Impact

The ultrasonic vibration process is integrated during the deposition phase. Unlike other methods, the ultrasonic vibration is not directly applied to the deposited bead but to the underlying substrate, where a vibrator operates at a frequency essential for the quality of the deposited bead. Chen et al. [163] explored Ultrasonic-assisted WAAM (UAM) for fabricating Inconel 625 alloy. UAM transformed coarse equiaxed grains into fine equiaxed grains. The UAM samples exhibited improved tensile and yield strength, with fractured surfaces indicating ductility. Xu et al. [164] applied UAM as a post-processing operation, resulting in equiaxed grain growth and enhanced hardness and elongation properties.

The ultrasonic impact technique (UIT) is utilized to enhance the mechanical and microstructural properties of fabricated parts [citation missing]. The equipment can be mounted on the WAAM torch head or used separately as a post-processing technique. It uses a vibrating indenter that impacts the targeted region at a specified frequency. Yuan et al. [165] applied an ultrasonic probe to stainless steel, resulting in refined grain size, increased microhardness, and improved yield strength.

3.1.2.6 Laser shock peeing

Laser shock peening (LSP) employs a high-energy laser directed at a confined region to release residual stresses and promote microstructural reorganization. Ermakova et al. [166] investigated the effects of LSP as a surface treatment on corrosion-fatigue crack growth (CFCG) behavior in samples fabricated via Wire Arc Additive Manufacturing (WAAM). LSP was applied to the samples post-extraction from the WAAM-built wall, as illustrated in Figure 35. The study demonstrated that LSP significantly reduced the rate of CFCG and improved the fatigue life of the samples. Jing et al. [167] also examined the use of LSP for controlling porosity in 2319 aluminum alloy samples. Their results indicated that LSP could affect a depth of 1.3 mm in the aluminum 2319 alloy, resulting in a 65% reduction in porosity and enhancements in yield strength, tensile strength, and fatigue life.


(a) (b)

Figure 35. Laser shock peening on a sample a). during the process, b). after the process [168]

3.1.2.7 Cold metal transfer (CMT)

Cold Metal Transfer-based Wire Arc Additive Manufacturing (CMT-WAAM) represents a cost-effective alternative for production of large components, characterized by high deposition rates and lower heat input. Metals and alloys produced through CMT-WAAM exhibit superior mechanical properties compared to both wrought and as-cast materials [169]. The establishment and patenting of CMT-WAAM dates back to 2004, with FRONIUS being the pioneer of this technology. CMT, a subset integrated with GMAW, governs the operational dynamics of CMT-WAAM. The process involves the transfer of molten metal droplets from the electrode wire during metal transfer. Upon detecting a short circuit, the system reduces the current to near-zero levels and retracts the feed wire to facilitate material cooling. This mechanism ensures a smoother and lower heat input process, distinguishing it from conventional WAAM methodologies [35]. After completion of the metal transfer to the deposited region, the system re-starts the arc by putting back the previous current value and advancing the wire. Bento et al. [35] mentioned that the CMT-WAAM offers superior productivity compared to conventional WAAM.

Various CMT variants, such as CMT-Pulse (CMT-P), CMT-Advance (CMT-A), and CMT-Pulse Advance, contribute to the versatility of CMT [170]. Tomar et al. [170] highlights in his review article that CMT-WAAM surpasses GTAW and PAW in terms of heat input, spatter generation, initial expenditure, wire feeding complexity, and material deposition rate, Figure 36. The results also indicated that the mechanical characteristics of materials manufactured by CMT-WAAM (titanium, steels, aluminum alloys, and nickel-based alloys) were enhanced over those of as-cast materials and equivalent to wrought materials.

Stinson et al. [171] performed a comparative investigation contrasting MIG and CMT welding processes. The study assessed factors including deposition rate, repeatability, geometric precision, and hardness of fabricated samples. Results revealed superior repeatability and reduced standard errors in samples produced via CMT. Additionally, CMT demonstrated enhanced productivity and material utilization efficiency compared to MIG. Mainly, irrespective of welding mode, material hardness was predominantly influenced by heat input. However, normal MIG exhibited a higher material deposition rate compared to CMT.

Senthil et al. [172] studied the material properties of SS316L multi-layer walls using CMT-WAAM. The constructed wall exhibited no discernible defects, and material tensile and impact tests demonstrated performance comparable to wrought manufactured parts. Additionally, fractured samples from CMT-WAAM exhibited a ductile microstructure, and hardness values decreased as the height of the samples increased.

Some of the other interesting studies, which investigated the CMT process and it's effect, are reported in *Table 9*.

Table 9 Some papers who studied the CMT process.

Ref	Material feed	Effect/ outcome
[173]	Al-4043 alloy	• Isotropic mechanical properties were observed. • Dendrite grains increased from the bottom to the top of the wall. • Similar corrosion resistance was observed from the top to the bottom of the wall.
[174]	Inconel 625	• Grain morphology varied through different regions of the part (top-middle-bottom). • Cellular grains-bottom region • Cellular & columnar grains-middle region • Columnar dendrites-top region • Anisotropic tensile properties were observed between horizontal (failure mode II and vertical samples (failure mode I). • Hardness value decreased as the height of the sample increased.
[175]	Stainless steel	• showed anisotropy in the as-built condition concerning mechanical parameters, with lower strength values in the vertical (Z) direction.
[176]	AZ91 magnesium alloy	• Equiaxed grains were found. • Travel direction samples showed better tensile and elongation properties compared to build direction.

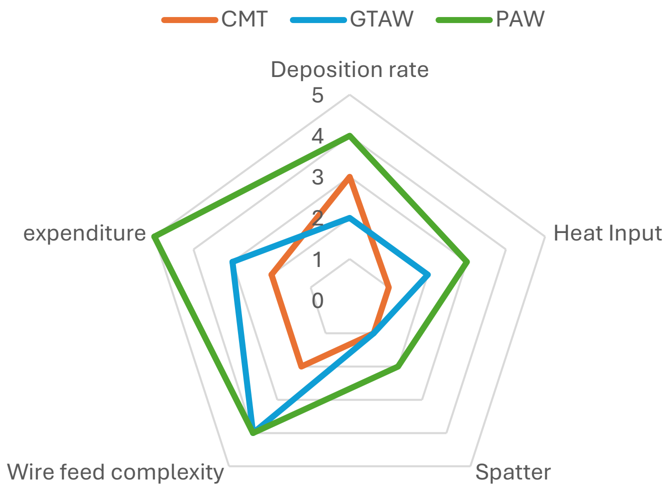

Figure 36. Radar diagram comparison of CMT, GTAW, & PAW. [170]

3.1.3 Feed wire material properties improvement

The incorporation of silicon (Si), nickel (Ni), titanium carbide (TiC), and titanium diboride (TiB) elements into the wire feedstock demonstrates a notable augmentation of their characteristics. TiC and TiB, acknowledged as high-performance ceramic materials, are utilized in metal matrix composites due to their heightened melting points, hardness, and thermal stability [177]. Nickel contributes to increased corrosion resistance and wettability [178], while Si may lead to the formation of silicide [179]. Chen et al. [180] investigated the impact of trace Si addition on the microstructure and properties of Ti6Al4V. The introduction of 0.1 wt% Si refined prior-β grains, led to a reduction in grain width and a discontinuity in the continuous α-phase grain boundary. This also contributed to enhanced tensile strength, diminished elongation, limited anisotropy, and improved ductility. Jiang et al. [181] investigated the impact of TiC particles on Nickel alloy 690 (Ni690) using CMT-WAAM. Results revealed enhanced microstructural and mechanical properties upon TiC particle addition. Specifically, incorporation of 1.0 wt% TiC led to significant reductions in grain size, tensile strength, and corrosion resistance. *Table 10* reports *some papers discussed about Si, Ni, TiC, & TiB inclusion effect on material properties.*

Table 10 Feed wire material properties improvement.

Ref	Process	material	Added element	Outcome
[182]	GMAW	Ti6Al$V	TiB & TiC	TiB & TiC powder particles dissolved and reacted with the matrix. Martensite structure in the top region. Net-backet and Niddle-like martensite structure in the bottom region. Ti was formed as a net-basket-like structure in the top region.

				Hardness increased as the wt% of powder particles (TiB&TiC) increased. But decreased wear resistance was observed in 10 wt% samples compared to 5 wt% samples.
[183]	CMT-GMAW	SS316L-Si	TiC	Refined grain structure. Improved hardness, tensile strength, and reduced anisotropy.
[184]	CMT-WAAM	Inconel 625	TiC (Cladding)	IN625+30% TiC content samples have elongated dendrites, that resulted in 2.25 times higher hardness. As the TiC powder content increased, wear resistance improved.
[177]	Laser cladding (L-DED)	Q235 low carbon steel	TiC-TiB2 (Cladding)	TiC particles were attached to the TiB2 particles. TiB2 had a dark rectangular shape, and TiC had a light grey spherical shape. Microhardness was 7 times more than the substrate and this automatically improved the wear resistance.

3.1.4 In-situ monitoring

WAAM is a highly intricate process since it involves several process parameters which affect the power supplied and thermal exchange mechanisms. These influence, the deposited bead geometry, mechanical characteristics, surface finishing, thermal distortions as well as the defects development. In addition, the temperature distribution is also highly sensitive to the geometry of the component and the deposition strategy. All these interdependencies make extremely challenging the process. To this end, in-situ monitoring emerges as an valuable tool for enhancing the WAAM process [185]. Everton et al. [185] reported the manufacturers' reluctance in adopting AM technology owing to the difficulty in part quality assurance. To overcome such limitations the authors suggested the adoption of different in-situ monitoring techniques tailored for AM. Xu et al. [127] used different in-suit monitoring techniques to monitor the WAAM process closely. In which, acoustic signal monitors the current signals and sound intensity emanating from the arc, serving as a widespread method for defect and feature detection. X-ray CT facilitates the monitoring of internal aspects, such as porosity formation and melt pool shape. Optical measurement focuses on the observation of bead geometry, while thermal measurement quantifies in-situ temperature levels. More recently, machine learning (ML) has emerged as a predominant problem-solving technique in various domains [186]. Le et al. [187] developed a robust surrogate model (SM) for predicting the temperature history in WAAM through the integration of machine learning and finite element model (FEM). The FEM results were used for model training. The resultant model exhibited a remarkable accuracy of 99%, with a prediction time of 38 seconds. Even tough, the ML model was not compared to real-time monitoring, the author suggested the feasibility of such an approach for future real-time monitoring applications.

Li et al. [188] applied a convolutional neural network (CNN) to detect defects in WAAM. This CNN is based on the deep learning solution You Only Look Once (YOLOv4), was trained on four distinct categories: weld, surface pores, groove, and slag inclusion. The model involved the utilization of DarkNet53 as a backbone, three feature maps for different levels of detail in the training data, max pooling for each feature map, and a detection layer to enhance the CNN model. Comparative analysis with other machine learning CNN models, his model reveals a superior accuracy for the proposed data. The terms commonly used in machine learning (ML) model training, such as data augmentation, data pooling, and feature mapping, may be unfamiliar to those without a background in ML. However, familiarity with these concepts is essential for understanding the underlying mechanisms of model operation.

Hamrani et al. [189] analyzed the current state-of-the-art in integrating machine learning into the WAAM process. The study addressed frequent challenges in WAAM that are mitigated through machine learning, exploring various ML models along with their respective advantages and disadvantages. As a data-driven process, machine learning requires large datasets for effective training and testing [192]. Despite these advancements, the adoption of machine learning in the AM process, including WAAM, remains in its emerging stages [190]. Serrati et al. [99] studied different in-line non-destructive testing (NDT) like phased-array ultrasonic testing, Electromagnetic acoustic transductor, Laser ultrasonic testing, Real-time radiography, X-ray backscatter, eddy current testing, Infrared thermography, and Laser thermography [189, 190].

3.1.5 Numerical simulation

Beyond optimization, numerical simulations substantially reduce the time and costs associated with experimental trials [191]. Once correctly calibrated and validated, numerical simulations can potentially provide a large amount of data in a short time. Moreover, numerical simulations offer temperature management and torch motion, employing control over deposition shape, which leads to the quality of the deposited components. Thus, numerical simulation represents an effective and pivotal tool in advancing the efficiency and efficacy of the WAAM process. The optimization of parameters within WAAM is crucial for strengthening parts quality and process efficiency, is a direct outcome of numerical simulations [187]. Ogino et al. [191] developed numerical model for an in-depth understanding of the underlying physical phenomena governing WAAM, such as heat transfer, fluid flow, cooling and solidification. The model was adopted to study the impact of travel direction and interlayer temperature on bead geometry of CMT-GMAW weld pool. The construction of a wall involving ten layers was modelled, are shown in Figure 37. Two walls were constructed, one with an interlayer temperature of 300K, and another without. Figure 37b presents the outcomes of the numerical simulation model. Cross-sectional images from Figure 37b reveal that the wall subjected to interlayer cooling exhibited reduced thickness and greater height compared to its counterpart without interlayer cooling Figure 37a.

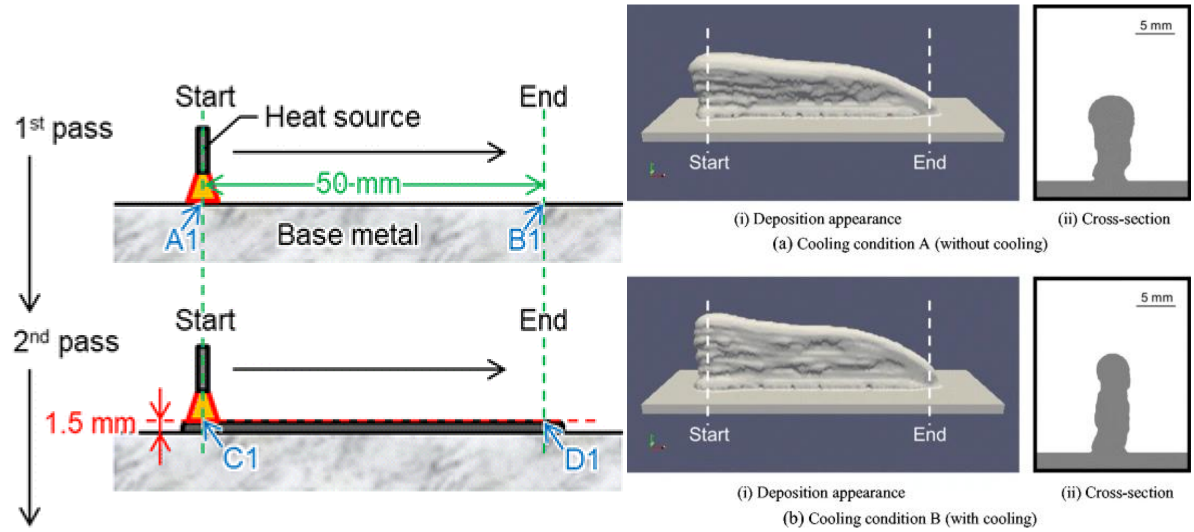

Figure 37. Uni-directional numerical simulation of wall, a). Without cooling, b). with cooling (300K) [191]

Figure 38, depict simulation and experimental outcomes for two walls, distinguished by same and reversed weld directions for each layer. Especially, the simulation models featured a 50 mm bead length with ten layers, while the experimental walls were constructed with a 100 mm bead length and 40 layers. The wall constructed with a reversed weld direction displayed a notably more uniform height than its counterpart with the same weld direction. Despite the inequality in dimensions, both simulation and experimental results demonstrated similar trend conditions with the varied process parameters. Therefore, from these studies it is clear that the numerical simulations can be reliable.

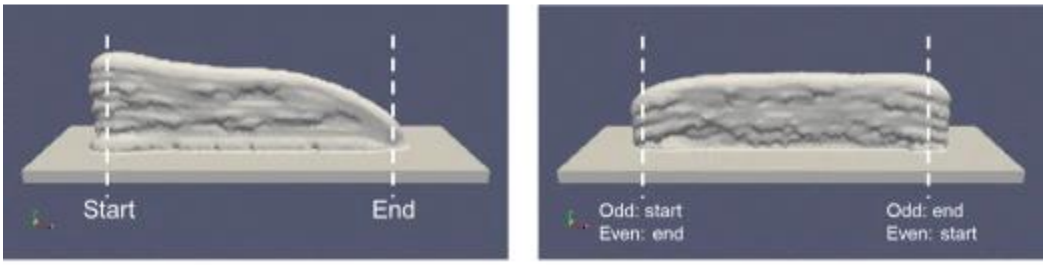

(a) Pattern L-A (b) Pattern L-B

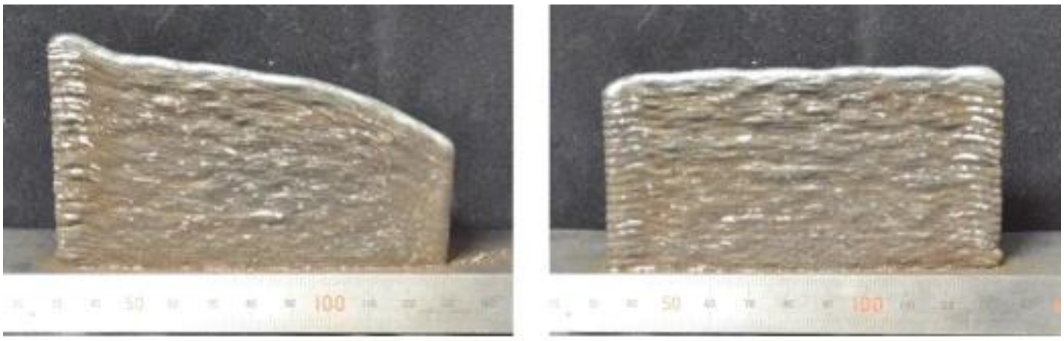

(a) Pattern L-A (b) Pattern L-B

Figure 38. Comparison of numerical simulation model and experimental samples, a). same-directional, b). reverse direction [191]

Zhao et al. [192] developed finite element model using MSC marc software to study the thermal, residual stress, and deposition direction effect. The FEM results showed a similar trend to the experimental data. The study found that as the number of layers increased, the heat source effect decreased as well as the stress peak, and the residual stresses were stable in the middle part of the component, while the starting and end of the part fluctuated. Zhao et al. also mentioned that the sample deposited in the reverse direction had smaller residual stresses than the sample deposited in the same direction.

3.1.6 Post-processing

3.1.6.1 Heat treatment

Heat treatment (HT) is largely employed to enhance the part quality within the field of AM [193] [s14][193]. The manufactured part undergoes controlled heating and subsequent cooling to attain specified material properties. The parameters governing HT, including temperature, process duration, and cooling, depends upon the specific material. For metals HT is employed to release the underlaying residual stresses, mitigate porosity, cracks, and enhance the microstructural and mechanical characteristics of the part. Chen et al. [194] conducted a study on the microstructural evolution and mechanical properties of GH4169 alloy in WAAM through the implementation of HT as a post-processing procedure. Two distinct heat treatments were employed, namely an industrial HT at 950°C, leading to partial dissolution of the Laves phase in GH4169 material and the generation of a new δ-phase in the previously Laves-infested regions. This resulted in decreased elongation when deformed at room temperature. The second treatment involved a modified HT at 1500°C, completely dissolving the Laves phase and enhancing elongation at room temperature. The study concluded that, particularly for Ni-based superalloys, the modified HT presented a better solution. Considering the known distortions in WAAM-produced samples due to residual stresses, HT emerges as a feasible solution for stress relief. Goviazin et al. [97] explored various HT conditions as stress relief techniques for WAAM-produced SS316L. Outcomes indicated that samples heat-treated at 600°C in a vacuum displayed minimal residual stress, by reducing the material strength. In contrast, Chen et al. [195] investigated the effects of HT on the material properties of WAAM-produced Inconel 718, revealing that the HT process effectively improved yield strength and elongation. HT can either enhance or diminish material properties, depending on the specific conditions applied. *Table 11* provides a summary of the effects of heat treatment on selected material properties.

Table 11 Heat treatment effect on WAAM produced parts

	Heat treatment effect	Ref
Distortion & Residual stresses	Improved	[97]
Hardness	Decreased	[196], [164],
Impact test		[195]
Tensile	Improved	[197], [196], [198], [164], [199], [197, 200]
Yield strength	improved	[197], [195], [196], [198], [164], [197, 200]
Elongation	Improved	[197], [195], [194], [196], [198], [164], [199], [197, 200]

Ductility	Improved	[197], [196], [198], [199],
Grain size	Increased	[196], [194], [164, 196]
Porosity	Reduced	[101], [101, 196]

3.1.6.2 Machining

Secondary machining operations, such as milling and sandblasting represent a key solution to achieve specified tolerance limits and surface roughness in WAAM parts [201]. Tankova et al. [202] investigated the influence of machining to determine the influence of the surface roughness on material properties. Samples were extracted from orientations aligned at 0°, 45°, and 90° to the built direction. Half of the samples underwent machining (surface finishing), while the other half remained in an as-built state. The results indicated that machined samples consistently exhibited enhanced strength and ductility across all test conditions indicating that machining also serves to enhance the material properties of WAAM-built components.

Felice et al. [203] calculated the surface waviness of the deposited wall by measuring the cross-sectional area, obtaining values of 104 µm and 125 µm for the lateral surfaces. Following machining to define the functional area of the wall (Figure 39), the deposition efficiency was determined through a comparative analysis of the material volume before and after machining, revealing the deposition efficiency of 53%. Even the machining operations can also be used to improve the fatigue life and corrosion resistance [204].

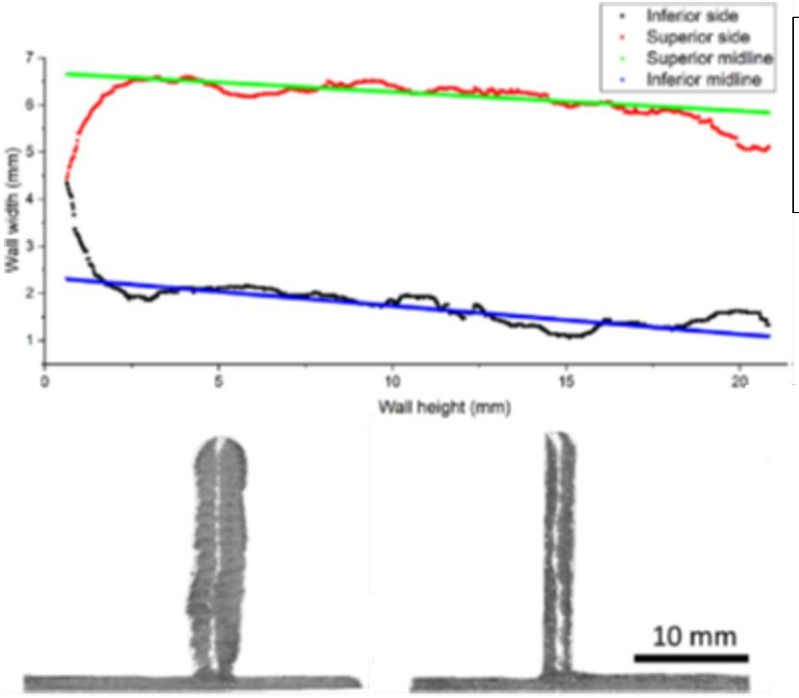

Inferior side
Superior side
Superior midline
Inferior midline

Figure 39. post-process milling of WAAM produced wall a). Before, b). After [203]

3.1.6.3 Other methods

Boriding, a thermochemical surface hardening process, involves the diffusion of boron atoms into metal components, resulting in the formation of metal borides characterized by elevated hardness and wear resistance [205], [206]. This technique is conducted by exposing the metal components to a boriding mixture, operating parameters such as temperature and duration can be varied to achieve desired boride layer depths. While boriding is conventionally employed on steel, its applicability extends to various metal alloys, allowing the attainment of desired material properties, including superior surface hardness, wear resistance, thermal stability, and corrosion resistance [205-207]

Günen et al. [208] applied the boriding process to machined and surface-cleaned rectangular blocks fabricated through WAAM. These blocks were exposed to a powder mixture (90% B4C + 10% NaBF4) at 1000°C for 1 hour in an atmosphere-controlled furnace and subsequently exposed to the ambient air. A distinct layer formed on these blocks was then subjected to comparative evaluation against the as-built samples. The results indicated a notable enhancement in surface hardness by a factor of four and a substantial increase in wear resistance by a factor of 31.78 when compared to the as-built samples

3.2 WAAM part characteristics

Quality assessment of components in WAAM requires comprehensive mechanical and microstructural analyses. Mechanical analysis evaluates part quality on a macroscale through tests such as microhardness, tensile strength, impact resistance, fatigue performance, bending behavior, liquid penetration, and laser ultrasonic inspection. Concurrently, microstructural analysis examines part quality on a microscale using techniques such as optical microscopy (OM), scanning electron microscopy (SEM), X-ray diffraction (XRD), electron backscatter diffraction (EBSD), transmission electron microscopy (TEM), and other non-destructive testing (NDT). The mechanical properties of fabricated components are intricately linked to their microstructure, especially grain formation. In the WAAM process, molten metal is deposited onto a cold substrate, initiating solidification from the bottom to the center of the melt pool [93]. The rapid solidification rate promotes the formation of columnar and equiaxed grains perpendicular to the fusion line [93], [209], Figure 40.

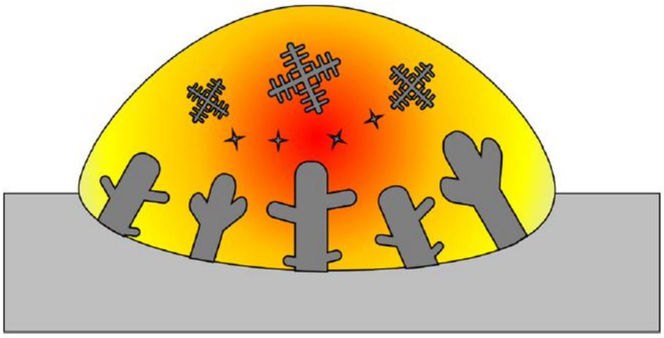

Figure 40. Schematic of solidification process [106]

Several factors influence microstructure and grain formation. Heat input affects the cooling rate and thermal gradients, with higher heat leading to coarser grains and more columnar grain formation. Cooling rate determines grain size and hardness, with faster rates producing finer grains. Interpass temperature between layers affects the thermal cycle, where maintaining consistency achieves uniform microstructure. Alloying elements such as manganese, silicon, and niobium modify microstructure by influencing phase transformations and grain growth. The initial layers experience a distinct thermal gradient due to the temperature differential between the substrate and the deposited layer [208]. This gradient amplifies with an increasing number of layers and height, primarily due to reduced heat exchange and cooling rates, leading to an inhomogeneous grain structure and material properties across component regions [202].

Vora et al. [210] study identified the presence of ferrite (BCC structure) and pearlite (laminar structure of cementite and ferrite), with cooling rates significantly influencing their distribution and formation in SS316L. Samples subjected to higher travel speeds exhibited reduced pearlite presence and smaller grain sizes due to rapid cooling, with grain size decreasing from the bottom to the top of the sample. Equbal et al. [211] similarly reported that faster cooling rates lead to a finer ferrite-pearlite microstructure in low carbon steels. This phenomenon occurs because less time is available for atomic migration, preventing the formation of larger grains. Rapid cooling increases nucleation sites, resulting in the formation of numerous small grains instead of fewer large ones, thus creating a finer grain structure [212]. Karmuhilan et al. [174] conducted a location-dependent microstructural and mechanical analysis on Inconel 625 fabricated using CMT-GMAW. The study identified distinct characteristics in different sections: columnar dendrites in the top section, a combination of cellular and columnar grains in the middle section, and predominantly cellular grains in the bottom section. Horizontal samples exhibited superior tensile strength compared to vertical samples, and microhardness decreased from bottom to top. Le et al. [213] reported similar results, with finer grains in the bottom region, vertically oriented columnar dendrites in the middle region, and randomly oriented equiaxed grains in the top region Figure 41. The interaction zone (heat-affected zone) between successive layers displayed coarser grains. The average microhardness decreased from the bottom to the top region Figure 42. Wang et al. [54] demonstrated that WAAM components fabricated from Ti-6Al-4V alloy exhibited an anisotropic microstructure, characterized by large equiaxed grains near the substrate and a finer microstructure in the top layers. Samples acquired horizontally and vertically exhibited differing mechanical properties, as Karmuhilan et al. and Le et al. reported. In a separate study, Wang et al. [214] examined the mechanical properties of AZ31 magnesium alloy and observed significant non-uniformity attributed to the repeated heating process, which influenced grain size, microhardness, tensile strength, and elongation. Additionally, Wang et al. [215] prepared quasi-in situ components, with the filling angle between every two deposited layers set at 90°, resulting in uniform microstructure and mechanical properties. However, as deposition height increased, heat accumulation led to increased porosity and decreased microhardness.

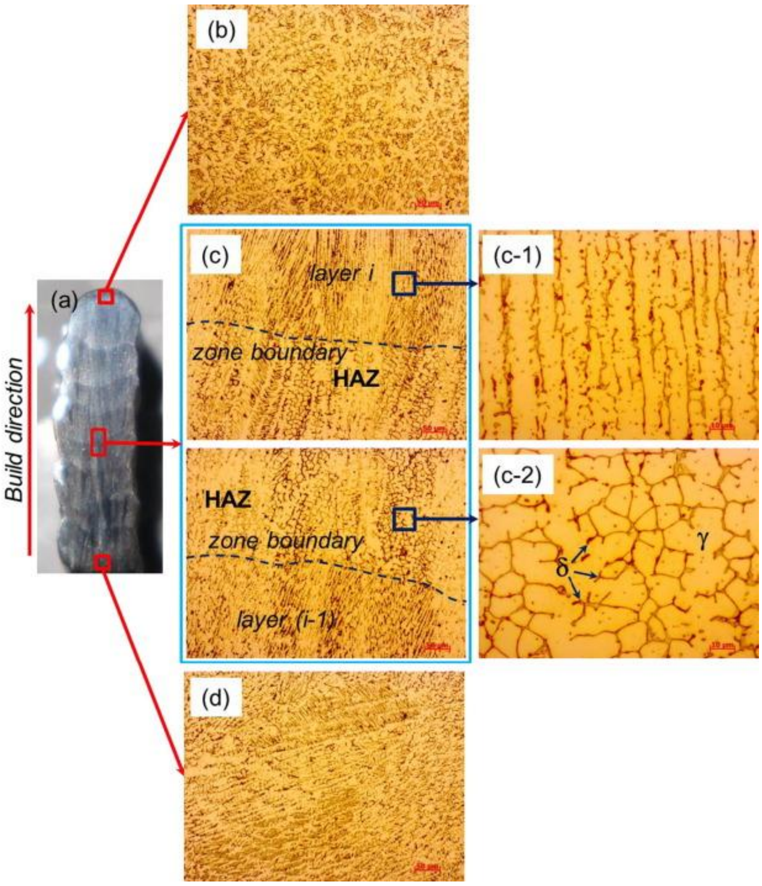

Figure 41. grain formation in different regions, a). Cross section of WAAM deposited wall, b). top region, c). middle region, d). bottom region [213]

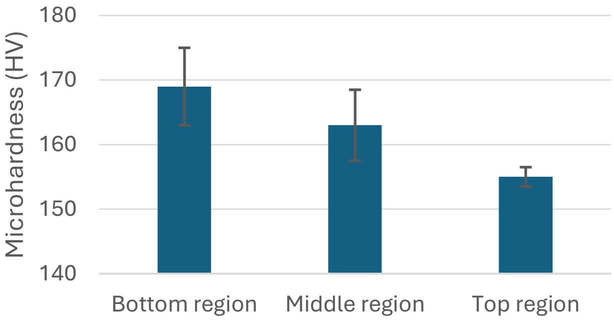

Figure 42. Microhardness of different regions of WAAM deposited wall [213]

Liberini et al. [148], the study involved constructing six walls (ER70S-6), each consisting of 15 layers with a dwell time of 60 seconds between layers. No significant differences, including porosity, were observed in the samples. The samples were divided into three microstructural zones: upper, middle, and lower. The lower and middle zones exhibited an equiaxed microstructure, while the upper zone showed a lamellar microstructure. The grain sizes in the lower, middle, and upper zones were measured at 17.8 µm, 22.1 µm, and 32.5 µm, respectively. Liberini et al. also found that the hardness of the upper zone increased, as shown in Figure 43. They claimed, this increase was attributed to the higher thermal shock in the upper zone, resulting in a bainitic microstructure, which influenced the hardness values. Chaudhari et al. [216] reported similar findings. However, Anand et al. [217] results indicated higher microhardness values in the top and bottom zones of the thin wall of mild steel. Generally, a decrease in grain size leads to improved hardness and other mechanical properties, highlighting the need for further research in this area.

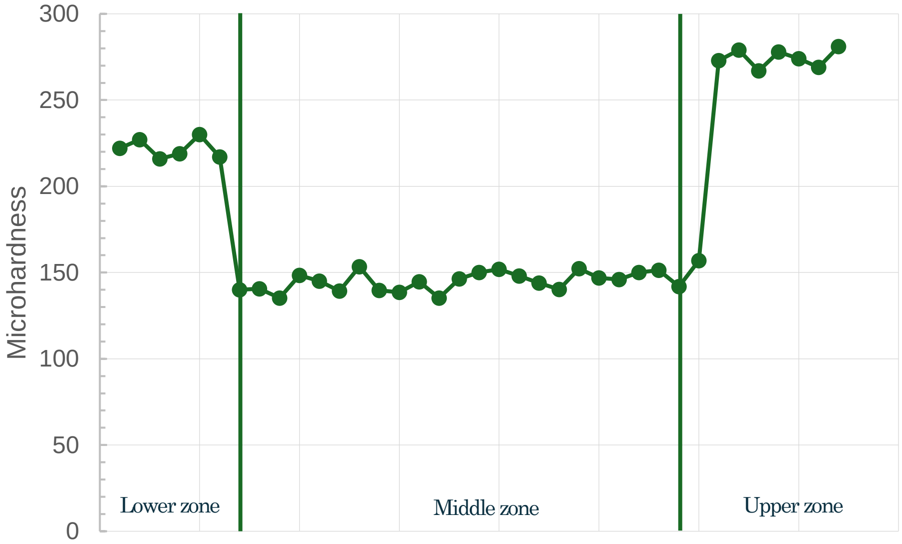

Figure 43. Microhardness of different regions of WAAM deposited wall [148]

Yu et al. [218] investigated the anisotropy of WAAM-fabricated SS304 by examining samples in longitudinal, diagonal, and transverse directions. The findings revealed notable differences in tensile properties based on orientation. Specifically, diagonal samples exhibited superior tensile strength, ductility, and uniform elongation compared to those oriented longitudinally and transversely. In contrast, the both transverse and longitudinal direction samples demonstrated a pronounced necking phenomenon, as shown in Figure 44, which was attributed to variations in grain formation between layers and interaction zones. This variation allowed layers to extend more than the interaction zones. The microstructure of diagonal samples was more robust, reducing the prominence of necking.

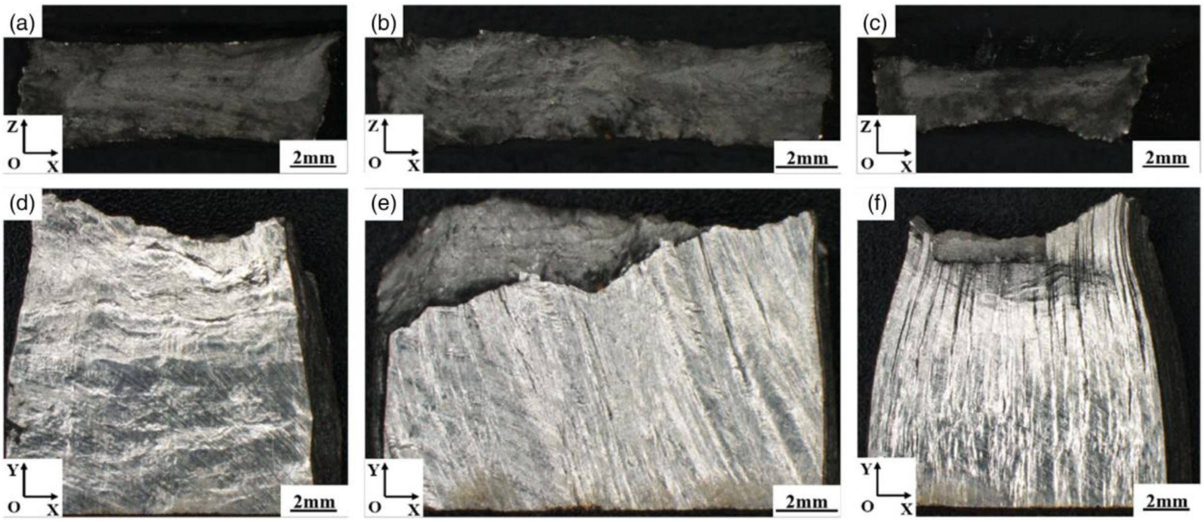

Figure 44. necking phenomenon in WAAM samples, a). Longitudinal direction, b) diagonal direction, c). transversal direction [218]

In a related study examining tensile properties across different regions of WAAM components, Anand et al. [219] extracted samples from the bottom, middle, and top regions of the built components of SS308L-T1. All samples displayed good elasticity during tensile testing, with the middle region samples showing the highest elongation and strength. SEM analysis of the fractured surfaces revealed approximately equiaxed dimples, characteristic of ductile fracture. The middle region samples exhibited finer and deeper dimples, suggesting enhanced ductile properties relative to samples from the top and bottom regions. This phenomenon was attributed to increased heat accumulation in the middle region of WAAM-built components.

Therefore, the Mechanical properties of WAAM fabricated materials show anisotropic behavior. The tensile strength, ductility, and elongation determine material suitability for structural applications. Corrosion behavior analysis, on the other hand, assesses the material's resistance to environmental degradation, which is crucial for ensuring durability and reliability in corrosive environments. Chigilipalli et al. [220] conducted a comparative analysis of the corrosion behavior of Inconel 825 alloy produced via WAAM and its wrought counterpart. Using the Potentio-Dynamic Polarization (PDP) technique in a 3.5% NaCl solution, the study revealed that the wrought alloy exhibited superior corrosion resistance compared to the WAAM-produced samples. This inequality was attributed to the grain size. A reduction in grain size, increased the number of exposed grains in the corrosive environment, leading to enhanced corrosion resistance in the wrought samples. *Table 12* reports some of the studies, who reported the process parameters effect on material properties.

Table 12 process parameters effect on mechanical properties of WAAM samples

	Microhardness	Tensile properties	Elongation	Microstructure	Corrosion
Current and voltage	[147], [21], [219], [221], [222], [147, 223]	[147], [21], [219], [224], [221], [15], [222], [147, 223]	[147], [21], [219], [224], [221], [15], [222], [147, 223]	[147], [21], [219], [224], [225], [39], [221], [15], [222], [147, 223]	[224],

Travel speed	[27], [21], [219], [147], [28],	[21], [219], [147], [15], [21, 28]	[21], [219], [147], [15], [21, 28]	[21], [219], [225], [39], [147], [15], [28], [21, 27]	
Wire feed speed	[21], [224], [147], [21, 34]	[21], [224], [147], [21, 34]	[21], [224], [147], [21, 34]	[21], [224], [225], [39], [147], [21, 34]	
CTWD					
Shielding gas	[45],	[45]	[45]	[217], [45, 217]	
Scan strategy	[217], [219], [173, 217]	[217], [219], [173, 217]	[173]	[217], [173, 217]	[173]
Dwell time	[226], [48]	[226], [48]	[226], [48]	[226], [48]	

Chapter 4 – Research aims and objectives

4.1 Introduction

Industrial growth throughout the years has produced exceptional results in terms of speed and quality. However, the consequences of that production, whether environmental, economic, or social, have been sometimes overlooked. The manufacturing industry, as one of the most polluting sectors, felt the need to adapt to this technological advancement and find ways to produce with increased sustainability goals while maintaining product quality and production time. In the recent years metal AM has emerged as a technological advancement in material efficiency, supply chain, sustainability, part complexity, performance…etc [227]. Which attracted the attention of researchers and manufacturing industries. However, industrializing a technology is not that simple, in terms of cost, availability of technology and most importantly reliability. Since the metal AM technologies are showing required maturity, now the companies have started integrating the AM technologies into their manufacturing process, but not completely relying on them [228]. Main industries like aerospace, automotive and healthcare have continuous demand for these technologies and their products. Now the companies are increasingly looking for ways to replace the traditional manufacturing by AM, where it financially feasible Lawand et al. [229]. There are different metal AM processes, however, due to the repairability, scalability and material efficiency, DED processes have the potential to sustain in manufacturing industries. A significant amount of research was going on in the powder-based process. Comparatively less research has been dedicated to wire-based processes like WAAM. Furthermore, there are still insufficient studies on process control, material properties, process efficiency, complex geometries, post-processing, cost effectiveness. By addressing these issues and research gaps could make WAAM a reliable process for industrialization.

4.2 Aim and Objectives

WAAM has demonstrated its capability to manufacture large-scale industrial components. This potential has prompted a variety of scientific research efforts focused on refining and understanding WAAM technology. However, despite these initiatives, industries remain hesitant to adopt WAAM as a primary manufacturing method due to the lack of technological advancements and limited accessibility to comprehensive research information.

This study aims to address these challenges using a custom-built machine, allowing for a focused investigation into the relationships between critical process parameters, in-process data monitoring, and their combined effects on bead geometry, microstructure, and mechanical properties. By analyzing the thermal cycles intrinsic to the WAAM process, the research also aims to uncover their influence on microstructural evolution, including grain morphology, phase transformations, and the anisotropic behavior of the deposited material. This approach provides a comprehensive understanding of how process dynamics shape the final material and geometrical characteristics, contributing to the optimization of WAAM process, part quality, Cost effectiveness and reliable manufacturing technology.

- WAAM Process and parameters optimization

- WAAM Material characterization
- WAAM In-process data monitoring

4.3 Research structure

To advance WAAM technology towards industrial-level performance, ensuring quality, and achieving sustainability, it is necessary to undertake systematic and optimal research. This involves a thorough examination of every input and output parameter to refine the process and enhance material performance. Consequently, the investigation of WAAM processes and their resulting material properties requires a structured, well-planned, and analytically rigorous approach.

The initial phase of this research entailed a comprehensive literature review, aimed at identifying the state-of-the-art developments in WAAM technology and pinpointing critical research gaps. Extensive research forms the foundation of this Ph.D. project, conducted under the supervision of academic advisors and professional experts with industry experience. The experimental phase will utilize industry-grade materials, such as steel, to align the research outcomes with practical industrial applications. To facilitate detailed analysis and strategic experimentation, simple geometries such as single beads, walls, U-shaped structures, and rectangular shells, will be selected as test cases. These designs offer manageable complexity while enabling precise evaluation of process parameters and material characteristics. Figure 45 outlines the structured research framework, illustrating the systematic approach adopted in this project. Each stage of the research, from the initial trials to material characterization and process optimization, is carefully planned to ensure meaningful results that contribute to the broader adoption and advancement of WAAM technology. By leveraging an interdisciplinary methodology, this project aims to bridge existing knowledge gaps and pave the way for the widespread industrial application of WAAM.

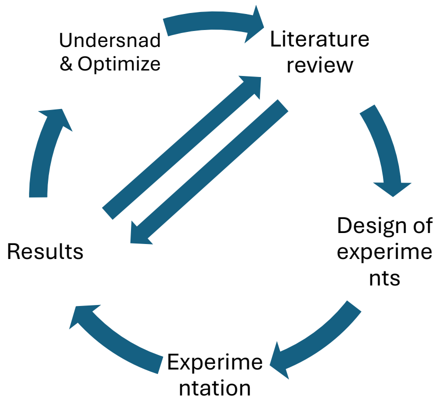

Figure 45 Research structure

Chapter 5 - Experimental equipment and tests

5.1 WAAM setup (CNC, MIG, Sensors)

This section of the thesis provides a comprehensive overview of the experimental setup and equipment configuration used to meet the research objectives. It details the selection, characteristics, and integration of each component in the system, including the MIG welding machine, CNC configuration, current and voltage transducers, and the FLIR thermal camera. The setup description encompasses the technical specifications and operational limits of each piece of equipment, explaining their relevance to the experimental process. Through careful calibration and configuration, each device was connected and optimized to ensure accurate data collection and reliable results, thereby aligning with the methodological requirements of this study machine (MIG) properties.

5.1.1. Machine (MIG) properties

For all the experimental work in this thesis, we utilized the Cebora MIG Weld 303C machine. This is a highly durable, industrial-grade welding machine designed for heavy-duty applications. It supports a wide current range from 30A to 300A, allowing it to handle light, medium, and heavy-duty tasks. The machine offers three duty cycles depending on current usage: 40% at 300A, 60% at 250A, and 100% at 190A. This means the machine can operate for a specific duration before requiring cooling, depending on the current setting. It features forced ventilation, thermal protection, and IP21 protection, which provides basic safety against dust and water ingress. The machine operates on a 230V or 400V, 50-60Hz three-phase supply.

For user interaction, there are two LED indicators: a green light indicates the machine is on, and a yellow light indicates operational interruptions, such as overheating. The machine has four control knobs: one for power on/off, one for power setting, one for wire feed control, and one for setting the weld timer. Figure 46 illustrates the machine's interface.

Figure 46 MIG welding machine

5.1.2. Materials

In this thesis, a low carbon electrode steel wire with 1 mm diameter was used in the experimental trails. *Table 13* depicts the chemical composition of this low carbon steel wire. The 1 mm diameter wires are commonly used in WAAM process, mainly due to the wide range of availability, control, arc stability, and stable material deposition. These conditions make the 1mm diameter wire ideal for medium to large scale metal parts with quality deposition.

Table 13 Chemical composition of the wire

Element	C	Cu	Mn	Ni	Ti	Zn
Wire [wt.%]	1.009	5.469	1.321	0.096	0.039	0.016

The base plate used in these experimental trials was also a steel alloy and its chemical compositions are mentioned ed in Table 14. Figure 47 illustrates the dimensions of the base plate. Substrates were cleaned with acetan before depositing the material to remove contaminations and any the oil strains.

Table 14 Chemical composition of the base plate

Element	C	Cu	Mn	Ni	Ti	Zn
Substrate [wt.%]	1.317	0.591	0.427	0.294	0.196	0.195

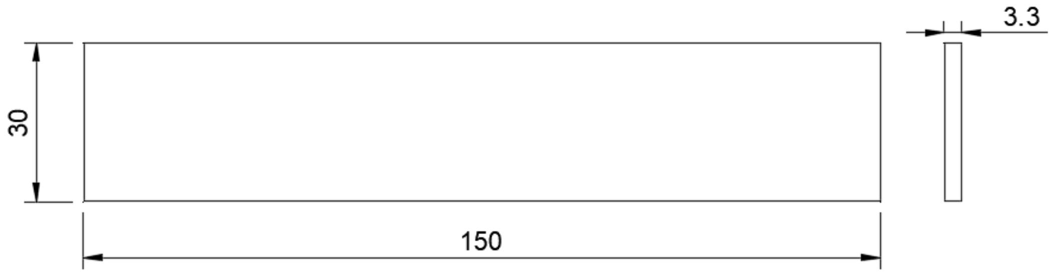

Figure 47. Base plate dimensions

Wire flow characterization: The machine features a control knob to adjust the Wire Feed Speed (WFS), which is labeled with values from 1 to 10. Higher numbers on the knob correspond to higher wire feed speeds. The table in the machine manual (referred to as Table 10) provides the specific wire speeds associated with each knob setting. This design allows for precise control over the wire feed rate during welding operations, enabling the user to optimize the process based on specific welding conditions and requirements. WFS is one of the important parameters, therefore, to ensure the nominal WFS mentioned in the manual, an experiment was conducted to characterize the WFS. For this, three tests were conducted for every knob indication and average values in mm/min were reported in Table 15. The measured values are almost closer to the nominal values, as depicted in Figure 48.

Table 15 Wire feed speed characterization [Measured Vs Theoretical]

Setting	Wire feed speed Theoretical [mm/min]	Wire feed speed measured [mm/min]
1		
2	2060	1958
3	4000	3925
4	6000	5802
5	8200	8440
6	10600	10554
7	12800	12651
8	16000	16518
[9	18200	18542
10	20600	20600

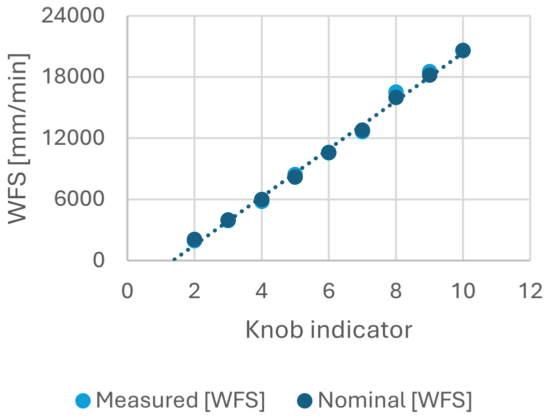

Figure 48. Wire feed speed characterization

5.1.3. CNC build platform & more

In this study, a custom-built CNC platform was developed to enable precise multi-directional movement across the X, Y, and Z axes. The CNC structure provides an extensive operational range, with the X-axis extending up to 660 millimeters, the Y-axis up to 740 millimeters, and the Z-axis reaching 500 millimeters. To achieve precise control and robust performance across all axes, each axis is driven by identical stepper motors, specifically, the M1233062 model from LAM Technologies (Figure 49). Table 16, highlights some of its technical data.

This model of stepper motor was selected due to its notable specifications, which include a torque capacity of 1.8 Newton-meters and a step angle of 1.8 degrees per rotation. Such characteristics are essential in applications requiring high precision and repeatability, making the M1233062 model particularly well-suited for CNC machining, 3D printing, robotics, and other domains that demand both fine control and substantial torque. The consistent use of the same motor model across all axes not only simplifies the design and assembly of the CNC system but also ensures uniform performance, enhancing both the accuracy and reliability of the platform during complex, multi-axis operations.

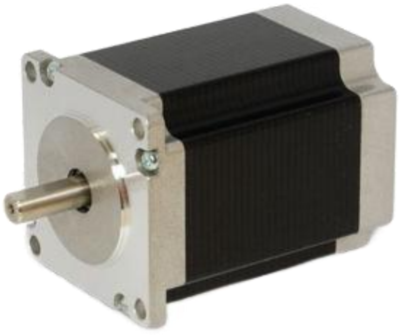

Figure 49. Stepper motor [https://www.lamtechnologies.com/Product.aspx?lng=EN&idp=M1233062]

Table 16. Stepper motor technical data

Bipolar Holding Torque	1.8 Nm

Bipolar Phase Current	4.2 Arms
Rotor Inertia	440 $g - cm^2$
Length	76 mm
Weight	1050 g
Flange	NEMA 23 56.4x56.4 mm
Leads Number	4
Full Step Angle	1.8°

5.1.4. Current & Voltage sensors

Current transducer (LF 306-S/SP10): This current transducer is suitable for measuring DC, AC, and pulsed current up to 500A, with a primary nominal current of 300A, Figure 50. It features galvanic isolation between the high-power primary circuit and the electronic secondary circuit, ensuring safety and precise measurement. Key features include excellent accuracy (±0.4%), fast response time (<1 µs), and a wide frequency bandwidth (up to 100 kHz). The device is typically used in industrial environments like motor drives, static converters, and welding power supplies. Its compact design allows it to be mounted on a printed circuit board (PCB), and it offers excellent immunity to external interference, making it ideal for robust industrial applications.

Figure 50. LF 306-S/SP10 current transducer

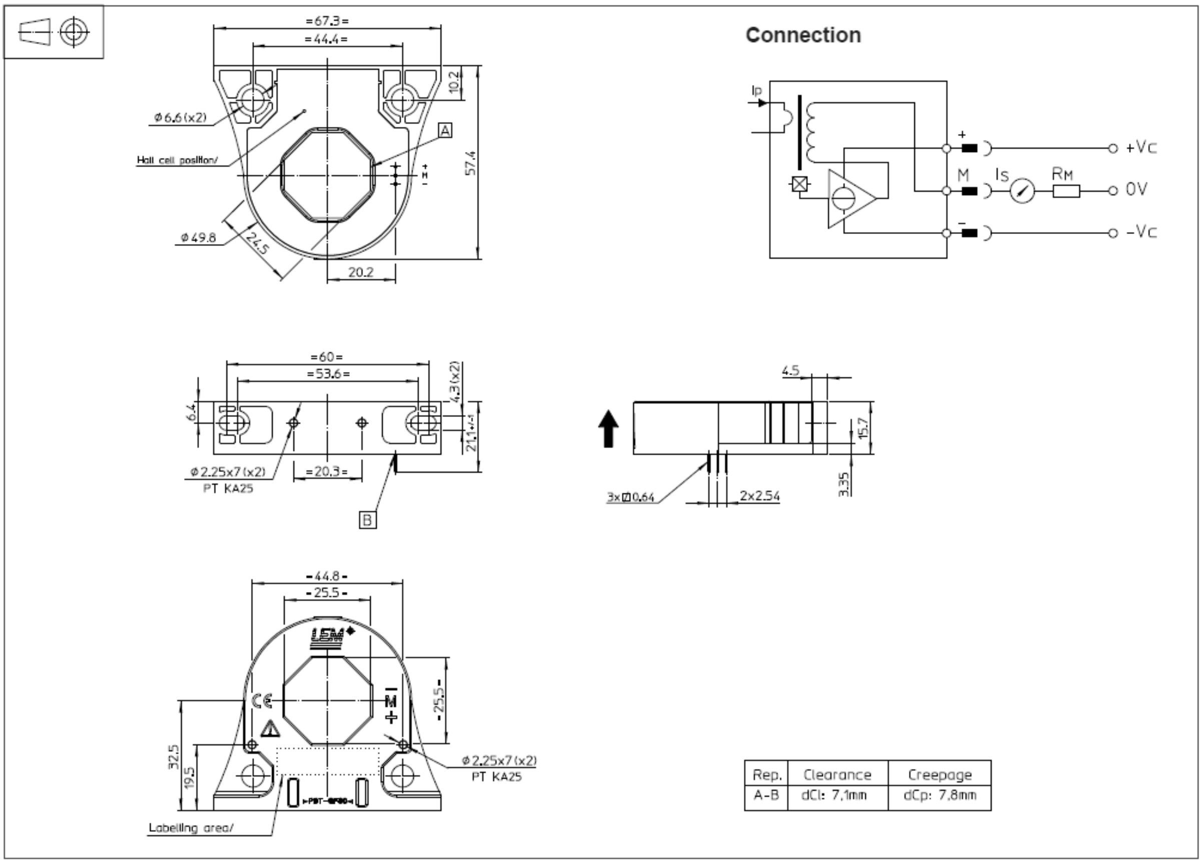

Voltage transducer (LV 25-P): This transducer is designed for accurate electronic measurement of voltages (DC, AC, and pulsed) with galvanic isolation between the high-voltage primary circuit and the secondary circuit (Figure 51). It operates over a wide voltage range, providing precise voltage feedback for power electronics and control systems. The key advantages include high accuracy, excellent linearity, and low temperature drift. It is commonly used in industrial applications such as power supplies, drives, and battery monitoring systems. The transducer's design ensures high performance and safe voltage isolation for critical applications.

Figure 51. LV 25-P voltage transducer

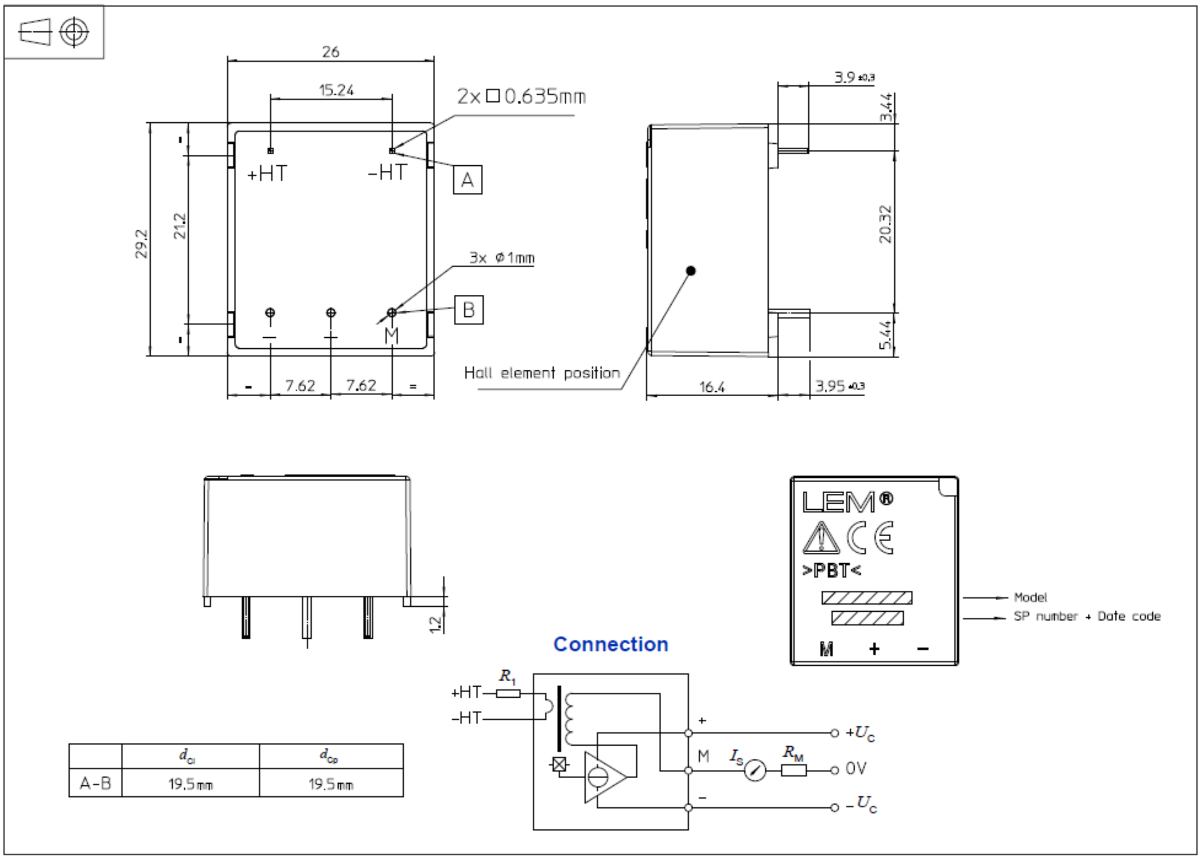

5.1.5. FLIR thermal camera A615

The FLIR thermal A615 series camera is a compact and high-quality thermal imaging camera designed for advanced thermal analysis, can be fully controlled by a PC, Shown in Figure 52. The A615 series uses an uncooled vanadium oxide (VoX) detector to capture the high-revolution thermal image at 640x480 pixels with adjustable frame rate, can be recorded with clarity and details when it is required. This series can detect the minute temperature differences, as small as 50 mK (millikelvin) which allows users to conduct precise and detailed thermal measurements even at longer distances. A615 is also compatible with GigE Vision that facilitates faster and efficient image transfer using Ethernet cable (GigE) and with standard ethernet cable up to 100 meters. Some of the main technical specifications are reported in Table 17. These features make the A615 thermal camera more adaptable in various thermal analysis and especially in this case of data monitoring.

Figure 52. FLIR thermal camera A615

Table 17. Technical specification of FLIR A615

Field of view (FOV) / Minimum focus distance	15°: 15° × 11° (19° diagonal) / 0.50 m (1.64 ft.) 25°: 25° × 19° (31° diagonal) / 0.25 m (0.82 ft.) 45°: 45° × 34° (55° diagonal) / 0.15 m (0.49 ft.) 7°: 7° × 5.3° (8.7° diagonally) / 2.0 m (6.6 ft.) 80°: 80° × 64.4° (92.8° diagonal) / 65 mm (2.6 in.)
Spatial resolution (IFOV)	15°: 0.41 mrad 25°: 0.68 mrad 45°: 1.23 mrad 7°: 0.19 mrad 80°: 2.62 mrad
Focal length	15°: 41.3 mm (1.63 in.) 25°: 24.6 mm (0.97 in.) 45°: 13.1 mm (0.52 in.) 7°: 88.9 mm (3.5 in.) 80°: 6.5 mm (0.26 in.)
F-number	1.0
Image frequency	50 Hz (100/200 Hz with windowing)

Object temperature range	-20 to +150°C +100 to +650°C +300 to +2000°C
Accuracy	±2°C or ±2% of reading
Emissivity correction	Variable from 0.01 to 1.0

All experimental trials were performed using the equipment setup illustrated in Figure 53, which comprises a MIG Weld 303C machine integrated with a 3-axis CNC system, thermal, current and voltage sensors to facilitate precision and repeatability in the WAAM process. The MIG weld head, securely mounted on the CNC machine. To ensure uniformity and reliability of the collected data, specific arrangements for in-process monitoring devices were established. A thermal camera was strategically positioned to capture real-time temperature profiles. Similarly, current and voltage sensors were consistently placed at fixed distances and orientations relative to the weld zone for every experiment. This standard placement minimized variability and provided consistent data across all trials.

This carefully designed setup underscores the importance of precision in the experimental methodology. The integration of advanced monitoring tools not only enhanced the reliability of the collected data but also facilitated a detailed analysis of the interdependencies between process parameters and material properties. These arrangements formed the backbone of the experimental strategy, enabling systematic exploration and characterization of the WAAM process under various conditions.

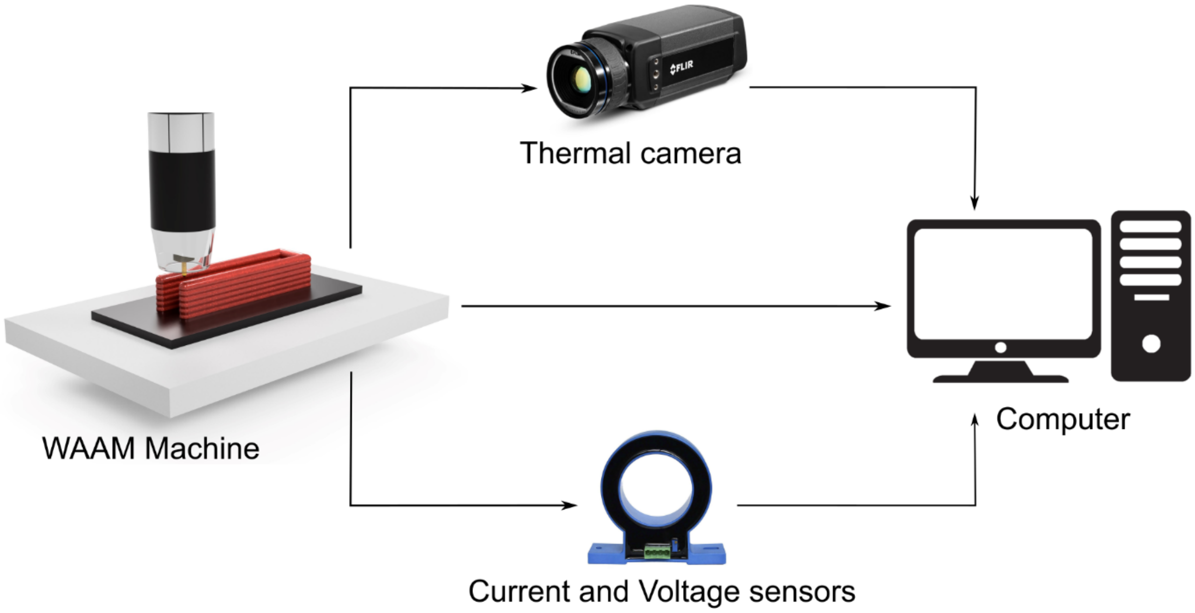

Figure 53 Experimental set-up

5.2 Material Characterization Workflow

This section is dedicated to explaining workflow sample preparation, testing and analysis process and its equipment. Material characterization workflow is depicted in Figure 54.

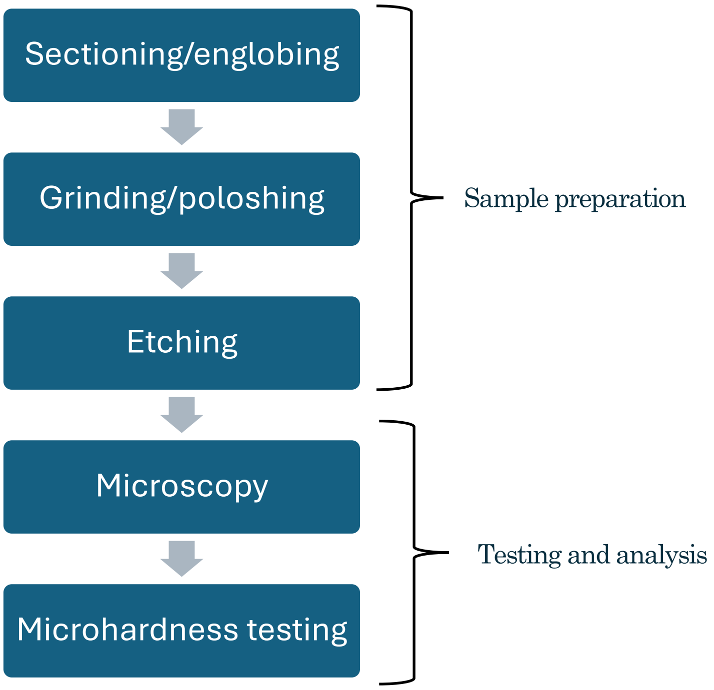

Figure 54. Material characterization workflow

5.2.1 Sectioning

HiTECH C301 is a water-cooled cutting machine Figure 55a, which makes ideas for cutting the WAAM sample. Because, when the samples are exposed to heating while sectioning, their material properties can be altered which later could influence the grain structure and mechanical properties. HiTECH C301 cutting machine has a 2200 W motor capacity, equipped with changeable abrasive wheel diameter up to 300 mm, which is capable of cutting thickness up to 90 mm.

The one who performs the sectioning operations should have some basic knowledge of the machine capabilities and how they can affect the process (even for safety purposes). For example, C301 doesn't have the adjustable cutting wheel speed, but C301K series does. Therefore, while cutting a sample without adjustable wheel speed the operator should maintain an appropriate pressure on the wheel handle. Excessive pressure can lead to over heating or uneven wear or even damage the abrasive wheel. With adjustable speed, the operator can control and match the wheel speed with material hardness, thickness, and thermal sensitivity. High speeds are suitable for soft/ductile materials and low speeds are suitable for hard/brittle materials. Therefor having a basic knowledge is crucial to achieve clean, precise, and faster cuts without compromising the quality.

Molding/englobing process: after sectioning carefully the interested part of a sample, the sectioned part is englobed epoxy resin to facilitate further operations, in our case we have used epoxy resin CEM1000 Blue. Depending on the epoxy resin used, it takes 2-8 hours to solidify. Figure 55b depicts the englobed sample.

Usually, englobing process is not mandatory all the time. However, it acts as a support when the sample is too small for grinding, polishing, and to place on the inverted microscopies.

Figure 55. a). HITECh C301 cutting machine, b) englobed samples

Table 18 summarizes the technical specifications of HiTECh C301 cutting machine.

Table 18. HITECH C301 Specifications

Model code	C301
Wheel diameter	Up to 300 mm
Cutting capacity	90 mm
Engine power	2.2 kW
Max. speed	2800 rpm
Power supply	400/440V- 50/60Hz-3ph
Cooling system	Water cooled
Dimensions	650x650720 mm
Weight	110 kg

5.2.2 Grinding/polishing

Grinding apparatus are designed for high precision grinding and polishing of various materials for research or industrial analysis to remove surface irregularities. Grinding and polishing operations were performed on the PRESI P230 grinding machine. The equipment is illustrated in Figure 56a. The P230 is a single plate/disk grinding machine with changeable base plate/disk for various operations (grinding/polishing). The P230 offers adjustable disk speed range from 20 to 600 RPM and adjustable pressure on sample [up to 2 bar] applied during the process. These features make P230 achieve desired surface finishing conditions for different materials. The P230 is a widely used user-friendly machine for surface preparation, which offers consistency, control and robust sample preparation.

Grinding is the first step in surface preparation before the polishing. Silicon carbide abrasive papers (Figure 56b) are used to grind the sample on the required surface. These papers are waterproof, and their abrasive grit size is determined using P220 0r P600, is varies from P8 to P4000. The lower the P value the higher the abrasive grit size. An efficient grinding process requires choosing the right grit order based on the type of material being grinded. To prepare a sample for microstructural level analysis, it is important to choose the right grit order for grinding. But It is not necessary to follow the highest grit possible to the lowest, which is nothing but a waste of time or resources. To explain better, grinding a hard material like steel require more number of papers when compared to soft material like aluminum. Since the experiments conducted in this thesis only deals with the steel-based alloys, after number of trails and errors, we choose these abrasive papers: P220, P600, P800, P1200, & P2500 for grinding operation.

For the final polishing, CT Dia Twin Poly with a diameter of 6 mm and Fumed Silica Suspension of 0.2 mm Alkaline were polished on a cloth type dick to get the mirror like surface finishing.

Figure 56 a). PRESI P 230 grinding machine, b) Silicon carbide abrasive paper

5.2.3 Chemical etching

Chemical etching is a metallurgical process, which enhances the microstructure of a material to analyze under the optical microscope. The process involves specific chemicals to etch the selected region of a sample. The chemical etching allows to reveal the microstructural features like, grain boundaries, phases, and other features which can be seen under optical microscope. These chemical reagents vary based on type of material needs to etched. The process follows, a polished sample (required face) is exposed to the chemical reagent for few seconds and immediately drenched in water to stop the further reaction and dried to remove the water strains. The time required for the appropriate etching process should be practiced. For this thesis, samples were etched using nital reagent (4 g of HNO_3 and 100 g of alcohol) for 10 seconds.

5.2.4 Microscopy

Microstructural analysis was conducted using the Leica DMI5000 M inverted microscope (Figure 57), operated through its integrated Leica LAS software. This advanced system is highly regarded for its precision and is tailored for use in both research and industrial settings, particularly for tasks requiring rigorous material testing and quality control. Its inverted design offers a distinct advantage, allowing the analysis of large samples without necessitating sectioning, thereby preserving the integrity of the material. Equipped with state-of-the-art optics, the DMI5000 M delivers exceptional resolution, illumination, and contrast, making it suitable for analyzing metals, polymers, ceramics, and composite materials. The motorized lens system, seamlessly integrated with LAS software, provides precise control and ensures high accuracy during analysis. Users can access advanced features such as automated focus and contrast adjustments, enhancing the reliability and efficiency of investigations. While the instrument's capabilities are extensive, leveraging its full potential requires familiarity with its features, often necessitating initial training. These sophisticated functionalities establish the Leica DMI5000 M as a unique and indispensable tool for detailed microstructural analysis, supporting advancements in materials science and quality assurance processes.

Figure 57. Leica DMI5000 M inverted microscope

5.2.5 Microhardness testing

The microhardness testing was conducted on the Mitutoyo HM-112 Vickers testing machine. The equipment is illustrated in Figure 58. The technical specifications of the equipment are shown in Table 19. The device is equipped with easy-to-read dual line digital filar eyepiece for quick and precise measurements. Indentation load of 1000gf for 15 s was employed since the testing material was low carbon steel. The tests were conducted according to the ASTM E18-22 standards. The Mitutoyo HM-112 is a manual microhardness testing machine. Therefore, Indentations were conducted at an interval of 0.4mm.

Figure 58 Mitutoyo HM-112 digital Vicker microhardness testing machine

Table 19 Mitutoyo HM-112 digital Vicker microhardness tester specifications

Model	HM-112
Code No.	810-126E
Test force selection	10, 25, 50, 100, 200, 300, 500, 1000 gf
Test force setting	By dial
Control unit	Touch screen type
Indenter/Objective turret	Manual type
Indenter mounts	1
Objective mounts	2 positions (10x, 50x)

5.3 Preliminary tests

Finding the process window and optimizing process parameters is a fundamental step in developing a customized WAAM system from the ground up. When a WAAM machine is purchased directly from a vendor, manufacturers typically receive recommended parameter settings to achieve specific material properties, both geometrically and metallurgically. However, since the WAAM system in this study was designed and assembled component by component, understanding and finding process window of each process parameter is crucial. This detailed approach not only enhances the efficiency and simplicity of the manufacturing process but also provides a comprehensive understanding of the system's operational aspects, ultimately enriching the user's expertise and control over the process.

The primary process parameters influencing WAAM include Wire Feed Speed (WFS), Travel Speed (Ts), Current and Voltage, Stand-off Distance (Sod), Shielding Gas Flow Rate, and Dwell Time. These parameters, discussed in detail in Section 2.3, collectively impact the quality, structure, and functionality of the manufactured component. However, finding the processing window of all parameters simultaneously is neither practical nor efficient, as it complicates the analysis and may hinder precise calibration of each individual factor. Therefore, a phased approach was adopted in this thesis to systematically optimize the process parameters, allowing for targeted adjustments and refined control over each experimental phase.

This whole phased preliminary analysis for optimizing and defining processing window of process parameters are conducted using the single bead deposition, Figure 59 illustrates the dimensions of the deposition.

5.3.1 Phase 1

The literature review identifies travel speed, current and voltage, wire feed speed, and stand-off distance as the primary parameters influencing the WAAM process [230]. To systematically investigate and optimize these parameters, an initial experimental plan was devised with these four key factors, each set at two levels, resulting in a total of 16 sample trials. This experimental configuration allowed for controlled assessment of parameter interactions and individual impacts on WAAM outcomes. Details on the specific parameter values are provided in Table 20, while Table 21 outlines the experimental design used for this phase.

Table 20. Process parameters [phase-1]

Power [kW]	Ts [mm/min	WFS [mm/min]	Sod [mm]
2.2	300	5800	8
3.3	600	16500	12

Table 21. Design of experiments [phase-1]

No:Of	Power [Level]	Wire Feed Speed [Level]	Torch Speed [mm/min]	Offset distance
1	2.2	4	300	8
2	2.2	4	300	12
3	2.2	4	600	8
4	2.2	4	600	12
5	2.2	8	300	8
6	2.2	8	300	12
7	2.2	8	600	8
8	2.2	8	600	12
9	3.3	4	300	8
10	3.3	4	300	12
11	3.3	4	600	8
12	3.3	4	600	12
13	3.3	8	300	8
14	3.3	8	300	12
15	3.3	8	600	8
16	3.3	8	600	12

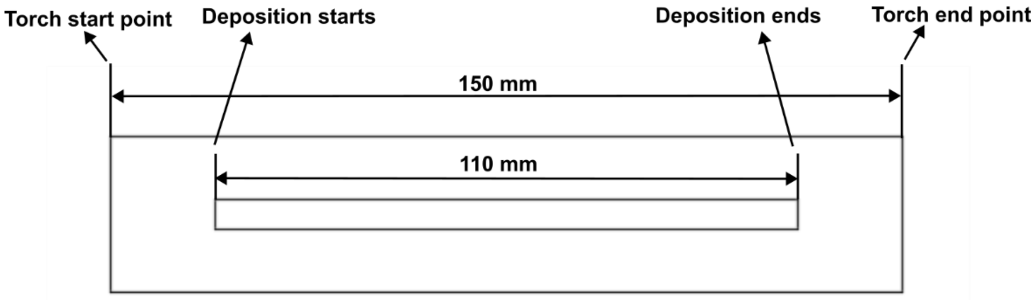

Figure 59 Schematic of single bead

The experimental tests were conducted in a randomized order with attention to detail. Figure 60 shows all 16 samples with their respective process parameters. Samples produced under low power (2.2 kW) and low WFS (5800 mm/min) (samples 1–4) exhibited discontinuous beads, likely due to arc instability. Conversely, samples produced at low power (2.2 kW) and high WFS (16,500 mm/min) (samples 5–8) showed continuous beads, although there was insufficient penetration of deposited material into the substrate, likely due to the insufficient power for high WFS. Samples produced with high power (3.3 kW) and low WFS (5800 mm/min) (samples 9–12, marked in green) demonstrated both stable arc performance and strong substrate bonding, suggesting an optimal combination for these conditions. However, samples with high power (3.3 kW) and high WFS (16,500 mm/min) (samples 13–16) again showed discontinuity in the beads. Samples producing continuous beads are marked in green, while those with discontinuities are marked in red for clear identification. The Sod did not show significant effects in this set of samples. However, the Ts particularly impacted bead geometry. Samples produced at low Ts (300 mm/min) resulted in thicker bead widths, whereas those at high Ts (600 mm/min) produced thinner bead widths, highlighting the role of Ts in controlling bead dimension.

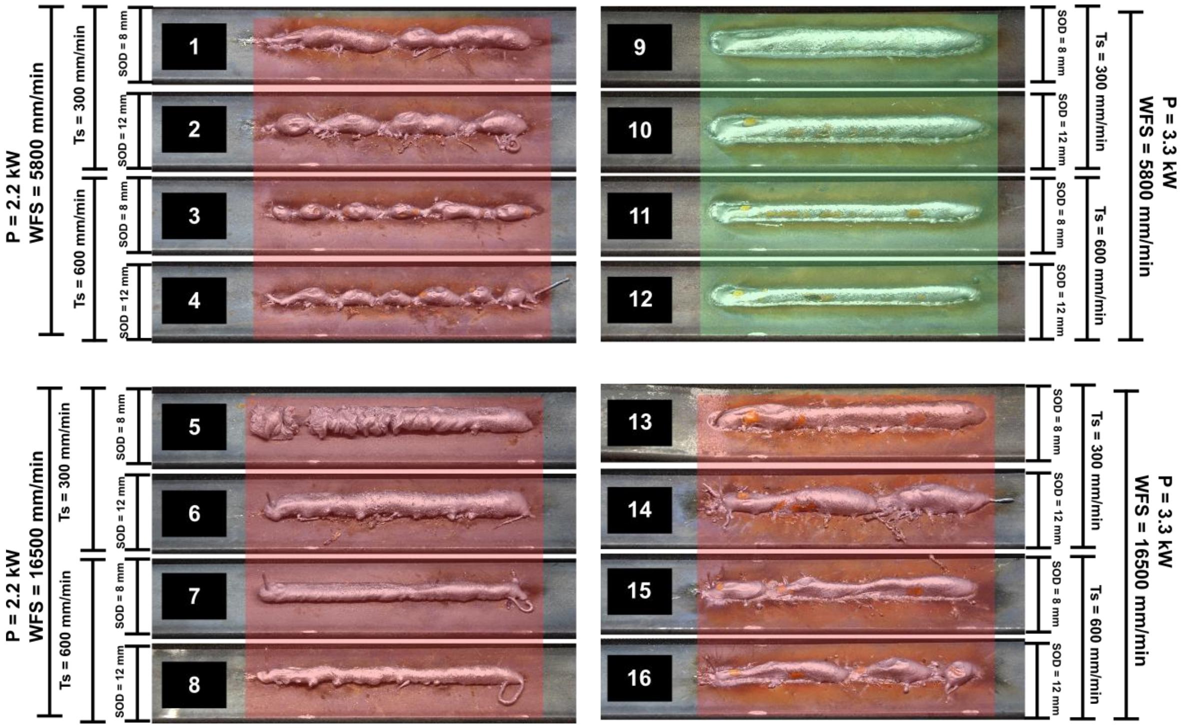

Figure 60. Phase 1 experimental plan

Since most of the samples were unsuccessful, further analysis would be no use.

5.3.2 Phase 2

In Phase 2 of optimizing the process parameters, the focus shifts specifically to the effect of power, while the WFS is maintained at a constant rate of 5800 mm/min throughout this phase. This structured approach allows for a more controlled analysis of how power variations impact the results, isolated from changes in WFS. For this phase, the experimental design included three levels of power combined with two levels each of Ts and SOD, resulting in a total of 12 experimental samples. The structured setup enables a clear examination of how variations in power, combined with Ts and SOD, influence deposition characteristics. Details of the specific parameter values are summarized in Table 22 & Table 23, which outline the process parameters and the experimental design matrix, respectively. This design enables systematic evaluation, offering clear insights into the influence of power and other conditions on the WAAM process outcomes while controlling for other variables.

Table 22. process parameters [phase-2]

Power [kW]	Ts [mm/min]	Sod [mm]
2[3] = 2.9	300	8
2[4] = 3.3	600	12
2[5] = 3.5		

Table 23. Design of experiments[phase-2]

Experimental order	Ref or DOE No: Of	Power [Level	Ts [mm/min]	Sod [mm]
5	1	2.9	300	8
8	2	2.9	300	12
12	3	2.9	600	8
3	4	2.9	600	12
7	5	3.3	300	8
9	6	3.3	300	12
4	7	3.3	600	8
11	8	3.3	600	12
1	9	3.5	300	8
10	10	3.5	300	12
2	11	3. 5	600	8
6	12	3.5	600	12

As in Phase 1, experimental tests in Phase 2 were conducted randomly and meticulously. The resulting samples are displayed in Figure 61. Unlike Phase 1, all samples in this phase were produced without any signs of discontinuity or defects, indicating a successful refinement of process parameters. To further analyse these samples, current and voltage measurements were recorded throughout the process to assess variations. The data collected was subsequently imported into MATLAB for processing, including reading, writing, and plotting, as well as calculating average current and voltage values. This MATLAB-based analysis provided detailed insights into the electrical characteristics of each trial, supporting a more precise evaluation of parameter effects on the WAAM process outcomes.

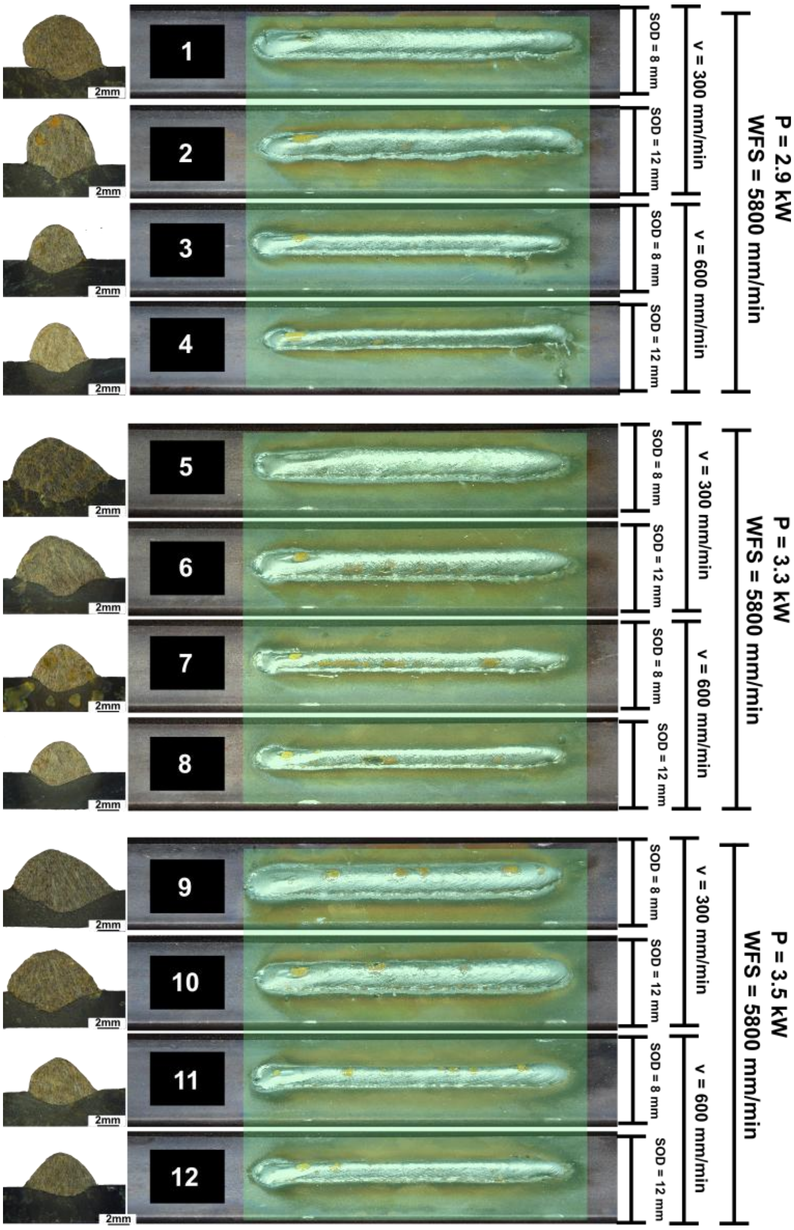

Figure 61. Phase 2 experimental plan

Results and discussion

The average current and voltage measurements, depicted in Figure 62, indicate that current increased as P was raised, while voltage showed an inverse trend, diminishing with higher power settings. This inverse relationship suggests a balance between current and voltage to maintain the set power level on the machine. Additionally, variation in Ts and SOD further influenced these parameters, increasing Ts raised the current and lowered voltage, whereas higher SOD decreased the current and raised voltage slightly. Particularly, the current exhibited greater variability than voltage under these changing conditions. Voltage showed minimal variation, remaining within a 1-2% range when Ts and SOD were adjusted, while current variations were more pronounced, between 2-4%. This difference highlights that current is more sensitive to changes in Ts and

SOD, potentially impacting the overall stability and quality of the WAAM deposition process. Thien et al. [36] also stated that during the WAAM process arc current could be better indicator than the arc voltage.

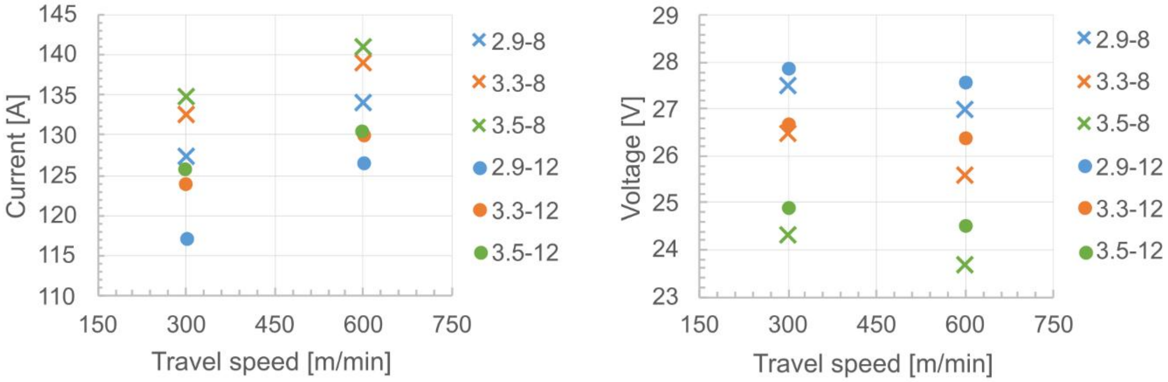

Figure 62 Average current and voltage

Following the sectioning of all samples at the center, measurements of each bead's height and width were taken to analyze the geometric impacts of the process parameters. The results indicated that Ts and P had a pronounced effect on bead morphology, while SOD demonstrated only a minimal influences on these dimensions. The measured height and width values are presented in Figure 63, providing a comparative overview of how each parameter shaped the bead profile. The data revealed that increasing Ts led to a noticeable reduction in both bead height and width, likely due to the reduced interaction time and decreased heat input per unit length at higher speeds. In contrast, a rise in P resulted in a broader bead width but a slight decrease in height, suggesting that higher power levels increase molten pool fluidity, causing the beads to spread laterally while reducing its height. While previous studies have frequently examined the effects of Ts and P on bead geometry, showing how these parameters influence dimensions and quality [24], there remains a lack of detailed information on temperature variations during the WAAM process. Temperature fluctuations during deposition directly impact the molten metal flow characteristics, thereby affecting bead height and width. This underscores the need for further exploration into thermal dynamics, as understanding temperature behavior during deposition could detail valuable insights into optimizing bead geometry and material properties to gain the deeper insights into these effects, temperature analysis will be the focused in Phase 3, allowing for a more comprehensive understanding of the WAAM process and its outcomes.

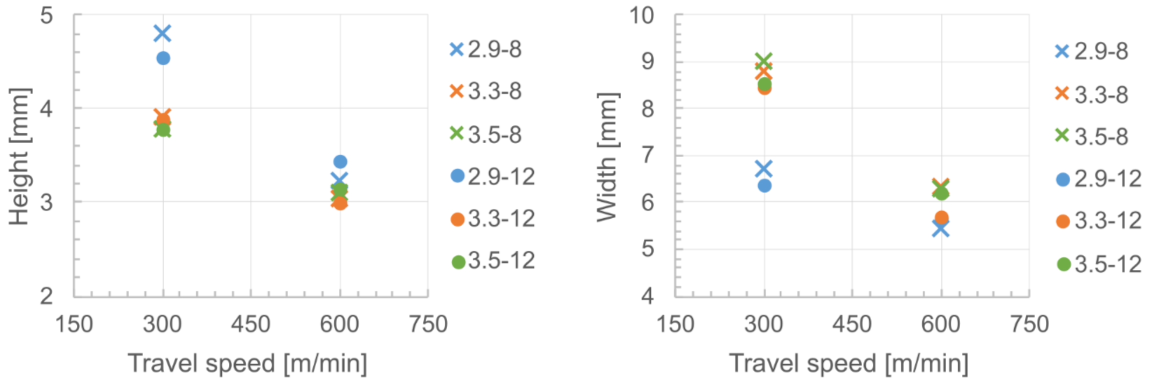

Figure 63. Ts and P effect on height and width

5.3.3 Phase 3

Building on the successful bead deposition achieved in Phase 2, Phase 3 introduced two additional levels of Ts, while keeping all other parameters consistent with those in Phase 2, as detailed in Table 24. This configuration expands the experimental scope to include four levels of Ts, three levels of P, and two levels of SOD, enabling a broader assessment of Ts on deposition outcomes. The complete experimental design, comprising 24 sample trials, is presented in Table 25. This expanded setup is intended to refine the understanding of Ts effects within the WAAM process, while providing insights on interactions with P and SOD under the newly introduced conditions.

Table 24. Phase 3 process parameter optimization

Power [kW]	Ts [mm/min]	Sod [mm]
2[3] = 2.9	300	8
2[4] = 3.3	450	12
2[5] = 3.5	600	
	750	

Table 25. Phase 3 design of experiments

Experimental order	Ref or DOE No: Of	Power [Level	Ts [mm/min]	Sod [mm]
15	1	2[3]	300	8
20	2	2[3]	450	8
1	3	2[3]	600	8
6	4	2[3]	750	8

10	5	2[4]	300	8
8	6	2[4]	450	8
22	7	2[4]	600	8
2	8	2[4]	750	8
17	9	2[5]	300	8
5	10	2[5]	450	8
13	11	2[5]	600	8
3	12	2[5]	750	8
16	13	2[3]	300	12
21	14	2[3]	450	12
19	15	2[3]	600	12
4	16	2[3]	750	12
9	17	2[4]	300	12
11	18	2[4]	450	12
23	19	2[4]	600	12
18	20	2[4]	750	12
7	21	2[5]	300	12
24	22	2[5]	450	12
12	23	2[5]	600	12
14	24	2[5]	750	12

As in Phases 1 and 2, all experiments in this phase were randomized to mitigate bias and enhance data reliability. Figure 64 illustrates the resulting samples after the trials, displaying the consistency achieved across tests. Each experiment was successfully executed, and key in-process data such as current, voltage, and temperature readings were recorded in real-time. This data collection provides a comprehensive basis for analyzing the interaction effects of these parameters, supporting the overall goal of optimizing the WAAM process with precise, reliable measurements.

Figure 64. Phase 3 all sample after the experiment

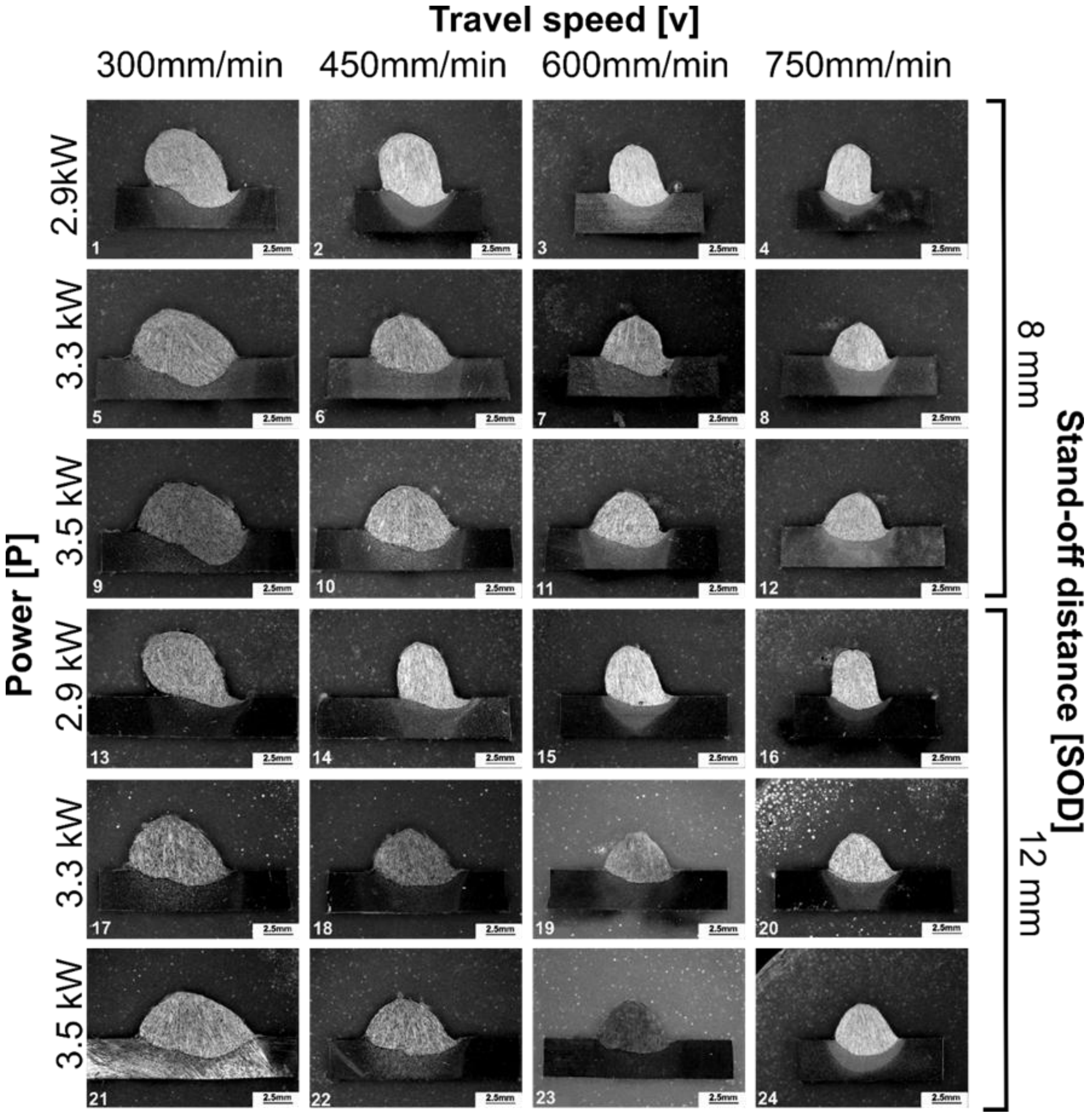

Figure 65. Sections of all Phase 3 samples

Results and discussion

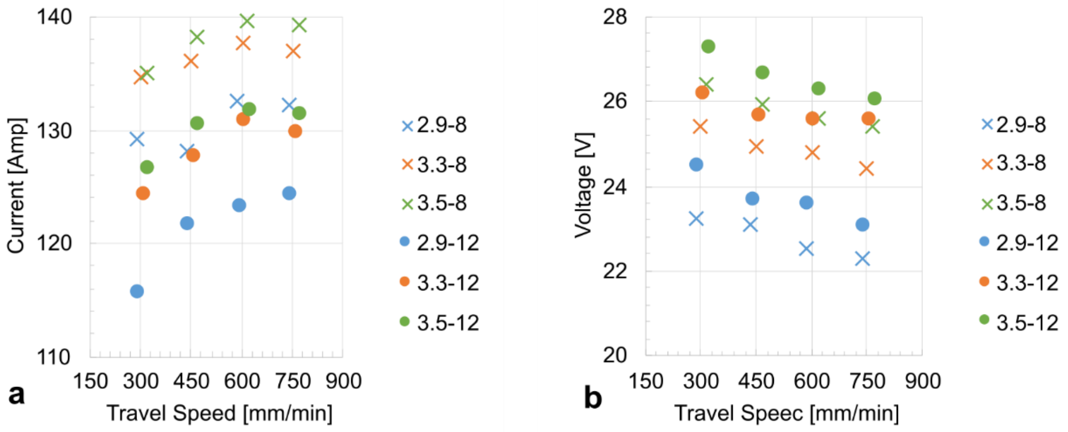

Figure 66. Average current and voltages

Figure 66 presents the average current and voltage measurements, revealing that current increased in correlation with higher levels of P and Ts, while a rise in SOD led to a reduction in current. As observed in Phase 2, voltage showed an inverse relationship to current, compensating for variations in the power level set on the MIG machine to maintain stability. Following these trials, samples were sectioned to assess geometrical characteristics such as height, width, and cross-sectional area of the beads. Cross-sectioned images of the samples are displayed in Figure 65, with detailed geometrical measurements shown in Figure 67. Key findings indicate that bead height decreased as both Ts and P were increased. The width of the beads also decreased with higher Ts but showed an increase with higher P. Conversely, SOD displayed no substantial influence on these geometrical characteristics. The cross-sectional area of the beads showed a decreasing curve with higher Ts. Interestingly, P appeared to have a limited effect on cross-sectional areas. This effect appeared to disappear at higher Ts with measurements stabilizing around 15 mm^2. These observations suggest that while Ts and P significantly shape bead geometry, their effects vary across different dimensional characteristics.

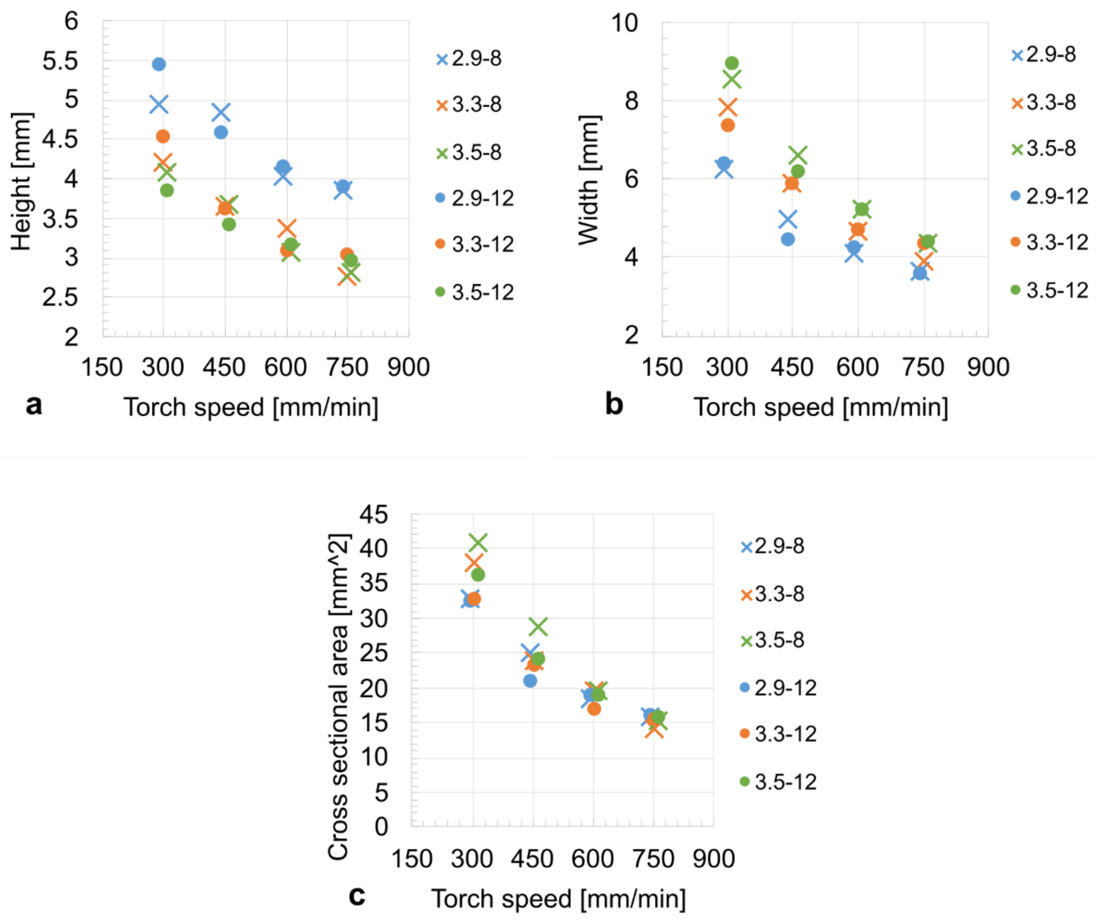

Figure 67 Geometrical details of Phase 3 samples, a). Height, b). Width, c). Cross sectional area

Figure 68 presents the infrared (IR) images captured during the deposition process, where the deposited bead and substrate are distinguishable due to the higher temperatures observed in the depositing bead. A vertical line ROI (Region of Interest) was placed at the center of the deposition area to closely examine the temperature variation throughout the process, as shown in Figure 68. This ROI provided a focused region for monitoring thermal changes over time. Temperature data collected along this ROI was subsequently processed in MATLAB, where it was plotted and analyzed to generate a temperature history profile at this specific position. This analysis in MATLAB facilitated a detailed understanding of thermal distribution and fluctuation during the deposition, offering insights into how temperature evolves in real-time and its potential influence on bead formation.

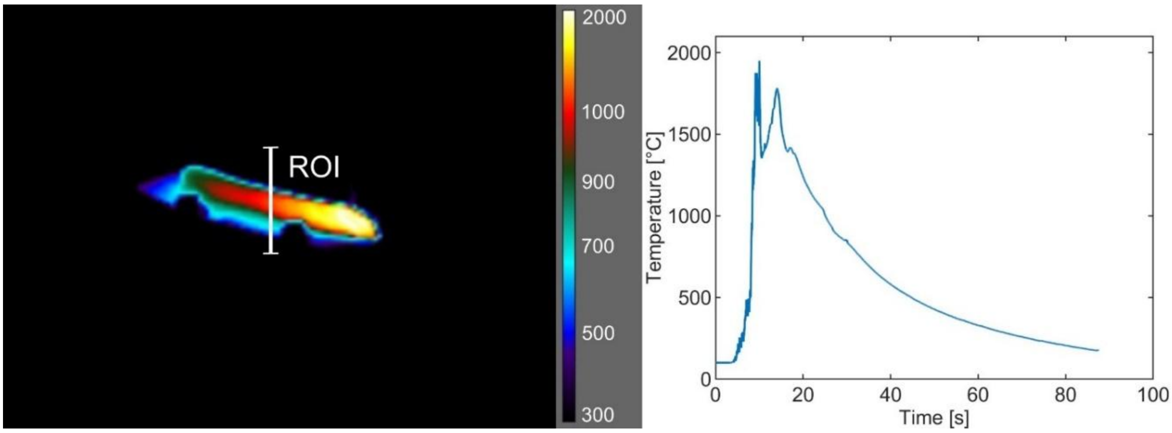

Figure 68. Infrared Image acquired during the deposition and temperature extraction at vertical ROI

Figure 69 illustrates the temperature variation at the ROI under different deposition conditions, with the temperature profiles displaying similar patterns across conditions. Initially, the temperature rises as the torch approaches the ROI, holding at a stable level for a certain period dependent on Ts. Once the torch moves away from the ROI, the temperature decreases accordingly. These consistent trends across the curves suggest that all key process parameters P, Ts, and SOD play a significant role in shaping the temperature profile. This influence indicates that these parameters collectively affect heat distribution and retention, impacting how thermal energy is absorbed and dissipated within the bead and substrate during deposition.

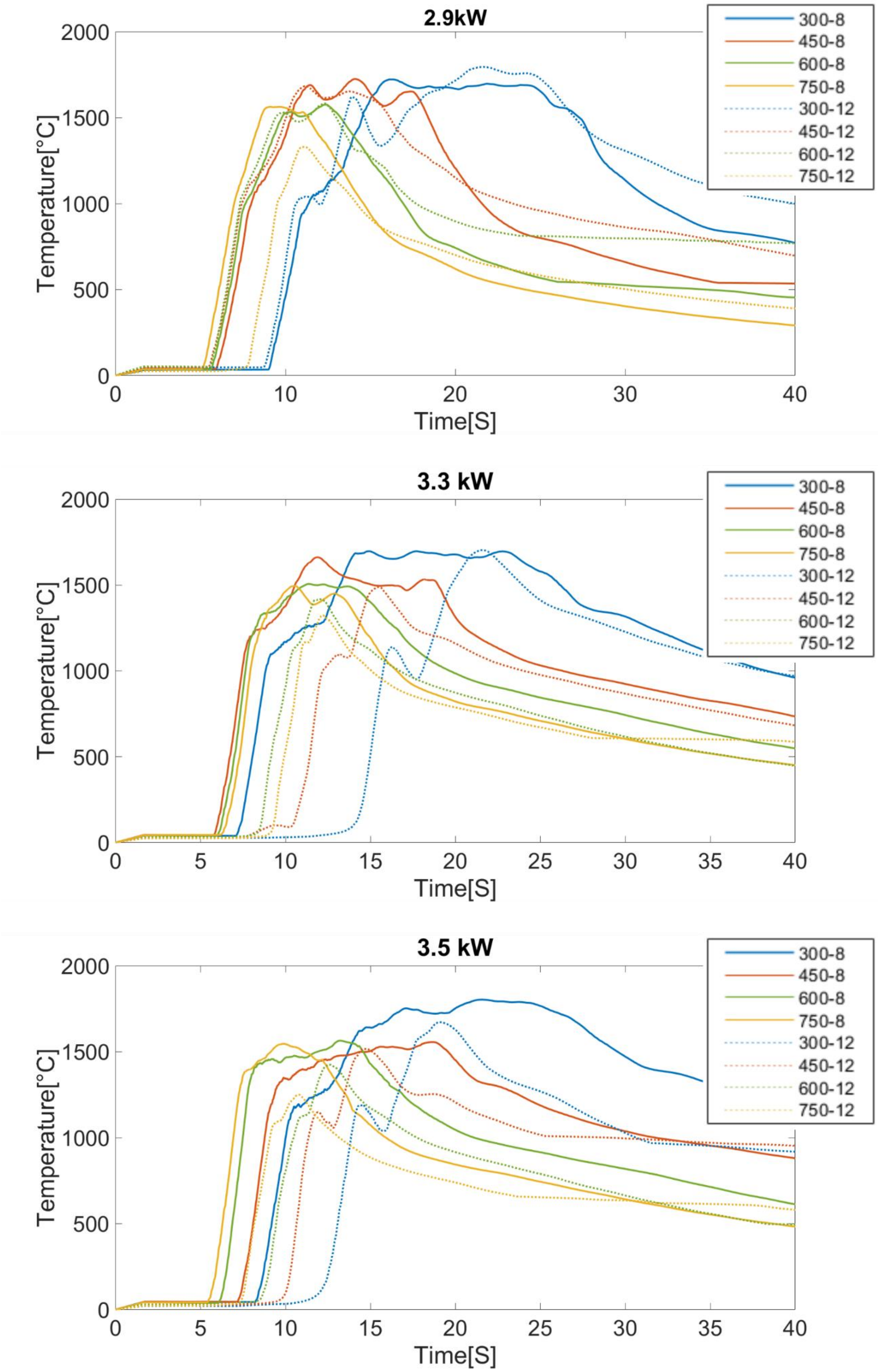

Figure 69. Temperature trends measured at the region of interest under different deposition conditions

To determine the influence of the process parameters on peak temperature, measurements were taken across all specified conditions. Figure 70 illustrates how these parameters affect peak temperature, highlighting that Ts had the most significant impact. Observations reveal that higher Ts corresponds to a reduction in peak temperature, a trend attributed to the decreased linear heat input (Ht) provided during deposition. This reduction in Ht aligns with expected thermal behavior, as the faster movement distributes heat more quickly, lowering the peak temperature at any given point. Ht can be calculated as described by the equation below, capturing the relationship between Ts and heat input in the WAAM process.

$$H_t = \frac{P \cdot 60}{Ts}$$

An increase in Ts results in a proportional reduction in interaction time, leading to a decreased heat input and, consequently, a smaller rise in temperatures and peak temperatures. This correlation occurs because as Ts rises, the arc moves more quickly across the substrate, distributing heat more rapidly and preventing concentrated thermal buildup. Interestingly, peak temperature decreases with higher P, an outcome better understood by examining how P affects the contact area between the bead and substrate. Higher P, while providing greater heating, also causes a wider bead with an increased contact surface. This expansion allows for more substantial heat diffusion into the substrate, leading to higher heat loss. Thus, despite the higher energy input, heat loss to the substrate becomes the predominant factor, reducing the peak temperature on the deposited bead. SOD also affects peak temperature, where a longer SOD (e.g., 12 mm) lowers peak temperature due to reduced current and a less concentrated arc, which supplies less heat. In contrast, a shorter SOD (e.g., 8 mm) enables higher energy input and peak temperatures. At higher Ts, the impact of SOD becomes more pronounced, as confirmed by the higher temperature differences between SOD settings (8 mm vs. 12 mm). This effect occurs because, at low Ts, prolonged interaction times ensure adequate heating regardless of SOD. However, at higher Ts, reduced energy input and increased thermal gradients lead to more significant peak temperature differences, emphasizing the combined influence of Ts and SOD on thermal distribution.

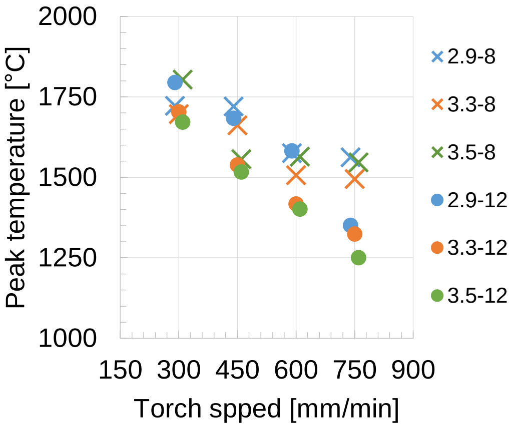

Figure 70. Influence of the process parameters on the peak temperature

In the WAAM process, high energy is required to melt the feed material and simultaneously heat the substrate, initiating a solidification process as the torch moves forward. The solidification rate is influenced by the peak temperature, which is led by the deposition material volume and thermal gradients during the deposition. The material undergoes two primary phase transitions: rapid melting due to energy absorption and cooling through heat diffusion. The temperature field and variations throughout the WAAM process have a profound impact on the microstructural characteristics of the deposited bead. Rapid heating and cooling rates, combined with thermal gradients and bulk temperature increments, affect key properties such as morphology and grain formation in the deposited material. These thermal dynamics result in distinct microstructural regions within the deposited material, influencing the mechanical performance of Directed Energy Deposition (DED) components. Figure 71 illustrates a cross-section of an etched WAAM sample, revealing the different regions formed within the component and substrate. These regions highlight how thermal effects shape the microstructure and indicate the temperature-dependent transitions that contribute to grain development and phase distribution across the bead.

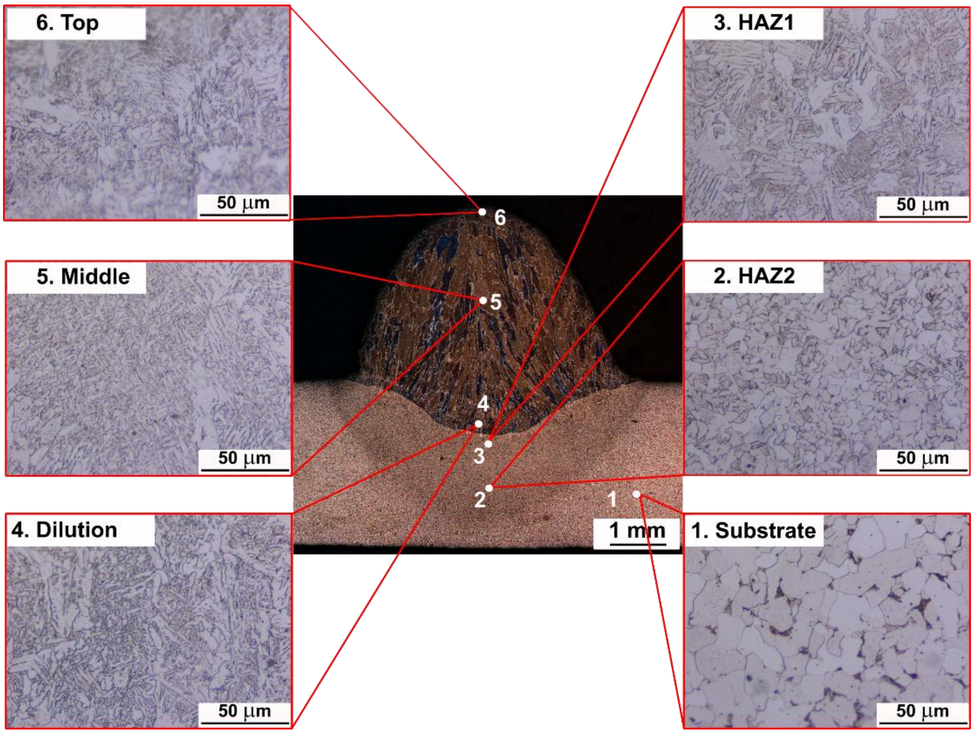

Figure 71. Microstructure of a WAAM deposited bead sample

Heat diffusion into the substrate occurs as material is deposited, which re-heats the substrate and modifies the microstructure within the heat-affected zone (HAZ) [231]. The HAZ is divided into two primary regions: HAZ1, situated directly beneath the deposited bead, where the heat fully decomposes the original base metal microstructure to form new grain structures, and HAZ2, which combines the microstructure of the substrate with that of HAZ1 [232]. Solidification in metal brings additional complexity. The high cooling rate in DED is driven by the direct contact between the melt pool and the cold substrate, as shown in Figure 71, which highlights distinct microstructures within the bead and substrate. Equiaxed grains form within the substrate, while cooling in the bead originates from the substrate (due to heat diffusion) and from the bead's top and sides (through radiation and convection). Consequently, elongated grains grow until they encounter a boundary, with needle-like grains forming within elongated grain pellets. These pellets orient in the solidification direction. Longer Sod promoted lower heat concertation. This involved lower temperature gradients and consequently lower cooling rates. Thus, longer Sod produced larger grains as compared to shorter Sod. Shorted Sod led to higher heat concentration. Consequently, steeper temperature gradients were produced which came with higher cooling rates. This involved rapid cooling and solidification rates that hindered grain growth, leading to finer grain structures. However, the Sod also influenced the heat provided. Indeed, for Sod = 8 mm the measured power was 3-4% higher than that measured with Sod =12 mm.

The travel speed exerted the main influence of the grain's morphology. Indeed, the travel speed is the key process parameter regulating thermal gradients since it directly affects the interaction time. Figure 72 shows this Ts effect on grain morphology of the deposited bead. As observed, larger and wider grains are produced under low travel speeds. Increasing the travel speed, which reduces the interaction time leading to steeper thermal gradients, led to smaller and thinner grains; besides, the grains were more aligned in vertical direction since the steeper thermal gradients.

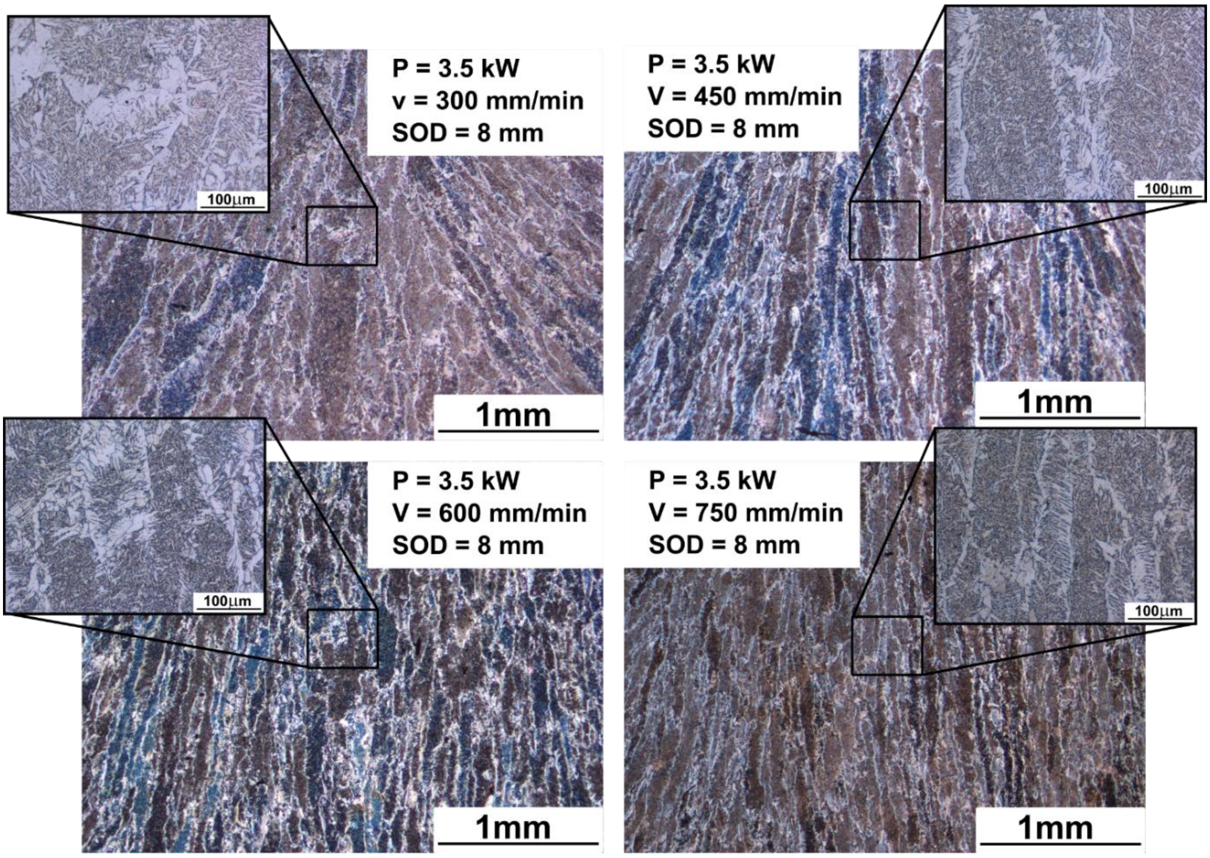

Figure 72. Grain structure of the deposited bead under the power (P=3.5 kW) and SOD=8mm with varying travel speed

Microhardness tests were conducted across different regions (from bottom to top) to assess the effects of process parameters on local mechanical properties. Six testing positions were selected for each deposition condition, as shown in Figure 71. Microhardness variation from bottom (position 6) to top (position 1) was calculated for each sample. Figure 73 shows this variation, revealing that the deposited bead consistently exhibited higher microhardness than the substrate, regardless of deposition conditions, with a notable peak at position 5. This peak may be due to position 6 proximity to the sample edge, which affects yield strength due to limited surrounding material [233]. The results in Figure 73 indicate that process parameters strongly influenced the deposited bead's microhardness. Higher power levels reduced bead microhardness, with values at point 2 ranging between 220–245 HV1 for P = 2.9 kW (depending on Ts), which decreased to 200–215 for P = 3.3 kW and 205–212 for P = 3.5 kW. Lower power levels resulted in steeper microhardness gradients from top to bottom, while higher power levels created smoother transitions due to enhanced contact length, promoting heat diffusion and reduced thermal gradients. Higher Ts led to lower peak temperatures and steeper thermal gradients, thus accelerating cooling rates and increasing hardness, as evidenced by the shorter hold time at higher Ts. The impact of SOD on microhardness was minimal, suggesting that thermal gradients influence microhardness more significantly than peak temperature, consistent with findings in [234].

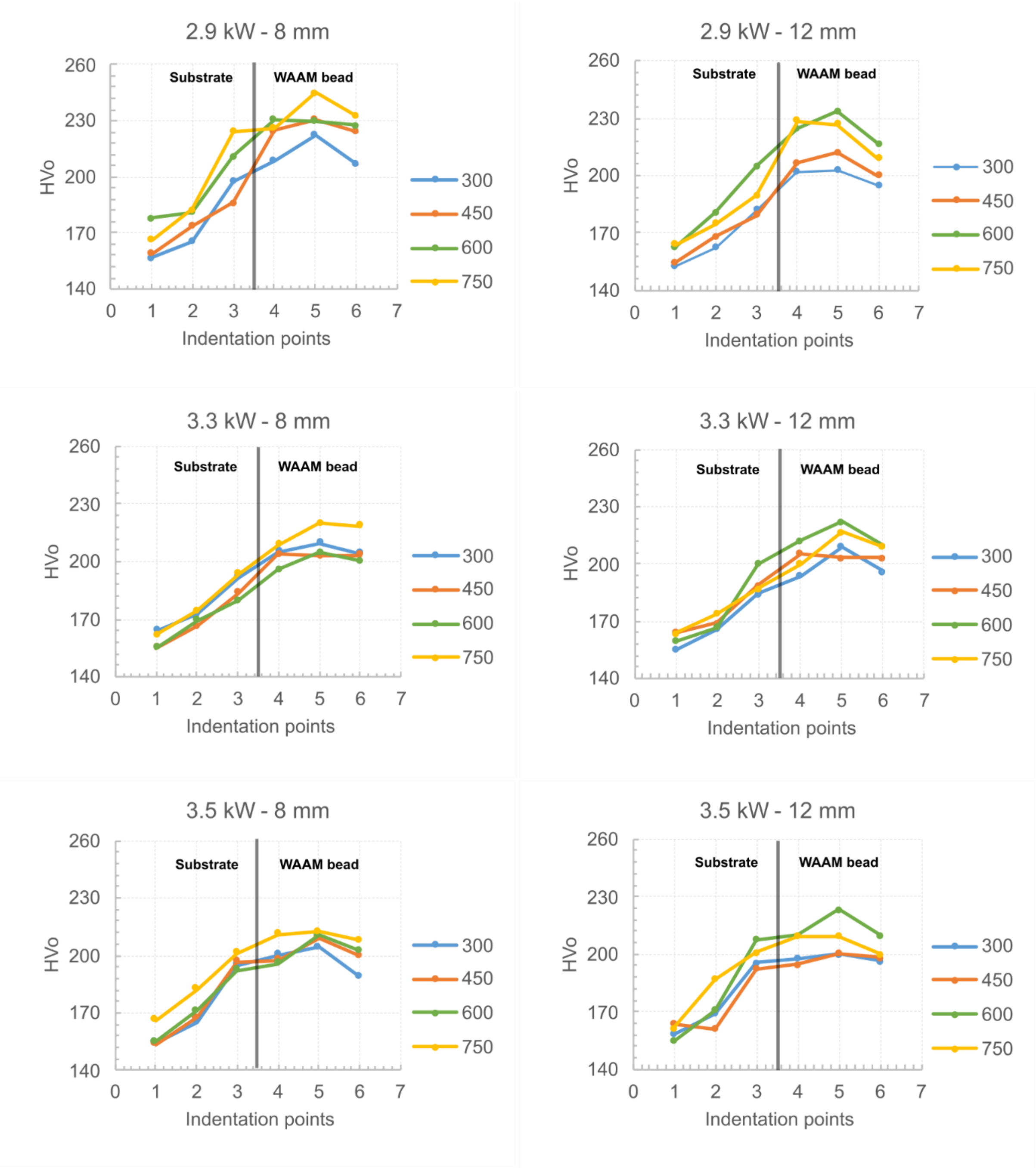

Figure 73. Influence of the deposition parameters on the microhardness measurements at different locations

The geometrical characteristics of deposited beads are crucial for accurately designing deposition paths in AM processes. Understanding the influence of process parameters on bead geometry and microstructure is essential for optimizing WAAM. Improper deposition conditions can introduce defects that compromise the layer-by-layer strategy required for building 3D components. Prominent macroscopic defects like unstable material flow, which emphasize the need for a well-defined parameter selection window to mitigate such issues. Figure 74 illustrates current fluctuations observed under different deposition conditions. Since power settings remained constant during testing, fluctuations in current, voltage (current alone was analyzed here), and temperature primarily depended on the shape and stability of the deposited bead. Figure 74a&b display significant current fluctuations, which were visibly correlated with material deposition irregularities. Drops in current led to discontinuities in the corresponding samples, suggesting a direct relationship between current stability and bead continuity. In contrast, Figure 74c&d show more stable, flat current profiles, which reflect consistently uniform deposition in the corresponding samples. This observation underlines the importance of stable current for achieving defect-free, continuous material flow and highlights the role of consistent parameter control in achieving the desired geometric and microstructural characteristics in WAAM.

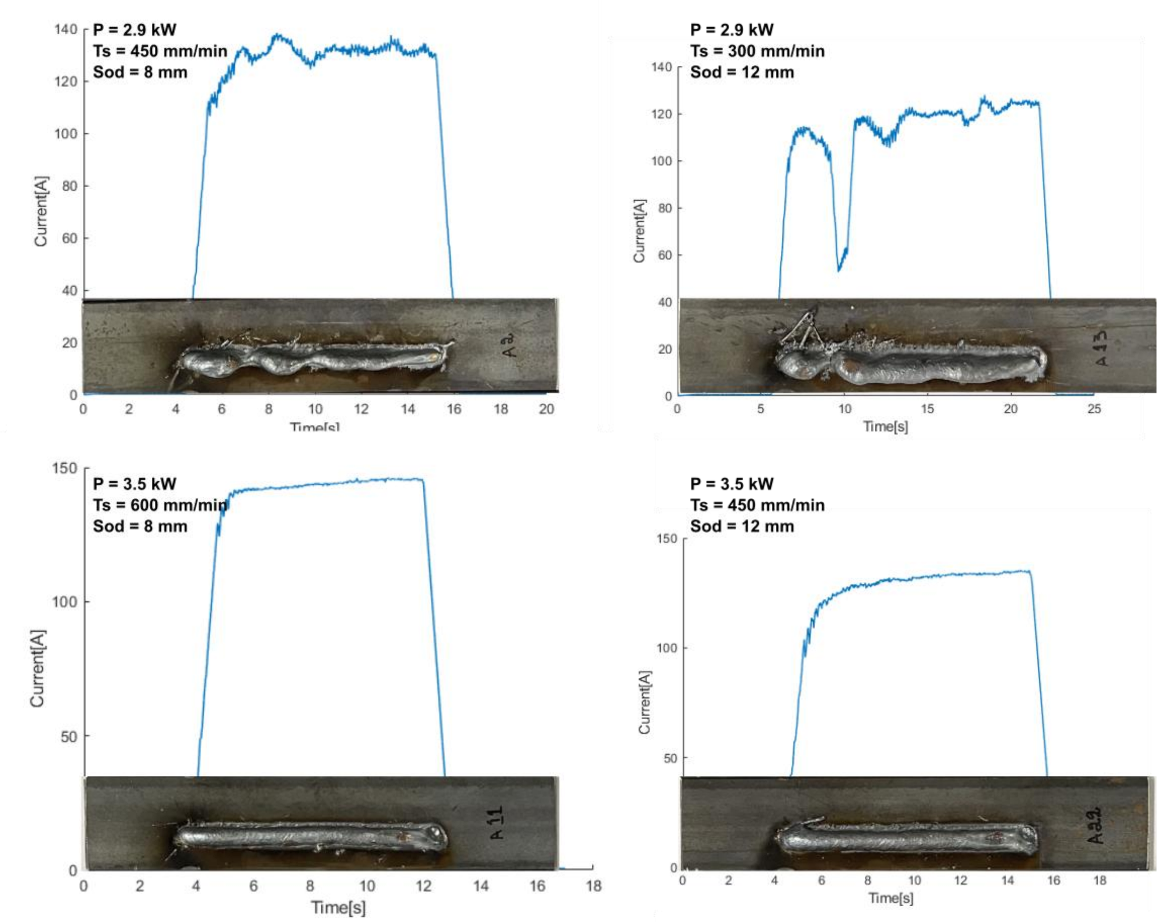

Figure 74. Current fluctuation during the deposition

From the in-process data monitoring, a comprehensive analysis of microstructure and temperature variation offered detailed insights into the influence of key process parameters, namely Ts, P, WFS, and SOD. This analysis facilitated a clearer understanding of how each parameter affects the deposition quality and stability in WAAM. Based on these findings, a summarized framework is presented in Table 26, which categorizes the process conditions: parameter combinations that successfully enabled material deposition are highlighted in green, while those that proved unsuitable are marked in red.

Table 26 Optimized process parameters

	300	450	600	750	900	1000
2.2	0	0	0			
2.9	1	1	1	1		
3.3	1	1	1	1		
3.5	1	1	1	1		
3.8						

Figure 75 added trails

To further refine the process window, additional experimental trials were conducted. These included tests under conditions of low P = 2.2 kW paired with higher Ts = 750 and 900 mm/min, as well as high P = 3.8 kW with a medium Ts = 450 and 600 mm/min. These trials aimed to better understand how extreme Ts and P combinations impact deposition stability, especially under varying thermal and material flow conditions. Figure 75 depicts these experimental samples, highlighting the different defects with these parameters. The samples produced under low P (2.2 kW) conditions exhibited discontinuous material deposition. As Ts increases, heat input per unit time decreases, limiting the energy available to sustain continuous deposition. Consequently, both tested conditions at Ts values of 750 mm/min and 900 mm/min displayed uneven material deposition during deposition. In contrast, samples produced under high P (3.8 kW) demonstrated different outcomes based on Ts settings. The sample with Ts = 450 mm/min exhibited burn-through to the substrate, caused by the increased heat input associated with a slower Ts. This combination allowed for excessive energy concentration, leading to substrate damage. However, the sample with Ts = 600 mm/min avoided burn-through, achieving a stable deposition without discontinuities. This result suggests that a moderate Ts, when paired with higher P, can effectively balance heat input, supporting consistent material flow and preventing damage to the substrate.

Table 27. Specific energy

Power, P [kW]	Specific Energy, E [J/mm^3]	
	WFS = 5800 mm/min	WFS = 16500 mm/min
2.2	13.9	9.3
2.9	18.3	12.3
3.3	20.9	14.0

3.5	22.2	14.9
3.8	24	16.1

For each of the specified processing conditions, specific energy (E) the heat supplied per unit volume of wire was calculated using equation below. In this equation, η represents efficiency, set at 0.8 [235]. A is the cross-sectional area of the wire (in mm^2); and WFS is the wire feed speed. Specific energy, as given by

$$E = \eta \frac{P}{A * WFS}$$

is directly influenced by arc power and material flow but remains independent of Ts. This measure is critical in ensuring sufficient heat is supplied, with typical values for low-carbon steels ranging between 9.3–11 J/mm^3 [236]. Table 27 summarizes specific energy values across the tested power levels in preliminary trials. Conditions producing good-quality beads are marked in green, while conditions resulting in unstable deposition are marked in red. Additionally, excessive heat and material flow at the highest power setting led to substrate breakdown, marked in blue in the table and shown in Figure 75. On the other hand, WFS = 5800 mm/min led to proper deposition conditions, if a minimum specific energy of 18.3 J/mm^3 (corresponding to 2.9 kW) was supplied. These findings allow for further refinement of the parameter boundaries, summarized in Table 28, outlining effective combinations for stable and quality WAAM deposition.

Table 28 Optimized processing window

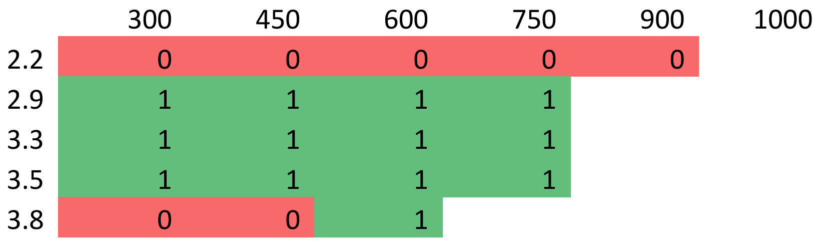

	300	450	600	750	900	1000
2.2	0	0	0	0	0	
2.9	1	1	1	1		
3.3	1	1	1	1		
3.5	1	1	1	1		
3.8	0	0	1			

5.4 Gas flow effect on molten droplet

In WAAM, shielding gas flow is often overlooked in favor of optimizing parameters like P, Ts, WFS, and SOD. Industrial settings frequently rely on prescribed ranges, while researchers often treat these values as fixed, assuming they are already optimized. However, recent studies, such as the simulation by Nigam et al. [237], highlight the significant influence of shielding gas flow on turbulence intensity. The findings revealed that turbulence intensity increases with shielding gas flow rate but decreases at higher velocities due to reduced fluctuations from stronger inertial forces.

In this study, all prior experiments utilized the recommended shielding gas setting of 0.7 bar (12 L/min). To further understand its impact, experiments were conducted with flow rates of 0, 0.7, 1, and 2 bar, as detailed in Table 29, with bead geometry results illustrated in Figure 76. At 2 bar (30 L/min), excessive gas flow caused turbulence near the nozzle, displacing the melt droplet to one side. This misalignment resulted in material being pushed sideways during deposition in the opposite direction, producing flat beads. As the flow rate decreased to 1 bar (15 L/min) and 0.7 bar (12 L/min), turbulence diminished, and at 0.7 bar, it disappeared entirely. The absence of shielding gas at 0 bar led to porosity in the beads, caused by oxidation and nitrogen absorption. Additionally, the lack of cooling altered the surface tension and wetting angle, negatively affecting bead quality [238].

These findings underscore the role of shielding gas, protecting the deposition material from atmospheric contamination and influencing cooling and bead geometry. Both excessive and insufficient gas flow rates can disrupt the material deposition process. In this context, the recommended flow rate of 0.7 bar (12 L/min) is confirmed as the optimal condition, ensuring bead integrity and efficient process performance.

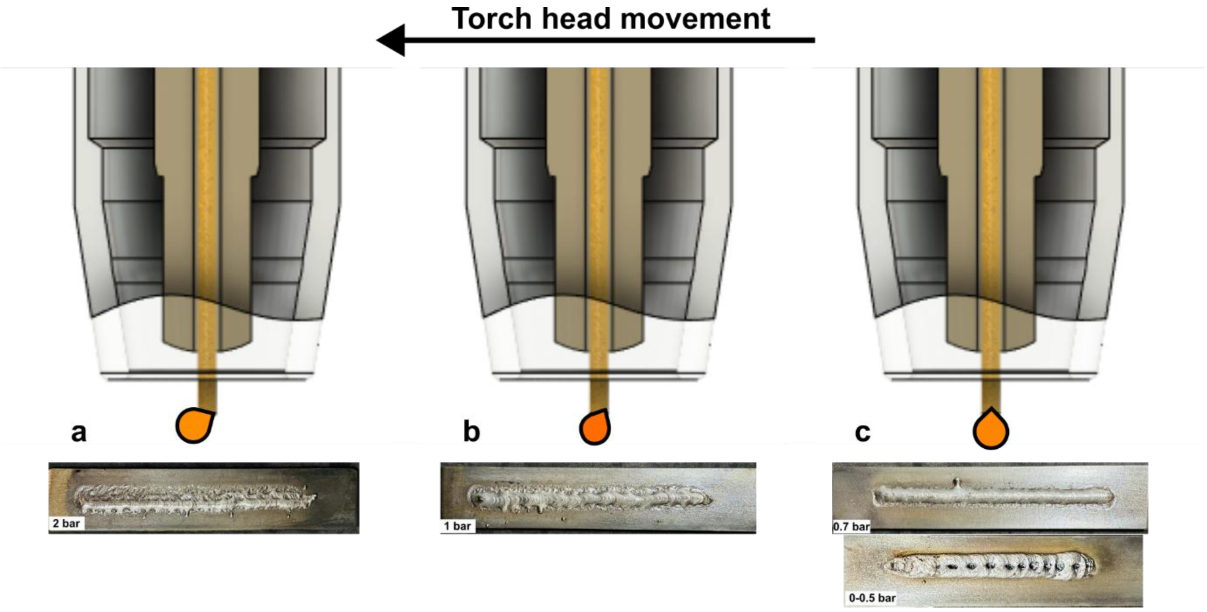

Figure 76. Gas flow effect on molten droplet, a) at 2 bars, b) at 1 bar, c) at 0.7 bar

Table 29 Recommended shielding gas flow rates

Bars	L/min
0-0.5	0-5
0.7	12
1	15
2	30

5.5 Multi-layer stacking

It was evident from the literature review and previous experimental results that in high-energy processes like DED-WAAM, the temperature of a previously deposited layer plays a crucial role in ensuring deposition quality. If the previously deposited layer does not sufficiently cool below a specific temperature, the next layer's penetration can increase, leading to geometrical inconsistencies [191], as shown in Figure 77. To address this, the dwell time, the time required for the previously deposited layer to reach a temperature below 50°C was calculated and found to be more than 10 minutes. Such prolonged cooling times are unsuitable for industrial applications, where reducing manufacturing time is vital for competitiveness.

Figure 77 Without forced air-cooling.

To overcome this limitation, a forced air-cooling system was integrated into the WAAM process. Forced air cooling not only significantly reduces dwell time but also enhances the material properties of the manufactured component. To implement this improvement, an air dispenser was designed and fabricated using SLA (stereolithography) technology, as depicted in Figure 78. Recalculating the dwell time with the inclusion of the air dispenser revealed a substantial reduction, bringing it down to just 2 minutes, demonstrating the efficiency and practicality of this advancement in reducing manufacturing time and improving the deposition material properties [161].

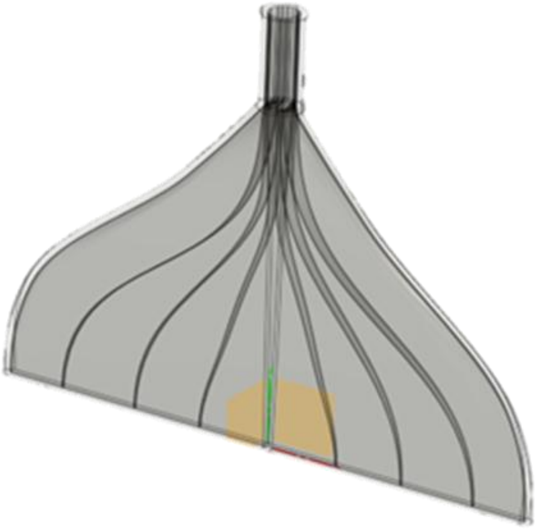

Figure 78. Air dispenser.

After establishing the processing window and determining the appropriate dwell time, the next step involved the actual additive manufacturing by depositing multiple layers. A 10-layer structure, resembling a simple wall (single bead, multi-pass), was constructed through layer-by-layer deposition. The resulting sample is presented in Figure 79. Each layer was deposited starting from the same side (left), which led to a common issue associated with the WAAM process: the humping effect. This effect occurred due to insufficient shielding gas coverage at the opposite end (right), leaving the deposited material vulnerable to atmospheric gases such as oxygen and nitrogen. This exposure resulted in porosity at the unprotected end of the wall. The literature review indicated several strategies to address the humping effect. Many authors suggested employing bi-directional deposition or increasing the deposition length [91]. However, simply increasing the length is not a feasible solution in all cases, as it depends on the specific design and manufacturing constraints. Thus, to mitigate this issue effectively, a bi-directional deposition approach was adopted. In this approach, the deposition alternated directions with each layer, while maintaining a Ts of 250 mm/min and keeping all other process parameters unchanged. This modification aimed to ensure uniform shielding gas coverage and minimize porosity. The outcome of this approach is shown in Figure 80, demonstrating improved bead quality and a significant reduction in defects at the ends of the structure. This adjustment highlights the importance of deposition strategy in achieving consistent shape and quality in multi-layer WAAM builds.

Figure 79. Humping effect in WAAM sample

Figure 80. Bi- directionally deposited sample

As discussed in Section 3.2 (microstructural characterization), deposition conditions alone are not the sole contributors to material properties; the temperatures generated during deposition play a crucial role in shaping these properties. Variations in thermal conditions influence not only the deposited material but also the substrate, as the heat from deposition interacts with the base material. This interaction is evident in Figure 71[Preliminary test microstructure at different regiones], which highlights the microstructure at various regions. The deposition of material directly onto the substrate alters its properties, creating a heat-affected zone (HAZ) and potentially leading to changes in hardness, grain morphology, and phase distribution. Understanding these effects requires analyzing both lateral and vertical heat flow during deposition. To investigate these phenomena, an experimental plan was devised to examine two specific scenarios, one with lateral deposition (depositing layers next to each other) and another vertical stacking (depositing multiple layers on top of each other). This plan aimed to assess how these approaches impact the geometrical, temperature, and microstructural profiles of the resulting samples. Key questions included how adjacent layers influence each other thermally and structurally, and how stacking layers alters the previously deposited material.

In this context, U-shaped layers were deposited to evaluate the pre-heating effect of lateral depositions. These U-shaped geometries help simulate the influence of overlaying thermal zones, offering insights into temperature distribution and subsequent material changes. Simultaneously, samples with varying numbers of vertically stacked layers were deposited to study the cumulative effects of layer stacking on bead geometry, cooling rates, and microstructure. A schematic illustration of both U-shaped and wall depositions is presented in *Figure 81*, providing a clear representation of the experimental approach. These setups aim to bridge the gap in understanding how deposition strategies and thermal effects interact to influence WAAM outcomes, ensuring a systematic exploration of these critical parameters.

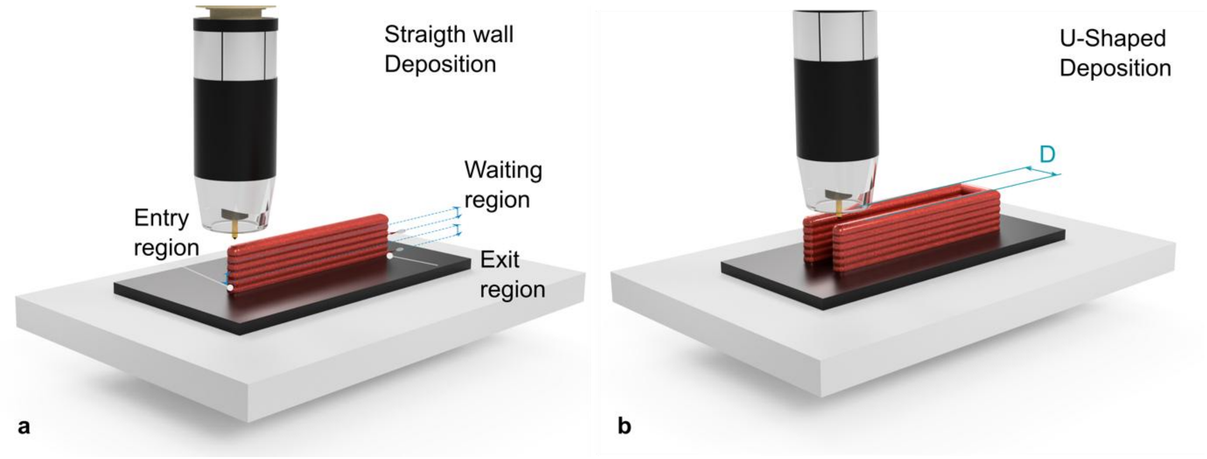

Figure 81. Schematic of the WAAM deposition equipment, a) wall deposition, b) U-shape deposition with D = 10 mm is the distance.

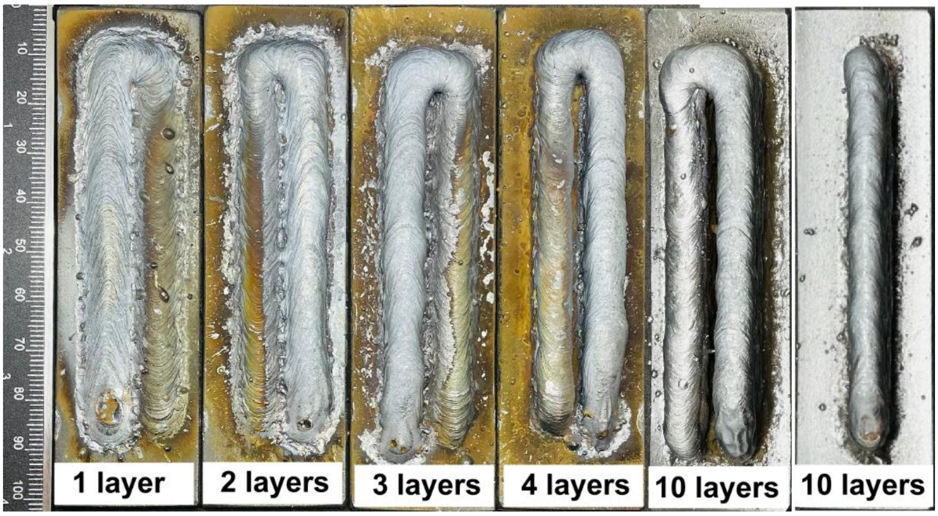

Figure 82. Multi-layer stacking samples (U-shape & Wall)

Based on preliminary tests aimed at identifying stable arc conditions, achieving regular material deposition, and optimizing shielding gas flow, the following process parameters were established for subsequent trials: P = 2.9 kW, Ts = 250 mm/min, and WFS = 5800 mm/min. These parameters provided the foundation for multi-layer deposition experiments. Cooling between consecutive layers was employed using forced air cooling, maintaining a dwell time of 2 minutes 30 seconds to ensure the substrate and previously deposited layers reached a temperature below 50°C. Alternate deposition directions were implemented to address the humping effect, a common issue in WAAM processes, ensuring improved uniformity and reduced external porosity. Figure 82 shows the experimental samples produced, including U-shaped layers deposited with a 10 mm gap between lateral beads. Deposition trials were conducted with samples containing 1, 2, 3, 4, and 10 layers, raising the layer height for each deposition while maintaining a constant SOD of 10 mm. As with previous experiments, in-process data such as current, voltage, and temperature were continuously recorded. After deposition, each sample was sectioned at the midpoint and molded for further analysis, as illustrated in Figure 83. Optical microscopy was employed for geometrical characterization, with a focus on key dimensions including bead width, height, and radius of curvature.

Results and discussion

The cross-sections of all U-shaped samples revealed symmetrical bead shapes on both the left and right sides, as shown in Figure 83, which reports the cross-section of a 10-layer U-shaped sample. The radius curvature analysis of these cross-sectioned samples demonstrated that during the deposition of the first layer, the bead exhibited deep penetration at the center, resulting in a characteristic dip. This central dip flattened in subsequent layers, as illustrated in Figure 84, consistent with findings by Dinovitzer et al. [24].

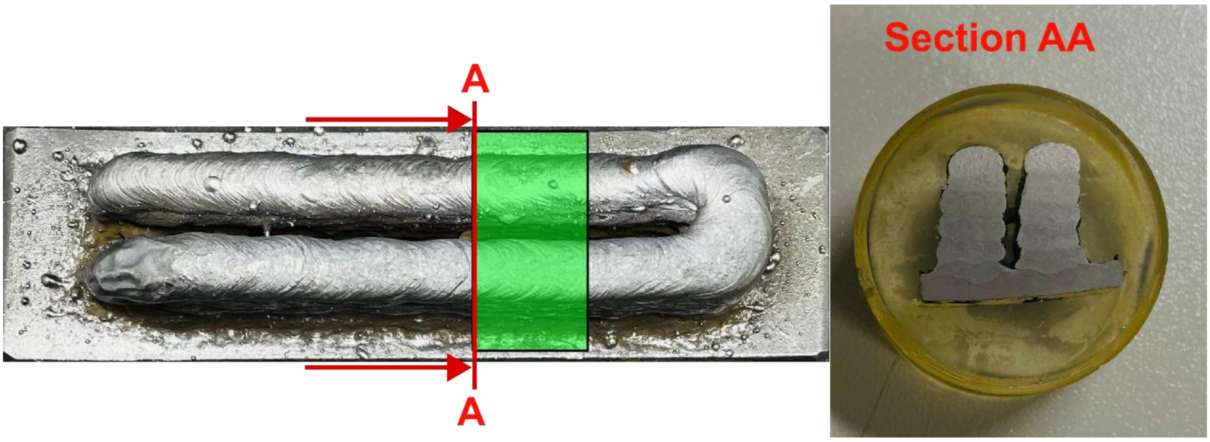

Figure 83. Cross sectioning and englobement of 10-layers U-shape sample

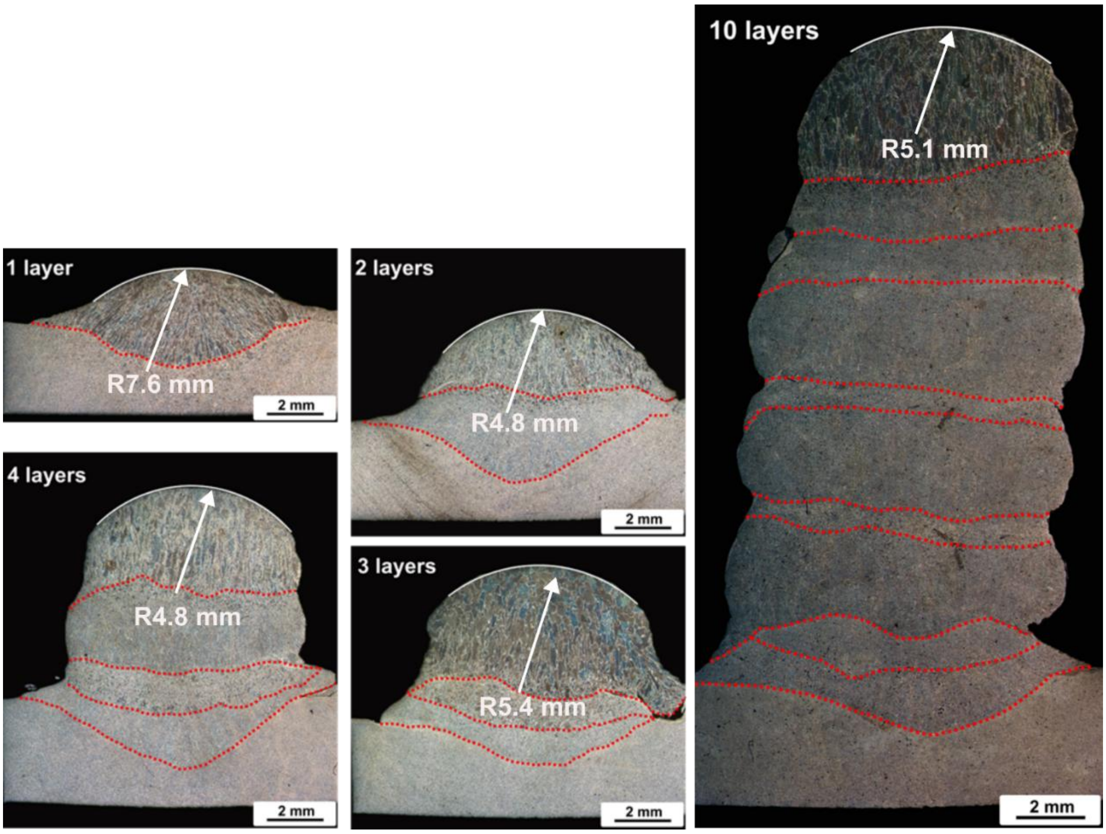

Figure 84. Radius curvature of the deposited bead

The variation in height and radius curvature of the last deposited layer was measured for all U-shaped samples and is presented in Figure 84, with the corresponding values reported in Figure 85. The bead height increased almost linearly with the number of deposited layers, irrespective of the deposition side (left or right). This uniformity is attributed to the two-way deposition strategy, which minimized the effects of directional deposition and produced homogeneous layers. Similar findings have been reported by Ogino et al. [191] and Yehorov et al. [239]. The radius of curvature for a single-layer U-shaped sample measured 7.6 mm but stabilized around 5 mm as the number of layers increased. This trend is likely due to the high current passage during the first layer deposition, which causes greater initial penetration and curvature that diminishes with subsequent layers as deposition stabilizes.

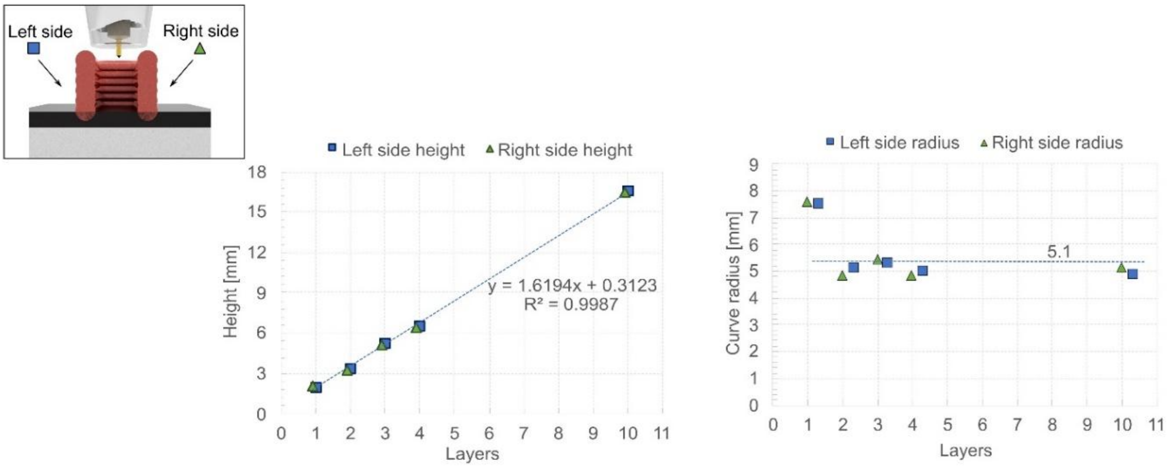

Figure 85. Variation of the height (a) and the radius curvature (b) of the deposited beads

During the deposition process, while the voltage signal remained nearly constant at approximately 25.5 V, the current signal exhibited localized drops. The differences in current levels across layers align with findings by Cambon et al. [39]. For clarity, Figure 86 presents current trends for selected layers, highlighting a higher current during the deposition of the first layer compared to subsequent layers. This variation is attributed to the changing geometrical configuration of the substrate. the first layer is deposited on a flat substrate, whereas later layers are deposited on a semi-spherical surface, impacting electrical resistance. Similar observations were reported by Le et al. [37].

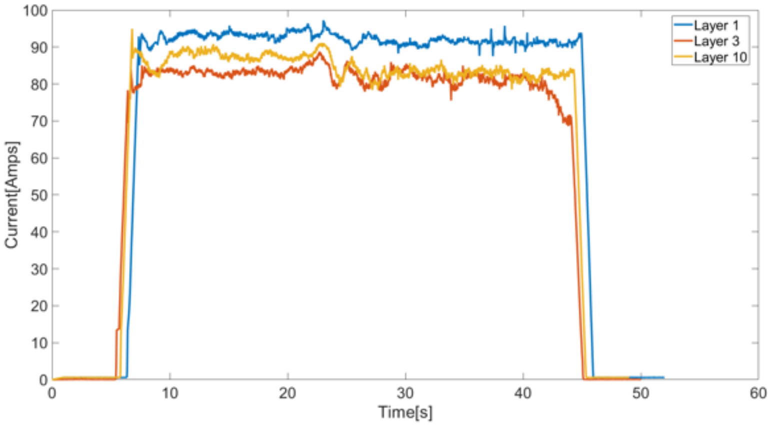

Figure 86. Comparison of current trends during deposition of layers

The current variations also resulted in a reduction in the average power supplied during deposition, as illustrated in Figure 87. The average power decreased from 2.40 kW during the first layer to 2.19 kW after four passes, reflecting a reduction of 8.7 %. This decline highlights how substrate geometry and resistance affect power dynamics in multi-layer WAAM.

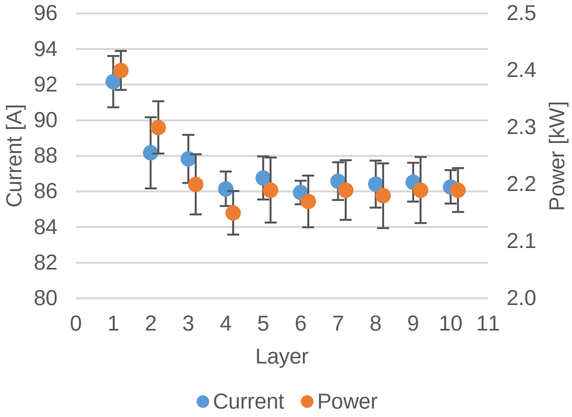

Figure 87. Variation of the mean current and power during the deposition of different layers. (U-shape)

To investigate these current drops further, a detailed examination of current, voltage, and the deposited layer was conducted for the 10th layer of the U-shaped sample, shown in Figure 88. Three distinct regions, 1. at the beginning, 2. within the U-shape, and 3. at the end of deposition, are highlighted in red, demonstrating the influence of deposition geometry on current behavior. Despite these fluctuations in current, voltage remained steady throughout the process, underscoring the sensitivity of current to substrate and bead geometry.

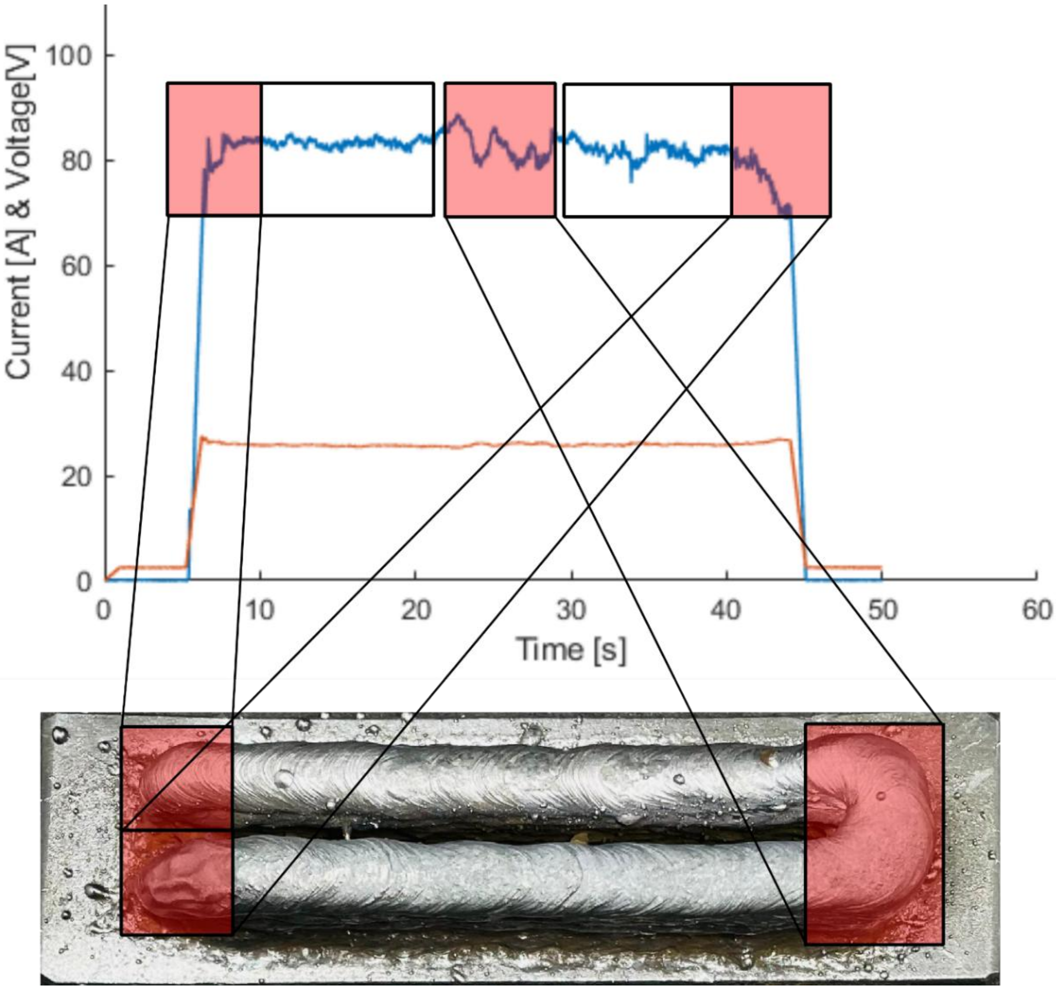

Figure 88. Current variations in U-shape samples

Despite the significant changes in emissivity expected near the melting point [240], the use of an IR camera facilitated a comparative analysis of temperatures during layer deposition. An emissivity coefficient of 0.45 was selected based on measurements reported by Goett et al. [240]. Figure 89a shows the temperature distribution during the first layer deposition, with a point ROI positioned at the layer's center to track temperature variations over time, as illustrated in Figure 89b. This method aligns with the approach described by Wang et al. [241]. The recorded temperature profile indicates rapid heating during deposition, followed by a decline as the torch moves away. Forced air cooling was applied after each bead deposition to prepare for the subsequent layer.

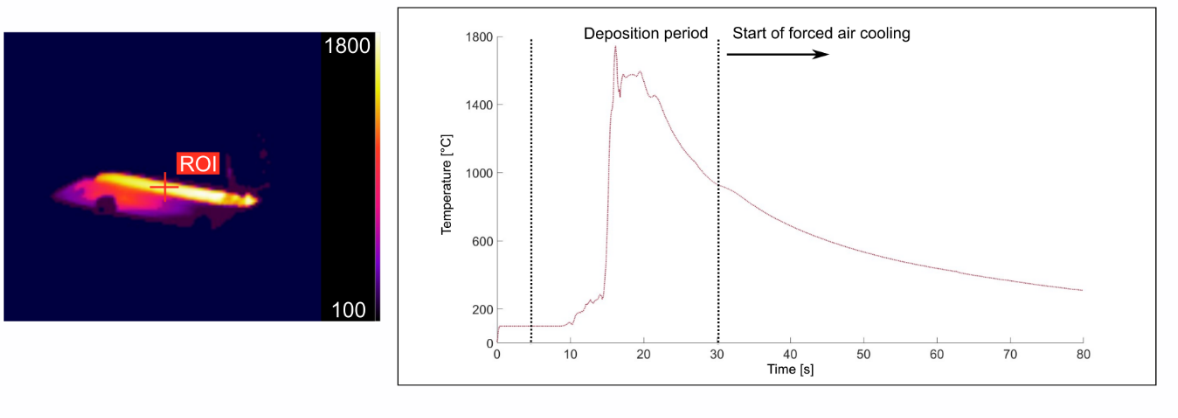

Figure 89. a) IR image after first layer deposition and b) temperature variation extracted at the ROI.

Temperature measurements were performed for all deposited layers, with Figure 90 depicting peak temperatures for the U-shaped sample. The data reveal an increase in the top layer's peak temperature as more layers were deposited, attributed to changes in heat dissipation dynamics. The first layer exhibited higher peak temperatures, approximately 5% greater, due to increased power input. Subsequent layers showed reduced heat loss by thermal diffusion as the distance from the base plate increased, resulting in elevated bead temperatures. After six layers, the peak temperature stabilized, maintaining nearly constant levels in subsequent layers.

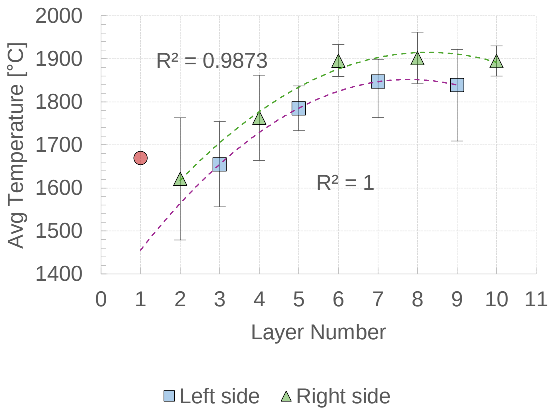

Figure 90. Variation of the mean current and power during the deposition of different layers. (U-shape)

In the U-shaped sample, temperature peaks on the right side were consistently about 60°C higher than on the left. This asymmetry occurred due to preheating effects, as the left side was deposited before the right during even-numbered layers (2, 4, 6, 8, and 10). Thermal history analysis of the base layer was conducted by placing an ROI at the center of the first layer (Figure 91a). The thermal history, reconstructed from IR data (Figure 91b), showed repeated thermal cycles as the number of layers increased. Higher layer counts corresponded to lower temperatures and reduced cooling rates at this ROI. Figure 91c illustrates the exponential decline in peak temperatures at the first layer with increasing deposits, with the layer still reaching nearly 500°C even after ten passes.

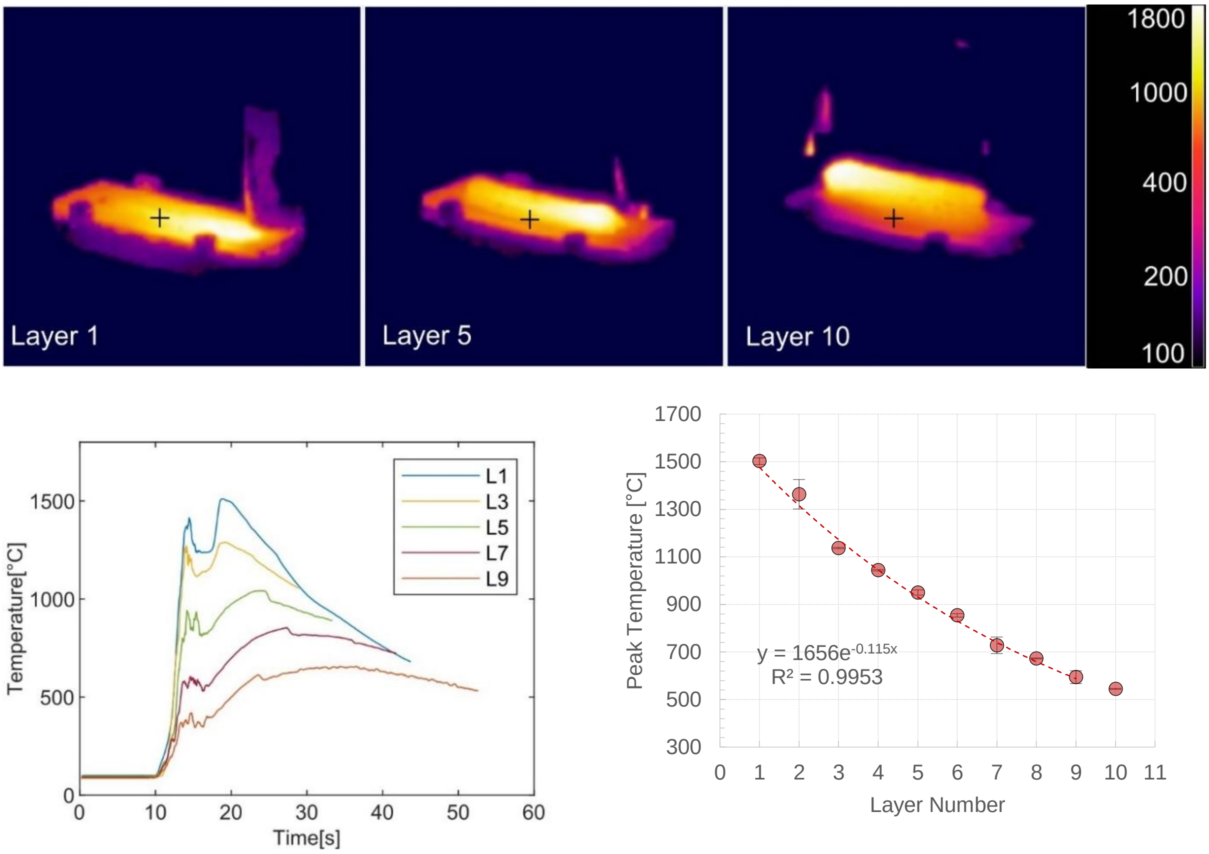

Figure 91. IR images of the temperature distribution during deposition of the 1, 5 and 10 layers; (b) measurement of the temperature trends at the ROI fixed on the first layer and (c) trend of the peak temperature experienced at the first layer when subsequent layer.

Microstructural analyses were carried out to assess the evolution of the metallographic structure in WAAM-produced samples under controlled conditions. Although parameters such as Ts, voltage, current, and WFS typically influence grain formation in WAAM [15], these parameters were maintained constant in this study to isolate the effects of thermal variations. Due to temperature gradients, WAAM samples often display an uneven microstructure throughout the build direction [242].

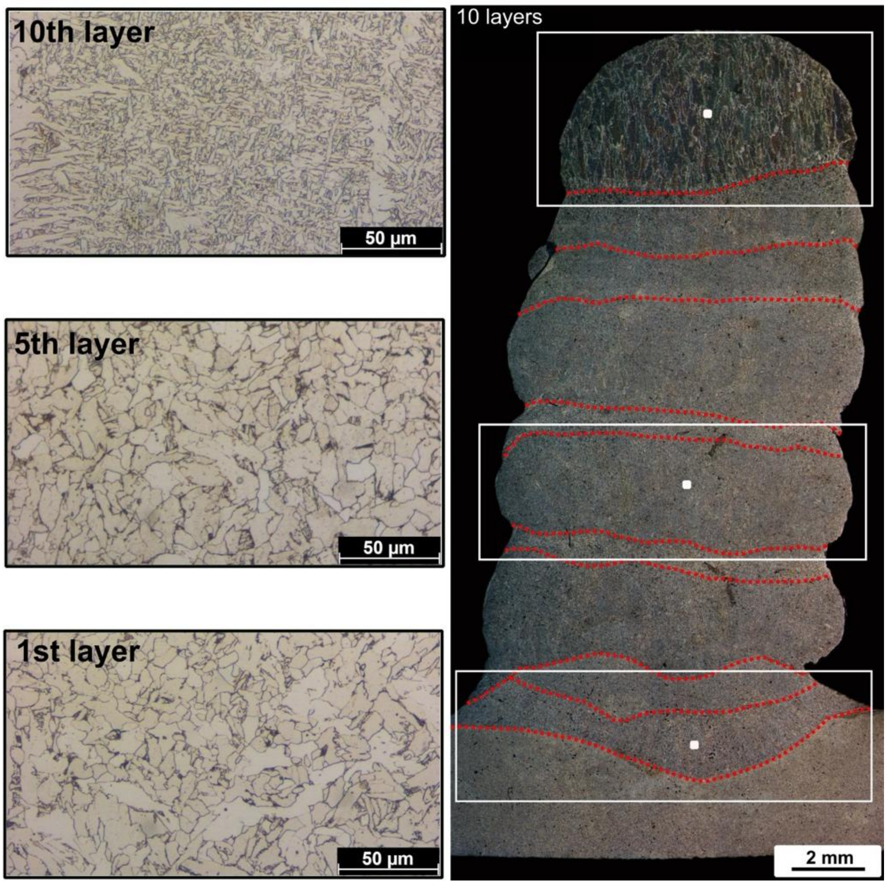

Figure 92. Microstructures of the first, fifth and tenth layer

In the initial deposited layer, the microstructure revealed radially oriented crystalline grains, which were attributed to the steep thermal gradients near the base plate. As additional layers were deposited, the crystalline structure in the initial layer experienced evident alterations. These changes resulted from partial remelting and mixing between layers. Repeated thermal cycles significantly enlarged the grains in the lower layers, as shown in Figure 92, which presents microstructures of the first, fifth, and tenth layers. The microstructure size gradually reduced from the lower to upper layers due to the varying frequency of thermal cycles. The upper layers exhibited smaller, vertically elongated grains formed under steep thermal gradients driven by heat diffusion to the lower layers. In contrast, the lower layers were characterized by larger equiaxed cellular grains, aligning with the findings of Karmuhilan et al. [174].

Grain size measurements were performed following ASTM E112-13 (2021) [243], using the equation:

$$Avg\ grain\ size = \frac{Line\ length}{Number\ of\ grains}$$

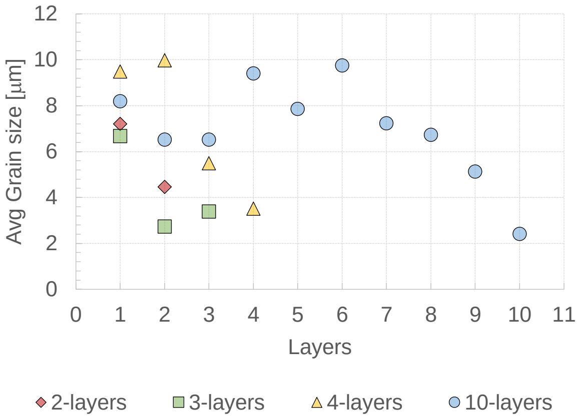

Figure 93. Average grain size at different locations when using different deposited layers

Three measurements were taken for each sample, and the average values are reported in Figure 93. The grain size of the top layer ranged between 2–4 µm, remaining consistent regardless of the total number of deposited layers. In the first layer near the substrate, the grain size varied between 7–10 µm, confirming that repeated thermal cycling caused significant grain enlargement. Interestingly, the middle portion of the ten-layer sample exhibited larger average grain sizes even compared to the lower layers. This phenomenon can be attributed to the rapid cooling of the bottom layers in contact with the room-temperature substrate at the beginning of deposition, while the middle layers experienced heat sinkage from both the warmer bottom layers and heat from the top layers during consecutive depositions. These findings align with observations made by Treutler et al. [244], who observed that small differences in energy input during WAAM can result in significant changes in microstructure morphology. Additionally, similar trends have been reported by Wang et al. [241], who found distinct microstructural variations across WAAM components. They observed equiaxed dendrites or grains in the top region due to heat accumulation and insufficient dissipation, periodic columnar and equiaxed dendrites in the middle layers due to partial remelting, and coarse columnar grains near the substrate resulting from rapid initial cooling.

The microhardness distribution across the deposited samples was examined to understand the mechanical properties influenced by the WAAM process. Figure 94a presents the vertical microhardness profile from the base plate to the top of the deposited bead, while Figure 94b shows the horizontal distribution. An almost linear increase in microhardness was observed from the base plate to the deposited bead. The base plate exhibited an average microhardness of 176 HV, as shown in regions far from the deposition area in Figure 94b, while the top of the deposited layer reached values near 250 HV. This increase in hardness at the top layer is attributed to the high cooling rates caused by forced air cooling, which promoted the formation of fine grains. Compared to preliminary tests where forced air cooling was not applied, and the average microhardness remained below 230 HV, these results demonstrate the effectiveness of cooling on improving hardness.

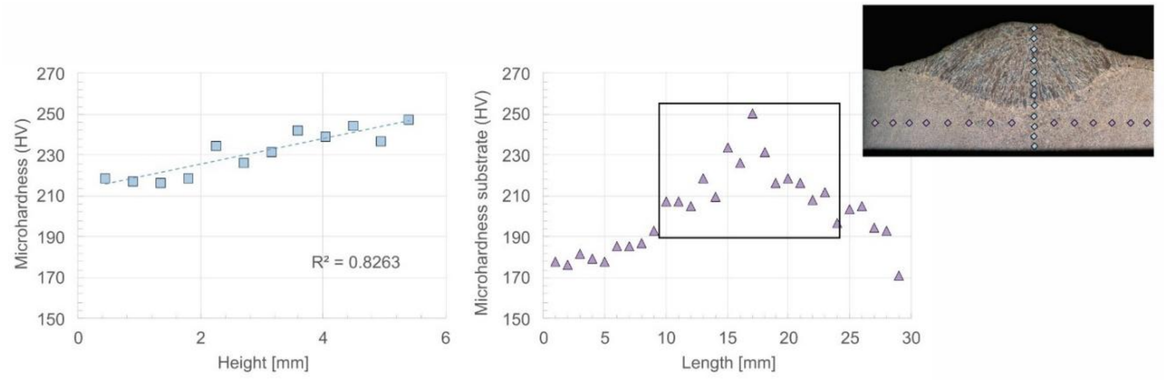

Figure 94. Microhardness (HV) a). first layer, b). and substrate

Vickers microhardness results for multilayer depositions are reported in Figure 95, showing that the top layers consistently exhibited higher hardness than the lower layers. The microhardness of the initially deposited layers decreased progressively as additional layers were deposited. For example, after the second layer, the first layer's average microhardness was 200 HV, decreasing to 150 HV after four layers. This decreases stabilized with further depositions, with the first layer maintaining an average hardness of 150 HV after tenth layer depositions. This reduction can be attributed to repeated thermal cycles that promoted grain growth, resulting in lower hardness, as also observed by Liberini et al. [148]. Particularly, the top layers showed consistent peak microhardness values of 250 HV, regardless of the total layers deposited, due to rapid cooling and minimal exposure to thermal cycling.

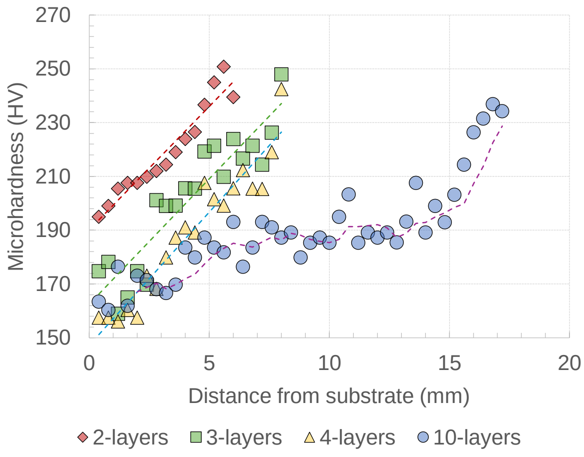

Figure 95. Microhardness at different locations when using different deposited layers.

In the 10-layer samples, a "saddle" pattern in the microhardness distribution was observed in the middle section of both the wall and U-shaped samples. To explore this further, a 20-layer sample was analyzed, with Figure 96 comparing the microhardness profiles of 10-layer wall, 10-layer U-shape, and 20-layer wall samples. Negligible differences were found between the 10-layer U-shaped and wall samples, despite higher peak temperatures in the U-shaped samples. Both exhibited the central saddle trend, followed by increasing hardness in the top 4 layers (corresponding to the top 8 mm). The extended saddle pattern in the 20-layer sample reinforced that fewer thermal cycles in the top layers contributed to increased microhardness.

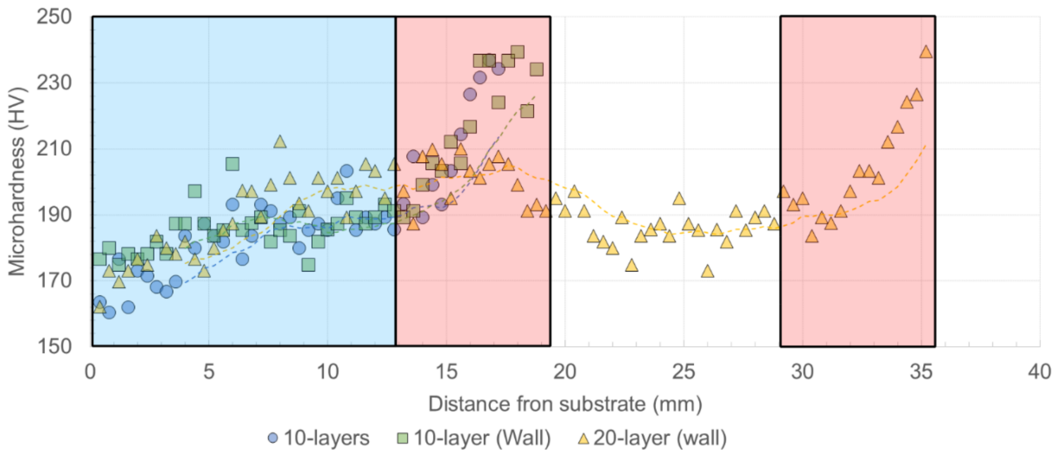

Figure 96. Microhardness comparison of 10-layers U-shape, 10-layers wall, 20-layers wall

These findings contrast with those reported by Rosli et al. [245], who observed higher microhardness at both the bottom and top regions of WAAM components. A critical factor influencing this divergence is the base plate thickness, as highlighted by Laghi [246]. Rosli et al. used a 9 mm thick base plate, while this study utilized a 3.3 mm plate, which had an average hardness of 150 HV. The relatively soft base plate used in this study significantly influenced the mechanical properties of the lower layers, presenting insights into the substrate's heat sink effect and its role in grain growth and hardness reduction. This provides a better understanding of how different heat exchange paths affect the mechanical characteristics of the deposited material.

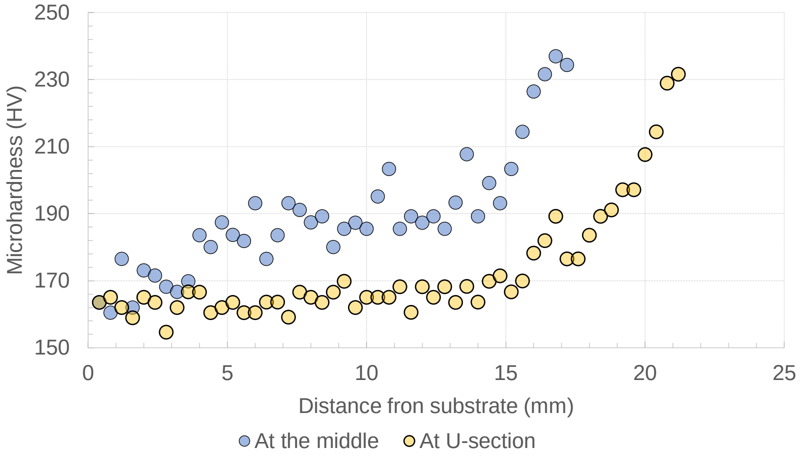

Figure 97. Microhardness of U-shape sample at different locations.

The U-shaped deposition samples provided an opportunity to analyze the microhardness values across different regions, particularly the center and the U-section. Despite a noticeable 60°C temperature difference between the left and right sides depositions due to pre-heating effects, no significant variation in microhardness was observed in these areas. This finding underscores that the thermal influence alone did not substantially affect the material's mechanical properties in this context. Figure 97 depicts the microhardness values at the center and the U-section of the U-shaped sample. While the material fed into the deposition zone is consistent across the structure, the geometry of the U-shape introduces unique mechanical and thermal dynamics. In the U-section, the inner and outer side of the deposited material experiences slightly different material spreading, this discrepancy results from the varying torch interaction times due to the curved geometry of the deposition path. These conditions induce current fluctuations, as previously highlighted, which in turn affect the microhardness profile. Inconsistent torch interaction times and current fluctuations led to a reduction in microhardness. The observed microhardness variations across the U-shaped sample were approximately 20 HV, corresponding to 10% below. This diminished microhardness in the U-section is likely linked to the mechanical stresses and thermal gradients introduced during the deposition process. These findings reinforce the importance of considering deposition geometry and its influence on process parameters and material properties in WAAM. The U-shaped deposition provided valuable insights into how localized stresses and variations in thermal exposure can impact the mechanical characteristics of the deposited material, even when the overall material and feed rate remain constant.

5.6 Ts and WFS effect on material properties of multi-layer walls

In this section, an experimental plan was designed to investigate the effects of Ts and WFS on the WAAM process, building on findings from previous studies. These earlier experiments established that Ts and WFS significantly influence the geometry and material properties of the deposited beads; however, those experiments were limited to single-bead analyses. The current study aims to address additional questions: How do variations in Ts and WFS affect current, voltage, and temperature profiles? How do these temperature changes influence the resulting microstructure and hardness of the deposited material?

Table 30. Process parameters [Ts & WFS]

Travel speed [mm/min]	Wire feed speed [mm/min]
250	3900
500	5800
750	
1000	

To explore these aspects, multi-pass wall structures were deposited with 10 layers in a two-way deposition strategy. Only Ts and WFS were altered, as outlined in Table 30, while other process parameters remained constant: P (2.9 kW), SOD (10 mm), shielding gas flow rate (0.7 bar), and a dwell time of 2 minutes and 30 seconds using forced air cooling to maintain substrate temperatures below 50°C. The experimental samples and their cross-sections are shown in Figure 98. The results demonstrated that Ts had a substantial impact on the geometry of the deposited walls. As Ts increased, the bead height and width were significantly reduced due to less material being deposited per unit length. This was attributed to the shorter interaction time at higher travel speeds. WFS exhibited a comparatively smaller effect (visually) on bead geometry due to the narrower range of variations tested. However, an increased WFS introduced more material into the melt pool, resulting in wider and taller beads, while a lower WFS reduced material deposition, leading to narrower and thinner beads. Cross-sectional analysis further revealed that at higher Ts and WFS, the depositions became less uniform. These irregularities likely result from the combined effects of faster cooling rates at higher Ts and the increased complexity of maintaining a stable melt pool at higher material input rates. This indicates that while higher WFS can compensate for reduced material deposition at higher Ts to some extent, achieving a balance between these parameters is essential for ensuring uniformity and consistent material properties in WAAM-produced structures.

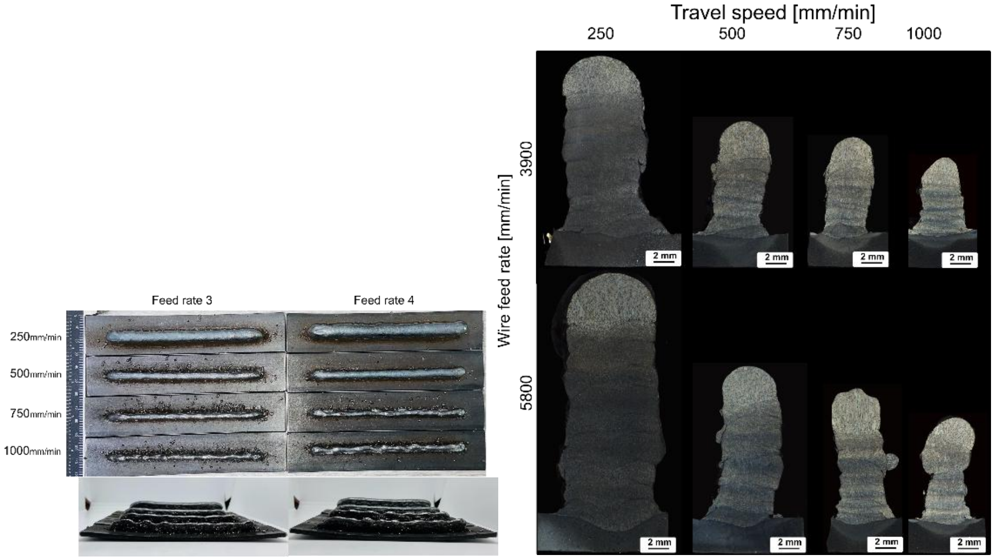

Figure 98. Macrograph of the experimental samples after deposition: (a) top and side view and (b), Cross-sectional images.

Results and discussion

During the process, current and voltage were continuously monitored. As established in earlier sections, current fluctuations are a common observation, while voltage remains constant during deposition. These fluctuations are influenced by bead regularity and arc stability, which are dictated by process parameters such as Ts and WFS. A deeper examination of power flow (Current and voltage) under different Ts and WFS conditions was undertaken. Figure 99a illustrates the power supplied at low Ts (250 mm/min) and low WFS (3900 mm/min), which showed the highest power drop among all conditions, as summarized in Figure 99c. Initially, power was higher during the first layer deposition, due to the flat substrate geometry providing lower electrical resistance. As layers accumulated, power stabilized, reflecting the influence of changing substrate geometry. The recorded power drops revealed a maximum decrease of 10.4% at low Ts and low WFS, with average power dropping from 2.6 kW in the first layer to 2.3 kW after three layers. Across all tested conditions, power drops consistently ranged between 5% and 8%, underscoring a predictable trend across varying deposition setups. Figure 99b further confirms that average power increased proportionally with higher Ts and WFS. Increased WFS required higher power to provide sufficient heat for melting, while higher Ts, reducing heat input per unit length, similarly demanded increased power to maintain energy balance.

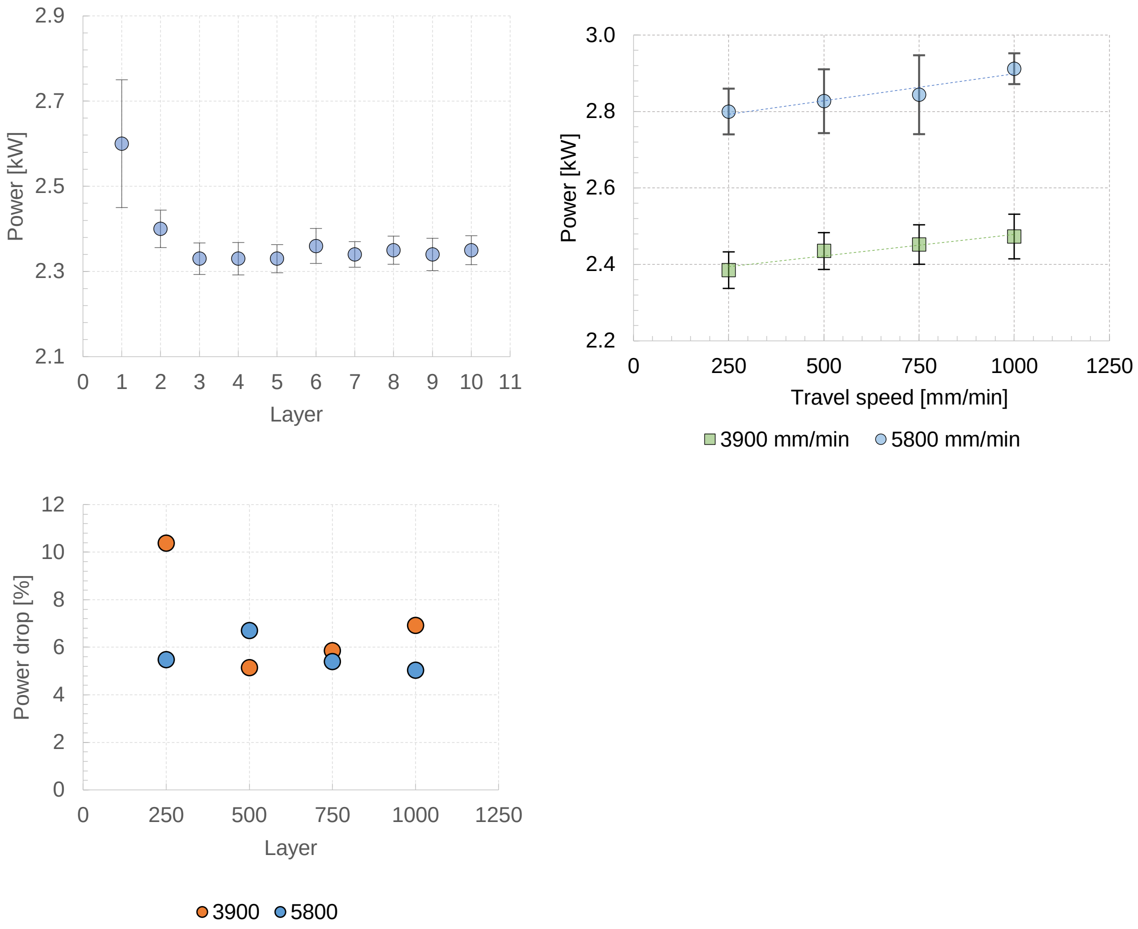

Figure 99. a). Power variation of 250-3900 sample, b) WFS effect on power flow, c). percentage of power drop

After the deposition process, the bead height was measured to assess the geometry and consistency of the deposited layers. The average layer height for each sample was calculated by dividing the total height of the 10-layer sample by the number of layers, as shown in Figure 100.

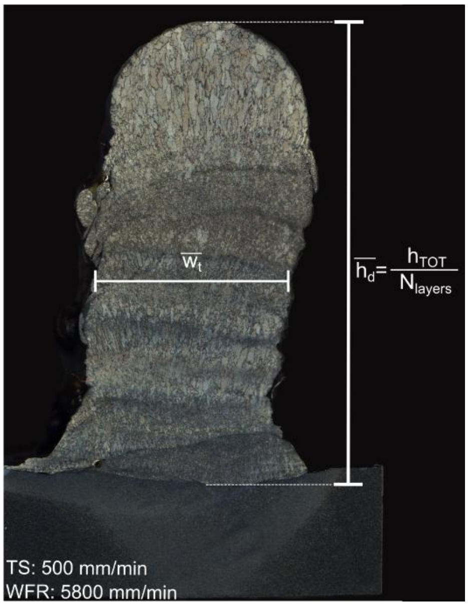

Figure 100. Measurements of geometric cross section characteristics: average deposition height ($\overline{h}_d$*) and average experimental width (*$\overline{w}_e$*)*

Further geometric analysis, including the average deposition height and width for each sample, is presented in Figure 101a & c, indicating that the layer height decreased logarithmically with increasing Ts. This behavior is explained by the reduction in material deposition as Ts increases. With a constant WFS, higher Ts reduces the interaction time, resulting in a lower volume of material being deposited per unit length. Additionally, WFS had a significant impact on the cross-sectional geometry of the bead. The vertical cross-sectional area of all sectioned samples was measured and depicted in Figure 101b. This also showed a logarithmic decrease with increasing Ts. This trend further emphasizes the interplay between material flow, deposition speed, and bead geometry. The aspect ratio of the deposited beads, calculated as the ratio of average bead height to bead width, ranged between 23% and 31%, as shown in Figure 101d. These measurements underline the importance of balancing Ts and WFS to achieve desired geometric consistency. The relationship between Ts, WFS, and deposition geometry can be predicted based on mass conservation principles, as detailed in Figure 102. The inverse of Ts corresponds to the time needed to cover a unit length, and the amount of deposition material cross-sectional area (DMCS) can be derived by multiplying this time by WFS and the wire's cross-sectional area (WCA).

$$DMCS = \frac{1}{T_s} \cdot WFS \cdot WCA$$

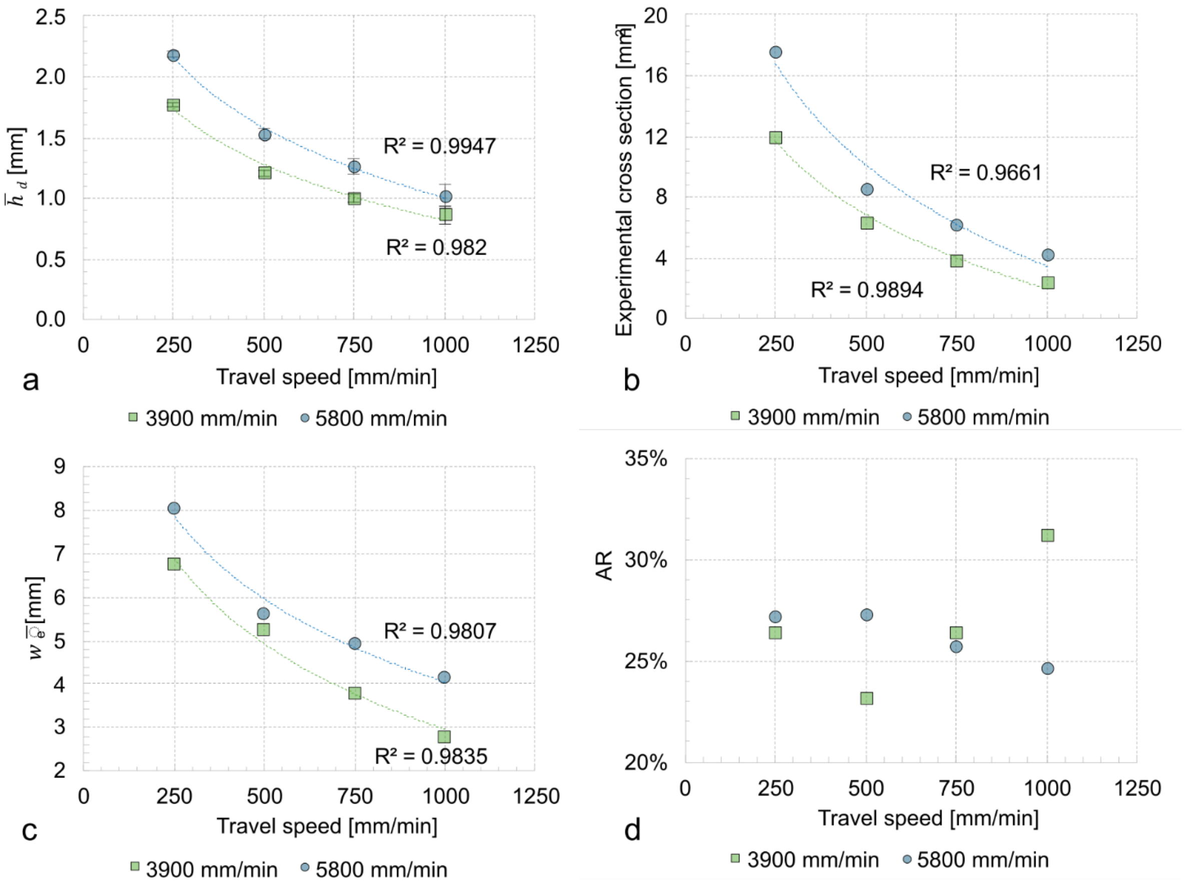

Figure 101. a). Average deposition layer height of the samples, b). Experimental cross section, c). Experimental average width, d). Aspect ratio.

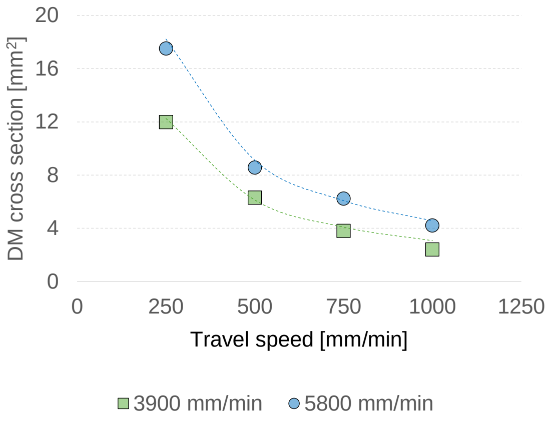

Figure 102. Cross sectional area per unit length

One of the primary concerns for industries, alongside part quality and production time, is material efficiency, which is closely tied to production costs. This relationship is dictated by the buy-to-fly ratio, a term that describes the amount of material wasted during manufacturing relative to the final part weight. High material waste not only increases production costs but also raises environmental concerns, particularly if the by-products or residues generated during the process are not properly managed or recycled. Unprocessed waste can contribute significantly to industrial pollution, adding another layer of complexity to sustainable manufacturing practices. To assess material efficiency in the context of WAAM, calculations were performed on sectioned samples of deposited wall-like structures. A rectangular region encompassing the useful deposited material was defined for this purpose, as shown in Figure 103a. This illustration clearly differentiates the material volume before and after machining. By comparing these volumes, the material efficiency of each deposition condition was determined, and the results are presented in Figure 103b.

The material efficiency for all tested conditions ranged between 60% and 80%, which is approximately twice the efficiency of conventional manufacturing techniques. In traditional subtractive methods, material efficiency typically falls between 30% and 50% [247], as large amounts of material are removed to achieve the desired geometry. While this comparison highlights WAAM's significant advantage in material conservation, it must be noted that AM technologies, including WAAM, inherently excel in material efficiency due to their layer-by-layer deposition strategy, which adds material precisely where needed. However, the material efficiency of WAAM remains lower compared to some other AM techniques. This is largely due to high material deposition rates and surface waviness, which necessitate additional machining to meet surface finish and tolerance requirements. Material removal in WAAM is often limited to these secondary processes rather than extensive reshaping, as is common in subtractive manufacturing. A brief discussion of WAAM's material efficiency advantages and limitations was provided earlier in the introduction section 1.3. Despite these limitations, the results reaffirm WAAM's role as a transformative manufacturing process that significantly reduces waste, aligning with industrial goals of cost reduction and environmental sustainability.

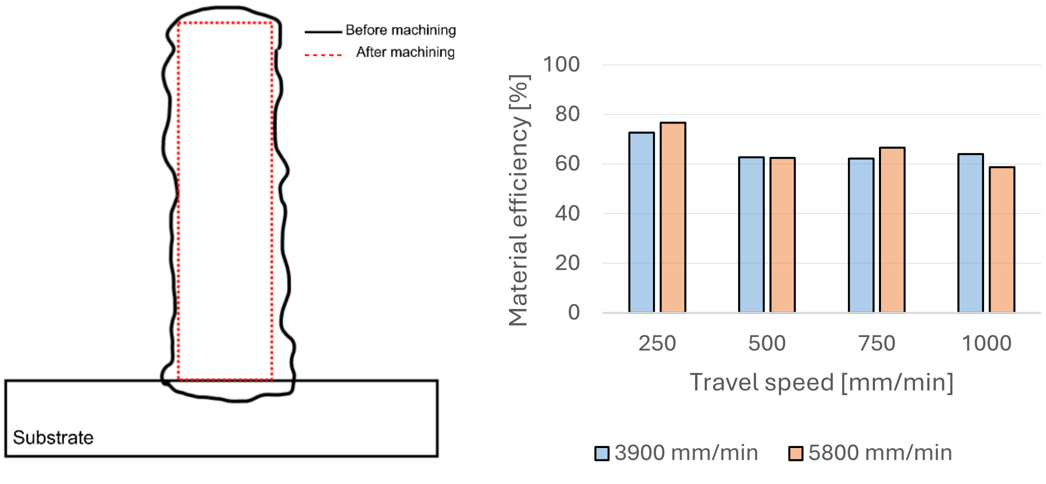

Figure 103. Material efficiency

Figure 104 illustrates the temperature evolution at the 5th layer for each tested deposition condition, highlighting the significant influence of Ts and WFS on the cooling rates. Faster Ts resulted in more rapid cooling rates due to reduced interaction time, which limited heat input and energy absorption by the deposited bead. In contrast, slower Ts, which involved longer interaction times, increased the energy supplied and the material deposited, enhancing thermal inertia of the bead. These combined effects prolonged the cooling process under slower travel speeds. A distinct temperature difference between the samples produced with WFS = 3900 mm/min and WFS = 5800 mm/min is also evident. Samples deposited at the higher WFS demonstrated slower cooling rates, attributed to increased thermal inertia due to the larger volume of material introduced into the melt pool. This underscores how both travel speed and wire feed rate interact to influence the thermal dynamics of the deposition process. The link between these cooling rates and material properties such as microhardness, strength, and toughness is critical, as cooling rates directly affect microstructural evolution. While peak temperature establishes conditions for phase transformations during solidification, it is the cooling rate that predominantly determines the resultant microstructure (e.g., martensitic, bainitic, or ferritic), which, in turn, defines the material's mechanical characteristics. Grain size is also indirectly influenced by these thermal conditions, as slower cooling promotes grain coarsening, while faster cooling tends to refine grains.

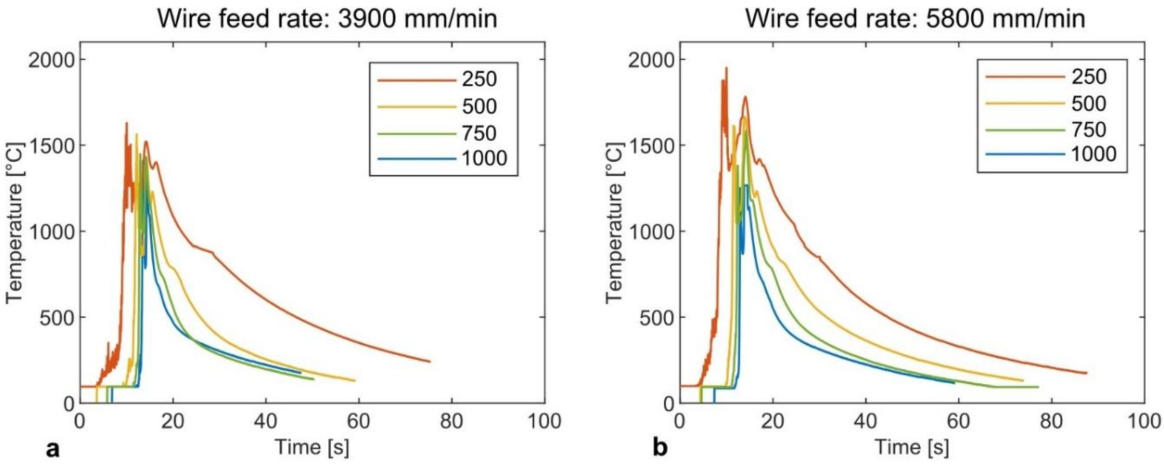

Figure 104. IR plots of the temperature distribution during deposition of different Ts with WFS at a). 3900 mm/min, b). 5800 mm/min.

To quantify cooling behavior across deposition conditions, the temperature variation (dT/dt) was measured, where T2 represented the peak temperature and T1 was set at 400°C, with t1 and t2 denoting their respective times. Figure 105 illustrates these measurements, with detailed temperature variation data provided in Figure 106.

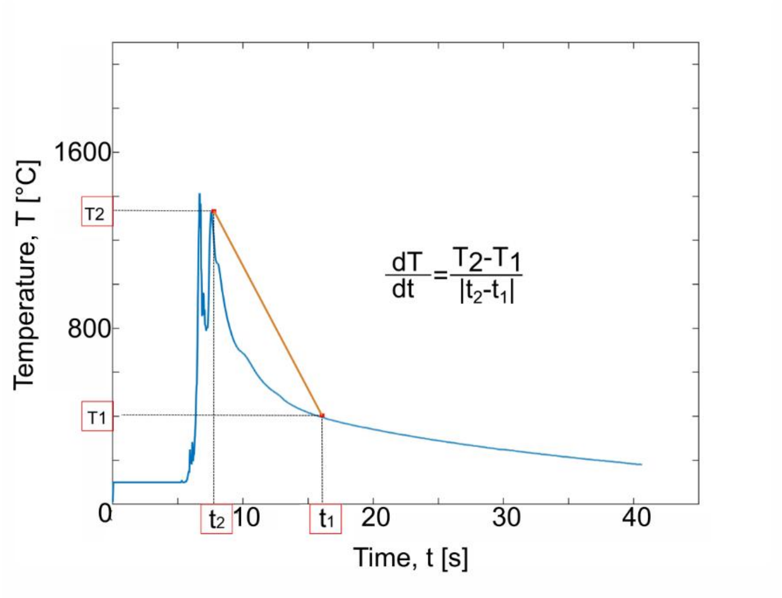

Figure 105. Schematic of thermal gradient determination

For samples deposited at low travel speed (250 mm/min), temperature variations across wire feed rate conditions remained nearly constant. However, at higher travel speeds (500, 750, and 1000 mm/min), temperature variation increased with layer number, peaking at the sixth layer for WFS = 3900 mm/min before declining. Irregular temperature variations were observed beyond the fourth layer for samples deposited with WFS = 5800 mm/min at Ts = 1000 mm/min, likely due to instability in the deposited beads.

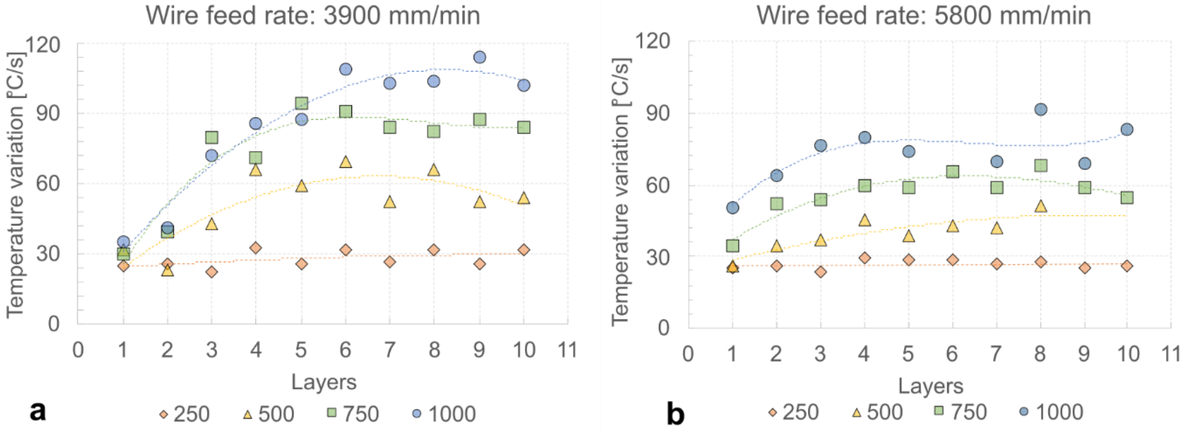

Figure 106. thermal gradient at different Ts, and WFS at a). 3900 mm/min, b). 5800 mm/min

Figure 107 presents the average temperature variations across all 10 layers for each sample, confirming that samples deposited at WFS = 5800 mm/min experienced lower temperature variations compared to WFS = 3900 mm/min. This emphasizes the role of thermal inertia and interaction time in governing cooling rates. An interaction effect between Ts and WFS was also observed, at low travel speeds, temperature variations were consistent at approximately 27°C/s, regardless of WFS. At higher travel speeds (Ts = 1000 mm/min), samples deposited with WFS = 3900 mm/min exhibited higher temperature variations (85°C/s) compared to those with WFS = 5800 mm/min (73°C/s). A substantial increase in temperature variation was noted as Ts rose from 250 mm/min to 1000 mm/min, amounting to a 315% increase for WFS = 3900 mm/min and a 270% increase for

WFS = 5800 mm/min. These results highlight the intricate interplay of Ts and WFS in controlling the thermal profile during deposition, which directly influences material properties and structural integrity in WAAM applications.

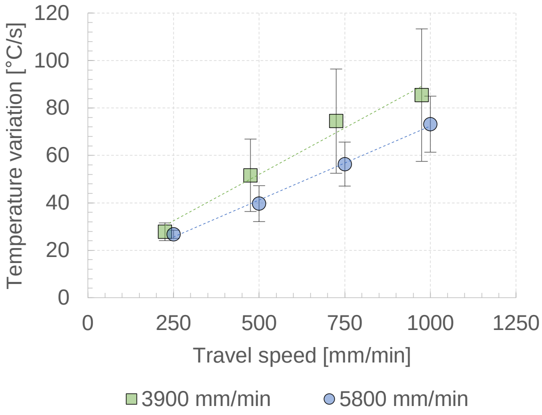

Figure 107. Average thermal gradience of each sample

Microstructural analysis was performed on the samples produced under all experimental conditions to evaluate the metallographic structure evolution. Figure 108 indicates the reference locations where microstructural observations were made, revealing how the process parameters influenced grain morphology and mechanical properties. As noted in the chemical composition of the materials, the substrate contained a slightly higher carbon percentage compared to the feed wire material, contributing to localized differences in microstructure.

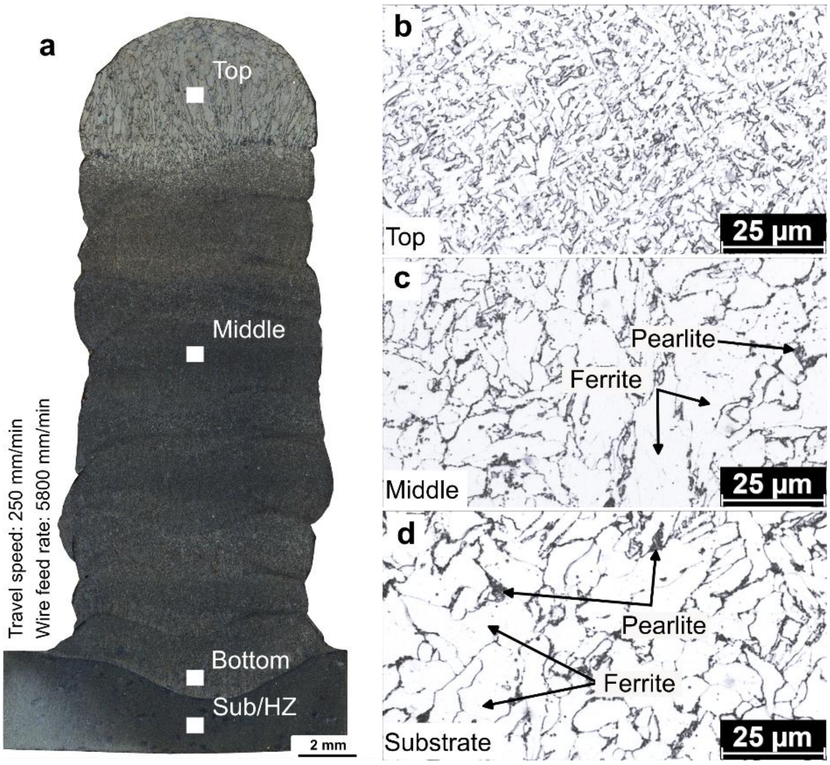

Figure 108. a). Grain size measurement locations, b). microstructure at the top, c). Middle, & d). Substrate/HZ.

Figure 108c&d illustrate pearlite and ferrite microstructures, with pearlite formation typically occurring under slower cooling rates. During rapid cooling, cementite formation is limited, and it spreads sparsely along the grain boundaries. For instance, Figure 108b&c, which share the same chemical composition as the feed wire, show distinct differences. The top region (Figure 108b) underwent rapid cooling, while the middle region experienced multiple heating cycles and slower cooling [248]. At higher travel speeds, the presence of pearlite was significantly reduced, becoming evenly distributed along the grain boundaries due to the accelerated cooling process.

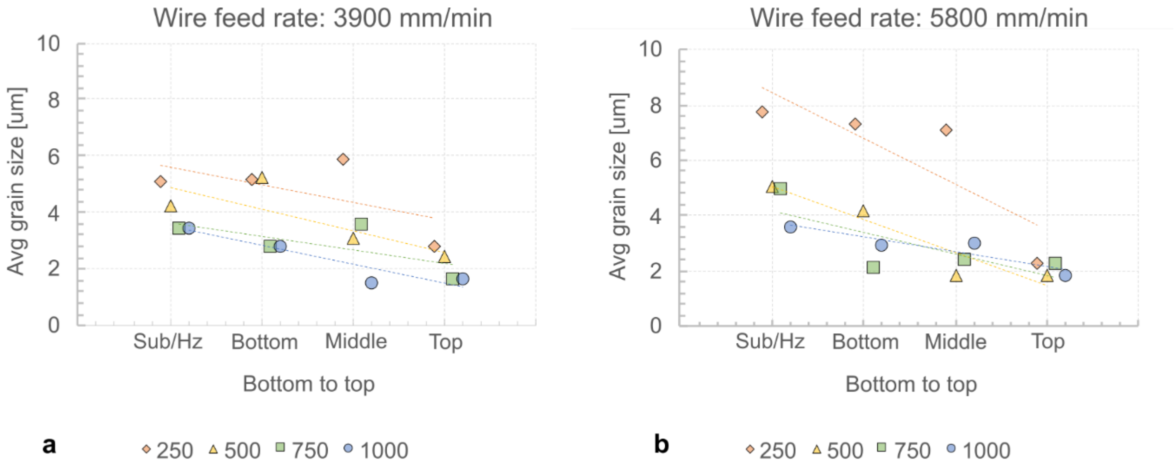

Figure 109. a). The average grain size of material feed rate 3900 mm/min, and b). material feed rate 5800 mm/min.

Figure 109 illustrates the average grain size across different sample regions, while Figure 110&Figure 111 present 1000X optical microscope images for samples deposited at WFS = 3900 mm/min and 5800 mm/min, respectively. The analysis shows that samples produced at WFS = 3900 mm/min exhibit smaller average grain sizes, ranging from 1–6 µm, compared to 1–8 µm for samples produced at WFS = 5800 mm/min. This difference is attributed to the slower cooling rates at higher wire feed speeds, which allow grains to grow larger due to prolonged thermal exposure. Grain size consistently decreased from the bottom to the top of the samples. Higher travel speeds also contributed to finer grain structures, where the top layers deposited at faster travel speeds exhibited the smallest grains due to the sharper thermal gradients and faster cooling rates. The WAAM samples showed a mixed microstructure of columnar and equiaxed grains [248]. Near the substrate and in the heat-affected zone, equiaxed grains dominated, while the proportion of columnar grains increased with the deposition height. This transition results from the thermal gradients and heat flow direction during deposition.

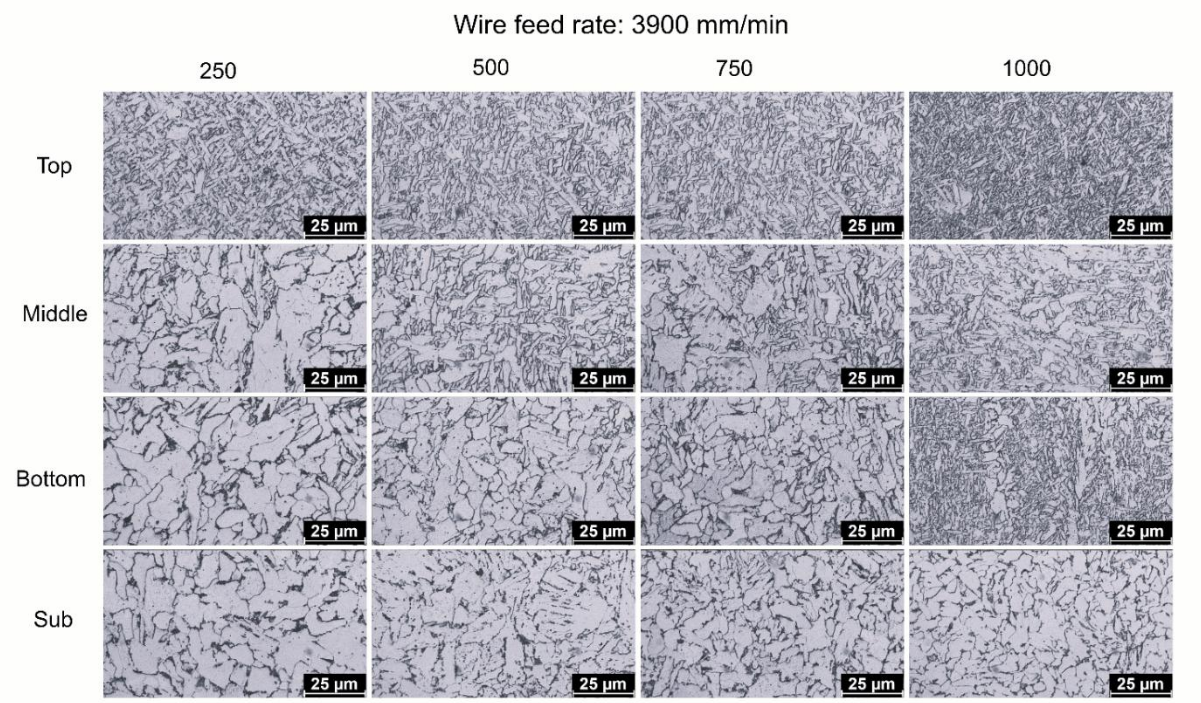

Figure 110. Microstructure of various Ts (250,500,750, &1000 mm/min) at WFS = 3900 mm/min

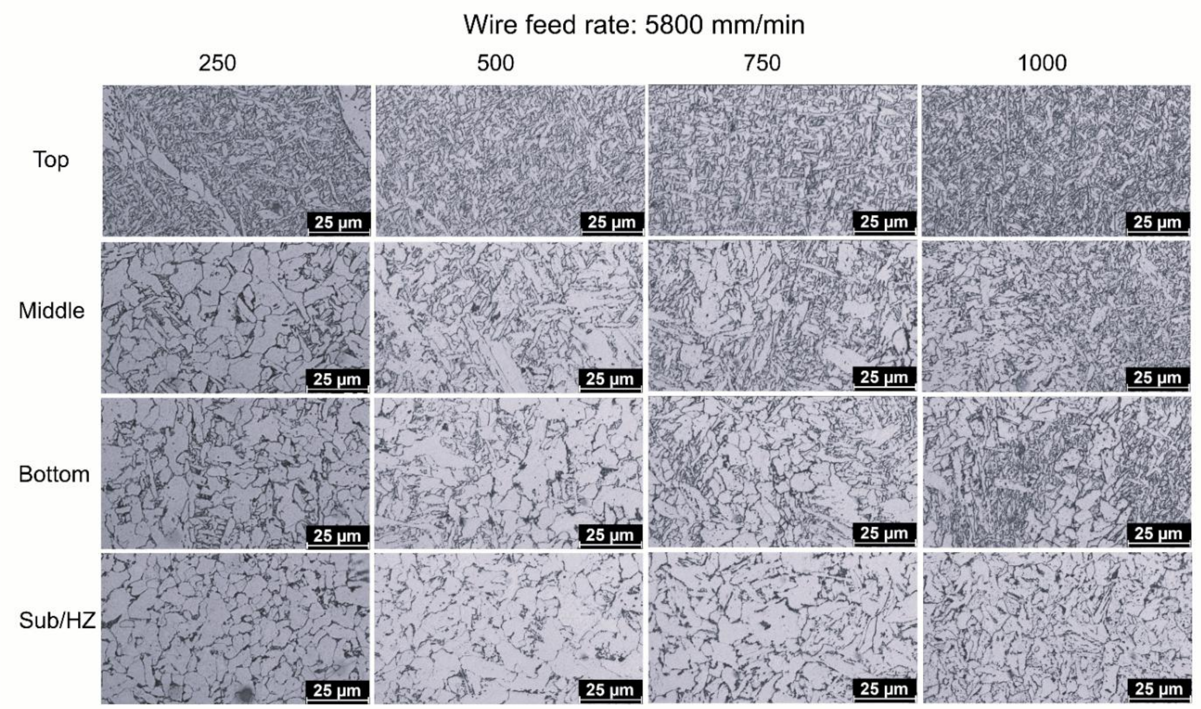

Figure 111. Microstructure of various Ts (250,500,750, &1000 mm/min) at WFS = 5800 mm/min

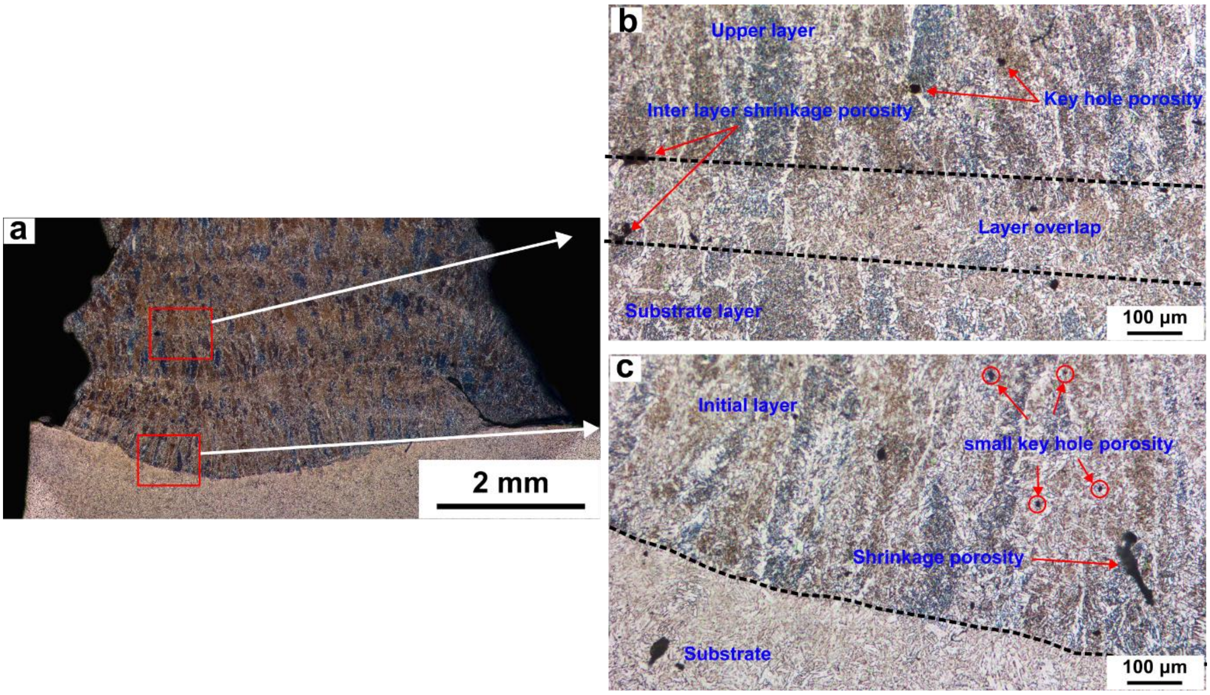

Figure 112. microstructure and defects at interaction zones in WAAM samples

During material deposition in the WAAM process, the deposited material undergoes a series of complex and simultaneous phenomena, including heat conduction, phase transformation, melt-pool dynamics, and vaporization effects [249]. These dynamic interactions play a pivotal role in determining the microstructural and mechanical properties of the final build. As previously mentioned, solidification begins at the substrate due to heat conduction. Given the anisotropic nature of crystalline growth, small nuclei form and grow energetically in favorable directions, often aligned with the deposition direction [250]. This process results in tree-like dendritic structures, as depicted in Figure 112c. These structures emerge due to the temperature gradients and directional solidification, which are characteristic of high-energy deposition processes like WAAM. As subsequent layers are deposited, an overlapping zone is formed between layers. This zone exhibits a distinct microstructure compared to the individual layers, primarily due to the repeated thermal cycles and material mixing that occur during deposition. Figure 112b illustrates this interaction zone, highlighting areas of microstructural variation and potential defects. The overlapping regions are particularly sensitive to imperfections, as they experience both thermal and mechanical stresses during layer addition. WAAM's layer-by-layer deposition involves the melting of feed wire into droplets, which subsequently interact with the melt pool. These droplets create ripples in the melt pool due to surface tension and dynamic flow, a phenomenon that directly impacts the uniformity of the deposited material. Improper melt flow and inconsistent droplet interaction can lead to defects such as keyhole porosity, and shrinkage. These defects are especially frequent near the overlay zones, where complex interactions between successive layers occur [251]. Figure 112 highlights several observed defects in this study, emphasizing the critical need to address melt-pool dynamics and interlayer interactions for quality improvement. For instance, keyhole defects can form due to unstable melt flow, trapping gas bubbles or creating voids within the deposited material. Similarly, ripples and surface irregularities may lead to stress concentration points, which can compromise the structural integrity of the final component. These observations underline the necessity for advanced monitoring techniques and process optimization to mitigate defects and ensure the reliability of WAAM-fabricated parts.

Microhardness analysis, presented in Figure 113&Figure 114, further confirmed the grain size's impact on mechanical properties. According to the Hall-Petch relationship [252], smaller grain sizes enhance mechanical strength by providing more grain boundaries, which impede deformation under load [253]. Samples produced at higher travel speeds displayed higher microhardness due to the smaller grain sizes formed under rapid cooling. The top layers consistently exhibited peak microhardness because they underwent the most severe thermal gradients and cooling rates, forming lamellar grains. These layers were also free from repeated thermal cycling, unlike the lower layers, which experienced thermal annealing effects. The microhardness distribution revealed a predictable trend, with the lowest values near the substrate and a linear increase moving upward. A saddle-shaped distribution was observed in the middle layers, where the microhardness stabilized due to competing effects of thermal gradients and reheating from subsequent layers. Towards the top layers, microhardness increased again as thermal cycling diminished. Across all samples, the substrate's microhardness remained consistent, but higher energy deposition conditions (characterized by increased WFS and thermal inertia) resulted in slightly lower average and peak microhardness values. These findings highlight the complex interplay between process parameters, thermal effects, and material properties in WAAM.

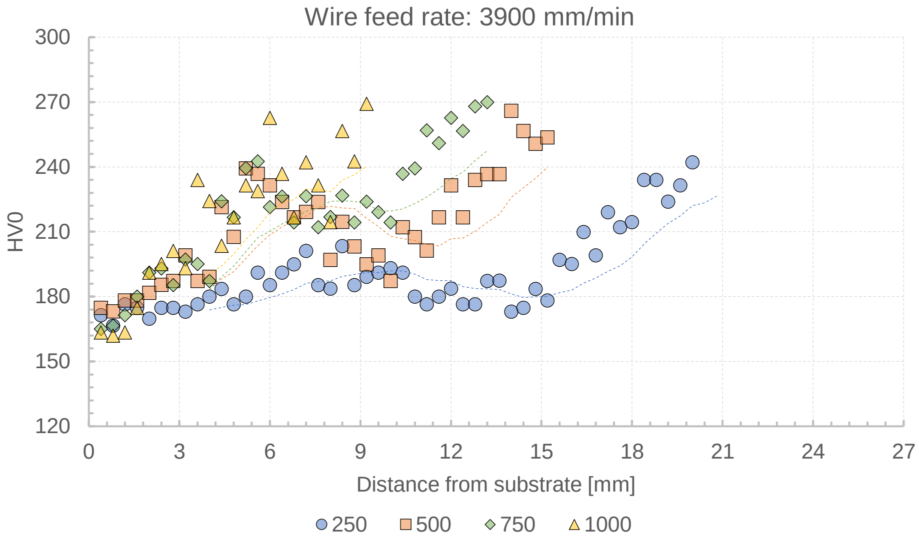

Figure 113. Microhardness of various Ts (250,500,750, and 1000 mm/min) at WFS = 3900 mm/min

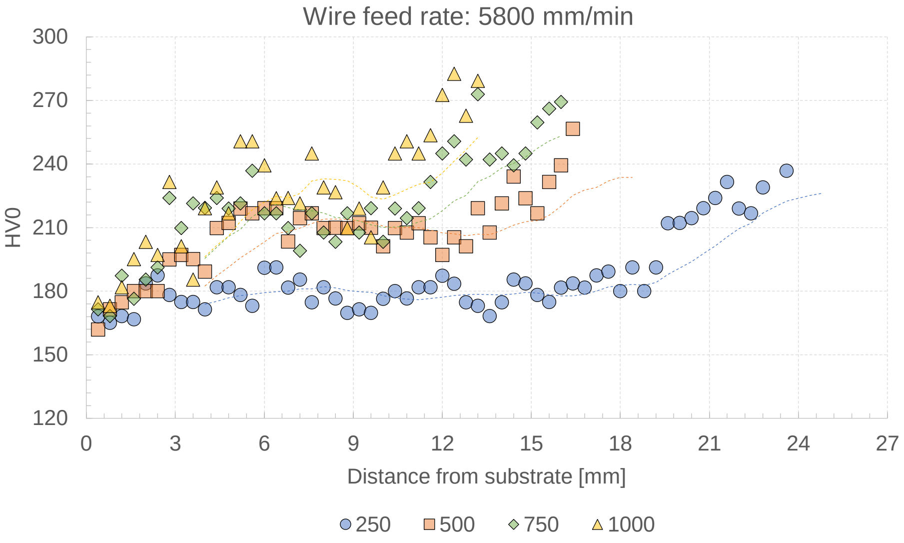

Figure 114. Microhardness of various Ts (250,500,750, and 1000 mm/min) at WFS = 5800 mm/min

5.7 Finding overhanging angle

Each manufacturing process adheres to specific parameters, encompassing aspects such as process optimization, material selection, and material property enhancement. While these parameters have seen considerable progress, researchers and manufacturers worldwide are still working to establish comprehensive frameworks for certain aspects of AM. One such critical parameter is the overhanging angle [254], a measure of the inclination angle of the deposited material relative to the deposition direction that can be fabricated without requiring external support structures beyond the previously deposited layer. In traditional AM processes, the maximum overhanging angle typically remains below 45° for most vertically deposited components, as supported by studies from [255], [256], [257]. This limitation arises due to the geometry and material behavior during deposition. However, AM processes can overcome this constraint by introducing support structures for overhanging regions. These supports stabilize the material during fabrication but require post-processing for removal, which can lead to increased costs, time, and potential issues with part integrity. The WAAM process, being distinct in its energy intensity and material deposition method, introduces additional challenges. WAAM struggles to utilize support structures for overhanging angles because the high energy involved often results in excessive material penetration, making it difficult or impossible to remove supports without affecting the part's functionality. Consequently, designers must optimize the part geometry in accordance with WAAM's capabilities, taking into account the specific constraints and thermal dynamics of the process. Moreover, as WAAM is a high-energy process, the overhanging angle can be directly influenced by the elevated temperatures generated during deposition. These thermal gradients can affect material flow and structural stability in overhanging regions. Advanced techniques, such as employing machines with greater degrees of freedom, have been developed to mitigate this issue. These machines can tilt the deposition head, aligning it with the inclination angle to achieve stable material deposition. However, tilting the head from a vertical to a horizontal position in multi-directional WAAM deposition introduces its own set of challenges, particularly in maintaining droplet transfer accuracy due to the effects of gravity [68]. Lei Yuan et al [68]. investigated this multi-directional deposition method and successfully demonstrated the fabrication of overhanging features without requiring additional support structures. Their work highlights the potential for innovative deposition strategies to expand the design possibilities of WAAM while addressing inherent challenges associated with overhanging angles.

To calculate the overhanging angle, a layer shift strategy was implemented based on the method described by Baffa et al. [41]. This strategy involved depositing 10 layers with incremental shifts between 0.5 and 2 mm per layer, under two different Ts of 250 and 500 mm/min. The process parameters were kept constant throughout, a WFS of 5800 mm/min, P of 2.9 kW, Sod of 10 mm, and shielding gas flow rate of 0.7 bar. The experimental results, shown in Figure 115, differentiate between successful samples (green) and failed samples (red), providing a clear visual representation of outcomes.

The inclination angle was derived using the following equations, which relate the geometry of the deposition to the angle:

$$Slope = \frac{Deposition\ Height}{Total\ layer\ shift}$$

$$Inclination\ angle = 90 - \left(Tan^{-1}(slope)\right)$$

The experiments revealed critical dependencies of the inclination angle on the deposition conditions. For samples deposited at 250 mm/min, a layer shift exceeding 1.5 mm resulted in failure after the fourth layer due to excessive heat accumulation, leading to material collapse. In contrast, at 500 mm/min, the thinner beads prevented stable deposition for layer shifts beyond 0.75 mm. These results highlight the influence of travel speed on both the inclination angle and the structural integrity of the deposited layers. At a travel speed of 250 mm/min, the maximum successful inclination angle was achieved with a 1 mm layer shift, producing an angle of 31.3°. Similarly, for a travel speed of 500 mm/min, successful inclination angles were recorded at 17.2° and 31.6° for layer shifts of 0.5 mm and 0.75 mm, respectively. These findings align with the results from Evjemo et al. [258], who observed that the application of layer shifts impacts the geometric and structural consistency of the layers. Vertical depositions without layer shifts maintain consistent height, but shifted layers exhibit reduced height due to incomplete overlap, leading to shrinkage.

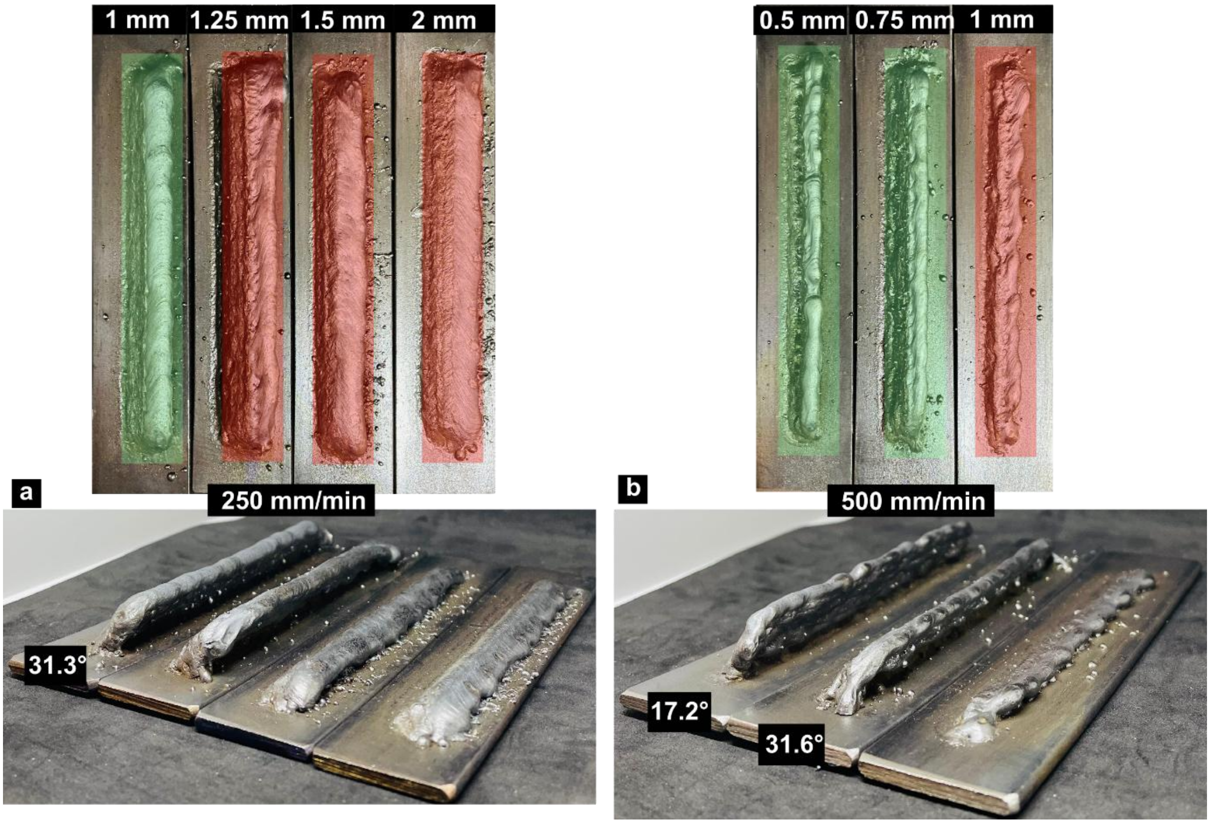

Figure 115. Finding inclination angle, a). at 250 mm/min, b). at 500 mm/min

A comparison was also made between the deposition heights of straight wall samples from earlier experiments and the inclined samples produced with layer shifts. The data revealed a height reduction of up to 30% in inclined samples, with the extent of reduction correlating to the magnitude of the layer shift. For instance, at a travel speed of 500 mm/min, a 0.5 mm layer shift resulted in a height reduction of approximately 10%, whereas a 0.75 mm shift caused a reduction of 30%. These observations emphasize the significant interplay between layer shifts, travel speed, and the resulting deposition geometry.

5.8 Defects

During the WAAM process, several defects were observed in the fabricated samples. Porosity concentrations were found near the outer surfaces of the deposited material, as shown in Figure 116a. The porosity inside the melt pool forms during deposition and attempts to escape to the top as the material begins to solidify. Since the cooling process in WAAM starts from the bottom layer, the upward escape of gas bubbles is influenced by the temperature gradient and the viscosity of the molten material. At higher temperatures, molten material has a lower viscosity, facilitating the movement of gas bubbles. However, as cooling progresses and viscosity increases, some pores are unable to reach the surface and become trapped near the border, leading to the observed porosity distribution. Cai et al. [225] identified a trend in porosity behavior relative to current levels, noting that porosity initially decreases and then increases with rising current. This relationship highlights the complex dynamics of melt-pool behavior and gas entrapment under varying electrical parameters. Despite employing forced air cooling in the present study, it had no observable effect on porosity levels since it was applied post-deposition, at which point the material had already solidified, locking in the existing porosity distribution. Other defects such as spatter, shrinkage, and macro- and micro-cracks were also evident in WAAM samples (Figure 116). Spatter defects, commonly found on the lateral surfaces, occur when small droplets of molten material are ejected from the melt pool during deposition and subsequently solidify on the sample surface. These defects result in rough surfaces and can weaken structural integrity by creating weak points susceptible to stress. The presence of both small and large spatter particles further illustrates the challenges of maintaining melt-pool stability during the deposition process. Shrinkage defects, depicted in Figure 116c, arise due to improper material flow within the melt pool. Bidare et al. [259] highlighted that shrinkage defects significantly compromise the density and mechanical properties of WAAM parts. Moreover, these defects serve as foundations for crack initiation under high-stress conditions. Compared to gas porosity, shrinkage defects are more critical as they feature sharp corners, which act as stress concentrators, unlike the rounded edges of gas porosity defects [260]. The presence of shrinkage not only undermines the structural integrity of the part but also propagates cracks when subjected to cyclic or tensile stress. Microcracks were another critical defect observed, as shown in Figure 116d, which highlights the cracks using image processing techniques such as edge detection. A specific occurrence of a microcrack was identified in a U-shaped sample, located at the U-section, inner side. This region experiences high thermal gradients and residual stresses during deposition, which promote crack formation. Microcracks, although initially small, can grow under thermal or mechanical loads, compromising the part's durability and performance.

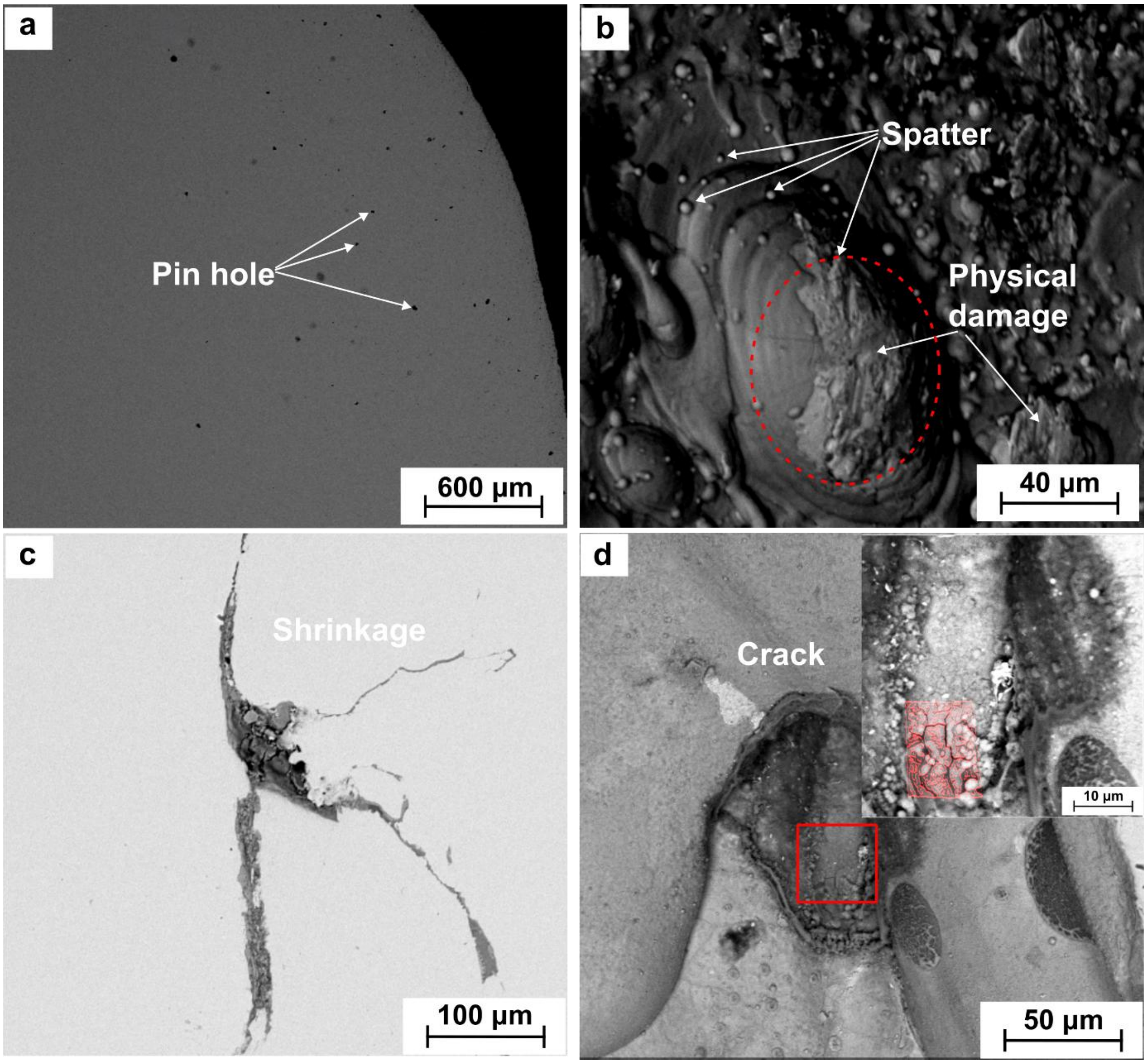

Figure 116. WAAM defects

On the surface of the WAAM samples, a distinct thin layer was observed, as illustrated in Figure 117. Sen Li et al. [261] similarly reported the formation of a thin nitride layer on WAAM samples. This phenomenon is attributed to reactions at elevated temperatures where oxygen from the shielding gas or atmospheric environment interacts with the molten pool and melt droplets, forming an oxidation layer on the surface [262], [263]. These interactions lead to the formation of oxides, which affect the surface properties of the manufactured parts. Typically, pure argon is employed in the WAAM process to minimize oxidation, but its use can compromise arc stability. According to Yamaguchi et al. [44], even with pure argon, a thin oxidation layer can still develop, although it is less pronounced than when using mixed shielding gases, such as argon with small percentages of oxygen ($Ar+O_2$). This layer's formation highlights the difficulty in completely isolating the molten material from environmental interactions during deposition, even with optimized shielding practices. The thin layer observed on the WAAM samples in this study is likely an oxide layer primarily composed of iron oxides (FeO, Fe_2O_3). These oxides form due to the oxygen present in the ambient environment or potential leaks in the shielding gas coverage during the process. Imperfections in shielding gas flow or coverage can exacerbate oxidation, particularly at high temperatures, where molten material is more reactive.

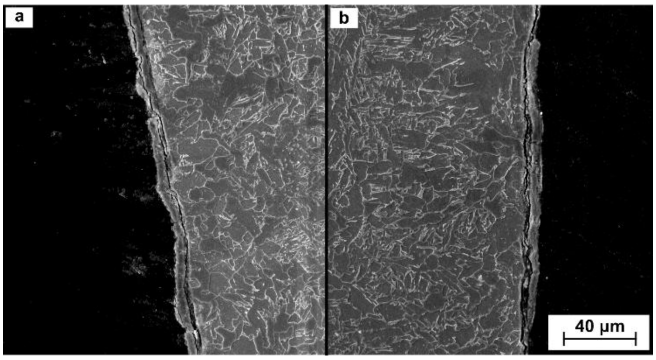

Figure 117. A thin layer of oxidation

5.9 G-code modification and part realization

Process planning is a critical step in WAAM, encompassing the systematic design and optimization of deposition paths, material properties, and operational parameters to achieve the desired manufacturing objectives[264]. While WAAM has demonstrated remarkable capabilities in producing large-scale industrial components, its full integration into mainstream industries faces significant hurdles. One of the most pressing challenges is the high cost and limited accessibility of commercial software solutions. WAAM Planner, Gefertec's 3DMP, and MX3D's MetalXL platforms are while effective, often fall short in addressing the diverse needs of research institutions and manufacturers. As a result, many academic and industrial researchers opt to develop in-house software, which offers greater flexibility, precise control, and cost efficiency.

Ferreira et al. [264] demonstrated this approach by creating an open-source software platform for WAAM process planning using the Scilab environment. The software's graphical interface supported fundamental operations like importing, part orienting, slicing, path planning, and exporting G-code. However, the platform also required users to account for overhanging angles, a key factor determining part rotation during the deposition process. Despite its potential, Ferreira et al. study did not extensively address the limitations posed by overhanging angles. Furthermore, Lam et al. [254] devised an innovative algorithm to address overhanging angles. Their data-driven interpolation method, termed adaptive process control, enabled the adjustment of travel speeds to maintain uniform layer thickness in overhanging regions. This technique successfully achieved open-loop deposition of parts with overhanging angles ranging from 0° to 37.5°, underscoring the importance of precise trajectory planning in WAAM. Another critical factor influencing WAAM part quality is residual stress, which is directly impacted by the deposition path strategy. Zhang et al. [265] investigated the role of trajectory planning in managing residual stresses, revealing that contour-based planning resulted in more uniform stress distributions compared to zig-zag patterns. Their findings highlight the intricate interplay between deposition paths, part shape, and material properties, emphasizing the need for strategic planning to mitigate stress-induced defects.

These studies collectively demonstrate the viability and cost-effectiveness of in-house process planning solutions. Leveraging this knowledge, a simplified approach was adopted in this study using G-code modification via MATLAB. The process began with the generation of G-code through Simplify 3D, a software chosen for its flexibility and compatibility with both FDM and WAAM. Simplify 3D allowed users to input critical parameters such as layer height (2 mm), layer width (6 mm), and deposition strategy. While the software enabled preliminary path planning, further refinement was necessary to adapt the G-code for WAAM-specific requirements. The exploration of in-house process planning techniques for WAAM underscores its practicality and cost-effectiveness. To address the unique demands of WAAM, a streamlined approach using MATLAB to modify the G-codes. This process takes advantage of the shared deposition trajectory principles of FDM extruders and WAAM torch heads. Simplify 3D, a robust software tool, is employed to generate initial G-codes from STL files, setting the stage for customization. The workflow, depicted in Figure 119, outlines the systematic steps leading to successful WAAM part deposition. A simple geometry was chosen for the trial to minimize complexities, as shown in Figure 120. The part was designed in Fusion 360 and exported in STL format, a standard widely used in 3D printing for representing 3D models via triangular facets. Simplify 3D was selected for its flexibility and user-friendly interface, particularly for tasks such as rotation, scaling, and setting layer dimensions. For this deposition process, a layer height of 2 mm and a width of 7 mm were selected, aligning with the established process parameters. Deposition strategy and overlap percentage, though generally significant in AM methods, were deemed inapplicable in this scenario due to the simple nature of the part being fabricated. However, based on insights from the study conducted by Zhang et al. [265], a simple deposition strategy (infill) is recommended even for more complex geometries, primarily to accommodate the high energy inputs characteristic of WAAM. Following these considerations, the final step involved generating a G-code file, which served as the instructional blueprint for the CNC systems employed during the WAAM process. The G-code compressed with all necessary commands to execute FDM the deposition sequence precisely, ensuring adherence to the specified dimensions and layer sequence. Figure 118 illustrates a representative G-code file generated using Simplify3D, showcasing the detailed information it contains.

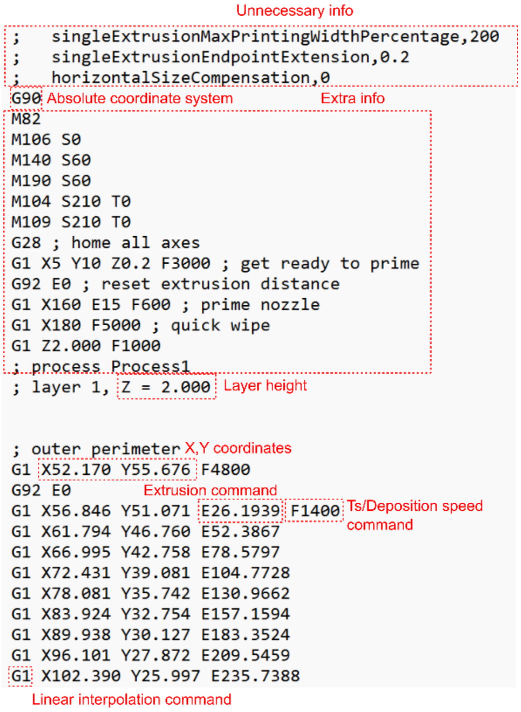

```
;   singleExtrusionMaxPrintingWidthPercentage,200
;   singleExtrusionEndpointExtension,0.2
;   horizontalSizeCompensation,0
G90
M82
M106 S0
M140 S60
M190 S60
M104 S210 T0
M109 S210 T0
G28 ; home all axes
G1 X5 Y10 Z0.2 F3000 ; get ready to prime
G92 E0 ; reset extrusion distance
G1 X160 E15 F600 ; prime nozzle
G1 X180 F5000 ; quick wipe
G1 Z2.000 F1000
; process Process1
; layer 1, Z = 2.000


; outer perimeter
G1 X52.170 Y55.676 F4800
G92 E0
G1 X56.846 Y51.071 E26.1939 F1400
G1 X61.794 Y46.760 E52.3867
G1 X66.995 Y42.758 E78.5797
G1 X72.431 Y39.081 E104.7728
G1 X78.081 Y35.742 E130.9662
G1 X83.924 Y32.754 E157.1594
G1 X89.938 Y30.127 E183.3524
G1 X96.101 Y27.872 E209.5459
G1 X102.390 Y25.997 E235.7388
```

Figure 118. Example G-code generated by Simplify 3D

Although the initial G-code generation was performed in Simplify 3D, MATLAB is pivotal for refining the code for WAAM deposit. FDM-generated G-codes often contain redundant data irrelevant to WAAM. To streamline the process, unnecessary lines were removed until the point where the first layer's deposition data began. The vertices (X, Y, Z coordinates) of the STL were analyzed, and unnecessary G-code lines for straight paths were consolidated. Function E (extrusion) was removed entirely, as WAAM processes do not use material extrusion. Similarly, the feed rate (F), critical for defining Ts in WAAM, was adjusted to match the required layer height and width. Another critical refinement involved the Z-axis adjustments. While Simplify 3D allows users to define a consistent layer height, the non-linear nature of WAAM layer deposition necessitated custom adjustments to ensure a constant Sod of 10 mm. This adjustment mitigates potential shielding gas inefficiencies and ensures adequate protection of the melt pool. Each layer's G-code was extracted and augmented with arc start and stop commands, ensuring precise execution during deposition. All modifications were consolidated into a MATLAB script, designed to automate the process and minimize human error. Before running the G-code on the WAAM machine, a final script review was conducted to ensure alignment with the intended part design and deposition strategy. This verification step, akin to a safety net, ensured the reliability of the process.

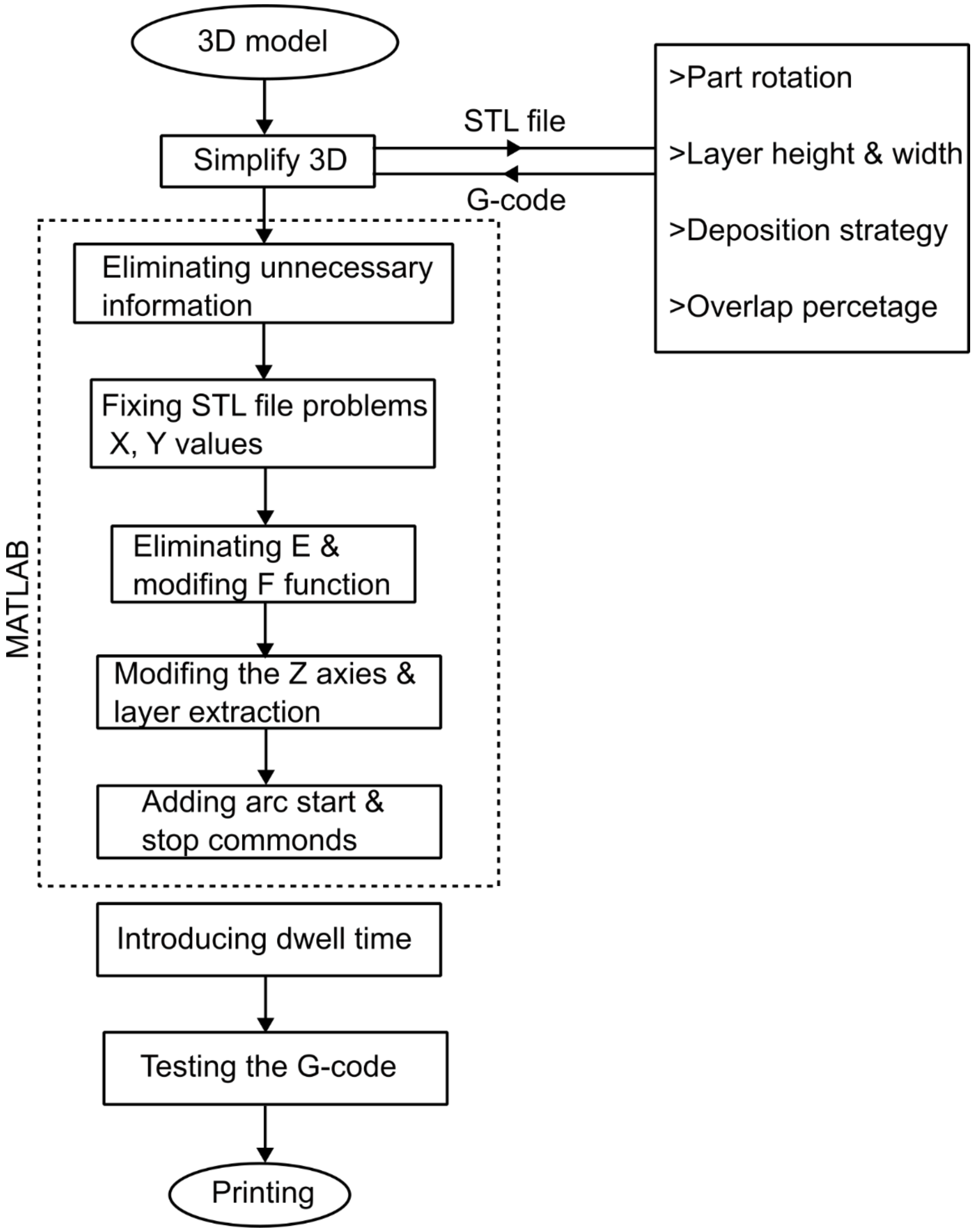

Figure 119. WAAM preprocessing flow chart

The final part was deposited using parameters of P = 2.9 kW, Ts = 250 mm/min, WFS = 5800 mm/min, Sod = 10 mm, and a dwell time of 2 minutes 30 seconds, with forced air cooling to maintain substrate temperatures below 50°C. The chosen substrate had a thickness of 20 mm to accommodate the high thermal loads which leads to distortions. The intended part design, as depicted in Figure 1, featured a 100 mm tall structure with a large rectangular base, a midsection inclined at 30°, and a smaller rectangle at the top. To address the non-linear layer height reductions observed during deposition, layer-specific G-codes were iterated until the target height was achieved. The nominal and actual dimensions of the deposited part, including any deviations, are reported in Figure 120.

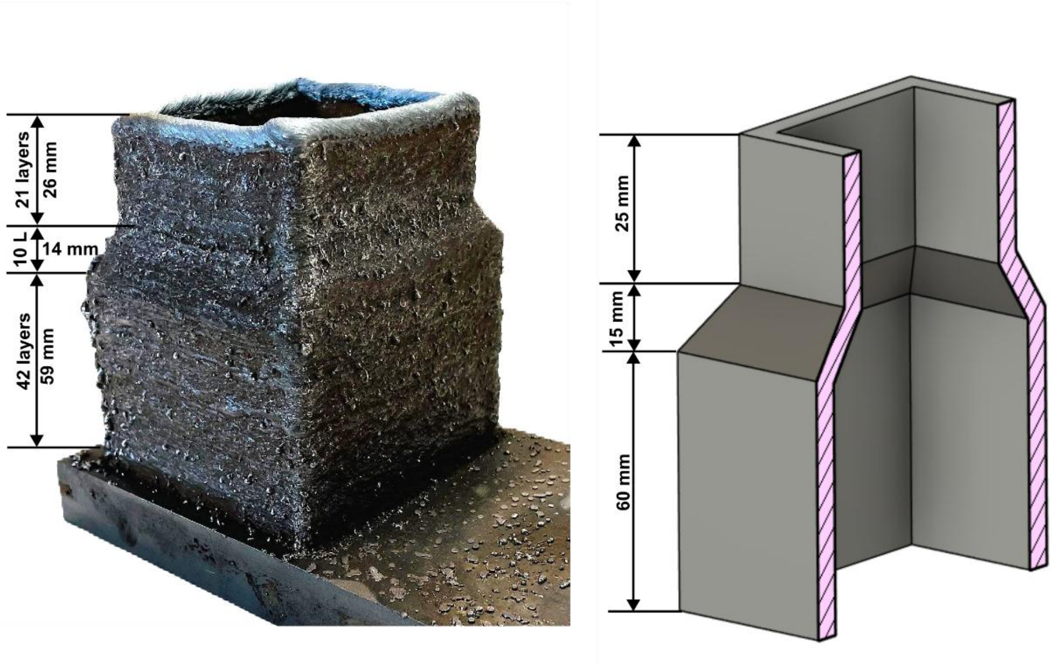

Figure 120. Deposited simple geometry and it's dimensions.

Results and discussion

The height of the deposited part was systematically monitored during the deposition process, with measurements taken every 10 layers to ensure precise tracking of dimensional changes. The calculated average layer height, derived by dividing the total measured height by the number of deposited layers, is presented in Figure 121. The initial deposition, under the set process parameters, typically produced single beads approximately 2 mm in height. However, as the deposition progressed, the average layer height steadily declined. After the deposition of 10 layers, the average layer height was observed to drop slightly above 1.5 mm, highlighting the gradual impact of cumulative thermal and geometric effects on layer consistency. Interestingly, this average layer height exhibited stability during the inclined deposition segment. This finding warrants deeper investigation since, in overhanging sections, part of the layer is deposited on the previously built structure while another portion is unsupported. This configuration generally results in additional shrinkage due to insufficient substrate support for the overhanging material [258]. The observed stability during inclination contrasts with expected trends, suggesting potential influences from process dynamics such as heat distribution or deposition speed that require further exploration. By the end of 73 layers, the average layer height reduced to 1.36 mm, demonstrating a progressive decline with increased deposition height. Such reductions are attributable to changes in the heat dissipation characteristics and deposition conditions as the torch moves away from the substrate.

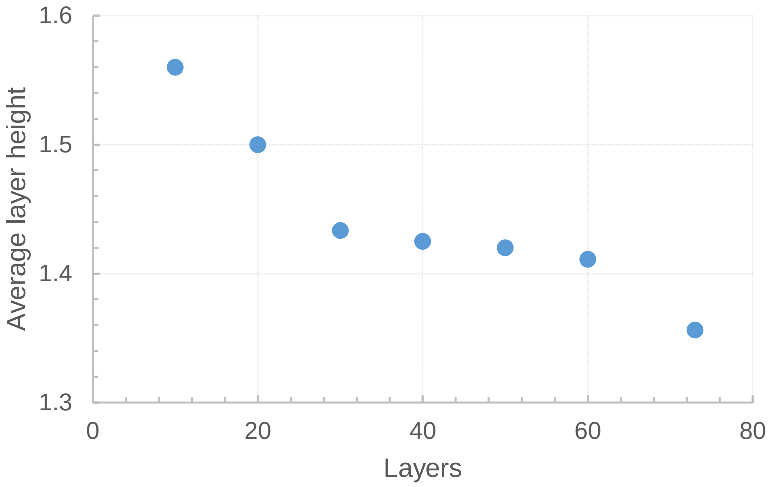

Figure 121. Average layer height

Any irregularity in the substrate or previously deposited layers can propagate through subsequent layers, compounding geometrical deviations over the build height. This cumulative effect is particularly pronounced at critical geometric features like corners, overhangs, and complex torch movement areas. Figure 122 highlights several challenges encountered during the deposition, including uneven geometry and shrinkage in specific regions. One side of the part profile exhibited visible shrinkage in the middle section, as shown in Figure 122b. Such defects, stemming from minor initial irregularities, underscore the critical need for adopting closed-loop monitoring systems to dynamically adjust parameters during deposition and mitigate error propagation (will be discussed in the future trends). To address these challenges and refine the geometry, two additional depositions were performed, detailed in Figure 122c&d. These trials aimed to counteract the observed irregularities by leveraging optimized parameters and deposition strategies, further emphasizing the iterative nature of WAAM process development.

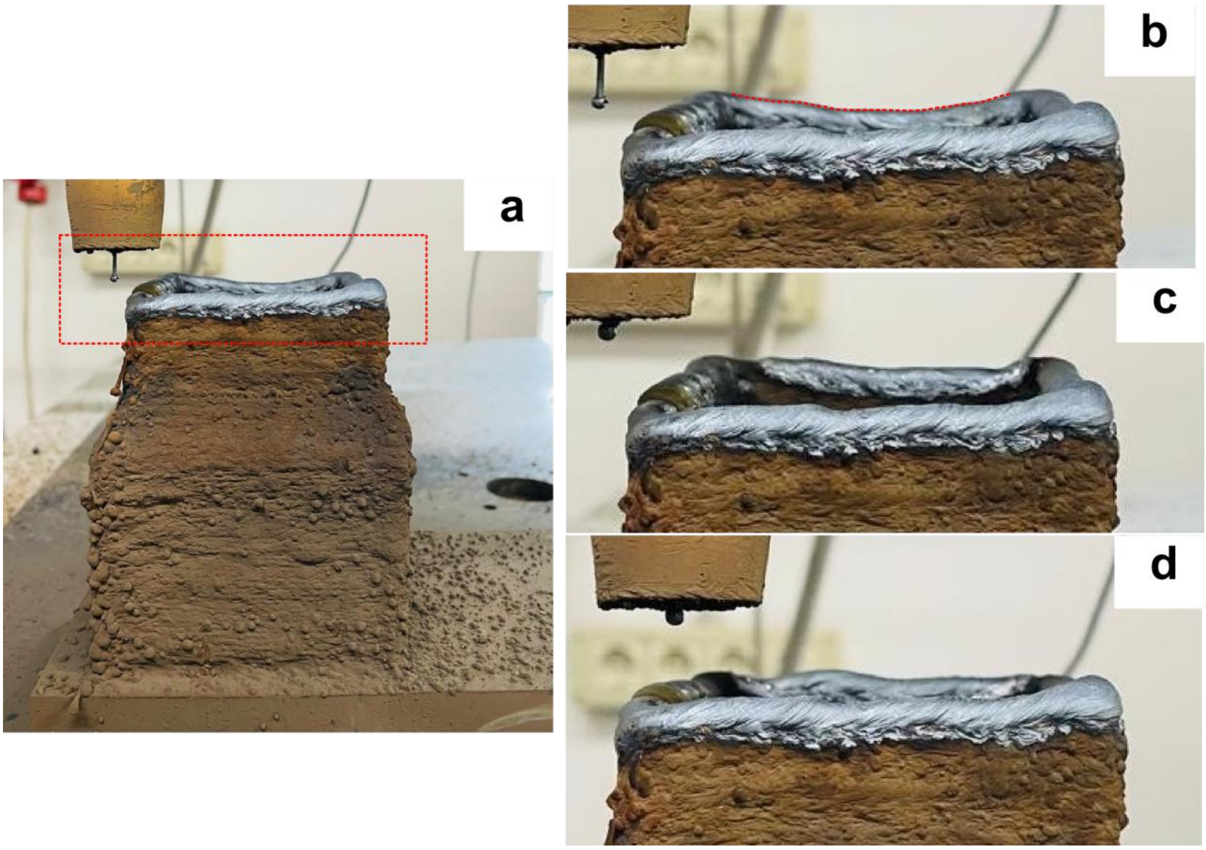

Figure 122. Shrinkage in the deposited part

Average current and voltage were systematically recorded for each deposited layer, with the results detailed in Figure 123. Consistent with observations from earlier sections, the voltage remained stable throughout the deposition process, averaging approximately 28 V. Meanwhile, the average current measured was around 73 A, resulting in an average power of approximately 2.0 kW. This recorded power was remarkably lower than the power setting configured on the MIG welding machine, a difference that can be attributed to the higher electrical resistance associated with the thicker substrate material [36]. When comparing substrates of different thicknesses, the resistance values reveal significant variation. For example, a 3.3 mm substrate exhibited an average resistance of 0.178 Ω, whereas the thicker 20 mm substrate used for this part realization displayed a higher resistance of 0.377 Ω. A similar trend was documented by Thien et al. [36], where power reduction was observed with an increase in layer height. In this study, the resistance exhibited a gradual and linear increase, with measured values starting at 0.35 Ω at the initial layer and reaching 0.37 Ω by the end of the deposition. This increase in resistance led to a corresponding reduction in power, with a maximum power drop of approximately 6.77%. Such trends underscore the interplay between material resistance and power stability during the WAAM process, providing critical insights for process optimization.

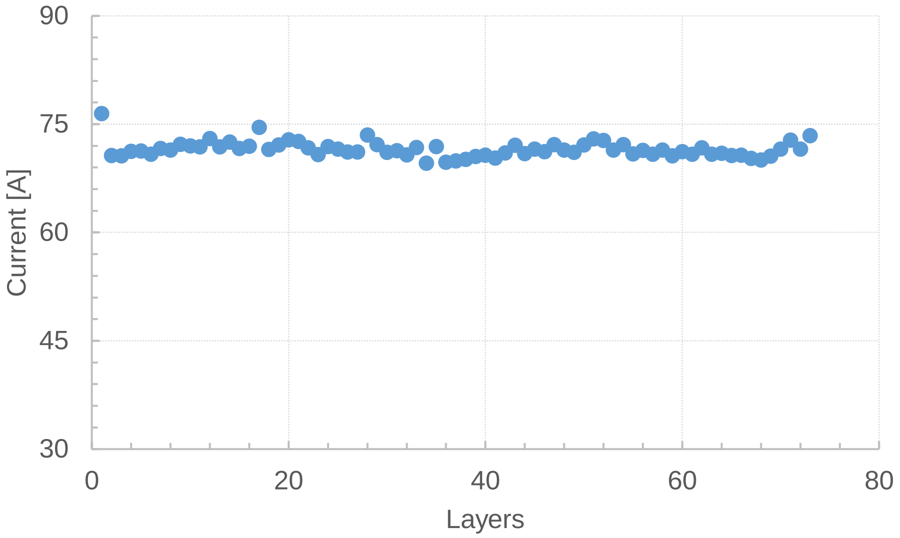

Figure 123. Average current passed during part deposition.

Current fluctuations were further analyzed, as illustrated in Figure 124, which highlights the behavior during the deposition. Consistent with earlier experimental results and the findings of Thien et al. [36], current was observed to be highly sensitive to deposition geometry. For instance, the rectangular deposition profile used in this study, characterized by its four corners, exhibited distinct current fluctuation patterns. One corner served as the starting and ending point for the torch, while the other three corners exhibited fluctuations marked in red (Figure 124). These fluctuations were shorter compared to those observed in U-shaped samples, which can be attributed to the geometric differences. While the rectangular deposition involved 90° corners, the U-shaped samples featured 180° curves, leading to more pronounced current instability. This comparison emphasizes the role of geometric features in influencing current behavior, highlighting the need for real-time monitoring and adaptive control strategies to ensure consistent deposition quality across complex geometries.

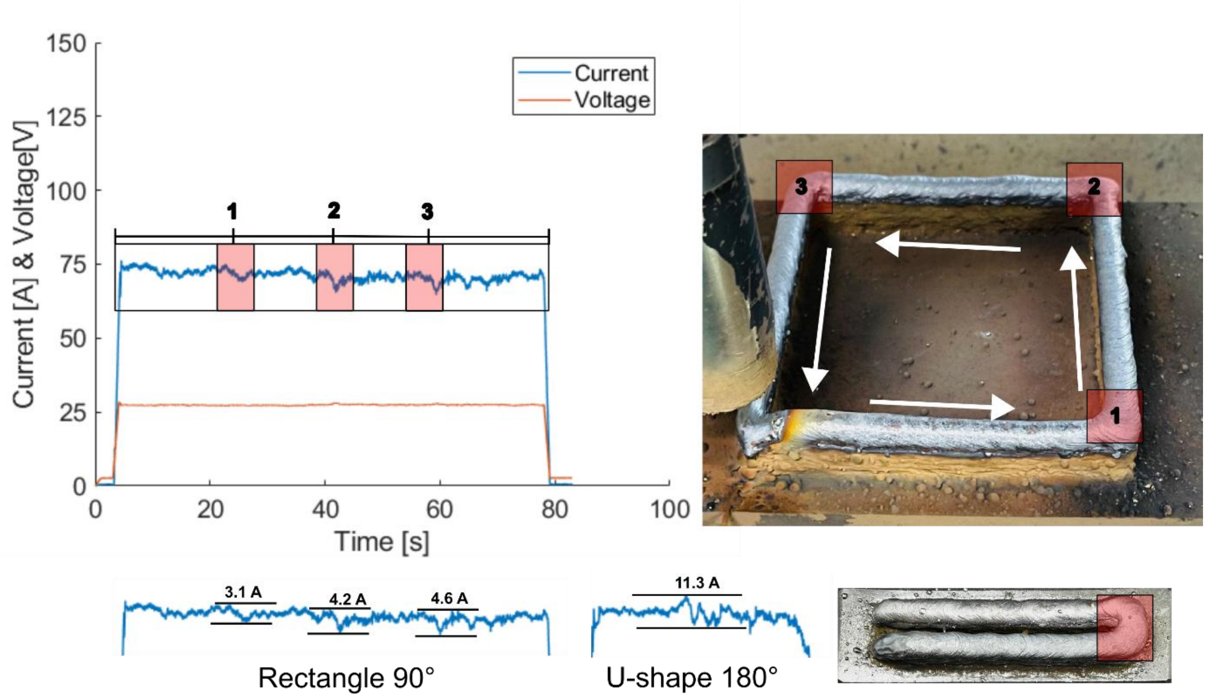

Figure 124. Variations in current flow

Chapter 6 – Results

This section of the thesis is dedicated to exploring all the findings made in this thesis. The findings are divided into 3 parts, namely, geometrical observations, in-process data monitoring, and material properties.

6.1 Geometrical Observations

The geometrical analyses conducted in this study underline the influence of critical process parameters on the morphology and structure of WAAM-fabricated components. This study began with preliminary analyses to understand single bead geometry and establish a processing window for key WAAM process parameters. Since each machine and material has unique properties, defining these boundaries is critical before advancing to complex part development. As highlighted by Nguyen et al. [15], Chen et al. [209], Chaudari et al. [266], such systematic parameter identification is a well-established practice in additive manufacturing research. The investigations made in this study reveal that the process parameters, including power (P), travel speed (Ts), wire feed speed (WFS), and stand-off distance (Sod), significantly affect bead geometry. Among these, Sod exhibited the least influence on bead geometry within the tested range of 8–12 mm. Henckell et al. [57], who reported that increasing contact-tip-to-work-distance (CTWD) can increase bead height and reduce bead width. However, the impact of Sod in this study was less pronounced due to the narrow testing range. Specific energy analyses indicate that a minimum specific energy of 18.3 J/mm^3 is necessary to achieve sufficient heat input for melting low-carbon steel, corresponding to P = 2.9 kW and WFS = 5800 mm/min. At higher Ts, irregular depositions were observed, consistent with findings by [27]. Shielding gas flow rate also emerged as a critical factor, higher flow rates led to turbulence at the nozzle end, flattening the deposited beads, as similarly observed by [267].

In multi-layer stacking, significant findings were observed. The radius of curvature stabilized at 5 mm from the second layer onward, following an initial radius of 7.6 mm for the first layer deposited on the substrate. Importantly, U-shaped sample analyses confirmed that preheating of one side did not affect the other, as both sides exhibited similar geometrical characteristics. The wall geometry evolved predictably with process conditions. Wall height decreased logarithmically with increasing Ts. Modeled mass conservation calculations underscored that the cross-sectional area of deposited beads is directly proportional to WFS and inversely proportional to Ts. Material efficiency, a key metric for industrial applications, exceeded 60% even at the highest Ts tested (1000 mm/min), demonstrating the feasibility of WAAM for high-speed operations. Managing overhanging structures proved more challenging. The maximum inclination angle achieved was 31.3° at Ts = 250 mm/min. This highlights WAAM's limitations in producing overhanging features without additional support structures. Height reductions of up to 30% were observed in overhanging samples, emphasizing the need for precise layer shift management to maintain stable geometries during complex deposition tasks. G-code modification experiments demonstrated the feasibility of in-house pre-processing planning. While successful in producing a 100-mm-high part with varying geometries, issues such as average layer height reduction (from 2 mm to 1.3 mm) and layer shrinkage in the middle were observed. These findings stress the importance of further refinement in path planning algorithms to address layer uniformity challenges.

6.2 In-Process Data Monitoring:

In-process data monitoring during WAAM provided crucial insights into current, voltage, and temperature variations throughout the deposition process. This study confirmed that current exhibits greater sensitivity than voltage during deposition, consistent with findings made by Thien et al. [36] and Xiong et al. [268]. Voltage fluctuations remained minimal, maintaining power stability set by the MIG machine. Multi-layer samples revealed a power stabilization effect after the initial three layers. Initial layers exhibited higher power flow, while subsequent layers maintained more consistent values. Power increased with Ts and WFS, correlating with greater heat input requirements. Temperature data also showed a stabilization trend after the 6th layer, with peak values ranging from 1600°C to 1900°C. Lower Ts resulted in smaller temperature gradients, while higher Ts produced steeper gradients. Thermal cycle analyses indicated that the first deposited layer experienced multiple thermal cycles, retaining temperatures above 500°C even after the 10th layer. This underscores the prolonged thermal impact of WAAM on lower layers, which contributes to distinct microstructural and mechanical property variations. Electrical resistance measurements revealed that thicker substrates (20 mm) caused higher resistance (0.377 Ω compared to 0.178 Ω for 3.3 mm substrates). However, the overall power drop from first layer to the last layer of deposited part stayed below 7%, even at 100 mm deposition height, a trend consistent with [36]. Current fluctuations were more pronounced in geometries with complex profiles, such as U-shaped samples, where curves induced larger variations compared to rectangular profiles with 90° corners.

6.3 Material Properties

WAAM samples exhibited distinct microstructural regions from bottom to top, influenced by thermal cycles and deposition conditions. Grain size decreased progressively from bottom to top. The substrate heat-affected zone (HAZ) contained two distinct regions. Single-bead analyses indicated that microhardness increased with Ts and decreased with P. The highest microhardness (~230 HV) was recorded at high Ts. In multi-layer walls, lower layers exhibited grain growth and reduced hardness due to repeated thermal cycles, while top layers maintained finer grains and higher hardness (~250 HV). Forced air cooling further improved microhardness, increasing it from 230 HV to 250 HV. At higher Ts, top layers, characterized by rapid cooling, showed finer, vertically aligned grains with excellent microhardness (~280 HV). A saddle pattern in microhardness was observed in 10-layer wall samples, with stable values in the middle and varying values in the first and last four layers. U-shaped samples exhibited diminished hardness at curved sections due to thermal stress and current fluctuations. Dendritic structures were identified throughout WAAM samples, forming due to rapid cooling and directional solidification. Layer overlap zones revealed distinct microstructures sensitive to imperfections, such as shrinkage porosity linked to melt-pool dynamics and material flow instabilities, underscore the need for precise parameter control. Other defects such as spatter, keyhole porosity, and microcracks were also observed. Oxidation layers, observed on WAAM surfaces, were attributed to oxygen exposure during deposition. These layers, composed of iron oxides (FeO, Fe_2O_3), can significantly influence surface hardness and corrosion resistance. As-built WAAM parts exhibited surface waviness, necessitating post-processing operations like machining to improve surface finish and mechanical properties, as suggested by Tankova et al. [202].

This research contributes to advancing WAAM technology, providing valuable insights into the process, thermal behavior and material properties to support its adoption in manufacturing large-scale, high-quality metal components.

Chapter 7 - Conclusions and Future trends

The findings from this research provide a comprehensive understanding of Wire Arc Additive Manufacturing (WAAM) for low-carbon steel, specifically focusing on the optimization of process parameters, geometrical characteristics, and material properties. The preliminary tests were essential for identifying the processing window, ensuring defect-free deposition under controlled conditions. When higher power levels (P = 3.8 kW) were applied, defects like burn-through were observed, underscoring the need to investigate unexplored process combinations. Future studies will expand the parameter range, including higher wire feed speeds (WFS), increased travel speeds (Ts), and adaptive power inputs to optimize deposition outcomes while maintaining desirable material properties. To investigate the stacking effects on geometry and material properties, multilayer walls were fabricated. U-shaped samples were analyzed to study pre-heating effects, and future work will extend this approach to lateral layer deposition with overlaps. This will enable the identification of lateral changes in material properties and potential anisotropy within complex structures. The observed anisotropic properties especially in the first and last four layers of deposited walls were attributed to variations in thermal cycles and current flow during deposition. Adaptive power control, particularly at the beginning and end layers, could mitigate this effect, enhancing consistency across the part. The corners and complex geometries of samples, such as U-shaped and rectangular profiles, experienced distinct thermal stresses and material variations. These regions were also prone to defects like microcracks. This highlights the importance of adaptive deposition speeds and optimized process parameters to manage thermal stresses and ensure uniform material properties across intricate geometries. Implementing dynamic process control for these regions will improve deposition quality and minimize defect formation.

The in-process data monitoring of current and temperature presented in this study is highly relevant for Finite Element Method (FEM) simulations, as suggested by works such as [269], [270]. The data acquired during deposition provided valuable insights into process stability, power variations, and thermal cycles. However, the WAAM process remains susceptible to irregularities due to high material deposition rates. Once the G-code is executed, deviations caused by arc instability or complex geometries cannot currently be corrected in real time. This limitation can lead to defects such as layer shrinkage and geometrical inconsistencies. To address these challenges, future work will focus on integrating a closed-loop monitoring system equipped with optical and thermal sensors. These sensors will enable real-time observation of melt-pool behavior and accurate measurement of geometrical features like layer height and width. This data will be processed by a controller, which will adjust key process parameters such as Sod and heat input to maintain process stability. Advanced technologies, such as machine learning, will also be implemented to develop predictive models for defect detection and process optimization. Real-time monitoring and control, combined with predictive algorithms, will ensure consistent material properties and reduce defects, as demonstrated in the work of Le et al. [187], and Wang et al. [271]. While the G-code modifications in this study were limited to simple geometries, future research will focus on enhancing pre-processing methods to accommodate complex components. One challenge that remains is the non-linear variation in average layer height as part height increases. The inability to predefine layer height in complex parts affects overall geometry and final dimensions. Since layer height is influenced by heat input, real-time adjustments will be necessary, guided by optical sensors and feedback systems. Future developments will emphasize the integration of pre-processing, in-process monitoring, and adaptive control systems to ensure WAAM can fabricate parts that adhere closely to original design specifications without deviations. In conclusion, the research establishes a robust foundation for WAAM process optimization, material characterization, and defect mitigation. However, to bring WAAM to an industrial level, future advancements must focus on integrating adaptive controls, expanding parameter studies, and implementing real-time monitoring systems. These developments will enable WAAM to achieve higher precision, better material properties, and enhanced reliability, solidifying its position as a viable alternative for large-scale additive manufacturing.

Reference

1. ISO/ASTM, *Additive manufacturing-general principles-fundamentals and vocabulary*. 2021.
2. Kazmer, D., *28 - Three-Dimensional Printing of Plastics*, in *Applied Plastics Engineering Handbook (Second Edition)*, M. Kutz, Editor. 2017, William Andrew Publishing. p. 617-634.
3. Fraunhofer, *world's largest SLM machine, PR_Official-launch-of-XLine-2000R*. 2017.
4. AISBL, E.P.M.A. *Metal Injection Moulding (MIM)*. Available from: https://www.epma.com/metal-injection-moulding.
5. Zahidin, M.R., et al., *Research challenges, quality control and monitoring strategy for Wire Arc Additive Manufacturing*. Journal of Materials Research and Technology, 2023. **24**: p. 2769-2794.
6. Joshi, S., et al., *Metal Additive Manufacturing Processes – Directed Energy Deposition Processes*, in *Additive Manufacturing with Metals: Design, Processes, Materials, Quality Assurance, and Applications*, S. Joshi, et al., Editors. 2023, Springer International Publishing: Cham. p. 111-150.
7. Ding, D., et al., *Wire-feed additive manufacturing of metal components: technologies, developments and future interests*. The International Journal of Advanced Manufacturing Technology, 2015. **81**(1-4): p. 465-481.
8. Strombergsson, A., *PIX uses WAAM to simplify car manufacturing*. 2021, VoxelMatters.
9. MX3D. *MX3D Bridge*. 2024; Available from: https://mx3d.com/industries/mx3d-bridge/.
10. Kladovasilakis, N., et al., *Impact of metal additive manufacturing parameters on the powder bed fusion and direct energy deposition processes: a comprehensive review*. Progress in Additive Manufacturing, 2021. **6**(3): p. 349-365.
11. Adebayo A, Mehnen J, and T. X, *Limiting travel speed in additive manufacturing*. 2012.
12. Brandl, E., C. Leyens, and F. Palm, *Mechanical Properties of Additive Manufactured Ti-6Al-4V Using Wire and Powder Based Processes*. IOP Conference Series: Materials Science and Engineering, 2011. **26**.
13. Dias, M., et al., *Economic and Environmental Potential of Wire-Arc Additive Manufacturing*. Sustainability, 2022. **14**(9).
14. Bhuvanesh Kumar, M., P. Sathiya, and S.M. Senthil, *A critical review of wire arc additive manufacturing of nickel-based alloys: principles, process parameters, microstructure, mechanical properties, heat treatment effects, and defects*. Journal of the Brazilian Society of Mechanical Sciences and Engineering, 2023. **45**(3).
15. Nguyen, V.-T., P.S. Minh, and T.M. Uyen, *WAAM Technique: Process Parameters Affecting the Mechanical Properties and Microstructures of Low-Carbon Steel*. Metals, 2023. **13**(5).
16. Sword, J.I., A. Galloway, and A. Toumpis, *An environmental impact comparison between wire + arc additive manufacture and forging for the production of a titanium component*. Sustainable Materials and Technologies, 2023. **36**.
17. Soundarapandiyan, G., et al., *A technical review of the challenges of powder recycling in the laser powder bed fusion additive manufacturing process*. The Journal of Engineering, 2021. **2021**(2): p. 97-103.
18. Saleh, B., et al., *Fundamentals and advances of wire arc additive manufacturing: materials, process parameters, potential applications, and future trends*. Archives of Civil and Mechanical Engineering, 2023. **23**(2).
19. Baker, R., *Method of making decorative articles*. 1925.
20. Gopal Krushna Mohanta and A.K. Senapati, *The effect of Welding Parameters on Mild Steel by MMAW*. 2018.
21. Ahsan, M.R.U., et al., *Effects of process parameters on bead shape, microstructure, and mechanical properties in wire + arc additive manufacturing of Al0.1CoCrFeNi high-entropy alloy*. Journal of Manufacturing Processes, 2021. **68**: p. 1314-1327.
22. Barath Kumar, M.D. and M. Manikandan, *Effect of continuous and pulsed current techniques on wire-arc additive manufacturing of a nickel-based superalloy*. Materials Letters, 2023. **338**.
23. Rosli, N.A., Alkahari, M.R., Ramli, F.R., Sudin, M.N., Maidin, S., *Influence of Process Parameters in wire and arc additive manufacturing (WAAM) process*. 2020.
24. Dinovitzer, M., et al., *Effect of wire and arc additive manufacturing (WAAM) process parameters on bead geometry and microstructure*. Additive Manufacturing, 2019. **26**: p. 138-146.
25. Jing, C., et al., *Impact of process parameters on forming quality and deposition efficiency of unsupported rods in wire arc additive manufacturing*. Journal of Manufacturing Processes, 2024. **124**: p. 12-23.

26. Lambiase, F., S.I. Scipioni, and A. Paoletti, *Accurate prediction of the bead geometry in wire arc additive manufacturing process.* The International Journal of Advanced Manufacturing Technology, 2022. **119**(11-12): p. 7629-7639.
27. Tawfik, M.M., M.M. Nemat-Alla, and M.M. Dewidar, *Effect of Travel Speed on the Properties of Al-Mg Aluminum Alloy Fabricated by Wire Arc Additive Manufacturing.* Journal of Materials Engineering and Performance, 2021. **30**(10): p. 7762-7769.
28. Zhou, Y., et al., *Influence of travel speed on microstructure and mechanical properties of wire + arc additively manufactured 2219 aluminum alloy.* Journal of Materials Science & Technology, 2020. **37**: p. 143-153.
29. Teixeira, F.R., et al., *Combined effect of the interlayer temperature with travel speed on features of thin wall WAAM under two cooling approaches.* The International Journal of Advanced Manufacturing Technology, 2023. **126**(1-2): p. 273-289.
30. Yildiz, A.S., et al., *Wire arc additive manufacturing of high-strength low alloy steels: study of process parameters and their influence on the bead geometry and mechanical characteristics.* The International Journal of Advanced Manufacturing Technology, 2020. **108**(11-12): p. 3391-3404.
31. Han, S.-W., et al., *Parameter Optimization of WAAM with Pulsed GMAW for Manufacturing Propeller-Shaped Blade.* International Journal of Precision Engineering and Manufacturing, 2023. **24**(7): p. 1103-1110.
32. Fuchs, C., C. Fritz, and M.F. Zaeh, *Impact of wire and arc additively manufactured workpiece geometry on the milling process.* Production Engineering, 2022. **17**(3-4): p. 415-424.
33. Wang, L., et al., *Microstructure distribution characteristics of LMD-WAAM hybrid manufacturing Ti-6Al-4V alloy.* Optics & Laser Technology, 2023. **165**.
34. Chen, X., et al., *A review on wire-arc additive manufacturing: typical defects, detection approaches, and multisensor data fusion-based model.* The International Journal of Advanced Manufacturing Technology, 2021. **117**(3-4): p. 707-727.
35. Bento, J.B., et al., *Process Control Methods in Cold Wire Gas Metal Arc Additive Manufacturing.* Metals, 2023. **13**(8).
36. Thien, A., C. Saldana, and T. Kurfess, *The effect of WAAM process parameters on process conditions and production metrics in the fabrication of single-pass multi-layer wall artifacts.* The International Journal of Advanced Manufacturing Technology, 2021. **119**(1-2): p. 531-547.
37. Le, V.T., et al., *Prediction and optimization of processing parameters in wire and arc-based additively manufacturing of 316L stainless steel.* Journal of the Brazilian Society of Mechanical Sciences and Engineering, 2022. **44**(9).
38. Chen, X., et al., *A Review of the Development Status of Wire Arc Additive Manufacturing Technology.* Advances in Materials Science and Engineering, 2022. **2022**: p. 1-28.
39. Cambon, C., et al., *A WAAM benchmark: From process parameters to thermal effects on weld pool shape, microstructure and residual stresses.* Materials Today Communications, 2022. **33**.
40. Vora, J., et al., *Optimization of Bead Morphology for GMAW-Based Wire-Arc Additive Manufacturing of 2.25 Cr-1.0 Mo Steel Using Metal-Cored Wires.* Applied Sciences, 2022. **12**(10).
41. Baffa, F., et al., *Effect of stepover and torch tilting angle on a repair process using WAAM.* Advances in Manufacturing, 2022. **10**(4): p. 541-555.
42. Gudur, S., et al., *A study on the effect of substrate heating and cooling on bead geometry in wire arc additive manufacturing and its correlation with cooling rate.* Materials Today: Proceedings, 2021. **41**: p. 431-436.
43. Ayed, A., et al. *Effects of WAAM Process Parameters on Metallurgical and Mechanical Properties of Ti-6Al-4V Deposits.* in *Advances in Materials, Mechanics and Manufacturing.* 2020. Cham: Springer International Publishing.
44. Yamaguchi, M., et al., *Influence of metal transfer behavior under Ar and CO2 shielding gases on geometry and surface roughness of single and multilayer structures in GMAW-based wire arc additive manufacturing of mild steel.* The International Journal of Advanced Manufacturing Technology, 2021. **119**(1-2): p. 911-926.
45. Jurić, I., et al., *Influence of Shielding Gas Composition on Structure and Mechanical Properties of Wire and Arc Additive Manufactured Inconel 625.* Jom, 2018. **71**(2): p. 703-708.
46. Xia, C., et al., *Modelling and prediction of surface roughness in wire arc additive manufacturing using machine learning.* Journal of Intelligent Manufacturing, 2021. **33**(5): p. 1467-1482.
47. Ali, M.H. and Y.S. Han, *Effect of Phase Transformations on Scanning Strategy in WAAM Fabrication.* Materials (Basel), 2021. **14**(24).

48. Turgut, B., U. Gürol, and R. Onler, *Effect of interlayer dwell time on output quality in wire arc additive manufacturing of low carbon low alloy steel components.* The International Journal of Advanced Manufacturing Technology, 2023. **126**(11-12): p. 5277-5288.
49. Xiong, J., et al., *Influences of process parameters on surface roughness of multi-layer single-pass thin-walled parts in GMAW-based additive manufacturing.* Journal of Materials Processing Technology, 2018. **252**: p. 128-136.
50. Spalek, N., et al., *WAAM-Fabricated Laminated Metal Composites.* Metals, 2021. **11**(12).
51. Majumder, P., A. Sinha, and A. Biswas, *Effect of preheating techniques on bead geometry and microhardness of weldment developed through the submerged arc welding process.* Materials Today: Proceedings, 2021. **46**: p. 5001-5007.
52. Barath Kumar, M.D. and M. Manikandan, *Assessment of Process, Parameters, Residual Stress Mitigation, Post Treatments and Finite Element Analysis Simulations of Wire Arc Additive Manufacturing Technique.* Metals and Materials International, 2022. **28**(1): p. 54-111.
53. Alomari, Y., M.T. Birosz, and M. Ando, *Part orientation optimization for Wire and Arc Additive Manufacturing process for convex and non-convex shapes.* Sci Rep, 2023. **13**(1): p. 2203.
54. Wang, F., et al., *Microstructure and Mechanical Properties of Wire and Arc Additive Manufactured Ti-6Al-4V.* Metallurgical and Materials Transactions A, 2012. **44**(2): p. 968-977.
55. Islam, S., et al., *Investigation of microstructures, defects, and mechanical properties of titanium-zirconium-molybdenum alloy manufactured by wire arc additive manufacturing.* International Journal of Refractory Metals and Hard Materials, 2023. **110**.
56. Trad, O., et al. *Parameters Effect Study on Bead Geometry Deposited by CMT Technology Based Wire Additive Manufacturing (WAAM) Process*. in *Advances in Additive Manufacturing: Materials, Processes and Applications*. 2024. Cham: Springer Nature Switzerland.
57. Henckell, P., et al., *Reduction of Energy Input in Wire Arc Additive Manufacturing (WAAM) with Gas Metal Arc Welding (GMAW).* Materials (Basel), 2020. **13**(11).
58. Rime. *MAG Welding*. Available from: https://rime.de/en/welding/mag-welding/#:~:text=Inert%20gases%20shield%20the%20weld,material%20to%20the%20welding%20area.
59. Halisch, C., et al., *Influence of oxygen content in the shielding gas chamber on mechanical properties and macroscopic structure of Ti-6Al-4V during wire arc additive manufacturing.* The International Journal of Advanced Manufacturing Technology, 2022. **124**(3-4): p. 1065-1076.
60. Hauser, T., et al., *Porosity in wire arc additive manufacturing of aluminium alloys.* Additive Manufacturing, 2021. **41**.
61. Wei, Y., et al., *Effect of arc oscillation on porosity and mechanical properties of 2319 aluminum alloy fabricated by CMT-wire arc additive manufacturing.* Journal of Materials Research and Technology, 2023. **24**: p. 3477-3490.
62. Liu, J., et al., *Wire and arc additive manufacturing of metal components: a review of recent research developments.* The International Journal of Advanced Manufacturing Technology, 2020. **111**(1-2): p. 149-198.
63. Chen, Y., et al., *An Experimental Investigation into Residual Stress Control of 24CrNiMo Alloy Steel by Selective Laser Melting.* Coatings, 2023. **13**(2).
64. Ma, D., et al., *Achieving fully equiaxed grain microstructure and isotropic mechanical properties in wire arc additive-manufactured Mg-Y-Nd-Zr alloys.* Journal of Alloys and Compounds, 2023. **962**.
65. Xiong, J., Y. Lei, and R. Li, *Finite element analysis and experimental validation of thermal behavior for thin-walled parts in GMAW-based additive manufacturing with various substrate preheating temperatures.* Applied Thermal Engineering, 2017. **126**: p. 43-52.
66. C.R.Cunningham, et al., *Characterization of austenitic 316LSi stainless steel produced by wire arc additive manufacturing with interlayer cooling 20+.* 2019.
67. Ding, J., et al., *Thermo-mechanical analysis of Wire and Arc Additive Layer Manufacturing process on large multi-layer parts.* Computational Materials Science, 2011. **50**(12): p. 3315-3322.
68. Yuan, L., et al., *Fabrication of metallic parts with overhanging structures using the robotic wire arc additive manufacturing.* Journal of Manufacturing Processes, 2021. **63**: p. 24-34.
69. Geng, H., et al., *Geometric Limitation and Tensile Properties of Wire and Arc Additive Manufacturing 5A06 Aluminum Alloy Parts.* Journal of Materials Engineering and Performance, 2016. **26**(2): p. 621-629.
70. Lockett, H., et al., *Design_for_wire+arc_additive_manufacture-design rules and build orientation selection.* 2017.

71. Bruggi, M., V. Laghi, and T. Trombetti, *Simultaneous design of the topology and the build orientation of Wire-and-Arc Additively Manufactured structural elements.* Computers & Structures, 2021. **242**.
72. Byun, H.S. and K.H. Lee, *Determination of optimal build direction in rapid prototyping with variable slicing.* The International Journal of Advanced Manufacturing Technology, 2005. **28**(3-4).
73. Sharma, K., *Titanium alloys: Definition, Properties, Types, Advantages, and Disadvantages*. 2023, Science Info.
74. Lin, Z., K. Song, and X. Yu, *A review on wire and arc additive manufacturing of titanium alloy.* Journal of Manufacturing Processes, 2021. **70**: p. 24-45.
75. Pant, H., et al., *Applications of wire arc additive manufacturing (WAAM) for aerospace component manufacturing.* The International Journal of Advanced Manufacturing Technology, 2023. **127**(11-12): p. 4995-5011.
76. Moore, S., *3D Printing Titanium in Aerospace Manufacturing Applications*. 2020, AZO Materials.
77. Palacios, B., et al., *Role of structural hierarchy on mechanics and electrochemistry of wire arc additive manufactured (WAAM) single phase titanium.* Journal of Manufacturing Processes, 2023. **93**: p. 239-249.
78. Artaza, T., et al., *Wire arc additive manufacturing Ti6Al4V aeronautical parts using plasma arc welding: Analysis of heat-treatment processes in different atmospheres.* Journal of Materials Research and Technology, 2020. **9**(6): p. 15454-15466.
79. Chi, Y., et al., *Wire arc additive manufacturing (WAAM) of nanotreated aluminum alloy 6061.* Rapid Prototyping Journal, 2023. **29**(7): p. 1341-1349.
80. Rodriguez-Gonzalez, P., E.M. Ruiz-Navas, and E. Gordo, *Wire Arc Additive Manufacturing (WAAM) for Aluminum-Lithium Alloys: A Review.* Materials (Basel), 2023. **16**(4).
81. Vimal, K.E.K., M. Naveen Srinivas, and S. Rajak, *Wire arc additive manufacturing of aluminium alloys: A review.* Materials Today: Proceedings, 2021. **41**: p. 1139-1145.
82. Wu, B., et al., *A review of the wire arc additive manufacturing of metals: properties, defects and quality improvement.* Journal of Manufacturing Processes, 2018. **35**: p. 127-139.
83. Gierth, M., et al., *Wire Arc Additive Manufacturing (WAAM) of Aluminum Alloy AlMg5Mn with Energy-Reduced Gas Metal Arc Welding (GMAW).* Materials (Basel), 2020. **13**(12).
84. Nagasai, B.P., S. Malarvizhi, and V. Balasubramanian, *Mechanical Properties and Microstructural Characteristics of Al–Mg Alloy Cylindrical Component Manufactured by Wire Arc Additive Manufacturing Process.* Metallography, Microstructure, and Analysis, 2022. **11**(2): p. 199-211.
85. Arana, M., et al., *Strategies to Reduce Porosity in Al-Mg WAAM Parts and Their Impact on Mechanical Properties.* Metals, 2021. **11**(3).
86. Ryan, E.M., *On Wire and Arc Additive Manufacture of Aluminium.* 2018.
87. TWI, *POROSITY AND THE MECHANICAL PROPERTIES OF ALUMINIUM ALLOYS.* 2024.
88. Albannai, A.I., *A Brief Review on The Common Defects in Wire Arc Additive Manufacturing.* International Journal of Current Science Research and Review, 2022. **05**(12).
89. Sun, R., et al., *Microstructure, residual stress and tensile properties control of wire-arc additive manufactured 2319 aluminum alloy with laser shock peening.* Journal of Alloys and Compounds, 2018. **747**: p. 255-265.
90. Zhang, C., M. Gao, and X. Zeng, *Workpiece vibration augmented wire arc additive manufacturing of high strength aluminum alloy.* Journal of Materials Processing Technology, 2019. **271**: p. 85-92.
91. Shah, A., et al., *A Review of the Recent Developments and Challenges in Wire Arc Additive Manufacturing (WAAM) Process.* Journal of Manufacturing and Materials Processing, 2023. **7**(3).
92. Raut, L.P. and R.V. Taiwade, *Wire Arc Additive Manufacturing: A Comprehensive Review and Research Directions.* Journal of Materials Engineering and Performance, 2021. **30**(7): p. 4768-4791.
93. Niu, F., et al., *Additive manufacturing of 304 stainless steel integrated component by hybrid WAAM and LDED.* Materials Today Communications, 2023. **35**.
94. Al-Nabulsi, Z., et al., *Mechanical and X ray computed tomography characterisation of a WAAM 3D printed steel plate for structural engineering applications.* Construction and Building Materials, 2021. **274**.
95. Xu, F.J., et al., *Effect of deposition strategy on the microstructure and mechanical properties of Inconel 625 superalloy fabricated by pulsed plasma arc deposition.* Materials & Design, 2013. **45**: p. 446-455.
96. Kumar, M.D.B. and M. Manikandan, *Evaluation of Microstructure, Residual Stress, and Mechanical Properties in Different Planes of Wire + Arc Additive Manufactured Nickel-Based Superalloy.* Metals and Materials International, 2022. **28**(12): p. 3033-3056.
97. Goviazin, G.G., D. Rittel, and A. Shirizly, *Achieving high strength with low residual stress in WAAM SS316L using flow-forming and heat treatment.* Materials Science and Engineering: A, 2023. **873**.

98. Wu, Q., et al., *Residual stresses in wire-arc additive manufacturing – Hierarchy of influential variables.* Additive Manufacturing, 2020. **35**.

99. Serrati, D.S.M., et al., *Non-Destructive Testing Inspection for Metal Components Produced Using Wire and Arc Additive Manufacturing.* Metals, 2023. **13**(4).

100. Cong, B., J. Ding, and S. Williams, *Effect of arc mode in cold metal transfer process on porosity of additively manufactured Al-6.3%Cu alloy.* The International Journal of Advanced Manufacturing Technology, 2014. **76**(9-12): p. 1593-1606.

101. McLean, N., et al., *Effect of Hot Isostatic Pressing and heat treatments on porosity of Wire Arc Additive Manufactured Al 2319.* Journal of Materials Processing Technology, 2022. **310**.

102. Gu, J., et al., *The effect of inter-layer cold working and post-deposition heat treatment on porosity in additively manufactured aluminum alloys.* Journal of Materials Processing Technology, 2016. **230**: p. 26-34.

103. Steel, K., *Weld imperfections and preventive measures.* Kobelco Weld: Tokyo, Japan, 2015: p. 9-17.

104. Jafari, D., T.H.J. Vaneker, and I. Gibson, *Wire and arc additive manufacturing: Opportunities and challenges to control the quality and accuracy of manufactured parts.* Materials & Design, 2021. **202**.

105. Nguyen, T.C., et al., *High speed fusion weld bead defects.* Science and Technology of Welding and Joining, 2013. **11**(6): p. 618-633.

106. Ji, L., et al., *Research on Mechanisms and Controlling Methods of Macro Defects in TC4 Alloy Fabricated by Wire Additive Manufacturing.* Materials (Basel), 2018. **11**(7).

107. Shamir, M., et al., *Predicting the Effect of Surface Waviness on Fatigue Life of a Wire + Arc Additive Manufactured Ti-6Al-4V Alloy.* 2023.

108. Wandtke, K., et al., *Influence of the WAAM process and design aspects on residual stresses in high-strength structural steels.* Welding in the World, 2023. **67**(4): p. 987-996.

109. Albannai, A., et al., *Effects of tandem side-by-side GTAW welds on centerline solidification cracking of AA2024.* Manufacturing Technology, 2021. **21**(2): p. 151-163.

110. Yuan, L., et al., *Investigation of humping phenomenon for the multi-directional robotic wire and arc additive manufacturing.* Robotics and Computer-Integrated Manufacturing, 2020. **63**.

111. Li, Y., et al., *Analysis of additional electromagnetic force for mitigating the humping bead in high-speed gas metal arc welding.* Journal of Materials Processing Technology, 2016. **229**: p. 207-215.

112. Wu, C.S., F. Yang, and J. Gao, *Effect of external magnetic field on weld pool flow conditions in high-speed gas metal arc welding.* Proceedings of the Institution of Mechanical Engineers, Part B: Journal of Engineering Manufacture, 2014. **230**(1): p. 188-193.

113. Shoichi, M., et al., *Study on the application for electromagnetic controlled molten pool welding process in overhead and flat position welding.* Science and Technology of Welding and Joining, 2013. **18**(1): p. 38-44.

114. Nomura, K., Y. Ogino, and Y. Hirata, *Shape control of TIG arc plasma by cusp-type magnetic field with permanent magnet.* Welding International, 2012. **26**(10): p. 759-764.

115. H.W.CHOI, D.F.FARSON, and M.H.CHO, *Using a hybrid laser plus GMAW process for controlling the bead humping defects.* WELDING RESEARCH, 2006.

116. Meng, X., et al., *High speed TIG–MAG hybrid arc welding of mild steel plate.* Journal of Materials Processing Technology, 2014. **214**(11): p. 2417-2424.

117. K.H.LI, J.S.CHEN, and Y.M.ZHANG, *Double-Electrode GMAW Process and Control.* WELDING JOURNAL, 2007.

118. Kanemaru, S., et al., *Study for TIG–MIG hybrid welding process.* Welding in the World, 2014. **58**(1): p. 11-18.

119. J. Zähr, U.F., M. Hertel, M. Lohse, and M.S.a.M. Schnick, *Numerical and experimental studies of the influence of process gases in TIG welding.* Welding in the World, 2012.

120. Wang, L., et al., *Backward flowing molten metal in weld pool and its influence on humping bead in high-speed GMAW.* Journal of Materials Processing Technology, 2016. **237**: p. 342-350.

121. Wang, L., et al., *Influence of the external magnetic field on fluid flow, temperature profile and humping bead in high speed gas metal arc welding.* International Journal of Heat and Mass Transfer, 2018. **116**: p. 1282-1291.

122. Wang, L., et al., *Effects of malondialdehyde-induced protein modification on water functionality and physicochemical state of fish myofibrillar protein gel.* Food Research International, 2016. **86**: p. 131-139.

123. Nguyen, T.C., et al., *The humping phenomenon during high speed gas metal arc welding.* Science and Technology of Welding and Joining, 2005. **10**(4): p. 447-459.

124. Wu, D., et al., *Understanding of humping formation and suppression mechanisms using the numerical simulation.* International Journal of Heat and Mass Transfer, 2017. **104**: p. 634-643.
125. Cho, M.H. and D.F. Farson, *Understanding Bead Hump Formation in Gas Metal Arc Welding Using a Numerical Simulation.* Metallurgical and Materials Transactions B, 2007. **38**(2): p. 305-319.
126. Williams, S.W., et al., *Wire + Arc Additive Manufacturing.* Materials Science and Technology, 2016. **32**(7): p. 641-647.
127. Xu, F., et al., *Realisation of a multi-sensor framework for process monitoring of the wire arc additive manufacturing in producing Ti-6Al-4V parts.* International Journal of Computer Integrated Manufacturing, 2018. **31**(8): p. 785-798.
128. Newswire, P., *Global Aerospace Additive Manufacturing Market to Reach $1.9 Billion by 2026*, in *PR Newswire*. 2022.
129. Rolls_royce. *Rolls-Royce successfully completes 100% Sustainable Aviation Fuel test programme.* 2023; Available from: https://www.rolls-royce.com/media/press-releases/2023/13-11-2023-poweroftrent-rr-successfully-completes-100-sustainable-aviation-fuel-test-programme.aspx.
130. Chakraborty, D., et al., *The State of the Art for Wire Arc Additive Manufacturing Process of Titanium Alloys for Aerospace Applications.* Journal of Materials Engineering and Performance, 2022. **31**(8): p. 6149-6182.
131. WAAM3d. *ARA NOSE CONE.* 2022; Available from: https://www.waam3d.com/case-studies/ara-nose-cone.
132. WAAM3d. *TITANIUM TANK.* Available from: https://www.waam3d.com/case-studies/titanium-tank.
133. Huang, L., et al., *A Review of Challenges for Wire and Arc Additive Manufacturing (WAAM).* Transactions of the Indian Institute of Metals, 2023. **76**(5): p. 1123-1139.
134. Kerns, J., *Metal-AM-Autumn-2022-magazine.* 2022.
135. Josten, A. and M. Höfemann, *Arc-welding based additive manufacturing for body reinforcement in automotive engineering.* Welding in the World, 2020. **64**(8): p. 1449-1458.
136. Scott, C., *Dutch Students Create a Unique 3D Printed Metal Bicycle with Help from MX3D.* 2016.
137. Ya, W. and K. Hamilton, *On-Demand Spare Parts for the Marine Industry with Directed Energy Deposition: Propeller Use Case*, in *Industrializing Additive Manufacturing - Proceedings of Additive Manufacturing in Products and Applications - AMPA2017.* 2018. p. 70-81.
138. Osborne, A., *Army Corps of Engineers 3D Prints New Poe Lock Arrestor Arm.* 2024.
139. staff, A., *Consortium Builds Ship Propeller Via Wire plus Arc Additive Manufacturing (WAAM).* 2019.
140. Nota, C., et al., *A first feedback on manufacturing and in-service behaviour of a WAAM-made propeller for naval application.* Welding in the World, 2023. **67**(4): p. 1113-1121.
141. Mohon, L. *NASA Looks to Advance 3D Printing Construction Systems for the Moon and Mars.* 2020; Available from: https://www.nasa.gov/technology/manufacturing-materials-3-d-printing/nasa-looks-to-advance-3d-printing-construction-systems-for-the-moon-and-mars/.
142. Sher, D., *MX3D Bridge removed after two-year permit expires.* 2023.
143. MX3D. *CONNECTOR FOR TAKENAKA.* 2024; Available from: https://mx3d.com/industries/construction/connector-for-takenaka/.
144. MX3D. *OPTIMIZED TRUSS.* 2024; Available from: https://mx3d.com/integradde/.
145. Osborne, A., *Finland's Largest Metal 3D Print Withstands Pressure Vessel Test, Vastly Exceeding Expectations.* 2023.
146. MX3D. *IMPELLER.* 2024; Available from: https://mx3d.com/industries/oilgas/impeller/.
147. Chernovol, N., et al., *Effect of welding parameters on microstructure and mechanical properties of mild steel components produced by WAAM.* Welding in the World, 2022. **67**(4): p. 1021-1036.
148. Liberini, M., et al., *Selection of Optimal Process Parameters for Wire Arc Additive Manufacturing.* Procedia CIRP, 2017. **62**: p. 470-474.
149. Novelino, A.L.B., G.C. Carvalho, and M. Ziberov, *Influence of WAAM-CMT deposition parameters on wall geometry.* Advances in Industrial and Manufacturing Engineering, 2022. **5**.
150. He, C., et al., *Improvement of microstructure and fatigue performance of wire-arc additive manufactured 4043 aluminum alloy assisted by interlayer friction stir processing.* Journal of Materials Science & Technology, 2023. **133**: p. 183-194.
151. Liu, L., et al., *Tailoring the microstructure and mechanical properties of wire and arc additive manufactured Al–Mg alloy via interlayer friction stir processing.* Journal of Materials Research and Technology, 2023. **25**: p. 1055-1068.

152. Qie, M., J. Wei, and C. He, *Microstructure evolution and mechanical properties of wire-arc additive manufactured Al–Zn–Mg–Cu alloy assisted by interlayer friction stir processing.* Journal of Materials Research and Technology, 2023. **24**: p. 2891-2906.
153. Yuan, T., et al., *Enhanced strength-plasticity of 2319 Al-Cu alloy formed by hybrid interlayer friction stir processing and wire-arc additive manufacturing.* Journal of Materials Processing Technology, 2023. **321**.
154. Zhang, X., Y. He, and Y. Wei, *Adopting continuous multi-pass friction stir processing to enhance the wire-arc additive manufactured ER2319 thin-walled part.* CIRP Journal of Manufacturing Science and Technology, 2023. **46**: p. 230-241.
155. Fu, Y., et al., *Investigation of mechanical properties for hybrid deposition and micro-rolling of bainite steel.* Journal of Materials Processing Technology, 2017. **250**: p. 220-227.
156. Colegrove, P.A., et al., *Microstructure and residual stress improvement in wire and arc additively manufactured parts through high-pressure rolling.* Journal of Materials Processing Technology, 2013. **213**(10): p. 1782-1791.
157. Zhou, S., et al., *Periodic microstructure of Al–Mg alloy fabricated by inter-layer hammering hybrid wire arc additive manufacturing: Formation mechanism, microstructural and mechanical characterization.* Materials Science and Engineering: A, 2022. **860**.
158. Niu, F., et al., *Synchronous-hammer-forging-assisted wire arc additive manufacturing Al-Mg alloy.* Journal of Alloys and Compounds, 2023. **965**.
159. Honnige, J.R., P. Colegrove, and S. Williams, *Improvement of microstructure and mechanical properties in Wire + Arc Additively Manufactured Ti-6Al-4V with Machine Hammer Peening.* 2017.
160. Xiong, X., et al., *Grain Refinement and Strengthening Mechanisms of In-situ Follow-up Hammering-Assisted Wire Arc Additive Manufacturing for Hydraulic Turbine Blade Repairing.* Metals and Materials International, 2022. **29**(6): p. 1796-1814.
161. Kozamernik, N., D. Bračun, and D. Klobčar, *WAAM system with interpass temperature control and forced cooling for near-net-shape printing of small metal components.* The International Journal of Advanced Manufacturing Technology, 2020. **110**(7-8): p. 1955-1968.
162. Wu, B., et al., *The effects of forced interpass cooling on the material properties of wire arc additively manufactured Ti6Al4V alloy.* Journal of Materials Processing Technology, 2018. **258**: p. 97-105.
163. Chen, Y., et al., *Grain refinement and mechanical properties improvement of Inconel 625 alloy fabricated by ultrasonic-assisted wire and arc additive manufacturing.* Journal of Alloys and Compounds, 2022. **910**.
164. Xu, M., et al., *Effect of post-heat treatment on microstructure and mechanical properties of nickel-based superalloy fabricated by ultrasonic-assisted wire arc additive manufacturing.* Materials Science and Engineering: A, 2023. **863**.
165. Yuan, D., et al., *Improvement of the grain structure and mechanical properties of austenitic stainless steel fabricated by laser and wire additive manufacturing assisted with ultrasonic vibration.* Materials Science and Engineering: A, 2021. **813**.
166. Ermakova, A., et al., *The influence of laser shock peening on corrosion-fatigue behaviour of wire arc additively manufactured components.* Surface and Coatings Technology, 2023. **456**.
167. Jing, Y., et al., *Improved tensile strength and fatigue properties of wire-arc additively manufactured 2319 aluminum alloy by surface laser shock peening.* Materials Science and Engineering: A, 2023. **864**.
168. Ermakova, A., et al., *The effect of surface treatment and orientation on fatigue crack growth rate and residual stress distribution of wire arc additively manufactured low carbon steel components.* Journal of Materials Research and Technology, 2023. **24**: p. 2988-3004.
169. Kah, P., *Advancements in Intelligent Gas Metal Arc Welding Systems*. 2021, Science Direct: Elsevier
170. Tomar, B. and S. Shiva, *Cold metal transfer-based wire arc additive manufacturing.* Journal of the Brazilian Society of Mechanical Sciences and Engineering, 2023. **45**(3).
171. Stinson, H., et al., *Comparison of Properties and Bead Geometry in MIG and CMT Single Layer Samples for WAAM Applications.* Metals, 2021. **11**(10).
172. Senthil, T.S., et al., *Experimental investigations on the multi-layered SS316L wall fabricated by CMT-based WAAM: Mechanical and microstructural studies.* Journal of Alloys and Metallurgical Systems, 2023. **2**.
173. Manjhi, S.K., et al., *An Experimental Investigation on Microstructure, Mechanical Properties and Corrosion Performance of CMT-Wire Arc Additively Manufactured Al-4043 Alloy.* Transactions of the Indian Institute of Metals, 2023. **76**(10): p. 2745-2756.

174. Karmuhilan, M. and S. Kumanan, *Location-dependent microstructure analysis and mechanical behavior of inconel 625 using Cold Metal Transfer(CMT) based wire and arc additive manufacturing.* Vacuum, 2023. **207**.
175. Rodriguez, N., et al., *Wire and arc additive manufacturing: a comparison between CMT and TopTIG processes applied to stainless steel.* Welding in the World, 2018. **62**(5): p. 1083-1096.
176. Yin, C., et al., *Microstructure and mechanical properties of AZ91 magnesium alloy fabricated by multi-layer and multi-pass CMT based WAAM technique.* Results in Engineering, 2023. **18**.
177. Yang, T., et al., *Mechanical Properties and Growth Mechanism of TiB2-TiC/Fe Composite Coating Fabricated in Situ by Laser Cladding.* Applied Composite Materials, 2020. **27**(6): p. 877-893.
178. Zhuang, H., Q. Zhang, and D. Zhang, *Microstructure and Tribological Properties of Ni-Based Laser-Clad Coatings by Rare Earth Modification.* Journal of Thermal Spray Technology, 2021. **30**(5): p. 1410-1431.
179. Li, N., et al., *Laser Additive Manufacturing on Metal Matrix Composites: A Review.* Chinese Journal of Mechanical Engineering, 2021. **34**(1).
180. Chen, Z., et al., *Influence of trace silicon addition on microstructure and properties of Ti6Al4V fabricated by wire arc additive manufacturing.* Journal of Materials Research and Technology, 2023. **23**: p. 1347-1359.
181. Jiang, X., et al., *Improvement of mechanical properties and corrosion resistance for wire arc additive manufactured nickel alloy 690 by adding TiC particles.* Journal of Alloys and Compounds, 2022. **928**.
182. Wang, Z., et al., *Wire arc additive manufacturing of network microstructure (TiB+TiC)/Ti6Al4V composites using flux-cored wires.* Ceramics International, 2023. **49**(3): p. 4168-4176.
183. Koppu, A.K., et al., *Mechanical and Microstructure Investigation of TiC-inoculated SS316LSi Thin Wall Deposited by CMT-WAAM.* Transactions of the Indian Institute of Metals, 2023. **76**(8): p. 2307-2314.
184. Rooprai, R.S., A. Bansal, and J. Singh, *Influence of TiC powder content on wear behaviour of Inconel 625 clads developed by hybrid-mode wire arc additive manufacturing (WAAM) on EN-8 steel.* Tribology International, 2023. **189**.
185. Everton, S.K., et al., *Review of in-situ process monitoring and in-situ metrology for metal additive manufacturing.* Materials & Design, 2016. **95**: p. 431-445.
186. Sarker, I.H., *Machine Learning: Algorithms, Real-World Applications and Research Directions.* SN Comput Sci, 2021. **2**(3): p. 160.
187. Le, V.T., et al., *Efficient prediction of thermal history in wire and arc additive manufacturing combining machine learning and numerical simulation.* The International Journal of Advanced Manufacturing Technology, 2023. **126**(9-10): p. 4651-4663.
188. Li, W., et al., *Deep learning based online metallic surface defect detection method for wire and arc additive manufacturing.* Robotics and Computer-Integrated Manufacturing, 2023. **80**.
189. Hamrani, A., et al., *Applying machine learning to wire arc additive manufacturing: a systematic data-driven literature review.* Journal of Intelligent Manufacturing, 2023.
190. Chigilipalli, B.K. and A. Veeramani, *A machine learning approach for the prediction of tensile deformation behavior in wire arc additive manufacturing.* International Journal on Interactive Design and Manufacturing (IJIDeM), 2023.
191. Ogino, Y., S. Asai, and Y. Hirata, *Numerical simulation of WAAM process by a GMAW weld pool model.* Welding in the World, 2018. **62**(2): p. 393-401.
192. Zhao, H., et al., *Three-dimensional finite element analysis of thermal stress in single-pass multi-layer weld-based rapid prototyping.* Journal of Materials Processing Technology, 2012. **212**(1): p. 276-285.
193. Additive, G., *Get the Facts on… Heat Treatment.* 2021, GE Additive.
194. Chen, S., et al., *Modified heat treatment and related microstructure-mechanical property evolution of arc melting additively manufactured GH4169 Ni-based superalloy.* Journal of Alloys and Compounds, 2023. **947**.
195. Chen, Z. and G.S. Soh, *Microstructure and mechanical properties of Wire Arc Additive Manufactured (WAAM) Inconel 718 parts via post heat treatments.* Materials Today: Proceedings, 2022. **70**: p. 567-573.
196. Diao, Z., et al., *Effect of heat treatment on the microstructure and properties of CuCrZr alloy manufactured by wire arc additive manufacturing.* Journal of Alloys and Compounds, 2023. **967**.
197. Lyu, Z., et al., *Simultaneous enhancements of strength and ductility of wire arc additive manufactured 17-4PH steel via intrinsic heat treatment.* Journal of Materials Processing Technology, 2023. **321**.

198. O S, S. and B. Kuriachen, *Influence of build direction and heat treatment on the microstructure and tensile characteristics of cold metal transfer based wire arc additive manufactured SS 304L.* CIRP Journal of Manufacturing Science and Technology, 2023. **47**: p. 59-70.
199. Zhang, J., et al., *In-situ heat treatment (IHT) wire arc additive manufacturing of Inconel625-HSLA steel functionally graded material.* Materials Letters, 2023. **330**.
200. Zhao, Y., et al., *Mechanical properties, microstructural characteristics and heat treatment effects of WAAM stainless-steel plate material.* Journal of Building Engineering, 2023. **75**.
201. Ozaner, O.C., D. Klobcar, and A. Sharma, *Machining Strategy Determination for Single- and Multi-Material Wire and Arc Additive Manufactured Thin-Walled Parts.* Materials (Basel), 2023. **16**(5).
202. Tankova, T., et al., *Characterization of robotized CMT-WAAM carbon steel.* Journal of Constructional Steel Research, 2022. **199**.
203. Felice, I.O., et al., *Wire and arc additive manufacturing of Fe-based shape memory alloys: Microstructure, mechanical and functional behavior.* Materials & Design, 2023. **231**.
204. RAMLAB. *WAAM 101.* Available from: https://www.ramlab.com/resources/waam-101/.
205. Wikipedia. *Boriding*. 2023; Available from: https://en.wikipedia.org/wiki/Boriding.
206. MDC. *The BOROFUSE Process*. Available from: https://www.materialsdevelopment.com/borofuse-process/.
207. SCIENCE, C., *Boriding: the process of surface Hardening*. 2022, borates today.
208. Günen, A., et al., *A new approach to improve some properties of wire arc additively manufactured stainless steel components: Simultaneous homogenization and boriding.* Surface and Coatings Technology, 2023. **460**.
209. Chen, C., et al., *Effect of equivalent heat input on WAAM Al-Si alloy.* International Journal of Mechanical Sciences, 2023. **238**.
210. Vora, J., et al., *Experimental investigations on mechanical properties of multi-layered structure fabricated by GMAW-based WAAM of SS316L.* Journal of Materials Research and Technology, 2022. **20**: p. 2748-2757.
211. Md Israr Equbal, Parwez Alam, and R. Ohdar, *Effect of Cooling Rate on the Microstructure and Mechanical Properties of Medium Carbon Steel.* 2016.
212. Rafieazad, M., et al., *Microstructural evolution and mechanical properties of a low-carbon low-alloy steel produced by wire arc additive manufacturing.* The International Journal of Advanced Manufacturing Technology, 2019. **105**(5): p. 2121-2134.
213. Le, V.T. and D.S. Mai, *Microstructural and mechanical characteristics of 308L stainless steel manufactured by gas metal arc welding-based additive manufacturing.* Materials Letters, 2020. **271**.
214. Wang, J., et al., *Microstructure and mechanical properties of AZ31 magnesium alloy prepared using wire arc additive manufacturing.* Journal of Alloys and Compounds, 2023. **939**.
215. Wang, J., et al., *Microstructural and defect evolution during WAAM resulting in mechanical property differences for AA5356 component.* Journal of Materials Research and Technology, 2023. **22**: p. 982-996.
216. Chaudhari, R., et al., *Effect of multi-walled structure on microstructure and mechanical properties of 1.25Cr-1.0Mo steel fabricated by GMAW-based WAAM using metal-cored wire.* Journal of Materials Research and Technology, 2022. **21**: p. 3386-3396.
217. Anand, M., et al., *Fabrication of multilayer thin wall by WAAM technique and investigation of its microstructure and mechanical properties.* Materials Today: Proceedings, 2022. **56**: p. 927-930.
218. Yu, H., et al., *Differences between Tensile Properties of WAAM SS304 Components in Different Directions.* steel research international, 2023. **94**(8).
219. Anand, S., et al., *Experimental investigation on microstructure and mechanical property of wire arc additively manufactured SS308L built part.* Sādhanā, 2023. **48**(4).
220. Chigilipalli, B.K. and A. Veeramani, *Investigation of the Corrosion Behavior of Wire Arc Additively Manufactured Alloy 825.* Transactions of the Indian Institute of Metals, 2022. **76**(2): p. 279-286.
221. Chen, C., et al., *Improvement of microstructure and mechanical properties of stainless steel TIG based wire arc additive manufacturing by using AC/DC mix current waveform.* Journal of Materials Research and Technology, 2023. **23**: p. 4355-4366.
222. Shi, B., et al., *Weld morphology, microstructure evolution, and mechanical properties of laser beam welding of wire arc additive manufactured Al-Cu substrate.* The International Journal of Advanced Manufacturing Technology, 2022. **127**(3-4): p. 1935-1949.
223. Veiga, F., et al., *Effect of the Heat Input on Wire-Arc Additive Manufacturing of Invar 36 Alloy: Microstructure and Mechanical Properties.* Welding in the World, 2022. **66**(6): p. 1081-1091.

224. Bayar, İ. and M. Ulutan, *Investigation of microstructure and mechanical properties of SiC and FeCrC reinforced components fabricated with plasma wire arc additive manufacturing (P-WAAM).* Materials Science and Engineering: A, 2023. **875**.
225. Cai, X., et al., *Effects of deposition paramaters on the microstructure evolution of wire arc additive manufactured Al–Zn–Mg–Cu alloy.* Journal of Materials Research and Technology, 2023. **26**: p. 1572-1583.
226. Pandey, A. and V. Gaur, *Effect of dwell time on fatigue properties of wire-arc additively manufactured IN718 alloy.* International Journal of Fatigue, 2023. **176**: p. 107863.
227. Niaki, M.K., S.A. Torabi, and F. Nonino, *Why manufacturers adopt additive manufacturing technologies: The role of sustainability.* Journal of Cleaner Production, 2019. **222**: p. 381-392.
228. Mojtaba Khorram Niaki and F. Nonino, *The management of additive manufacturing.* 2018.
229. Lawand, L., et al. *Industrialization of Additive Manufacturing: Assessing the Impact of Excess Margins on Manufacturing Costs.* in *Design in the Era of Industry 4.0, Volume 3.* 2023. Singapore: Springer Nature Singapore.
230. Jin, W., et al., *Wire Arc Additive Manufacturing of Stainless Steels: A Review.* Applied Sciences, 2020. **10**(5).
231. Kistler, N.A., et al., *Effect of processing conditions on the microstructure, porosity, and mechanical properties of Ti-6Al-4V repair fabricated by directed energy deposition.* Journal of Materials Processing Technology, 2019. **264**: p. 172-181.
232. Hamza, S., et al., *Simulated Heat Affected Zone in Welded Stainless Steel 304l.* Acta Metallurgica Slovaca, 2019. **25**(3): p. 142-149.
233. ASTM, *ASTM E384: Standard Test Method for Microindentation hardness of Materials/ ISO 6507.*
234. Kamble, A.G. and R.V. Rao, *Experimental investigation on the effects of process parameters of GMAW and transient thermal analysis of AISI321 steel.* Advances in Manufacturing, 2013. **1**(4): p. 362-377.
235. Wang, S., et al., *The Influence of Heat Input on the Microstructure and Properties of Wire-Arc-Additive-Manufactured Al-Cu-Sn Alloy Deposits.* Metals, 2020. **10**(1): p. 79.
236. Lawrence, A., et al., *Specific Energy Consumption/Use (SEC) in Energy Management for Improving Energy Efficiency in Industry: Meaning, Usage and Differences.* Energies, 2019. **12**(2): p. 247.
237. Nigam, A., et al., *Effect of inlet gas velocity on laminar flow behavior in shielding device for WAAM process.* Materials Today: Proceedings, 2023. **80**: p. 298-306.
238. Manokruang, S., *Phenomenological_model_of_thermal_effects_on_weld.* 2022.
239. Yehorov, Y., L.J. da Silva, and A. Scotti, *Exploring the use of switchback for mitigating homoepitaxial unidirectional grain growth and porosity in WAAM of aluminium alloys.* The International Journal of Advanced Manufacturing Technology, 2019. **104**(1): p. 1581-1592.
240. Goett, G., et al., *Emissivity and temperature determination on steel above the melting point.* Welding in the World, 2013. **57**(4): p. 595-602.
241. Wang, L., et al., *Evolution of Microstructure and Mechanical Property of Wire Arc Additive Manufactured Al–Cu Metallic Component after Simulated Thermal Service.* Metals and Materials International, 2023. **29**(12): p. 3679-3696.
242. Fonseca, P.P., et al., *Orthogonal cutting of Wire and Arc Additive Manufactured parts.* The International Journal of Advanced Manufacturing Technology, 2022. **119**(7-8): p. 4439-4459.
243. E112-13(2021), A., *Grain Size Determination.* 2021.
244. Treutler, K., et al., *Properties oriented WAAM—microstructural and geometrical control in WAAM of low-alloy steel.* Welding in the World, 2023. **68**(2): p. 247-257.
245. Rosli, N.A., et al., *Analysis of microstructure and mechanical properties of micro-plasma arc-welding-based additive manufacturing.* Progress in Additive Manufacturing, 2024.
246. Laghi, V., et al., *Mechanical and microstructural features of wire-and-arc additively manufactured carbon steel thick plates.* The International Journal of Advanced Manufacturing Technology, 2023. **127**(3-4): p. 1391-1405.
247. Pereira, T., J.V. Kennedy, and J. Potgieter, *A comparison of traditional manufacturing vs additive manufacturing, the best method for the job.* 2019.
248. Crimp, M.A. and K.M. Vedula, *The relationship between cooling rate, grain size and the mechanical behavior of B2 Fe□Al alloys.* Materials Science and Engineering: A, 1993. **165**(1): p. 29-34.
249. Otto, A. and M. Schmidt, *Towards a universal numerical simulation model for laser material processing.* Physics Procedia, 2010. **5**: p. 35-46.
250. Greg Stuart, Nelson Spruston, and M. Hausser, *dendrites_fiala_harris_dendrite_structure.* 1999.

251. Pal, S., et al., *Evolution of the metallurgical properties of Ti-6Al-4V, produced with different laser processing parameters, at constant energy density in selective laser melting.* Results in Physics, 2020. **17**.

252. Pelleg, J., *Grain Size Effect on Mechanical Properties*, in *Mechanical Properties of Silicon Based Compounds: Silicides*, J. Pelleg, Editor. 2019, Springer International Publishing: Cham. p. 243-254.

253. Xu, Z.-z., et al., *Relationships between microhardness, microstructure, and grain orientation in laser-welded joints with different welding speeds for Ti6Al4V titanium alloy.* Transactions of Nonferrous Metals Society of China, 2020. **30**(5): p. 1277-1289.

254. Lam, T.F., et al., *Adaptive process control implementation of wire arc additive manufacturing for thin-walled components with overhang features.* The International Journal of Advanced Manufacturing Technology, 2019. **108**(4): p. 1061-1071.

255. Ga, B., N. Gardan, and G. Wahu, *Methodology for Part Building Orientation in Additive Manufacturing.* Computer-Aided Design and Applications, 2018. **16**(1): p. 113-128.

256. Roschli, A., et al., *Designing for Big Area Additive Manufacturing.* Additive Manufacturing, 2019. **25**: p. 275-285.

257. Giannatsis, J. and V. Dedoussis, *Decision support tool for selecting fabrication parameters in stereolithography.* The International Journal of Advanced Manufacturing Technology, 2006. **33**(7-8): p. 706-718.

258. Evjemo, L.D., et al., *Wire-arc additive manufacturing of structures with overhang: Experimental results depositing material onto fixed substrate.* CIRP Journal of Manufacturing Science and Technology, 2022. **38**: p. 186-203.

259. Bidare, P., et al., *Porosity, cracks, and mechanical properties of additively manufactured tooling alloys: a review.* Advances in Manufacturing, 2021. **10**(2): p. 175-204.

260. Sedlaček, M., A.Z. Guštin, and B. Žužek, *Influence of Laser Surface Texturing Sequence on Fatigue Properties of Coated Cold Work Tool Steel.* Metals, 2020. **10**(12).

261. Li, S., et al., *Microstructures and properties of wire-arc additively manufactured 5356 aluminium alloy protected by different proportions of nitrogen and argon.* Journal of Materials Science, 2021. **56**(31): p. 17785-17804.

262. Kesarwani, S. and N. Yuvaraj, *Optimization of CMT-WAAM process parameters to minimize the porosity and surface roughness in bimetallic wall of aluminium alloys.* Welding in the World, 2024.

263. Zhang, X., et al., *Effect of Pre-strain on High-Temperature Oxidation Behavior of Inconel 617 Superalloy Fabricated by Wire Arc Additive Manufacturing at 900 °C.* Journal of Materials Engineering and Performance, 2024.

264. Ferreira, R.P., L.O. Vilarinho, and A. Scotti, *Development and implementation of a software for wire arc additive manufacturing preprocessing planning: trajectory planning and machine code generation.* Welding in the World, 2022. **66**(3): p. 455-470.

265. Zhang, C., et al., *Influence of wire-arc additive manufacturing path planning strategy on the residual stress status in one single buildup layer.* The International Journal of Advanced Manufacturing Technology, 2020. **111**(3-4): p. 797-806.

266. Chaudhari, R., et al., *Parametric Study and Investigations of Bead Geometries of GMAW-Based Wire–Arc Additive Manufacturing of 316L Stainless Steels.* Metals, 2022. **12**(7).

267. Holzinger, C., S. Peters, and A. Trummer, *3DWelding – additive Herstellung von Stahlbaukomponenten.* Stahlbau, 2023. **92**(5): p. 318-326.

268. Xiong, J., G. Zhang, and W. Zhang, *Forming appearance analysis in multi-layer single-pass GMAW-based additive manufacturing.* The International Journal of Advanced Manufacturing Technology, 2015. **80**(9-12): p. 1767-1776.

269. Mishra, I. and R. Srivastava, *Thermal simulation of Al alloy developed by wire arc additive manufacturing using finite element analysis.* International Journal on Interactive Design and Manufacturing (IJIDeM), 2024.

270. Gokhale, N.P. and P. Kala, *Thermal analysis of TIG-WAAM based metal deposition process using finite element method.* Materials Today: Proceedings, 2021. **44**: p. 453-459.

271. Wang, Y., et al., *Coordinated monitoring and control method of deposited layer width and reinforcement in WAAM process.* Journal of Manufacturing Processes, 2021. **71**: p. 306-316.

Tesi redatta con il sostegno finanziario del programma
FSE-REACT-EU, PON "Ricerca e Innovazione" 2014-2020 (D.M. 1061/2021)
Asse IV "Istruzione e ricerca per il recupero – REACT-EU"
Azione IV.4 "Dottorati e Contratti di ricerca su tematiche dell'innovazione"